

The Influence of Microstructure and Nanostructure on Magnetization and its Temporal
Decay in Bi:2212 and YBCO Superconductors at Low Temperatures

Dissertation

Presented in Partial Fulfillment of the Requirements for the Degree Doctor of Philosophy
in the Graduate School of The Ohio State University

By

Cory Myers

Graduate Program in Materials Science and Engineering

The Ohio State University

2020

Dissertation Committee

Prof. Michael D. Sumption, Advisor

Prof. Tyler Grassman

Prof. Alan Luo

Dr. Xiaorong Wang, External Co-advisor

Copyrighted by

Cory Steven Myers

2020

Abstract

This work has shown that the magnetization and magnetic flux creep of Bi:2212 and YBCO superconductors are strongly influenced by their geometry, microstructure, and nanostructures. By modifying these, magnetization and flux creep can be altered. Bridging between filaments in Bi:2212 wire composites has been shown to lead to increased persistent current magnetization, and its subsequent decay, in the composite. The bridging increases the current loop area in the composite and therefore also the magnetization. Thus, the amount of observed magnetization is influenced by sample length and the presence of wire twist pitch. The decay rate was also seen to increase suggesting that the pinning strength of the bridges are lower than the filaments themselves. The influence that additions to the YBCO nanostructure, such as Y211 precipitates and BZO nanocolumns have on the magnetic properties have been studied. It has been shown that, whereas Y211 additions can increase the composite critical current density (J_c), these additions do not increase the strength of the individual pins. The magnetization of cabled strands (cables) of HTS composites has also been studied and shown to be influenced by the cabling geometry, and the magnetization decay of cables at low to moderate fields is modified by the higher flux penetration fields of cables.

The implications of these results for precision field applications has also been explored. High temperature superconductor (HTS) composites, such as Bi:2212 wire and

YBCO-based tapes, are being considered to make future high field magnets for particle accelerators, which require higher magnetic fields than currently achievable with low-temperature superconductor (LTS) composites. High magnetization and decay are unwanted because the magnetization and its decay can lead to high values of field error and field error drift in magnets made from the composites. However, the magnetization and its subsequent decay of HTS composites is shown to be much higher than in low temperature superconducting (LTS) composites even near 4 K. Field excitation profiles to minimize these effects are explored.

Dedication

This document is dedicated to my family and friends. My mom and dad have been very supportive of my studies throughout my life. When I was young my dad always made time to help me with my schoolwork after he came home from work in the evening. Sadly, my mom passed away a few weeks before my defense. She was not able to see me graduate, but I know that she was proud of my work.

Acknowledgments

I would like to thank Dr. Sumption, Dr. Collings, and Dr. Xiaorong Wang (who served as my co-advisor at Berkeley National Laboratory), for the guidance and support they have given me throughout the completion of my work. I would also like to thank the members of my dissertation committee, Dr. Grassman and Dr. Luo, for their advice and constructive criticism. I would also like to thank Dr. Daehn for his advice during the overview process. In addition, I would like to thank the co-workers and colleagues with whom I have worked while at The Ohio State University, including but not limited to Michael Susner, Scot Bohnenstiehl, Yuan Yang, Milan Majoros, Chris Kovacs, Mohammed Mahmud, Yuan Yang, Guangze Li, Hyun-Sung Kim, Yi Ding, Danlu Zhang, Fang Wan, Jacob Rochester, and Xingchen Xu. Furthermore, I would like to thank the staff of the Department of Materials Science and Engineering, particularly Ken Kushner, Ross Baldwin, Steve Bright, Mark Cooper, and Mei Wang. Additionally, I would like to thank Henk Colijn, Cameron Begg, and Dan Huber of the Campus Electron Optics Facility for their help with XRD, TEM, SEM, and FIB training. I would also like to thank the United States Department of Energy, Office of High Energy Physics for their financial support under Contract No. DE-AC02-05CH11231 and part of the work was supported under grant No. DE-SC0011721. Additionally, a portion of this work was performed at Lawrence Berkeley National Laboratory, and I would like

to thank the scientists and technicians who gave me useful advice and made me feel welcome during my stay, and I would like thank the Department of Energy for funding the work under the Science Graduate Student Research program. Finally, and most importantly, I would like to acknowledge the support of my loving family.

Vita

2008.....B.A. Physics, Ohio Wesleyan University

2014.....M.S. Materials Science and Engineering,

The Ohio State University

2014 to present.....PhD candidate, Department of Materials

Science and Engineering, The Ohio State

University

Publications

1. C. Myers, M. D. Sumption, and E. W. Collings, *Magnetization and Creep in YBCO Tape and CORC Cables for Particle Accelerators: Value and Modification Via Preinjection Cycle*, IEEE Trans. Appl. Supercon. 29 (2019) 8201405, DOI: 10.1109/TASC.2019.2898119

2. L. Brouwer, S. Caspi, K. Edwards, A. Godeke, R. Hafalia, A. Hodgkinson, A. Huggins, C. Myers, S. Myers, M. Schillo, J. Taylor, M. Turqueti, X. Wang, W. Wan, and S. Prestemon, *Design and test of a curved superconducting dipole magnet for proton therapy*, Nuclear Instrument and Methods in Physical Research, 957, 163414 doi: <https://doi.org/10.1016/j.nima.2020.163414>.

3. C. Myers, M. D. Sumption, and E. W. Collings, *Magnetization and Flux Penetration of YBCO CORC Cable Segments at the Injection Fields of Accelerator Magnets*, IEEE Trans. Appl. Supercon. 29 (2019) 4701105, DOI: 10.1109/TASC.2019.2896625

4. E. W. Collings, M. D. Sumption, C. S. Myers, X. Wang, D. R. Dietderich, K. Yagotyntsev and A. Nijhuis, *Persistent-current magnetizations of Nb₃Sn Rutherford cables and extracted strands*, IOP Conf. Series: Materials Science and Engineering 279 (2017) 012037 doi:10.1088/1757-899X/279/1/012037

5. C. S. Myers, H. Miao, Y. Huang, M. D. Sumption, and E. W. Collings, *Reduced Magnetization and Loss in Ag-Mg Sheathed Bi2212 wires: Systematics with Sample Twist Pitch and Length*, IEEE Trans. Appl. Supercon. 25 (2015) 8201604, DOI: 10.1109/TASC.2014.2372614

6. C. S. Myers, M. A. Susner, L. Motowidlo, J. Distin, M. D. Sumption, and E. W. Collings, *Specific Heats of Composite Bi2212, Nb₃Sn, and MgB₂ Wire Conductors*, IEEE Trans. Appl. Supercond. 23 (2013). 8800204 doi: 10.1109/TASC.2013.2246812

7. C. S. Myers, M. A. Susner, L. Motowidlo, J. Distin, M. D. Sumption, and E. W. Collings, *Transport, Magnetic, and SEM Characterization of a Novel Design Bi-2212 Strand*, IEEE Trans. Appl. Supercond. 21 (2011) 2804-2807 doi: 10.1109/TASC.2010.2093494

8. M. Majoros, M. Kanuchova, M. A. Susner, M. D. Sumption, C. S. Myers, S. D. Bohnenstiehl, and E. W. Collings, *Effects of Heat Treatments on the Properties of SmFeAsO_{1-x}F_x Oxyprictide Bulks Prepared via a Single-Step Route*, IEEE Trans. Appl. Supercond. 21 (2011) 2853-2857 doi: 10.1109/TASC.2010.2080253

9. R. A. Kaye, C. S. Myers, J. Döring, S. L. Tabor, S. M. Gerbick, T. D. Baldwin, D. B. Campbell, C. Chandler, M. W. Cooper, M. A. Hallstrom, C. R. Hoffman, J. Pavan, L. A. Riley, and M. Wiedeking, *Linear polarization measurements and negative-parity states in Sr-80*, Phys. Rev. C 78, 037303 doi: 10.1103/PhysRevC.78.037303

Fields of Study

Major Field: Materials Science and Engineering

Table of Contents

Abstract.....	ii
Dedication.....	iv
Acknowledgments.....	v
Vita.....	vii
List of Tables	xi
List of Figures.....	xiii
Chapter 1. Introduction and Motivation.....	1
Chapter 2. Experimental Methods	42
Chapter 3: Bi:2212 Microstructure and Magnetic Property Correlation	49
Chapter 4: YBCO Nanostructure, Additions, and Magnetic Property Correlation	93
Chapter 5: Magnetic Properties of Cables and their Influence on Accelerator Magnets	143
Chapter 6: Effects of Magnetization and Creep on Magnetic Field Error in HTS Accelerator Magnets	189
Chapter 7: Summary and Conclusions.....	256
Appendix A: List of Acronyms.....	269
Appendix B: List of Latin Symbols	271
Appendix C: List of Greek Symbols.....	276
Bibliography	278

List of Tables

Table 1. γ_2 extracted using the linear part of equation 3.4. Published in [70].	70
Table 2. Bi:2212 2D-ROSS strand specifications. Published in [80].	83
Table 3. Physical parameters of the strands. Published in [80].	84
Table 4. Critical current vs peak melt temperature of strands measured at 4.2 K and self-field. Published in [80].	85
Table 5. Critical current density, d_{eff} , filament and subelement sizes of strands measured at 12 T. Published in [80].	88
Table 6. YBCO thin film specifications	101
Table 7. Comparison of J_{cs} of the PLD and MOCVD processed samples.	106
Table 8. Comparison of J_{c} modification and raw decay measurements in PLD and MOCVD samples.	118
Table 9. Fitting parameters for the PLD processed sample magnetic relaxation measurements.	132
Table 10. Extracted pinning parameters from the PLD sample measurements	132
Table 11. Fitting parameters for the MOCVD sample magnetic relaxation measurements	136
Table 12. Extracted pinning parameters for the MOCVD processed samples	137
Table 13. Extracted pinning parameters for the MOCVD processed samples	140
Table 14. Extracted pinning parameters for the PLD processed samples.	141
Table 15. Parameters of the CORC [®] wire used for the present measurements, data from [3].	156
Table 16. Initial magnetization and change in magnetization (ΔM) of the 2G HTS tape and the CORC [®] cable sample. Published in [111].	169
Table 17. The parameter values used to reproduce the CORC [®] cable hysteresis loop. .	223

Table 18. The calculated and measured harmonics at 77 K at the magnet center. 240
Table 19. The calculated and measured field harmonics at 4 K at the magnet center.... 248

List of Figures

Figure 1. The superconducting phase diagram of a HTS, from [7].	7
Figure 2. Plot of critical current density vs applied magnetic field for various superconducting composites, from [8].	8
Figure 3. A schematic illustration of a fluxon showing the coherence length, penetration depth, and supercurrent flow [10].	13
Figure 4. A schematic of fluxons inside a superconducting slab.	14
Figure 5. A schematic of the flux density gradient in a semi-infinite slab of superconductor. Here H is $\mu_0 H$	20
Figure 6. A schematic illustration of how different pinning strengths affect the flux density gradient in a semi-infinite slab of superconductor. Stronger pinning generates larger gradients.	22
Figure 7. The magnetic field profile inside a superconductor in the Bean critical state model as the applied field is increased from zero.	23
Figure 8. The magnetic field profile inside a superconductor in the Bean critical state model as the applied field is decreased.	24
Figure 9. The hysteresis loop of a type-II superconductor according to the Bean critical state model.	26
Figure 10. The current density distribution in an isotropic semi-infinite superconducting slab.	27
Figure 11. (Left) An example of the magnetic relaxation in a YBCO single crystal, measured using different temperatures, from [10]. (Right) Magnetic relaxation in a Bi:2212 single crystal in different externally applied magnetic fields, from [31]	33
Figure 12. A schematic of a nonlinear functional form of $U(J)$ at a constant externally applied magnetic field. The approximation leads to an effective pinning potential which is smaller than the true potential $U_0 (J = 0)$. J_c is the critical current density, from [10].	35

Figure 13. (a) Plots of $T \ln(dM/dt)$ vs $M - M_{eq}$ for different temperatures. (b) Plots of the same data as in (a), but with a constant for each temperature ($C = 18$) added to each data set, after [45].	37
Figure 14. The field harmonic drift of accelerator magnets during particle injection, after [50].	38
Figure 15. (Left) A schematic of the process used to make Bi:2212 strands. (Right) The unreacted cross-section of a strand [69].	53
Figure 16. The microstructure of a Bi:2212 round wire after heat treatment. During heat treatment, liquid from filaments can traverse the matrix and connect with other filaments. These connections can remain after cooling and may carry significant current.	55
Figure 17. A schematic illustration of the shielding current flow in two uncoupled filaments in a strand subjected to a perpendicular magnetic field. The red arrows are the current.	56
Figure 18. A schematic illustration of the shielding current flow in two bridged (or coupled) filaments in a strand subjected to a perpendicular magnetic field.	57
Figure 19. $M - \mu_0 H$ of twisted coil samples with different L_p s plotted alongside $M - \mu_0 H$ s of non-twisted coil samples with similar L . The magnetization of the twisted samples is significantly reduced compared to the non-twisted samples. Published in [70].	61
Figure 20. $M - \mu_0 H$ of non-twisted coil samples with various lengths, L . The magnetization clearly depends upon L . Published in [70].	62
Figure 21. 12 T d_{eff} vs sample length for twisted and non-twisted samples. d_{eff} of the twisted samples is clearly smaller than that of the corresponding non-twisted sample. Published in [70].	64
Figure 22. Dependence of 12 T d_{eff} on sample length or twist pitch. Published in [70].	66
Figure 23. Transverse SEM micrographs of Bi:2212 coil strand cross-sections showing filamentary bundles being nearly fully bridged.	71
Figure 24. Transverse SEM micrographs of Bi:2212 coil strand cross-sections showing filamentary bundle bridging and inter-bundle bridging.	72
Figure 25. SEM micrographs of longitudinal cross-sections of Bi:2212 strands.	73
Figure 26. Longitudinal cross-section of a strand extracted from a Bi:2212 coil sample with lines drawn to count bridge intercepts.	74

Figure 27. The magnetic relaxation of the non-twisted Bi:2212 strand samples of different lengths.	76
Figure 28. The magnetic relaxation of Bi:2212 strand samples with different twist pitches.	78
Figure 29. The magnetic relaxation of Bi:2212 strand samples with different lengths and twist pitches.	79
Figure 30. The effective pinning potential, U_{eff} , extracted for the non-twisted samples and twisted samples as a function of L or L_p . The lines are guides to the eye.....	80
Figure 31. (Left) Cross-sections of the 2D-ROSS-186 aspected filament (filament size ~ 20 x 50 μm) design after heat treating with a melt temp. of 886°C, and (Right) the CONV-7-37 design (fil. size ~ 20 μm) with an optimization temp. of 890°C. Published in [80]......	83
Figure 32. (Left) SEM micrograph of the transverse section of the 2D-ROSS-186 strand with HT at 886°C. (Right) The CONV-7-37 design with HT at 890°C. Fewer bridges are in the 2D-ROSS-186 strand compared to the conventional design. Published in [80].....	86
Figure 33. The critical current dependence on applied magnetic field at 4.2 K for the 2D-ROSS-186 and CONV-7-37 strands. Published in [80]......	87
Figure 34. (Left) DC susceptibility for the 2D-ROSS-186 design and (Right) DC susceptibility for the CONV-7-37 design. Published in [80]......	89
Figure 35. 4.2 K $M-\mu_0H$ of 2D-ROSS-186 and (Right) 4.2 K $M-\mu_0H$ of CONV-7-37. Published in [80]......	90
Figure 36. Conceptual “Washboard Potential” local energy for fluxon as a function of distance into the center of a superconductor in the shielding mode (outside of conductor to left, and inside to right), after [6]......	97
Figure 37. The 5 K $M-\mu_0H$ of the PLD processed samples with Y211 and BZO additions. The moment is normalized to the superconductor volume.	104
Figure 38. The 4.2 K $M-\mu_0H$ of the MOCVD processed samples with BZO additions. The moment is normalized to the superconductor volume.	105
Figure 39. TEM image of Y211 precipitates in the YBCO matrix. The precipitates were approximately 100 nm by 30 nm. From [83]......	107
Figure 40. TEM image of BZO nanocolumns in the PLD processed YBCO thin film matrix. From [83]......	108

Figure 41. BZO nanocolumns in the YBCO thin film matrix. The width of the columns is 4-6 nm. From [55].	109
Figure 42. BZO nanocolumns shown threading the entire YBCO thin film thickness. From [55].	110
Figure 43. Schematic illustration of the Y211 precipitates in the PLD grown YBCO thin film matrix. The precipitates are sparse and short, with height = 100 nm, width = 30 nm, and spacings of approximately 200 nm.	111
Figure 44. Schematic illustration of the BZO precipitates in the MOCVD grown YBCO thin film matrix. The precipitates are dense, long, and thinner than the Y211 precipitates.	112
Figure 45. The magnetic relaxation of the PLD processed samples at 1 T, 5 K. Additions of 10 vol. % Y211 reduce the overall relaxation rate slightly whereas the addition of 5 vol.% Y211 increases the relaxation rate.	114
Figure 46. The magnetic relaxation of the PLD processed samples at 8 T, 5 K. Additions of 10 vol. % Y211 reduce the overall relaxation rate slightly (and less so than at 1 T) whereas the addition of 5 vol.% Y211 again increases the relaxation rate.	115
Figure 47. The magnetic relaxation of the MOCVD processed samples at 1 T, 4 K. Additions of Zr reduce the overall relaxation rate by about 1.5 X, but there is little difference in the rate for the samples with additions.	116
Figure 48. The magnetic relaxation of the MOCVD processed samples at 8 T, 4 K. Additions of 25 mol.% Zr reduce the overall relaxation rate by about 1.6 X over the control sample. There is some difference in the relaxation rate of the 7.5% and 25% Zr-added samples.	117
Figure 49. The creep rate, r , extracted using (4.6) for the MOCVD processed control sample (open symbols) and the 25 mol.% Zr-added MOCVD sample (closed symbols).	122
Figure 50. U_{eff} extracted by fitting the magnetic relaxation data to the creep equation, (4.6), assuming the potential has a linear dependence on J for the MOCVD control (open symbols) and the 25 mol.% Zr-added MOCVD samples (closed symbols).	123
Figure 51. The percentage of the moment from the sample that exist at the beginning of the relaxation measurement, after 1200 s, for the MOCVD processed control sample (open symbols) and the 25 mol.% Zr-added MOCVD (closed symbols).	124

Figure 52. Magnetic relaxation-generated $U(J)$ for the PLD processed control sample. Measurements are shown for 65, 60, 50, 40, 30, 20, 10, and 5 K. At each temperature, measurements were made at 1 T, 2 T, 6 T, and 8 T.....	128
Figure 53. Magnetic relaxation-generated $U(J)$ for the 5 vol.% Y211 sample. Measurements are shown for 77, 70, 65, 60, 50, 40, 30, 20, 10, and 5 K. At each temperature, measurements were made at 1 T, 2 T, 6 T, and 8 T.....	129
Figure 54. Magnetic relaxation-generated $U(J)$ for the 10 vol.% Y211 sample. Measurements are shown for 77, 70, 65, 60, 50, 40, 30, 20, 10, and 5 K. At each temperature, measurements were made at 1 T, 2 T, 6 T, and 8 T.....	130
Figure 55. Magnetic relaxation-generated $U(J)$ for the 2 vol.% BZO sample. Measurements are shown for 65, 60, 50, 40, 30, 20, 10, and 5 K. At each temperature, measurements were made at 1 T, 2 T, 6 T, and 8 T.....	131
Figure 56. Magnetic relaxation-generated $U(J)$ for the MOCVD control sample. Measurements are shown for 60, 50, 30, 20, 10, and 4 K. At each temperature, measurements were made at 1 T, 2 T, 6 T, and 8 T.....	134
Figure 57. Magnetic relaxation-generated $U(J)$ for the MOCVD 7.5 mol.% Zr-added sample. Measurements are shown for 60, 50, 40, 30, 20, 10, and 4 K. At each temperature, measurements were made at 1 T, 2 T, 6 T, and 8 T.....	135
Figure 58. Magnetic relaxation-generated $U(J)$ for the MOCVD 25 mol.% Zr-added sample. Measurements are shown for 60, 50, 30, 20, 10, and 4 K. At each temperature, measurements were made at 1 T, 2 T, 6 T, and 8 T.....	136
Figure 59. 1 T magnetic relaxation-generated $U(J)$ for the PLD processed samples.	139
Figure 60. 1 T magnetic relaxation-generated $U(J)$ for the MOCVD processed samples.	140
Figure 61. A CORC [®] wire (top of figure) and CORC [®] cable (bottom of figure), from [99]......	146
Figure 62. The 12 T conduction-cooled superconducting magnet system used to measure the magnetic properties of the superconducting cables. The central gray cylinder is the cryogen-free magnet with a room temperature bore.....	148
Figure 63. The sample holder used to mount the cable samples.	149
Figure 64. A CORC [®] cable section mounted onto the end of the sample holder. GE varnish is used to adhere the ends of the sample to the holder.	150

Figure 65. A schematic of the Hall probe magnetometer sample mounting setup [103].	152
Figure 66. Plot of expected nickel magnetic moment vs measured background corrected magnetic flux density. A value of the constant which converts B_z to m is extracted by a linear fit to the data. Published in [103].	154
Figure 67. The 4.5 T $M-\mu_0H$ loop of the CORC [®] cable sample. The moment has been normalized to the cable volume. Published in [103].	158
Figure 68. The 8 T $M-\mu_0H$ loop of the CORC [®] cable sample. The moment has been normalized to the cable volume. Published in [103].	159
Figure 69. The 4 K $M-\mu_0H$ loops of the CORC [®] cable sample and a tape extracted from the sample. The magnetic moment has been normalized to the total volume of tape. ...	161
Figure 70. The $M-\mu_0H$ loops of the CORC [®] sample measured during various field cycles (“pre-injection cycles”). The moment has been normalized to the cable volume. Published in [111].	164
Figure 71. Bean critical state profiles, from [112].	166
Figure 72. Magnetization decay in the CORC [®] sample at 1 T applied field after different hold fields. The moment has been normalized to the cable volume. Published in [111].	167
Figure 73. Absolute change in magnetization of CORC [®] cable sample, over 1200 s, at different initial magnetizations. The moment has been normalized to the cable volume. Published in [111].	168
Figure 74. The 14 T $M-\mu_0H$ loop of the 2G HTS tape. The moment has been normalized to the tape volume. Published in [111].	170
Figure 75. Magnetization decay of the 2G HTS tape at 1 T applied magnetic field after different hold fields. The moment has been normalized to the tape volume. Published in [111].	172
Figure 76. The absolute change in the magnetization of the 2G HTS YBCO tape, over 1200 s, at different initial magnetizations. The moment has been normalized to the tape volume. Published in [111].	173
Figure 77. Rutherford cable (bottom right) with cross-sectional image of the different superconducting strands (top right) and a cross-sectional image of an individual strand (top left). See [2] for more strand details.	174

Figure 78. A plot of the derivative of the fit for the initial ramp-up of the 8 T $M-\mu_0H$ loop. The susceptibility at 0 T is -0.1628.....	177
Figure 79. A plot of the 8 T $M-\mu_0H$ loop, with no-sample background subtracted, multiplied by a susceptibility determined calibration factor to obtain the magnetization in kA/m. The moment is normalized to the sample volume.	178
Figure 80. A plot of the $0 \rightarrow 2.5 \rightarrow x \rightarrow 1$ T $M-\mu_0H$ loops, with no-sample background subtracted, multiplied by a susceptibility determined calibration factor to obtain the magnetization in kA/m. The moment is normalized to the sample volume.	179
Figure 81. A plot of the 8 T $M-\mu_0H$ loop, with no-sample background subtracted, multiplied by a nickel replacement calibration factor to obtain the magnetization in kA/m. The moment is normalized to the superconductor volume.	181
Figure 82. A plot of $0 \rightarrow 2.5 \rightarrow x \rightarrow 1$ T $M-\mu_0H$ loops, with the no-sample background subtracted. Here x refers to a pre-injection field of 0, 0.25, 0.75, and 0.85 T. The moment is normalized to the superconductor volume.	182
Figure 83. The temporal change in the normalized moment of the Bi:2212 Rutherford cable at 1 T, 4.2 K.....	185
Figure 84. An illustration of the HD3b Nb ₃ Sn Rutherford cable-based block-type dipole accelerator magnet, from [115]. The Nb ₃ Sn coils are red, with the aperture centered between the coils (white). The yoke is blue and is composed of iron.	193
Figure 85. A schematic for a 2-layer, 3 turn canted $\cos\theta$ magnet developed at Berkeley National Lab, from [3].	196
Figure 86. A layer of a 40 turn, 4-layer canted $\cos\theta$ (CCT) prototype dipole made from CORC [®] wire.....	197
Figure 87. The cross-section and field lines of one quadrant of each of the Nb ₃ Sn accelerator magnets (a) HD3 block dipole. (b) MBHSP02 $\cos\theta$ dipole. (c) HQ02 $\cos(2\theta)$ quadrupole. From [114]. Individual rectangles are the Nb ₃ Sn cables. Each magnet has 2 layers.	199
Figure 88. The results of the measurements and calculation of the sextupole component of the magnetic field of the block-type dipole magnet (HD3b) at 4.4 K. The lines are the measured values and the symbols are the calculated values. From [114].	199
Figure 89. The $M-\mu_0H$ loops of the CORC [®] cable presented alongside that of a Nb ₃ Sn strand used to build an accelerator magnet presented in [114]. The peak magnetization of the CORC [®] is greater than 2 X that of the Nb ₃ Sn.	200

Figure 90. The block dipole layout of the Nb ₃ Sn magnet (HD3b), studied in [114], but with the Nb ₃ Sn cable substituted with the CORC [®] cable (shown in green and numbered) presented in Chapter 5.	203
Figure 91. The hybrid CORC [®] cable and Nb ₃ Sn Rutherford cable magnet design. The CORC [®] cable has a round cross-section (darker green) and the Nb ₃ Sn cable cross-section is rectangular (lighter green).....	204
Figure 92. The magnet load line plotted with the I_c of the CORC [®] cable. The intersection of the two curves determines the maximum operating field of the magnet. In this case, it is about 6.7 T.....	204
Figure 93. The calculated TF of the two-layer CORC [®] -based block dipole as a function of the current in the magnet, for 4 cases: Geometric ramp (red triangles); virgin ramp up (blue triangles); 1 st down ramp (red squares); and 2 nd up ramp (black circles).....	207
Figure 94. The calculated TF of the two-layer CORC [®] -based dipole, as a function of the field in the bore of the magnet, for 4 cases: Geometric ramp (red triangles); virgin ramp up (blue triangles); 1 st down ramp (red squares); and 2 nd up ramp (black circles).....	208
Figure 95. The calculated dipole transfer function of the two-layer Nb ₃ Sn-based block dipole, as a function of the dipole field in the bore of the magnet, for three different cases: virgin up ramp (blue triangles); 1 st down ramp (black circles); and 2 nd up ramp (red squares).	209
Figure 96. The calculated relative b_3 of the two-layer CORC [®] -based dipole, as a function of the bore field in the magnet, for 4 cases: Geometric ramp (red triangles); virgin ramp (blue triangles); 1 st down ramp (red squares); and 2 nd up ramp (black circles).....	211
Figure 97. The calculated relative sextupole component, b_3 , of the two-layer Nb ₃ Sn-based block dipole for three different cases: virgin up ramp (blue triangles); 1 st down ramp (black circles); and 2 nd up ramp (red squares).	212
Figure 98. The calculated TF of the hybrid dipole for 4 cases: geometric ramp (red X); parallel ramp (gray squares); CORC [®] ramped and then Nb ₃ Sn coil ramped (blue diamonds); Nb ₃ Sn coil ramped and then CORC [®] coil ramped (black triangles).	215
Figure 99. The calculated b_3 of the hybrid CORC [®] and Nb ₃ Sn-based dipole for 4 cases: geometric ramp (red X); parallel ramp (gray squares); CORC [®] ramped and then Nb ₃ Sn ramped (blue diamonds); Nb ₃ Sn ramped and then CORC [®] ramped (black triangles). ..	216
Figure 100. A schematic hysteresis loop of the Bean critical state model.	218
Figure 101. Bean Profile for initial virgin curve.....	219

Figure 102. The magnetic hysteresis loop calculated using the analytical model (red open triangles) plotted alongside the measured hysteresis loop (black line)..... 223

Figure 103. The b_3 calculations of the standalone CORC[®] dipole design using the calculated magnetizations (filled symbols) and the measured magnetizations (open symbols) for the virgin, 1st down, and 2nd up branches of the hysteresis loop. 225

Figure 104. The scaled $M-\mu_0H$ (blue squares) of the CORC[®] cable calculated using the analytic model. The measured values and the original model results are also plotted, using black lines and open red triangles, respectively..... 226

Figure 105. The calculated b_3 for different current ramps using the scaled CORC[®] cable $M-H$ (closed symbols) plotted alongside the calculated b_3 using the original measured values (open symbols)..... 227

Figure 106. The calculated b_3 , of the field for the 2nd up ramp (from 0 A) of the current in the standalone block dipole magnet. The analytic model was used to calculate the $M-\mu_0H$, and it was scaled by the fraction of the original $M-\mu_0H$ seen after 10 min. and 20 min. 230

Figure 107. The fully assembled 40 turn, 4-layer canted cosine theta accelerator magnet. 232

Figure 108. The rotating coil fluxmeter used to measure the magnetic fields and their decay in the 40 turn, 4-layer CORC[®]-based canted $\cos\theta$ accelerator magnet..... 233

Figure 109. An example of a 20-turn (10 on front/back), 4-winding, PCB with amplifier circuit, from [124]. 234

Figure 110. The dipole field generated at magnet currents up to 400 A using ramp rates of 25, 50, 100, 150, and 200 A/s. There is no significant dependence on ramp rate. 236

Figure 111. The transfer function generated at magnet currents up to 400 A using ramp rates of 25, 50, 100, 150, and 200 A/s. There is no significant dependence on ramp rate. 237

Figure 112. The calculated geometric sextupole component of the field, b_3 (blue triangles) and the measured b_3 , using the rotating coil fluxmeter, as a function of position along the bore of the magnet..... 238

Figure 113. The calculated geometric decapole component of the field, b_5 (blue triangles) and the measured b_5 , using the rotating coil fluxmeter, as a function of position along the bore of the magnet. 239

Figure 114. The calculated geometric b_7 component of the field (blue triangles) and the measured b_7 , using the rotating coil fluxmeter, as a function of position along the bore of the magnet.	240
Figure 115. The dipole field as a function of magnet current (I_{mag}) at current ramp rates of 10, 20, 50, 100, 200, and 300 A/s.	242
Figure 116. The transfer function (TF) as a function of magnet current (I_{mag}) using ramp rates of 10, 20, 50, 100, 200, and 300 A/s.	243
Figure 117. The dipole field as a function of magnet current (I_{mag}) using ramp rates of 10 and 300 A/s.	244
Figure 118. The calculated geometric sextupole component of the field, b_3 (blue triangles) and the measured b_3 , using the rotating coil fluxmeter, as a function of position along the bore of the magnet.	246
Figure 119. The calculated geometric decapole component of the field, b_5 (blue triangles) and the measured b_5 , using the rotating coil fluxmeter, as a function of position along the bore of the magnet.	247
Figure 120. The calculated geometric b_7 component of the field (blue triangles) and the measured b_7 , using the rotating coil fluxmeter, as a function of position along the bore of the magnet.	248
Figure 121. The sextupole component, b_3 , of the magnetic field as a function of dipole field during up ramp from 0 T.	250
Figure 122. The relative harmonics b_2 , b_5 , and b_7 as a function of dipole field.	251
Figure 123. The main dipole change with time with the magnet current held at 4 kA...	252
Figure 124. The change in the relative sextupole, b_3 , component of the magnetic field, in the bore of the magnet, with time.	253

Chapter 1. Introduction and Motivation

1.1 Motivation

Large magnetic fields are required for the next generation of NMR and MRI magnets, as well as high energy physics (HEP) magnets. Superconducting composites are presently used to make these magnets because they can carry large amounts of current, and thus generate large magnetic fields, without excessive heating of the conductor. Nb-based superconductors such as NbTi are widely used in HEP magnets. However, future HEP magnets will be required to generate magnetic fields larger than those currently obtainable with these Nb-based superconductors. The primary materials being considered to replace Nb-based superconductors are the high temperature superconductors (HTS) $\text{Bi}_2\text{Sr}_2\text{Ca}_1\text{Cu}_2\text{O}_x$ (Bi:2212) [1, 2] and $\text{YBa}_2\text{Cu}_3\text{O}_{7-x}$ (YBCO) [3-5]. These materials are being considered partly because they have superior upper critical fields, B_{c2s} , and superior critical current densities, J_{cs} , in high magnetic fields. The high critical temperature, T_c , allows these materials to be used in a larger operating temperature range than the Nb-based superconductors, and they will possibly possess increased resistance to thermal quench due to heating from flux motion and mechanical vibrations. Compared to Nb-based superconductors, the J_{cs} of Bi:2212 and YBCO are relatively independent of magnetic field at high fields, allowing them to carry large amounts of current in very high magnetic fields.

Higher magnetic fields are desirable for accelerator magnets because the larger magnetic fields allow for higher energy particle accelerations. The energy of the particles that can be kept in an orbit of radius, r , is proportional to the product of the magnetic field strength they experience and r ($E \propto B \times r$). Therefore, two methods of generating higher energy particles are: (1) increase the radius of the particle trajectory or (2) increase the applied magnetic field the particle experiences. It is desirable to upgrade existing infrastructure rather than build a new accelerator ring each time a new energy of particle beam is required. Increasing this field is achieved by increasing the strength of the magnetic field generated by the superconducting electromagnets. This field strength is limited by the current-carrying capacity, or critical current, I_c , of the composite, and this current carrying capacity is a function of the applied magnetic field the superconducting composite is exposed to. Bi:2212 has an advantage over YBCO in that it can be manufactured in composite round wire form, allowing it to have isotropic properties, but Conductor on Round Core (CORC[®]) technology has allowed the manufacture of cables of YBCO-based composites that also have isotropic properties [3, 4]. However, even though the HTS composites have some advantages over LTS-based materials, the magnetic properties of the composites must be characterized at relevant conditions (such as 4.2 K and 1 T) and considered before the composites can be used.

If the J_c s of HTS-based composites and conductors are sufficiently high that they are useful in applications, the magnetization and the magnetic relaxation must be considered at the relevant conditions for the application. This is because the magnetization

of the composite or conductor influences the spatial field homogeneity in the magnet, and the magnetic relaxation affects the temporal stability of the magnetic field. The magnetic field can be represented using a multipole expansion (a sum of harmonic field strength components). A dipole magnet should have a very large dipole component whereas the magnitude of the other components (such as quadrupole, sextupole, etc...) should be minimal. If the unwanted magnetic field components are large, the magnet has large field error. For a dipole magnet, typically the most significant component other than the dipole component is the sextupole component. Dipole magnets are used to guide charged particles in accelerator magnets, and a large sextupole component causes defocusing of the particle beam. In addition to the magnetization of the composite/conductor, any temporal variation in the magnetization is problematic. This is because it is much more difficult to correct for the spatial inhomogeneity in the magnetic field if its magnitude is changing with time. An insufficient field quality or a temporal decay in the field can lead to a spread in the size of the particle beam, a spread in its trajectory, or both.

Superconductors become magnetized (the magnetization is sometimes called persistent-current magnetization) when they are exposed to an applied magnetic field. In an electromagnet, the turns of superconducting composite are exposed to the magnetic field generated by neighboring turns. This field, in addition to the self-field, causes an irreversible magnetization in the turns. This irreversible magnetization is due to flux pinning, which is necessary to maintain high current density within the superconductor during magnet operation. Sometimes the magnetic field (and the associated field errors)

generated by a magnet changes with time although there is a constant current in the magnet, and the field should be constant. This change in the field is unwanted because it is more complicated to correct than a static field error. One contribution to a temporal change in the primary field and the field errors is the decay of the magnetization of the superconductor. This decay is caused by magnetic flux creep, which is especially rapid in HTS even at low temperatures. Both field errors and temporal changes in the field are observed in present day accelerator magnets made from LTS-based composites [6]. However, the origin of the temporal changes of the field in LTS magnets is not due to flux creep. Conversely, it is due to the interaction of coupling currents and their decay with the hysteretic magnetization. In any case, detailed study of how the persistent current magnetization of HTS composites affects the magnet field quality and any temporal drift has not yet been performed. This study is one of the areas of focus in this thesis.

Prior to this thesis work, little work existed on magnetization and the magnetic relaxation in state-of-the-art HTS-based composites/conductors with a focus on relevant conditions and parameters for accelerator applications. It was not clear what the magnitude of the magnetization or the magnitude of the magnetic relaxation in HTS-based composites was at low temperatures, and it was not clear exactly how the microstructure of the composite influenced either of these two properties for Bi:2212. Studies of nanostructure and pinning correlations are well known for YBCO, but there are few studies correlating nanostructure and magnetic flux creep, especially at 4 K, the temperature of accelerator operation.

This thesis examines how the geometry, microstructure, and nanostructure of conductors made from two HTS materials, YBCO and Bi:2212, affects the persistent current magnetization of the superconductor and its temporal decay. It is found that the magnetization and its subsequent decay in Bi:2212-based composites are influenced by a microstructural change in the filament connectivity of the composite, that occurs during heat treatment, called interfilamentary bridging. The bridging causes the magnetization and magnetization decay to increase with increasing length of the composites, and there are indications that the bridging material has weaker pinning than that of the filamentary material. It was shown that two different types of secondary phase additions to YBCO affect the pinning strength of the material differently. It was shown that the geometry of HTS-based cables, relevant for magnet applications, influences the magnetization and its subsequent decay. After this, the magnetization of the cables was input into magnetic models of accelerator magnets, and the field error and its temporal decay was calculated. Finally, direct measurements of prototype HTS accelerator magnets were made, and the field errors and field error decay were measured.

1.2 Superconductivity: Background and Phenomenology

All superconductors generally possess two defining characteristics: (1) the absence of resistance to current flow; i.e., below a critical temperature, T_c , the resistance to electric current drops to an immeasurable level, and (2) in a suitably small externally applied magnetic field, the expulsion of magnetic flux from the body of the superconductor (this is

the Meissner effect.). The current loops in a superconductor exhibiting the Meissner effect are of such a polarity as to create a magnetic field which opposes and cancels the applied field; that is, the magnetic moment of the superconductor is diamagnetic. The technologically relevant superconductors, including Bi:2212 and YBCO, are Type-II superconductors. In a Type-II superconductor, the Meissner effect persists only up to a critical value of the externally applied magnetic field: the lower critical field H_{c1} . Externally applied magnetic fields larger than H_{c1} , but less than some upper critical field H_{c2} , put the superconductor in the so-called mixed state. The superconducting state is defined by a critical surface as shown in **Figure 1**, where T_c is the critical temperature, B_{c2} is the upper critical magnetic field, and J_c is the critical current density. Below this critical surface, the superconductor has an immeasurably small DC electrical resistivity. $J_c(T, B)$ dictates how much current can be carried by the superconductor.

The magnetic field, B , generated by a superconductor is limited by its current carrying capacity, which is called the critical current, I_c . This current carrying capacity is often normalized by the cross-sectional area of the composite, $A_{\text{composite}}$, giving an engineering current density, J_e ($J_e = I_c/A_{\text{composite}}$). Alternatively, the current carrying capacity can be normalized by the cross-sectional area of the superconducting phase (or filament), A_{sc} , giving a critical current density, J_c ($J_c = I_c/A_{\text{sc}}$).

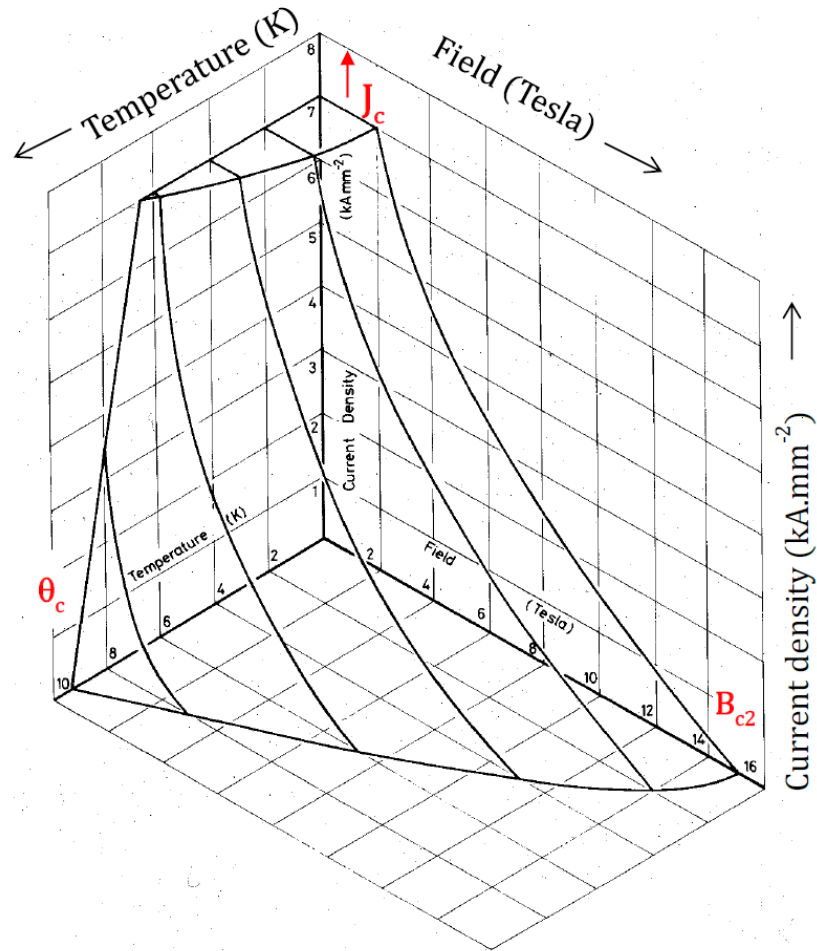


Figure 1. The superconducting phase diagram of a HTS, from [7].

High-temperature superconductors (HTS) are being considered for use in future particle accelerators because they can carry large current when exposed to large magnetic fields. A plot of the critical current density vs applied magnetic field for present day LTS and HTS composites is shown in **Figure 2**, from [8].

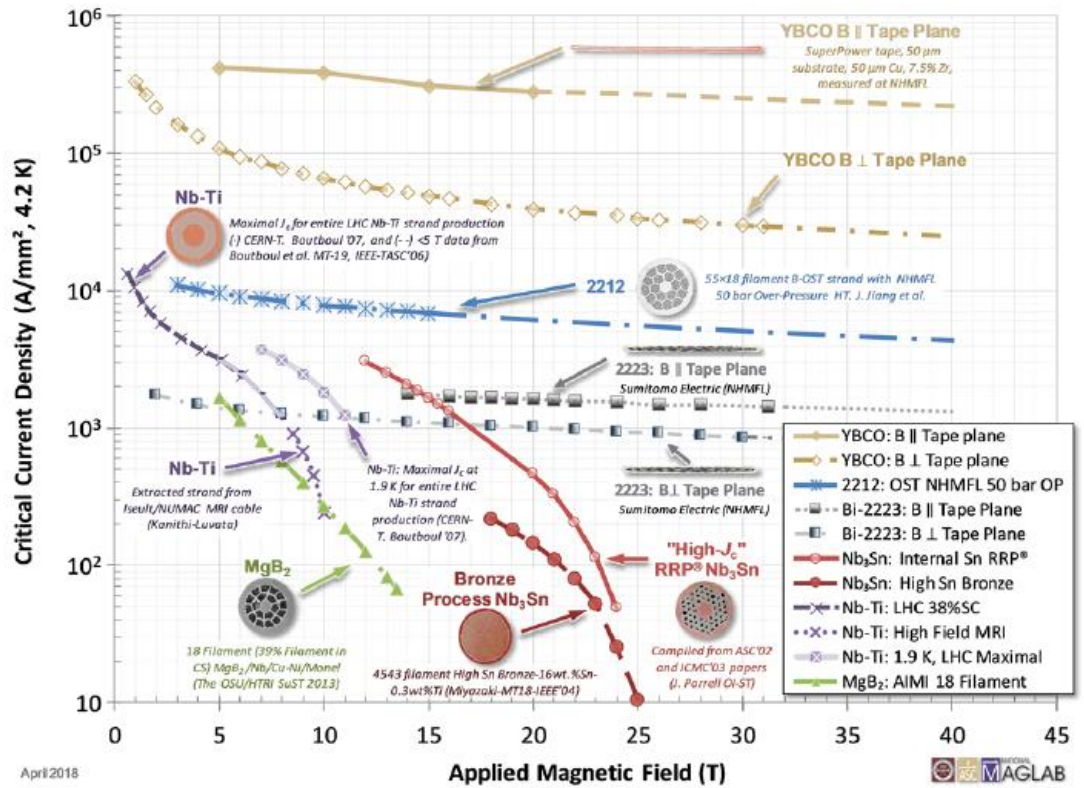


Figure 2. Plot of critical current density vs applied magnetic field for various superconducting composites, from [8].

From the plot, it is apparent that the critical current density of the LTS composites drops off much more rapidly with applied magnetic field than that of the HTS composites. At 25 T, the critical current density of the highest performing LTS composite (Nb_3Sn) is orders of magnitude smaller than that of the Bi:2212 round wire and YBCO tape HTS composites.

The Maxwell-Faraday equation states that a time-varying magnetic field is accompanied by a spatially varying electric field. That is,

$$\nabla \times E = -\frac{\partial B}{\partial t}. \quad (1.1)$$

When a normal electrical conductor is exposed to the time-varying magnetic field, eddy currents are generated in the conductor which flow in an orientation to generate a magnetic field which opposes the time-varying magnetic field. These eddy currents decay due to the resistivity of the conductor. Heuristically, we can consider what would happen for a “perfect” conductor. In that case, since such a conductor would have no electrical resistivity, any screening currents resulting from the time-varying magnetic field would tend to persist. These currents would produce a magnetic moment according to $m = IA$, where m is the moment, I is the induced current, and A is the area the current encloses. Normalizing this magnetic moment by a volume would give a magnetization, M . In fact, in a superconductor, screening currents develop to expel flux already present in the superconductor when it is cooled through the transition temperature (T_c). Therefore, it is distinct from the case of a “perfect” conductor.

A superconductor is distinct from a “perfect” conductor because the superconducting state is a distinct thermodynamic phase, with an associated free energy density, $f_s(T)$. In the absence of an applied magnetic field, the difference in the free energy densities between the normal and superconducting phases is

$$f_n(T) - f_s(T) = \frac{1}{2}\mu_0 H_c^2(T), \quad (1.2)$$

where $f_n(T)$ is the Gibbs free energy density of the normal state and H_c is the thermodynamic critical field. This expression represents the energy reduction per volume when the material undergoes a phase transition from the normal state to the superconducting state. It is the so-called condensation energy. At T_c , $H_c = 0$ and the free energy densities are equal.

When a magnetic field is applied to the superconductor, the free energy per unit volume of the superconductor increases due to the magnetization. Because the normal state of the material is non-magnetic and therefore acquires no magnetization, the application of the magnetic field does not change the value of the free energy of the normal state. If the applied magnetic field strength is increased sufficiently high, the free energy of the superconducting state will be raised above that of the normal state and a phase transition to the normal state will occur.

1.2.1 Type-I Superconductivity

In type-I superconductors, a state of perfect diamagnetism exists below the critical field, H_c . In an applied field below H_c , a screening supercurrent is created at the surface of the superconductor that directly opposes the external applied field. This current penetrates over a depth λ , called the penetration depth [9]. The screening currents induce a magnetic moment in the superconductor which can be normalized to the volume of the sample to

give a magnetization, M . This magnetization represents the difference between the external and internal magnetic fields and can be represented as

$$M = \frac{B}{\mu_0} - H. \quad (1.3)$$

As mentioned above, the screening currents generate a moment which directly opposes the external applied magnetic field, so that the volume average of the magnetic induction within the superconductor is zero, and therefore $M = -H$. This state exists if the superconductor is in the superconducting state, that is $T < T_c$ and $H < H_c$. If the temperature is increased so that the material transitions to the normal state, the magnetic flux from the external field will penetrate the entire sample volume.

1.2.2 Type-II Superconductivity

HTS are type-II superconductors and type-II superconductors have found applications as the building blocks of high-field magnets. In type-II superconductors, the screening currents completely expel the magnetic flux only up to a lower critical field, H_{c1} . In HTS, H_{c1} is on the order of tens of millitesla. Externally applied magnetic fields larger than H_{c1} , but less than the upper critical field, H_{c2} , put the superconductor in the so-called mixed state. In the mixed state, it is energetically favorable for magnetic flux to penetrate from the surface of the superconductor into the bulk of the superconductor in the form of vortices of quantized magnetic flux, called fluxons. Lossless supercurrents circulate around the fluxons with current density J , according to Ampere's law

$$\nabla \times B = \mu_0 J . \quad (1.4)$$

The region enclosed by the circulating current is a region of normal state material.

In applied fields greater than H_{c2} , the superconductivity is extinguished.

1.2.3 Fluxon Structure

A single fluxon, illustrated in **Figure 3**, consists of a tubular non-superconducting core with a radius, ξ , called the coherence length. Supercurrents flow around the core to generate the magnetic flux quantum that opposes the external applied field.

The coherence length, or radius of the fluxon is the distance over which the superconducting order parameter, Ψ , the square of which is the fraction of the number of superelectrons (or superholes) to the maximum number of superelectrons (or superholes) in the material, goes from its maximum value of 1, at the edge of the fluxon, to 0 at its center over a distance ξ . The magnetic flux density increases over a distance, λ , the London penetration depth, to its maximum at the fluxon center. Because the core of the fluxon is non-superconducting, its appearance is associated with an increase in the free energy of the material

$$E_c = \pi \xi^2 \frac{1}{2} \mu_0 H_c^2 . \quad (1.5)$$

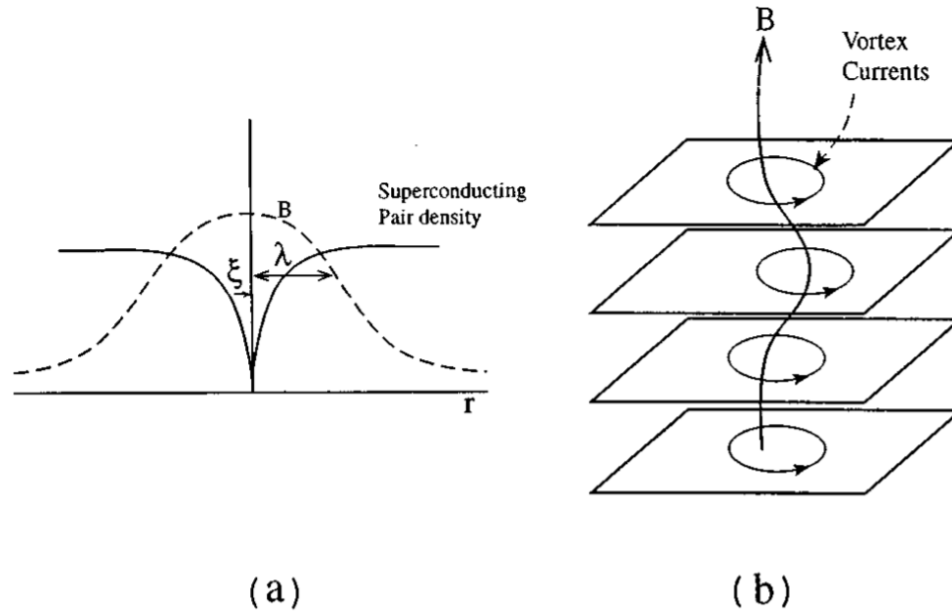


Figure 3. A schematic illustration of a fluxon showing the coherence length, penetration depth, and supercurrent flow [10].

Of course, this energy increase would tend to oppose the entry of flux into the material, except that if flux continues to be excluded, there is additional field concentrating just outside of the superconductor, leading to an increase in the energy density of the regions just outside of the superconductor (due to magnetic energy which goes as B^2). Thus, it is energetically favorable for field to enter the superconductor, which it does as quantized flux vortices.

After this flux penetration has begun, increases in the applied magnetic field cause more fluxons to enter from the surface of the superconductor. As the field is increased, the number of fluxons within the superconductor increases and the spacing between them, a_0 ,

decreases. As the fluxons begin to overlap with increasing applied fields, they repel each other due to the interaction of the magnetic fields of one fluxon with the circulating current of another. A schematic of fluxons inside a superconducting slab is shown in **Figure 4**.

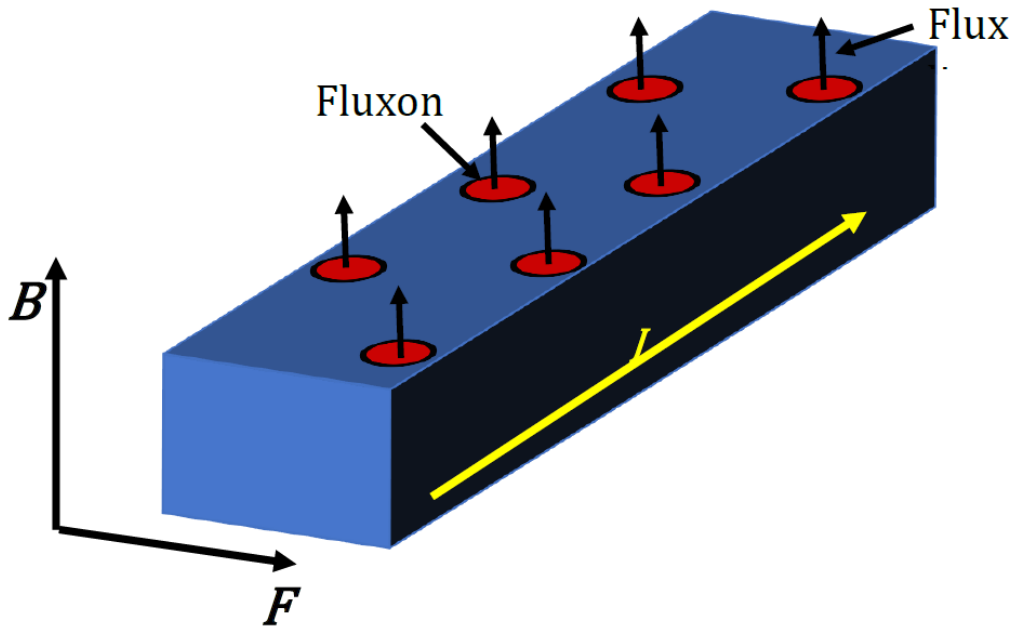


Figure 4. A schematic of fluxons inside a superconducting slab.

Abrikosov [11] demonstrated that the fluxons penetrate the superconductor in the form of a regular lattice of magnetic flux lines, formed parallel to the applied field. The circulating supercurrent of a fluxon produces a magnetic field equal to the magnetic flux quantum, $\Phi_0 = 2.0678 \times 10^{-15}$ Wb. Therefore, the magnetic field inside the superconductor is equal to the density of fluxons inside the superconductor. That is, $B = n\Phi_0/a_0^2$, where n

is the number of fluxons per cm^2 , and a_0 is the average distance between the fluxons. Due to the small H_{c1} in HTS, the difference between the magnetic flux density and applied magnetic field strength is often neglected, as long as the applied field is well above H_{c1} [10].

In a pure superconductor, that is, one absent of imperfections, as the applied magnetic field is increased above H_{c1} , fluxons move freely from the surface of the superconductor into the bulk. Consequently, in a defect-free superconductor, the fluxons arrange themselves in a regular lattice array [11]. Typically, a triangular flux line lattice is formed [12] with a lattice parameter

$$a_0 = \left(\frac{2}{\sqrt{3}}\right)^{\frac{1}{2}} \left(\frac{\Phi_0}{B}\right)^{\frac{1}{2}} \approx \left(\frac{\Phi_0}{B}\right)^{\frac{1}{2}} . \quad (1.6)$$

As the applied magnetic field is increased further, the distance between the fluxons decreases until their cores overlap. The point at which this happens is called the upper critical field, H_{c2} , and at this field superconductivity is extinguished and the magnetization is zero.

If a type-II superconductor is completely homogenous, extremely small transport currents will cause the fluxons to move and cause electrical dissipation as the normal cores move through the material. There is an electromagnetic (Lorentz) force between the circulating currents of the fluxons and the transport current. The Lorentz force, $J \times B$, acts on each fluxon, at right angles to the direction of the transport current and the direction of the flux. When the fluxons move, lossy energy dissipation will occur according to $E \cdot J$, and

an effective electrical resistance is present in the superconductor. Type-II superconductors which are relatively defect-free, and therefore have nothing to restrict the motion of flux, have small critical current densities because a small Lorentz force can cause flux motion and energy dissipation. High critical current densities are required for practical applications and therefore flux motion must be restrained in a useful superconductor. Intentionally introducing inhomogeneities or flux pins is a method to increase the critical current density.

Inhomogeneities in the superconductor are regions of increased free energy within the material, that is, these regions do not have the energy reduction associated with the condensation into the superconducting state. These are regions of reduced superconducting order parameter, such as intentionally introduced secondary phases. Other examples include dislocations, twins, grain boundaries, strain fields, and chemical dopants. In any case, they have a higher Gibbs energy per unit volume than the surrounding superconducting regions. The fluxon, the core of which is in the normal state, represents a cylinder where this free energy reduction is also not present. If, then, the fluxon runs through the inhomogeneity (i.e., the fluxon overlaps with the inhomogeneity), the total energy increase due to the fluxons presence in the superconductor (remember the fluxon was pushed into the superconductor to minimize B^2 energy that would result from potential flux concentration outside of its boundaries) is reduced from what it would otherwise be. Thus, the total energy of the system is reduced if the fluxons overlap with these inhomogeneities. The attractive interaction between the inhomogeneities and the fluxons acts to pin the fluxons, and the regions are called “pins” or “pinning sites”.

The pinning sites act as potential wells which possess a pinning barrier energy U_0 . The variation in energy caused by the overlap of the fluxon with the pinning site causes a pinning force, f_p , on the fluxon equal to the gradient of the energy. As mentioned above, energy (the condensation energy) is required to create the fluxons in the normal material. Some, or all, of this energy can be regained if the fluxons overlap with regions of reduced order parameter, Ψ . Non-superconducting regions will have $\Psi = 0$, and the entire condensation energy can be regained if the fluxon overlaps with this region. Secondary phases, such as the Bi:2201 phase in Bi:2212 superconductors, have lower T_c s than the primary phase and therefore have lower, but not zero, order parameters. The geometry and Ψ of the pinning site determine its pinning strength. The pinning force is maximized when the pinning site size and density matches that of the fluxon size and density. That is, the pinning site threads the entire superconductor and has a radius of approximately ξ . HTS materials possess a strong intrinsic pinning due to their anisotropic nature. The coherence length of the fluxon in the c -axis direction is shorter than the CuO_2 interlayer spacing. A strong pinning force acts on the fluxons that lie within the CuO_2 layers. However, the fluxons sit between these layers only when the applied magnetic field is applied parallel to the ab -plane of the crystal.

A simplistic estimate of the total pinning force in the material is to directly sum all the pinning forces on all the fluxons in the material. This method is valid when each pinning site pins a single fluxon. This occurs when there is a low density of fluxons and therefore each fluxon can be pinned by a single pinning site. In reality, the flux line has some

elasticity that allows the flux line to bend to positions that maximize the free energy reduction. Therefore, this method is not strictly applicable in all scenarios.

Due to the pinning and the repulsive nature of the fluxons, a flux density gradient develops within the superconductor bulk. Electric current flows within the region of the gradient according to Ampere's law, see equation 1.4.

The Lorentz force from the currents acts to reduce the energy barrier for flux motion, and when it exceeds the average pinning force density F_p , flux motion will occur, and an effective resistance will be present in the superconductor. The value of the current density at which the Lorentz force matches the average pinning force is the critical current density, J_c ,

$$J_c \times B = F_L = -F_p . \quad (1.7)$$

Therefore, the critical current density, J_c , is the maximum current density that can exist before an effective resistance presents in the superconductor. It is a material dependent property that can be increased by increasing the pinning in the material. The gradient of the fluxons in the material is therefore a critical gradient as described by Bean's critical state model.

1.3 Bean's Critical State Model

At the critical state, $F_L = F_p$. The critical state model developed by Bean [13, 14] states that there is a maximum slope to the magnetic flux density gradient, and that the flux

density gradient always takes this slope as long as the superconductor can carry current. This critical slope leads to a critical current density, J_c . The model assumes that J_c is independent of applied field. Above the critical field, $J_c = 0$. Therefore, there are three possible values of the current density, J_c , $-J_c$, and 0. A key result of the model was the prediction that the magnetization of the superconductor depended upon its dimensions.

A schematic of how the flux density gradient develops in a semi-infinite slab, infinite in the y and z directions, of superconductor is shown in **Figure 5**. The magnetic field is applied parallel to the z -axis of the slab and fluxons penetrate from the surfaces on the x -axis.

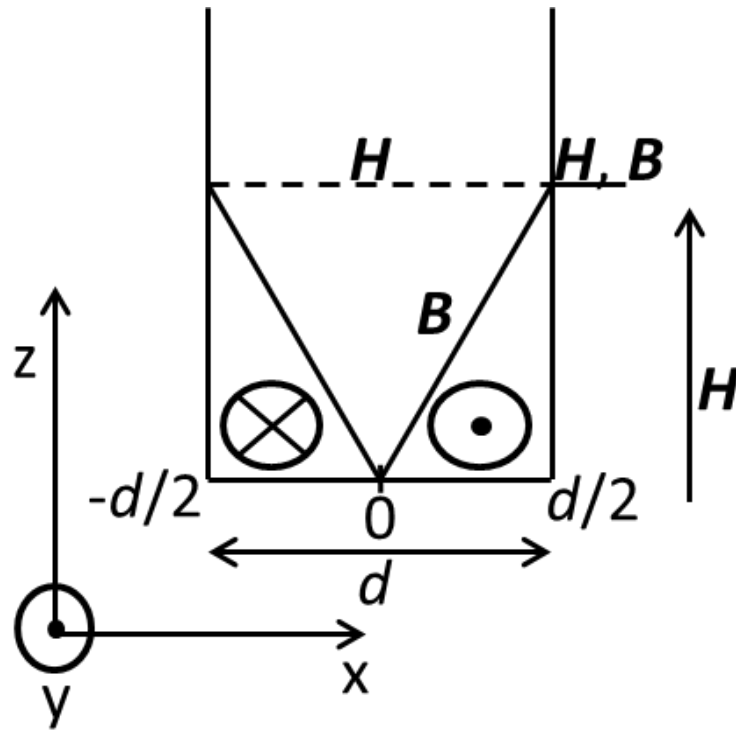


Figure 5. A schematic of the flux density gradient in a semi-infinite slab of superconductor. Here H is $\mu_0 H$.

$\mu_0 H$ in the diagram is the applied magnetic field strength and B is the magnetic flux density (in **Figure 5**, H should be read $\mu_0 H$). The circle with the dot indicates current flowing out of the page, and the circle with the cross indicates current flowing into the page. The current density flows within a surface layer of depth a . The constitutive equation for magnetic flux density is

$$B = \mu_0(H_a + M), \quad (1.8)$$

where B is the magnetic flux density, H_a is the applied magnetic field strength, and M is the magnetization. H_a is the same in the bulk of the superconductor as at its surface. The expression for the magnetization is therefore

$$M = \frac{B}{\mu_0} - H_a \quad (1.9)$$

or alternatively,

$$\mu_0 M = \langle B_{\text{local}} - B_a \rangle. \quad (1.10)$$

Therefore, the magnetization is a measure of the difference between the average internal field and the applied field. From the Bean critical state model, the J_c in the slab is given by

$$\frac{\partial B_z}{\partial x} = -\mu_0 J_y = \mu_0 J_c. \quad (1.11)$$

Therefore, the flux density gradient, which is determined by the pinning in the material, determines J_c . An illustration of how the flux density gradient is influenced by different pinning strengths in the material is given in **Figure 6**.

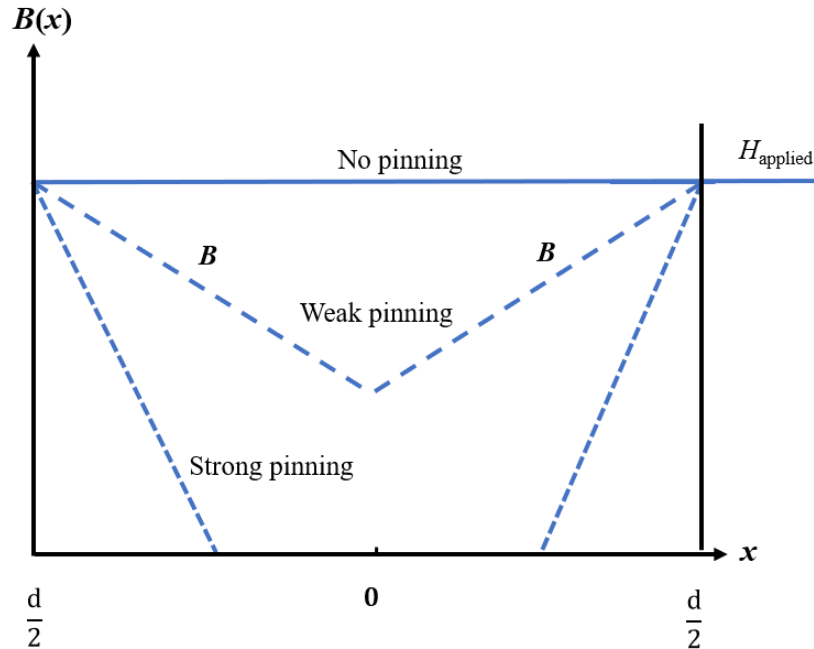


Figure 6. A schematic illustration of how different pinning strengths affect the flux density gradient in a semi-infinite slab of superconductor. Stronger pinning generates larger gradients.

If a superconductor starts out with $B = 0$ in its interior, and a magnetic field, $H > H_{c1}$ is applied to the superconductor, the field profile inside the superconductor is a linearly decreasing function of the distance from the surface. The depth to which the field extends is given by $B_a/\mu_0 J_c$. As the applied magnetic field is increased, the flux penetrates deeper into the superconductor and the depth to which the current flows increases concomitantly. This process is illustrated schematically in **Figure 7** for increasing applied fields from zero and **Figure 8** for decreasing fields.

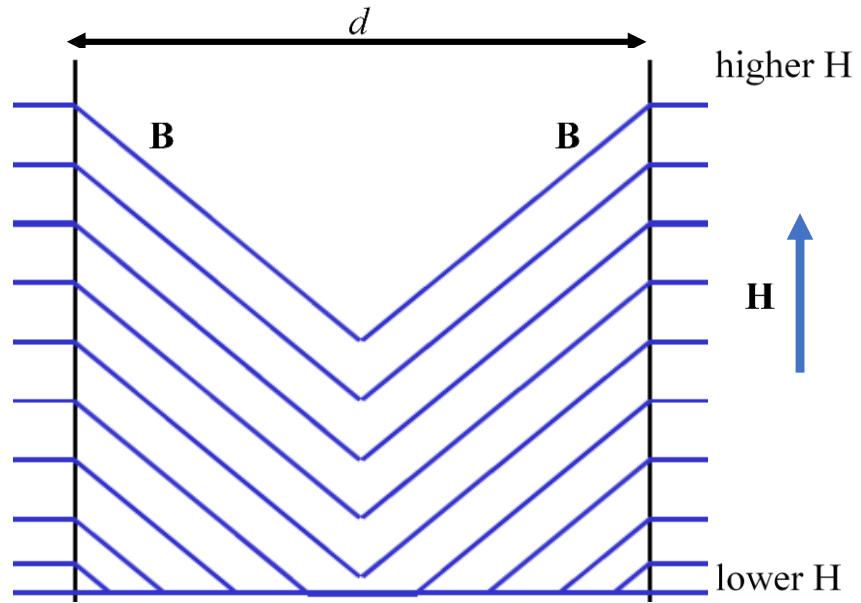


Figure 7. The magnetic field profile inside a superconductor in the Bean critical state model as the applied field is increased from zero.

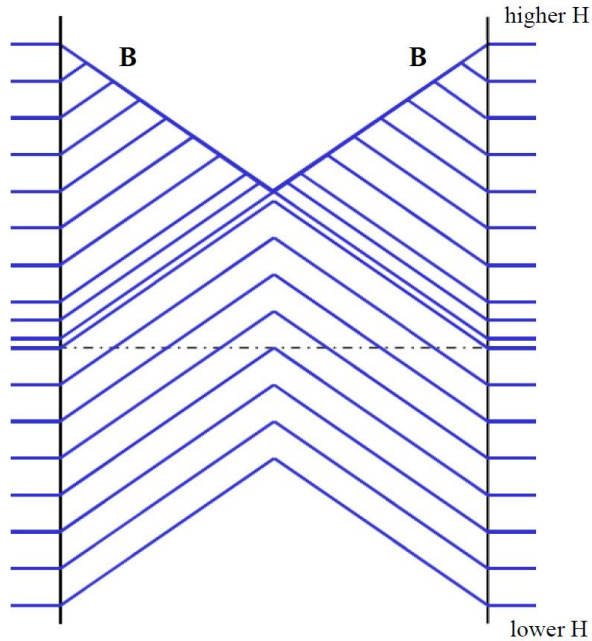


Figure 8. The magnetic field profile inside a superconductor in the Bean critical state model as the applied field is decreased.

At an applied magnetic field, $H_p = J_c d/2$ called the penetration field, magnetic flux penetrates to the center of the superconductor. As the applied magnetic field is increased above H_p , the magnetic flux density inside the superconductor continues to rise, but the magnetization remains constant.

If the applied magnetic field is reduced, the flux density gradient and therefore the direction of the currents will reverse at the surface of the superconductor. The magnetic flux density distribution for this field reversal process is illustrated in **Figure 8**. As the field is decreased further, the depth to which the reversed currents extend increases. However,

if the applied magnetic field is reduced to zero, magnetic flux remains inside the superconductor. This trapping of the magnetic flux is a result of the pinning of the fluxons by the pinning centers, and it leads to a remnant magnetization in the superconductor in zero applied field. To reduce the internal field inside the superconductor to zero, the applied magnetic field needs to be reversed to $-2H_p$.

The pinning of the fluxons in a superconductor leads to a magnetization that is hysteretic, or irreversible. If the superconductor starts out unmagnetized, and a magnetic field is applied to it, on the initial up branch of the hysteresis curve (the virgin curve) magnetic flux is shielded from the interior of the superconductor and the magnetization is negative. As the applied magnetic field strength increases, the magnetization saturates until the upper critical field is reached, at which point the superconductor transitions to the normal state. When the applied field is reversed, magnetic flux becomes trapped inside the superconductor and the magnetization is positive. The branches of the hysteresis loop anticipated by the Bean critical state model are illustrated schematically in **Figure 9**. Realistically, the magnetization (and J_c) of the superconductor depends upon the applied magnetic field, and the Bean model is modified to take this field dependence into account.

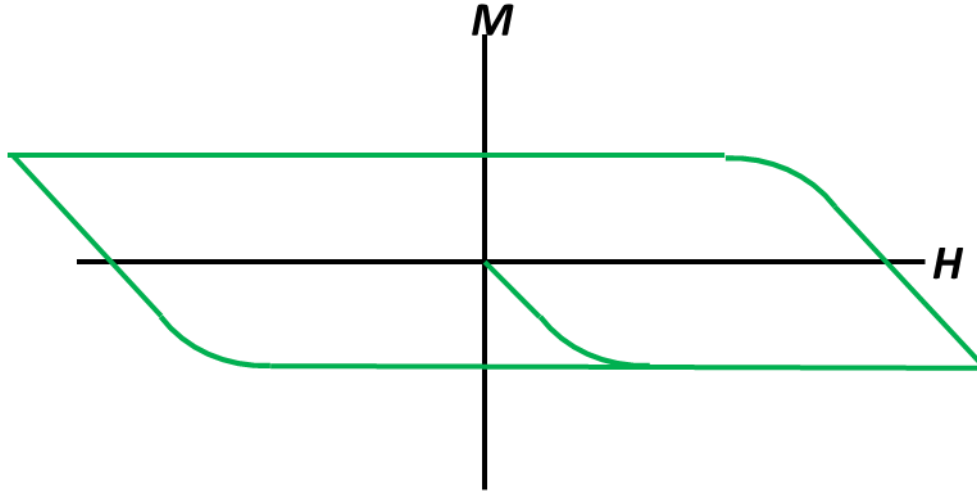


Figure 9. The hysteresis loop of a type-II superconductor according to the Bean critical state model.

The critical state model allows for the determination of the critical current density using the width of the magnetic hysteresis loop, ΔM , if $H > H_p$. The critical current density is proportional to ΔM ($J_c \propto \Delta M$) with the exact relation depending on the geometry of the sample. The expressions for a few different geometries can be found in [15, 16]. The width of the hysteresis curve in terms of the width, d , of the isotropic semi-infinite superconducting slab is given by

$$\Delta M = \frac{1}{(d)} \int_0^{\frac{d}{2}} J_c x dx = \frac{J_c d}{2} . \quad (1.12)$$

For a semi-infinite cylindrical sample in a perpendicular applied magnetic field, the expression for the magnetization is

$$\Delta M = \frac{4J_c d}{3\pi}, \quad (1.13)$$

where d is the diameter of the cylinder.

These equations are valid for samples which are infinitely long in the direction perpendicular to the applied magnetic field, and the current closure due to Kirchoff's circuit law is neglected. The current density distribution for this case is illustrated in **Figure 10**.

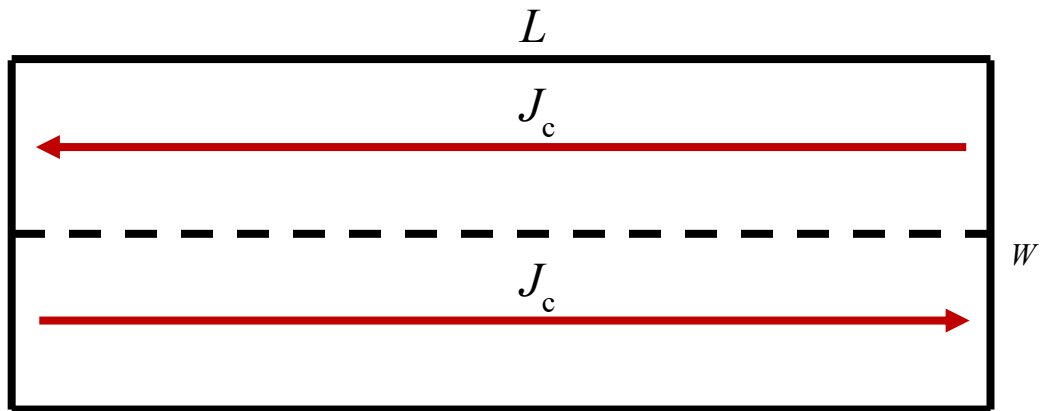


Figure 10. The current density distribution in an isotropic semi-infinite superconducting slab.

The situation represented in **Figure 10** is that which would occur if the magnetic field is applied perpendicular to the L - w plane of the slab. The slab is assumed to be infinite in the L and thickness (out of page) directions and finite in the w direction. In this situation, the flux penetrates the superconductor along the w direction and current flows along the length, L , with direction given by the red arrows. The current which should transfer across the

width of the sample to obey Kirchoff's circuit law is neglected in this case. In samples of finite length, the currents which close the loop from the curl of the electric field add correction terms to the magnetization equations.

1.5 Expressions for the Magnetization of Finite Length Samples

1.5.1 Isotropic Finite Slab

In rectangular parallelepiped samples, which are finite in length and subject to an applied magnetic field perpendicular to the basal plane, magnetic flux penetrates in two directions, and therefore the current flows in two directions. The flux density distribution inside the sample forms either a "rooftop" or an "inverted rooftop," depending on the applied magnetic field cycle. If the sample is not sufficiently long in a direction, the current flowing perpendicular to that direction will be reduced as there is not enough length for full penetration of the field, and the current is lower than in the full penetration case. The expression for the magnetization of a sample of finite length has been considered in [17-20], and is given by

$$M_{\text{short}} = \frac{J_c w}{4} \left(1 - \frac{w}{3L}\right) \quad (1.14)$$

where w is the width of the sample and L is the length of the sample.

1.5.2 Anisotropic Finite Slab

A further correction for the magnetization must be considered when a sample has properties that are anisotropic. For example, if the pinning strength is larger in one of the basal plane directions, the critical current density parallel to this direction will be larger. The calculation of the magnetization of anisotropic superconductors, in transverse applied magnetic fields, with rectangular geometry was presented in [21, 22]. The expression for samples of cylindrical geometry was given in [23] and extended in [24]. As described in [23], the expression for the magnetization of a cylindrical sample, that is sufficiently long to allow full flux penetration on both axis perpendicular to the field is

$$\Delta M = \frac{0.8J_{c3}R}{3\pi} \left(1 - \frac{3\pi RJ_{c3}}{16LJ_{c2}} \right), \quad (1.15)$$

where J_{c3} is the critical current density along the length of the cylinder and J_{c2} is the transfer critical current density that crosses over the cylinder to obey Kirchoff's current law. The expression for the magnetization of a cylindrical sample that is too short to allow the full transfer of the current across the sample is given by

$$\Delta M = \frac{J_{c2}L}{20} \left(1 - \frac{2J_{c2}L}{3\pi J_{c3}R} \right). \quad (1.16)$$

These equations were extended to treat cylindrical superconducting composites which possess electrical coupling in the radial direction in [24]. This model will be discussed further in chapter 3. The importance of the model is that it predicts that samples which are electrical coupled, or bridged, in the radial direction, such as, for example, Bi:2212 HTS composites, will possess a magnetization which is length dependent. This dependence is

important when evaluating the magnetization of the superconductor because it is often the case that the bores of conventional magnetometers are not large enough to hold samples long enough for the magnetization to saturate.

1.6 Magnetic Relaxation Due to Flux Creep

In all superconducting materials, there is a phenomenon, “flux creep”, where fluxons can hop out of their pinning sites due to thermal energy. Anderson [25, 26] described this flux creep as a thermally activated process to explain the data of Kim *et al.* [27]. At $T > 0$, the fluxons can acquire enough energy to overcome the potential barrier energy, U_0 , and hop down the flux density gradient. This phenomenon was first discovered in LTS, but was seen to be much larger in HTS, and was described initially as “giant flux creep” [28]. In any case, the basic process is the same. When the fluxons hop down the flux density gradient, the gradient tends to zero as the fluxons become more homogeneously distributed throughout the sample, and the magnitude of the current density and magnetic moment decrease over time. This process whereby the magnitude of the magnetic moment of the superconductor decreases over time is called magnetic relaxation or magnetization decay.

The underlying origin of flux creep is the thermal activation of the fluxon motion. One must now think of the magnetization as being proportional to the current density, J , in the superconductor at a particular time. As mentioned above, the phenomenon of flux creep

was studied by Anderson [25] as early as the 1960s. Of course, the detailed explanation for flux creep was more complicated than a simple hopping of fluxons from one pin site to the next. Instead, it assumed that the fluxons hopped as bundles, called flux bundles. The bundle behavior occurs because the magnetic fields and supercurrents of the fluxons interact with each other and the forces from these interactions act to pin fluxons even when they do not sit on a pinning site themselves [26]. Thus, flux bundles are assumed to be moving during fluxon motion, rather than single fluxons.

Like other diffusion processes, the flux bundle motion is assumed to follow an Arrhenius rate equation, which gives the probability for the flux bundle to overcome the barrier for each attempt, of the form

$$t = t_0 \exp \left[\frac{-U_{\text{eff}}}{k_B T} \right], \quad (1.17)$$

where t represents the hopping time, t_0 is the “effective” hopping attempt time, k_B is the Boltzmann constant, T is the temperature, and U_{eff} is an effective energy barrier to flux motion. This effective barrier energy approximates the true volume pinning energy, U_0 , of the material only when negligibly small currents exist in the conductor and the driving force due to the Lorentz forces is zero. When shielding or transport currents are present, the pinning energy is reduced by an energy which has often been described as the energy due to the Lorentz force [25, 29], but which was slightly more accurately described by Friedel *et al.* [30] as the Lorentz force density multiplied by a suitably correlated volume (V_c) and hop distance (a), that is, $U_{\text{eff}} = U_0 - J_c V_c a$. Therefore, the potential energy landscape inside the superconductor is that of a “washboard” potential.

The effective energy barrier for thermally activated flux flow has often been assumed to depend linearly on the current density [10]

$$U_{\text{eff}} = U_0 \left[1 - \frac{J}{J_{c0}} \right] \quad (1.18)$$

where U_0 is the barrier height in the absence of a driving force (i.e., when $J = 0$), and J_{c0} corresponds to the critical current density required to tilt the barrier to zero without the assistance of thermal fluctuations. Combining the previous two equations and solving for J gives

$$J = J_{c0} \left[1 - \frac{k_B T}{U_0} \ln \left(\frac{t}{t_0} \right) \right], \quad (1.19)$$

which given in terms of magnetization, M (since $M \propto J$) becomes

$$M = M_0 \left[1 - \frac{k_B T}{U_0} \ln \left(\frac{t}{t_0} \right) \right]. \quad (1.20)$$

Here, M_0 is the magnetization before any relaxation has taken place. This equation is commonly rewritten as

$$M = M_0 \left[1 - r \ln \left(\frac{t}{t_0} \right) \right], \quad (1.21)$$

where $r = k_B T / U_0$ is the so-called relaxation rate. This equation predicts that M will decay logarithmically in time and will drop with temperature, and therefore, if one takes the slope of the magnetization vs $\ln(t)$ data, a value for r , and therefore U_0 , can be obtained.

The linear model presented above has been used to extract a pinning potential, U_0 , in Bi:2212 single crystals [31-36], Bi:2212 ceramics [37, 38], and Bi:2212 round wire

composites [39]. The procedure is to plot the magnetization vs $\ln t$ at an externally applied magnetic field and temperature, and then to fit a linear curve to the data, **Figure 11**. The slope of the linear curve is given by $k_B T/U_0$, which is often called a relaxation rate ($r = k_B T/U_0$), and U_0 can be extracted from this. Thus, the procedure involves determining the pinning potential from the relaxation rate. Whereas this procedure is relatively simple to perform, a linear dependence of the pinning potential on J is unrealistic and, assuming a linear dependence results in a pinning potential which is different from the pinning potential when $J = 0$, and one which increases monotonically with temperature.

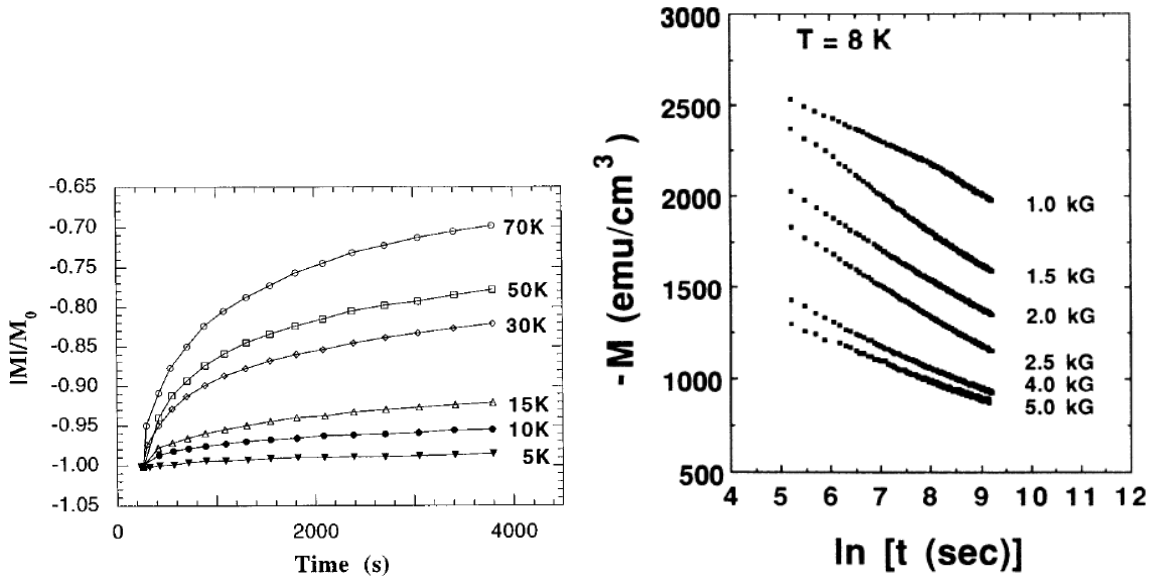


Figure 11. (Left) An example of the magnetic relaxation in a YBCO single crystal, measured using different temperatures, from [10]. (Right) Magnetic relaxation in a Bi:2212 single crystal in different externally applied magnetic fields, from [31]

Xu *et al.* [40] found that the pinning potentials calculated assuming the conventional linear dependence on J increased rather than decreased with temperature. **Figure 12** gives an illustration of why this is the case using a schematic of a nonlinear pinning potential $U(J)$. In the figure, U_0 is the pinning potential (or activation barrier) at $J = 0$, J_m is the experimentally measured current (or, equivalently, magnetization) and U_{eff} is the so-called effective activation barrier, which corresponds to the U -axis intercept of the straight line tangent to $U(J)$ at J_m , resulting from the use of the linear model. The U_{eff} obtained using the linear model is smaller than the pinning potential U_0 at $J = 0$. Additionally, U_{eff} may strongly vary with J , depending on the curvature of $U(J)$. Because J in a superconductor decreases with increasing temperature, magnetic relaxation measurements performed at higher temperatures move the starting point for the relaxation measurements to smaller values of J (or equivalently smaller values of M) and larger values of U_{eff} , causing the intercept to increase monotonically. This explains the anomalous increase in the pinning potential with temperature.

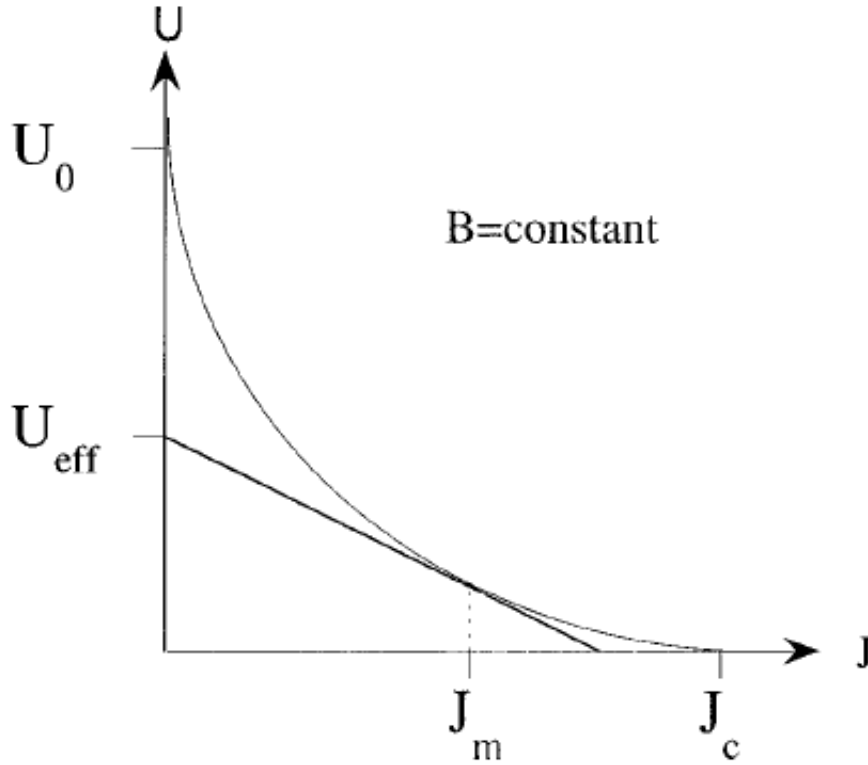


Figure 12. A schematic of a nonlinear functional form of $U(J)$ at a constant externally applied magnetic field. The approximation leads to an effective pinning potential which is smaller than the true potential U_0 ($J = 0$). J_c is the critical current density, from [10].

Beasley *et al.* [38] recognized that a more realistic pinning potential should exhibit a nonlinear dependence on current density. Beasley *et al.* [38], Griessen [41] and Lairson *et al.* [42] found that the pinning potential has a power law dependence on J near J_c . Because of the relatively large magnetic relaxation in high temperature superconductors, the dependence of the pinning potential on J when $J \ll J_c$ is of more interest. Zeldov *et al.* [43, 44] proposed a logarithmic barrier,

$$U = U_0 \ln \left(\frac{J_c}{J} \right). \quad (1.22)$$

The logarithmic dependence was supported by the extensive magnetic relaxation studies of Maley *et al.* [45], McHenry *et al.* [46], and Ren and de Groot [47]. Maley *et al.*, were able to experimentally determine the functional form of the pinning potential. To do this, they started with the Arrhenius equation for thermally activated motion of flux [38]

$$\frac{dM}{dt} = \frac{B\omega a}{\pi d_g} \exp \left(\frac{-U_{\text{eff}}}{k_B T} \right), \quad (1.23)$$

where ω is the attempt frequency, a is the hop distance, and d_g is the average grain diameter of the sample. Taking the natural logarithm of both sides leads to

$$\frac{U}{k_B} = -T \ln \left| \frac{dM}{dt} \right| + T \ln \left(\frac{B\omega a}{\pi d_g} \right). \quad (1.24)$$

Maley *et al.* then plotted their magnetic relaxation data, taken at different temperatures and thus different values of the initial magnetization, in the form $T \ln(dM/dt)$ vs M , which they recognized should be equivalent to within an additive constant to U/k_B vs M . Through trial and error, they found the constant which caused all their data to fall on the same smooth $U(M)$ curve. The result of their procedure is shown in **Figure 13 (a)** and **(b)**. As can be seen in the figure, the data appear to fall on a smooth $U(M)$ curve which exhibits a logarithmic decay of the pinning potential with magnetization (or J). Other experimental approaches for determining the dependence of U on J have been tried [36, 48, 49], and they all support the logarithmic dependence of U on J .

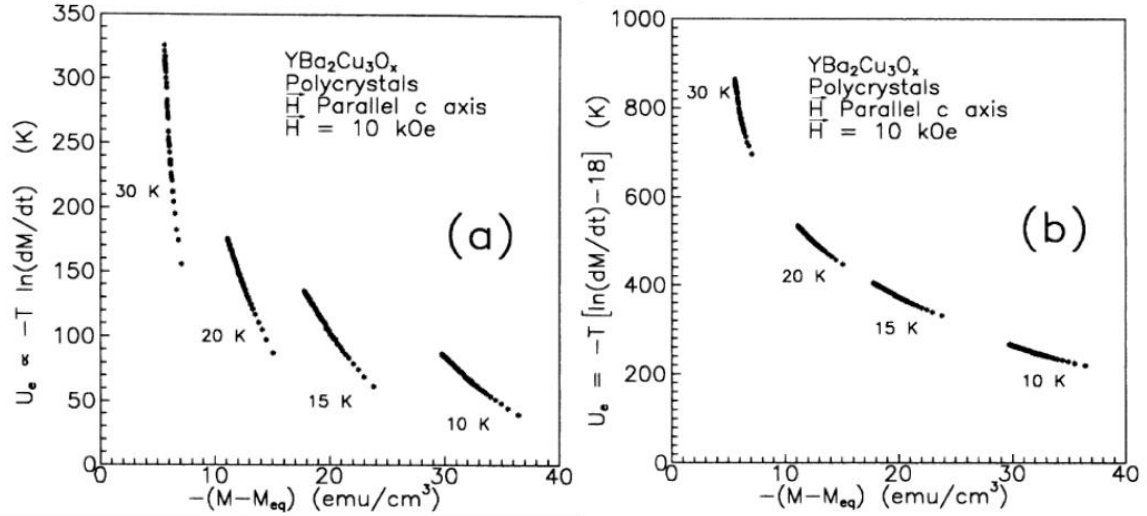


Figure 13. (a) Plots of $T \ln(dM/dt)$ vs $M - M_{eq}$ for different temperatures. (b) Plots of the same data as in (a), but with a constant for each temperature ($C = 18$) added to each data set, after [45].

Even though flux creep was first studied by Anderson in LTS, it is not a major phenomenon in LTS except at temperatures near T_c . It is true that when LTS conductors are used in accelerators there is a time decay of field errors at injection, however, these errors are due to interactions of the coupling current with the hysteretic currents of the superconductor, rather than flux creep [6]. But in any case, this is problematic, since the magnetic field harmonics change over time even though the current in the magnets is kept constant, as shown in **Figure 14**. During accelerator magnet operation, the magnetic field of the magnets are ramped (by increasing the current in the magnet windings) to a set magnetic field (usually 0.5 – 1 T) where the field is held constant for the 20 minutes to 2 hours required to inject the particles, depending on the accelerator. Whereas, a constant

magnetic field is desired during injection, it is often seen that the harmonics of the field can decay by several units. This change in the harmonics can lead to a loss of particles or require complicated active correction techniques to offset.

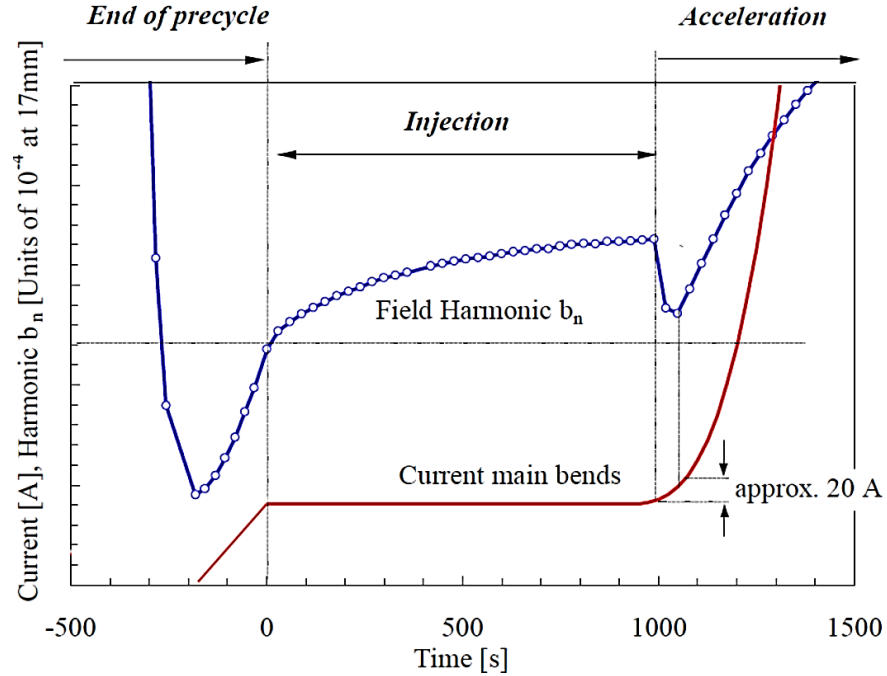


Figure 14. The field harmonic drift of accelerator magnets during particle injection, after [50].

Accelerator magnets made from HTS may suffer similar field errors to due coupling currents and interactions with the hysteretic magnetization, this is yet to be seen. However, they will certainly observe a very similar effect due to the intrinsic flux creep of HTS. One reason flux creep is greater for HTS is the smaller coherence length, ζ , in HTS which leads

to smaller pinning energies [51]. Because the stability of the magnetic field is of great importance in accelerator magnets, the flux creep behavior of HTS is an important practical consideration.

Finding the functional form of $U(J)$ for HTS-based composites will allow the prediction of the magnetic relaxation rate at magnetic fields which are relevant to application but are difficult or inconvenient to access using given equipment. Furthermore, it will tell something about the strength of the pinning in the composite. It could prove useful for assessing how different dopants and processing methods affect the pinning in the conductors. Most of the experimental methods to determine the functional dependence of U on J rely on measuring the magnetic relaxation of the sample at different temperatures while keeping the externally applied magnetic field constant. The temperature ranges are generally 10 K to 40 K for Bi:2212 single crystals and the externally applied magnetic fields are generally no larger than 1 T. These fields and temperatures are not representative of those which would be present in an accelerator environment. Another avenue to explore $U(J)$ in HTS-based composites is to hold temperature constant and vary the applied field. The applied field would change the initial magnetization, like the temperature changes used by Maley *et al.* An issue with this method may come from the generally flat J_c - B dependence of HTS.

1.7 Collective Creep

As mentioned above, collective pinning theory is often used to assess the pinning strength in HTS materials [51]. A basic premise of this theory is that fluxons in HTS are not pinned on an individual basis with single, strong, pins that pin individual fluxons. In fact, the fluxons are pinned by the collective interaction of many weaker pins, which surround the fluxon. A consequence of this theory is that the intrinsic pinning strength is not the pinning strength of an individual pin, but that of the interaction of a collection of pins that act on a fluxon. Therefore, the pinning strength extracted using this theory would be higher than what is expected from a simple, strong pinning theory. In fact, in collective pinning theory, an intrinsic energy scale is extracted rather than a single, direct, value for the intrinsic pinning strength. The interpolation formula as described in [51] and discussed in Chapter 4 is used to extract this intrinsic pinning energy scale. This formula accounts for the differences between creep close to J_c ($J \sim J_c$) and $J \ll J_c$ (where significant creep has already occurred. When the current density in the material is low compared to the critical current density, such as would be the case after some time which allows the fluxons to creep, lowering the flux density gradient.

This introduction has described the basic phenomenology of superconducting materials and has given the motivation for the study. Chapter 2, immediately following focuses on experimental methods. Chapter 3 reports on measurements of magnetization and magnetization decay in Bi:2212 strands, and correlations to microstructure. Chapter 4 discusses magnetization and magnetization creep for YBCO, extracting fundamental

pinning strengths, and correlating to nanostructure. Chapter 5 focusses on the magnetization of Bi:2212 and YBCO cables, and Chapter 6 uses these results to compute expected field errors and field error decay for HTS accelerator magnets. Chapter 7 summarizes the work.

Chapter 2. Experimental Methods

Several YBCO and BiI2212 HTS conductors and materials were studied in this thesis, and were characterized using various techniques, including: (1) vibrating sample magnetometry (VSM), (2) Hall sensor magnetometry, (3) scanning electron microscopy (SEM), and optical microscopy. Selected results of TEM studies from collaborators are also included to enable some analyses. Below I first discuss the characterization techniques, followed by the samples measured.

2.1 Magnetometry

Two kinds of magnetometry were used in this thesis, VSM using an existing commercial system, and a Hall Probe cable magnetometer made in the execution of this thesis. The latter is described in detail in Chapter 5, here we focus on the commercial VSM measurements. The VSM of a Quantum Design Physical Property Measurement System (PPMS) was used to measure the magnetization and its temporal change for several samples including Bi:2212 round wire composites and YBCO-based conductors (2G tapes). The magnetization of the superconducting composites and conductors can be used to determine the magnetic critical current density (J_c) and the critical temperature (T_c) of the superconductor in the composite. The decay can be used to extract pinning potentials.

In a VSM, the sample is vibrated in and out of two pickup coils which are wound anti-parallel. Winding the coils anti-parallel increases the signal. If the sample possesses a magnetic moment, a voltage will be induced in one of the pickup coils as the sample is moved into its bore. The change in flux with time, $d\Phi/dt$ seen by the coil induces an e.m.f in the coil, which is converted to a voltage according to:

$$V_{coil} = \frac{d\phi}{dt} \quad (2.1)$$

$$V_{coil} = \left(\frac{d\phi}{dz}\right) \left(\frac{dz}{dt}\right) \quad (2.2)$$

$$V_{coil} = 2\pi f C_c m A \sin(2\pi f t) \quad (2.3)$$

where ϕ is the magnetic flux, f is the frequency of vibration (or oscillation), which is generally 40 Hz in this system, A is the amplitude of the vibration, m is the magnetic moment of the sample, t is time, and C_c is a coupling constant (similar to a mutual inductance). As is seen above, the voltage induced in the pickup coils is proportional to the magnetic moment of the sample and can therefore be used to determine that moment, m . This moment can be normalized by the sample volume or sample mass to give a magnetization, $M = m/V_s$, where V_s is the sample volume. Therefore, the VSM can be used to measure the magnetization, M , of the sample as a function of applied magnetic field, $\mu_0 H$ (alternatively called $M-H$ or $M-B$ loop). The VSM is calibrated with a 262.7 mg palladium standard at 298 K and 2 T.

The VSM of the Quantum Design M6000 PPMS is used to measure the magnetic properties of the Bi:2212 and YBCO samples in this work. This VSM can be operated from 400°C down to 1.8 K with a sensitivity of 10^{-6} emu. Our system has a maximum field of ± 14 T. The VSM can be used to measure the DC susceptibility as well as the magnetization loop, or $M-H$. It is sometimes important to achieve a zero-field cooled “virgin” state, where there is no magnetic flux inside the sample in its superconducting state. This can be achieved by a procedure called a zero-field cool (ZFC) sequence. The ZFC sequence used in this work is as follows. First, the sample is warmed to a temperature above its T_c and then magnetic field generated by the magnet is set to 0 T. Then the sample is cooled to below its transition temperature to some set point. The sample is then in a zero-field cooled state (ZFC). After this, a small magnetic field can be applied. The VSM can also be used to measure the hysteresis $M-\mu_0H$ curves of superconducting samples. The $M-H$ loops are hysteretic and are as discussed in Chapter 1. The difference in the magnetization between the shielding and trapping branches, ΔM (the “width” of the hysteresis loop), at an applied field can be used to calculate J_c of the superconductor using the Bean critical state model [13, 14], where $J_c = C\Delta M$, where C is a constant that depends on the sample geometry, as described in detail in Chapter 1. The samples and detailed geometries are presented in the chapters which detail the measurement results, namely Chapter 3 for Bi:2212 strands, Chapter 4 for YBCO tapes, and Chapter 5 for Bi:2212 and YBCO-based cables.

2.2 I_c Measurements

Transport I_c measurements, at 4 K, in several different applied magnetic fields, were performed on selected Bi:2212 round wire samples. The current-voltage (I - V) transition was measured as a function of applied magnetic field. A $1 \mu\text{V}/\text{cm}$ electric field criterion was used to determine the I_c ($\mu_0 H$) from the I - V curves. The technique uses the standard 4-point technique to minimize the contact and lead resistances, as detailed in [52]. Current is sourced through the sample until the electric field criterion is reached or the sample is damaged. Approximately 3 cm long Bi:2212 composite round wire samples were submerged in a liquid helium bath inside of an Oxford Instruments 15 T solenoid magnet. Submerging the samples in liquid helium ensured they were at 4 K before measurement. Current was supplied with a HP 6671 current source. A Keithley 182 nanovoltmeter was used to measure the voltages. The voltage tap spacing was approximately 5 mm. An in-house Labview program was used to control the current, record the voltage, and calculate I_c . Engineering J_c (J_e) was calculated by dividing I_c by the round wire composite cross-section. J_c was calculated by dividing I_c by the cross-sectional of the composite occupied by superconductor.

2.3 Scanning Electron Microscopy

Scanning electron microscopy (SEM) is a technique to create an image of the surface of a sample by rastering a focused beam of electrons across the sample surface.

The electrons are emitted by an electron source at the top of the microscope column and focused using magnetic lenses. The electrons from the beam can interact with the sample inelastically and elastically. Secondary electrons (SE) are electrons which are emitted from the sample due to inelastic collisions with the electron beam. The electron beam ejects K orbital electrons from the sample, and these electrons are detected in the microscope with a scintillation detector. SE are emitted from a smaller depth into the sample than BSE, and they have lower energy than BSE. Therefore, SE are more useful for obtaining topographic features of the sample. BSE elastically scatter from the atoms within the sample. They have higher energy than SE and are emitted from deeper within the sample. BSE are more useful for obtaining Z number contrast. Both SE and BSE images were taken in this document using a Philips XL-30F ESEM, the focus was on Bi:2212 composites to quantify their filament bridging. Generally, accelerating voltages of 5- 20 kV were used. The samples were mounted in either ConductoMet or low viscosity epoxy from Struers. The samples were polished using SiC papers with different grit sizes. The final polish was often conducted using a Vibromet using colloidal alumina as the polishing medium.

2.4 Samples

2.4.1 Bi:2212 Round Wire Composites

Two different kinds of Bi:2212 round wire composites were measured. The first were round strands provided by Oxford Superconducting Technologies, they had strand

diameters of 0.8 mm and filament configuration of (a) 18 bundles with 37 filaments in each bundle, (b) 7 bundles with 37 filaments in each bundle. The second strand type was manufactured by Supramagnetics Inc. and were Bi:2212 round wire composites with a single restack of randomly oriented highly aspected filaments (single bundle). Selected *I-V* measurements and magnetic measurements were performed on these Bi:2212 samples.

2.4.2 YBCO Thin Films and Conductors

Two kinds of YBCO samples were measured. The first were YBCO thin films made by Pulsed Laser Deposition (PLD). These were provided by the Air Force Research Labs in a collaboration. Pulsed laser deposition (PLD) is a physical vapor deposition technique. A pulsed laser is used to strike a target material. The laser causes rapid heating of the surface of the sample, causing a plasma of the target material to form on the target surface. The plasma is ejected perpendicular to the plasma surface and impinges on a substrate, onto which the species of the plasma are deposited [53]. Thin films of YBCO, created using PLD, with different volume fraction of secondary phases were studied in this document. The laser of the PLD system is a Lambda-Physik KrF excimer laser with a wavelength of 248 nm. The energy density of the laser was 3 J/cm². The repetition rate used was 4 Hz. The target to substrate distance was 5.5 cm and atmosphere was 300 mTorr of O₂. The sample details are described in Chapter 4.

The second kind of YBCO sample measured in this thesis were YBCO tapes, or coated conductors. These samples were provided by the University of Houston in a collaborative program. These are fabricated in relatively long lengths using a Metalorganic Chemical Vapor Deposition (MOCVD) approach, which is a chemical vapor deposition technique. It is useful for the manufacture of HTS composites as it can provide high volume throughput. In this technique, the cationic organic molecules of the HTS material (precursors) are vaporized and transported onto a heated substrate in the reactor [54]. The precursors were made by mixing the organometallic tetramethyl heptanedionate (thd) compounds of Zr, Gd, Y, Ba, and Cu in tetrahydrofuran solvent in the desired molar concentrations [55]. The precursors were delivered to the evaporator at a constant rate using a pump. Argon gas was used to carry the vaporized precursors to the reaction chamber. The substrate for the tapes was 12 mm wide and 50 μm thick Hastelloy C-276. On top of the substrate was a buffer layer of $\text{Al}_2\text{O}_3/\text{Y}_2\text{O}_3/\text{IBAD-MgO/MgO/LaMnO}_3$. (Gd, Y)BCO superconductor tapes with mol% Zr additions of 0, 7.5, and 25 were fabricated using a reel-to-reel process at a deposition rate of 80 nm min^{-1} . Sample details are given in Chapter 4.

Chapter 3: Bi:2212 Microstructure and Magnetic Property Correlation

This chapter focusses on the microstructure and magnetic property correlation for Bi:2212 composites. It is shown that the magnetization and its temporal change in Bi:2212 round wire composites are influenced by the geometry and microstructure of the composite. Direct measurements are reported which show that both the magnetization and its temporal change are larger in longer samples and/or samples that have larger twist pitches. The enhanced magnetization with sample length is attributed to a microstructural feature prominent in Bi:2212 round wire composites, called filament-to-filament (or interfilamentary) bridging. An analytic mathematical model, which treats the round wire composite as an anisotropic continuum, is used to quantify the level of connectivity between the filaments in the composite. The results of using this model are compared to an assessment of the level of bridging detected using microscopy.

Bi:2212 round wire composite conductors are of great interest for future accelerator applications [1, 56-59]. High upper critical (B_{c2}) and irreversibility field (B_{irr}) are needed for new magnets which will need to operate near or above the B_{c2} limit of Nb_3Sn . The critical current density of LTS conductors such as Nb_3Sn decrease rapidly with increasing field above 15 T, whereas the Bi:2212 field dependence is relatively constant up to very high fields, making it promising for the high field magnets required of the next generation NMR spectrometers, MRI scanners, and particle accelerators. Until relatively recently, the

intrinsic current density and fill factor of Bi:2212 composites were too low to be suitable for high field magnet applications. Now that these have been increased to suitable levels, other issues such as the field quality, and its change with time, of magnets built from HTS materials must be considered, especially for particle accelerator applications where very high field quality and temporal stability are required. Bi:2212-based composites compete with YBCO (or REBCO)-based composites for these prospective applications. The field quality depends on the magnetization of the cable, and hence that of the strand. This magnetization in turn depends on the filament diameter, or an effective filament diameter, d_{eff} , to which the magnetization is proportional [60]. NbTi strands have filament diameters of typically 6 μm or so [61], and Nb₃Sn d_{eff} s are typically around 50 μm [62, 63]. For multifilamentary NbTi/Cu composites d_{eff} is simply the filament diameter, whereas for Nb₃Sn, d_{eff} is typically the subelement diameter. For Bi:2212, it has typically been the case that d_{eff} is the entire filamentary array diameter (the diameter of the strand, excluding the outer sheath). Then, since the strand outer diameters (ODs) are typically 0.8 mm or so, this can lead to d_{eff} s of 500-600 μm . These large values of d_{eff} are caused by small filament-to-filament or bundle-to-bundle intergrowths (also called bridges) which form during the partial melt process heat treatment. These bridges may enhance the transport J_c by providing a superconducting path around current limiting mechanisms such as pores and secondary phases [64], but they couple the filaments together and lead to a large d_{eff} [24, 65, 66].

Multifilamentary strands experience hysteretic loss due to circulating currents induced by a transverse magnetic field. One method to reduce hysteresis loss, though not developed specifically to address bridging, is to twist the filaments during manufacture of the wire. Whereas twisting reduces eddy-current loss, it should also reduce the coupling due to bridging because, as the twist becomes tighter (i.e., as the twist pitch length decreases), the number of bridges within the twist pitch length decreases, reducing the amount of transverse current and hence the circulating current. Twisting has recently been applied to Bi:2212 round wires and has indeed been shown to lead to a reduction in AC loss compared to non-twisted samples [67].

Bridging induced magnetization in Nb₃Sn conductors has been seen to depend on sample length (and twist pitch) up to a critical length, at which saturation occurs [68]. Thus, it is not strictly correct to describe the magnetization due to bridging in terms of d_{eff} unless the length dependence is considered. Expressions based on the anisotropic critical state (ACS) model which provide quantitative descriptions of bridging in ACS terms, and which account for the length (and twist pitch) dependencies, were developed by Sumption [24]. Based on these expressions, bridging induced magnetization is expected to depend linearly on both twist pitch (L_p) and sample length (L) for shorter L_p and L , with a saturation for large L_p or L .

The dependence of the magnetic properties on sample length is important from a technical perspective in that the sample spaces of typical measurement devices used to quantify the magnetic properties, such as vibrating sample magnetometers (VSMs) and

superconducting quantum interference devices (SQUIDs), are a few millimeters in diameter at maximum. Therefore, historically, the magnetic properties of samples of short lengths have been used to estimate the magnetic properties of larger magnet structures from which the short samples are made. Although d_{eff} has been used historically to quantify excess magnetization due to electric coupling between filaments, it is shown below that d_{eff} depends upon sample length.

3.1 Bi:2212 Round Wire Composite Form

Bi:2212 round wire composites are manufactured using the powder-in-tube (PIT) process, see **Figure 15**, during which Bi:2212 powder is packed into a silver tube and drawn to form a wire (top and middle on left side of **Figure 15**). This assembly becomes a “filament” in the final composite round wire. The stacking is performed several times to produce several filaments. A group of filaments is assembled in a larger diameter silver tube and re-drawn (bottom on left side of **Figure 15**). This assembly becomes a “bundle” in the final composite round wire. Several bundles are stacked into a larger silver or silver-alloy tube (the matrix material) and the assembly is drawn to form a round wire composite (cross-section shown to right in **Figure 15**).

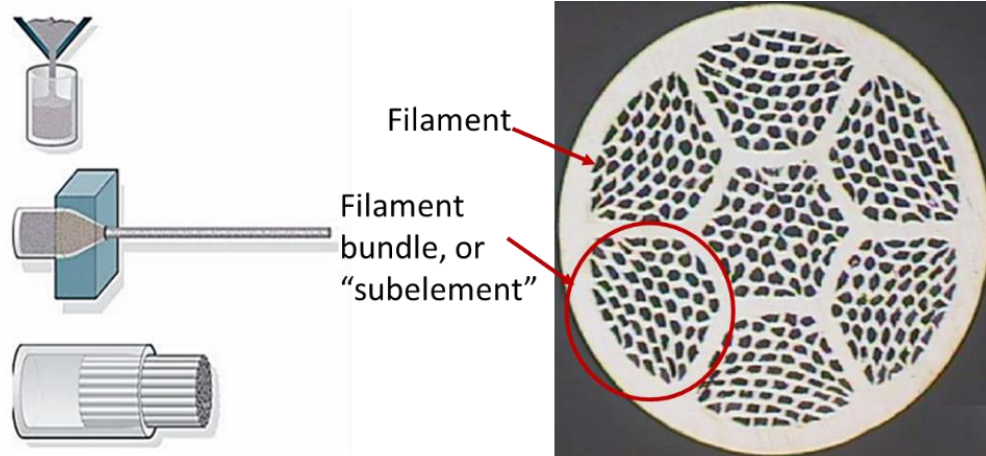


Figure 15. (Left) A schematic of the process used to make Bi:2212 strands. (Right) The unreacted cross-section of a strand [69].

One of the reasons to manufacture a superconducting round wire composite in the form of a filamentary composite is to minimize the magnetization due to shielding currents which are generated when the superconductor is exposed to a magnetic field. The magnetization of a monocoil is proportional to its diameter. The monocoil must be relatively large in order to carry the needed magnet current. A monocoil which has a large diameter would have an unacceptably large magnetization unless filamentary subdivision is applied. However, the effectiveness of filamenting the strands to reduce the composite magnetization becomes degraded in Bi:2212 round wire composites due to filament-to-filament (or interfilamentary) bridging.

3.2. Filament-to-Filament Bridging

After manufacture, the round wire, consisting of Bi:2212 powder stacked into tubes that are arranged into bundles of filaments, **Figure 15**, is heat treated using the partial melt-process [69]. The primary aim of this heat treatment is to provide a continuous current path down the length of the wire as, upon cooling, the melted Bi:2212 powder solidifies to form large, well-connected, grains. During the partial melt process, some of the liquid Bi:2212 traverses out of the filaments and impinges upon liquid material from other filaments. Thus, upon cool down the microstructure of the Bi:2212 round wire consists of filaments bridged by Bi:2212 which has traversed the matrix, as shown in **Figure 16**. In the figure, the filaments are the many black shapes within the grey cylinder (the silver sheath). These filaments are arranged into bundles (There are 18 bundles in the figure.). These bundles are confined to the filamentary array array (enclosed by the blue circle). The connections between individual filaments are the interfilamentary bridges. It has been proposed that some of the bridges can carry significant electric current and provide a route for current to bypass blockages down the filament length [64]. However, if these bridges can carry significant electric current while the superconductor is in the superconducting state, then the shielding currents generated when the Bi:2212 superconductor is exposed to a magnetic field can traverse a larger current path and yield a larger magnetization than that of a fully filamentary composite. This phenomenon is illustrated schematically in **Figure 17** and **Figure 18**.

The two shaded parallelepipeds with square cross-section, **Figure 17**, represent semi-infinite slabs, or filaments, of superconductor in a strand. They are separated spatially and electrically and embedded in the strand matrix. Each filament has a width, d , and length, L .

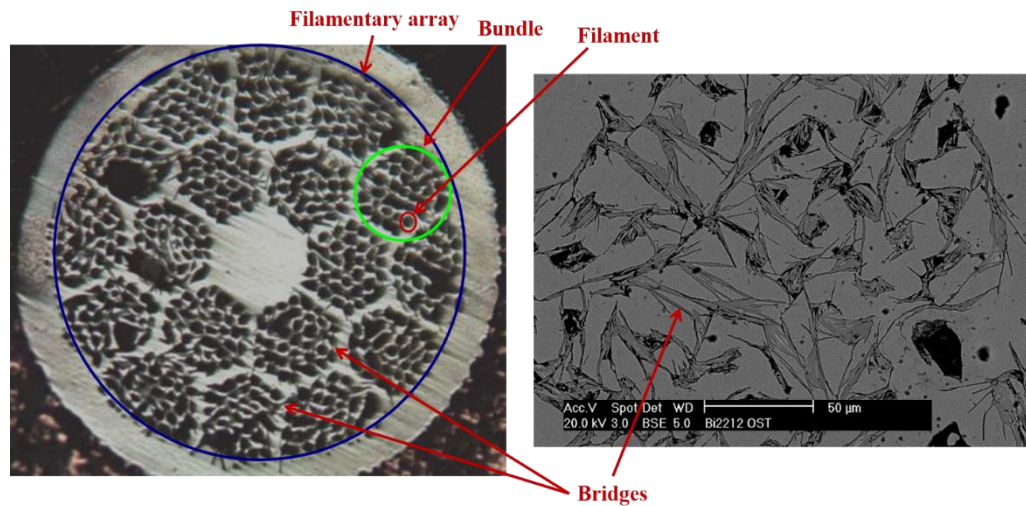


Figure 16. The microstructure of a Bi:2212 round wire after heat treatment. During heat treatment, liquid from filaments can traverse the matrix and connect with other filaments. These connections can remain after cooling and may carry significant current.

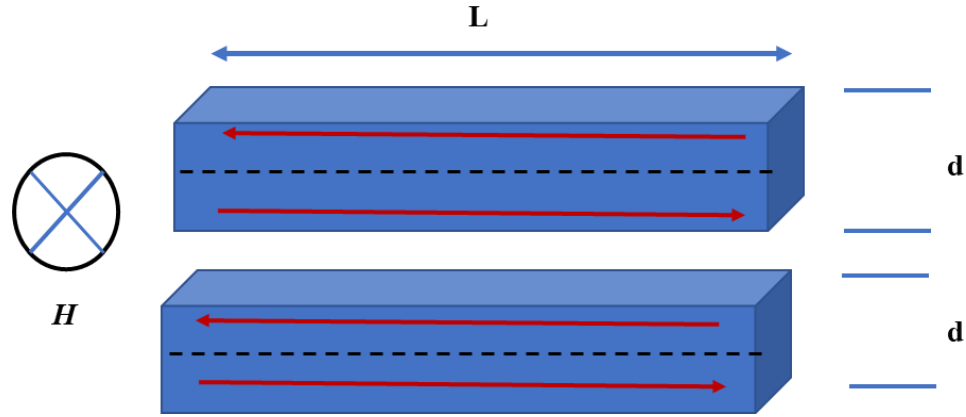


Figure 17. A schematic illustration of the shielding current flow in two uncoupled filaments in a strand subjected to a perpendicular magnetic field. The red arrows are the current.

As a magnetic field, H , is applied perpendicular to the strand (and thus the filaments), currents (red arrows in the figure) flow in each filament, which act to shield magnetic flux from entering the filaments. The magnetic moment from a single filament is given by $m = IA$, where I is the current and A is the area of the loop enclosed by the current. If the critical current density is J_c , the current flowing in each filament is $J_c(d)(d/2)$, or $I = J_c d^2/2$. The area enclosed by the current loop is the product $d*L$. Therefore, the magnetic moment from one filament is $m = J_c d^2/2(dL) = J_c d^3 L/2$. The volume of a single filament is $d^2 L$, so that the filamentary volume normalized magnetization of a single filament is $J_c d/2$. If the filaments are isolated, this is the total magnetization of any number of filaments which have identical length and cross-section. The situation when the filaments are bridged, or electrically coupled is shown schematically in **Figure 18**.

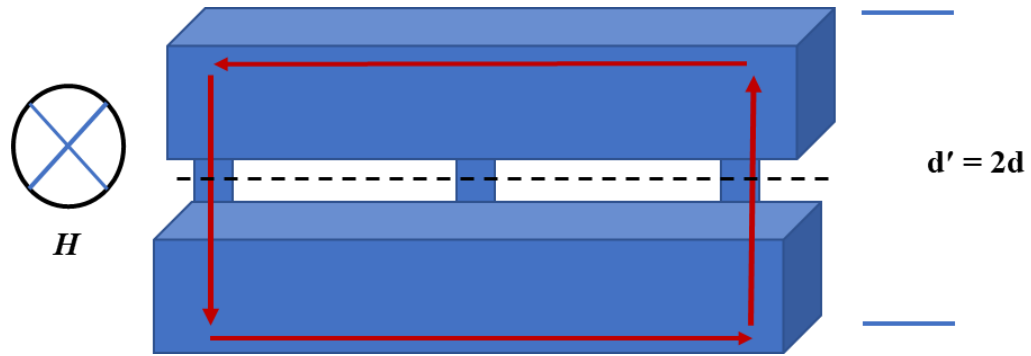


Figure 18. A schematic illustration of the shielding current flow in two bridged (or coupled) filaments in a strand subjected to a perpendicular magnetic field.

In this case, current can flow across the bridges to shield a larger volume than the filamentary volume. The two, previously separated, filaments now act as a single filament with an effective filament diameter of $d' = 2d$, and the current now encloses an area at least twice that of a single filament, and the magnetization, M , is now at least twice as large, or at least *equal to* $J_c d$. If more than two filaments are coupled, the magnetization increases accordingly. Many early Bi:2212 strands had magnetization large enough to indicate that the entire filamentary array was electrically coupled, meaning that the magnetization was like that of a monocoil of radius equal to that of the filamentary array.

Traditionally, rather than give a value for the magnetization, M , of a sample of strand directly, it has been customary to use an expression that relates J_c to M and the diameter of the superconductor filament, d , to extract a value of d that represents an effective filament diameter, d_{eff} , using

$$d_{\text{eff}} = \frac{3\pi \Delta M}{4 J_c}. \quad (3.1)$$

However, this expression does not account for a sample length dependence of M . As depicted in **Figure 16**, the cross-section of the filament-to-filament bridges is irregular, and the amount of current a single bridge can carry is difficult to discern. It is likely that some of the bridge cross-section is void space, non-superconducting phase, or high-angle grain boundaries, among other possibilities. Each of these are current limiting mechanisms in the Bi:2212 microstructure. Therefore, it is not hard to imagine that many bridges may be required to carry the full filamentary current transversely across the matrix from filament to filament. If that is the case, there ought to be a sample length small enough that there are too few bridges to carry the full filamentary current, and the measured magnetization would be less than that of samples which are longer and which subsequently have a larger number of bridges. The bore diameters of typical magnetometers are only a few millimeters, and, therefore, often the magnetization of samples which are a few millimeters long are relied on for field error calculations or assumed to be valid for long lengths of strand or cable. However, if a few millimeters is not large enough for the magnetization to saturate, for example, because there are not enough bridges to carry the full filamentary current across to other filaments, then these magnetizations would not be representative of the magnetizations of longer strands and cables used to build magnets, and any conclusions from the short sample measurements could be erroneous. Therefore, whether the magnetization of Bi:2212 samples depends upon length, at least for lengths above the typical short sample lengths measured in conventional magnetometers, should

be studied. If there is a length dependence, a more fundamental expression that quantifies the amount of connectivity between the filaments is needed to replace the traditional expression for d_{eff} .

3.3. Magnetization Measurements on Bi:2212 Samples of Different Length and Twist Pitch

3.3.1. Samples

To study the length dependence of the magnetization of the Bi:2212 round wire composite, a series of samples of different lengths were cut from four coil samples of Bi:2212 round wire composites that were manufactured by Oxford Superconducting Technologies (OST) [56, 67]. The sheath material of the composites was a silver-magnesium alloy. The strand diameter was 0.813 mm, and each strand had 18 bundles consisting of 37 filaments (OST 0.8 mm, 37 x 18 wire). The bundle diameter was 130 μm , and the filament diameter was 15 μm . The coil samples had twist pitches, L_p , of 25.4 mm, 12.7 mm, and 6.35 mm. The fourth segment was not twisted (i.e., it had infinite L_p). The coil segments were reacted by OST and provided in the form of helical coils, with coil diameter ~ 5 mm. From these coils, segments were cut for measurement in the PPMS; the maximum coil segment length was 6 mm, corresponding to about 5-6 turns. The I_c (4.2 K, 12 T) and J_c (4.2 K, 12 T) values, as measured by OST on a 1 m barrel sample at 12 T, were 130 A and 1050 A/mm², respectively. The fill factor (λ_{sc}) was determined from the J_c (via $\lambda_{\text{sc}} = I_c/AJ_c$) to be 0.246. The magnetization of two different types of samples was

measured: (i) non-twisted samples of various lengths (L), where L is the total length of the strand (sample) and not the length of the coil, and (ii) samples of various twist pitches, L_p s, (where $L > L_p$). The approximate sample length to twist pitch ratios (L/L_p) for the samples with L_p s = 25.4 mm, 12.7 mm, and 6.35 mm were 3, 7, and 12, respectively. Nine different lengths were cut from the non-twisted coil in order to study the length dependence of the magnetization.

3.3.2. DC Magnetization Measurements

DC magnetization measurements were performed at 5.1 K using DC extraction magnetometry with the ACMS option of a Quantum Design Model 6000 PPMS. M - $\mu_0 H$ loops were measured from -2 to 14 T with the magnetic field applied to the open face of the coils and ramped at 13 mT/s.

3.4. Results

3.4.1. M - $\mu_0 H$

The 5.1 K M - $\mu_0 H$ loops of both the twisted and non-twisted samples were obtained by normalizing the measured magnetic moments by the volume of the Bi:2212 in the samples. The results of the measurements on the twisted samples of different lengths are shown in **Figure 19** along with the results of the measurements on the non-twisted samples whose lengths most nearly match the lengths of the twisted samples. The magnetizations

of the twisted samples are clearly smaller than those of the non-twisted samples (for the same sample length), as might generally be expected, and as demonstrated recently in OST strands [67]. It should also be noted, however, that the magnetizations of the non-twisted samples depend upon sample length. This length dependence is further explored in the results of the non-twisted sample measurements shown in **Figure 20**. The functional forms of the L_p and L dependencies of magnetization and d_{eff} are explored below in Section 3.5.

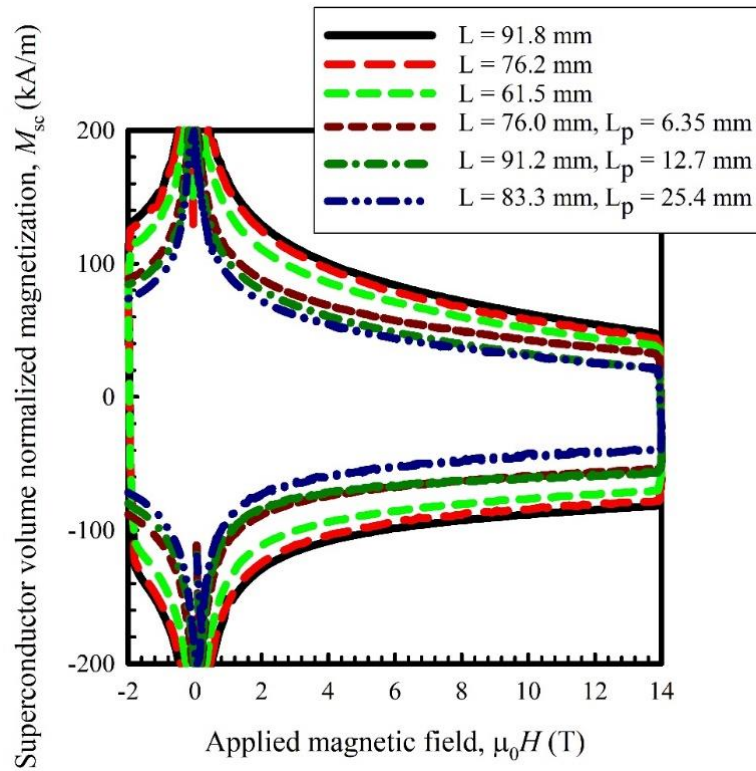


Figure 19. $M-\mu_0H$ of twisted coil samples with different L_p s plotted alongside $M-\mu_0H$ s of non-twisted coil samples with similar L . The magnetization of the twisted samples is significantly reduced compared to the non-twisted samples. Published in [70].

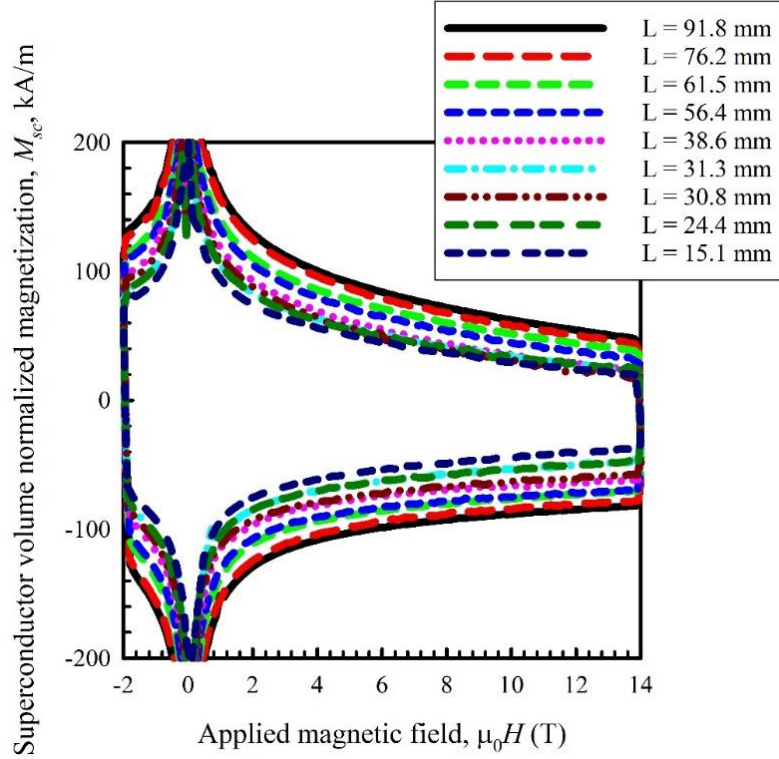


Figure 20. $M-\mu_0H$ of non-twisted coil samples with various lengths, L . The magnetization clearly depends upon L . Published in [70]

3.4.2. d_{eff} vs L or L_p

The height of the hysteresis loop, ΔM_{sc} , at 12 T and the transport J_c (4.2 K, 12 T), provided by OST, for a 1 m barrel sample made from 37 x 18 filament design strand were used as inputs to the standard critical state expression for the J_c of a superconducting rod in a transverse magnetic field

$$d_{\text{eff}} = \frac{3\pi\Delta M_{\text{sc}}}{4J_c} \quad (3.2)$$

to calculate d_{eff} at 12 T for all samples. The results are presented in **Figure 21**, as a function of sample length. The d_{eff} s of the twisted samples are substantially smaller (by factors of 1.5-3) than those of the non-twisted samples at any given sample length, consistent with the results of Huang *et al.* [67]. Furthermore, the d_{eff} s of the non-twisted samples appear to depend linearly on sample length. The M - $\mu_0 H$ loops presented in **Figure 19** for the coil samples with $L_{ps} = 6.35$ mm, 12.7 mm, and 25.4 mm correspond to the points in **Figure 21** with d_{eff} s of 156, 191, and 211 μm , respectively.

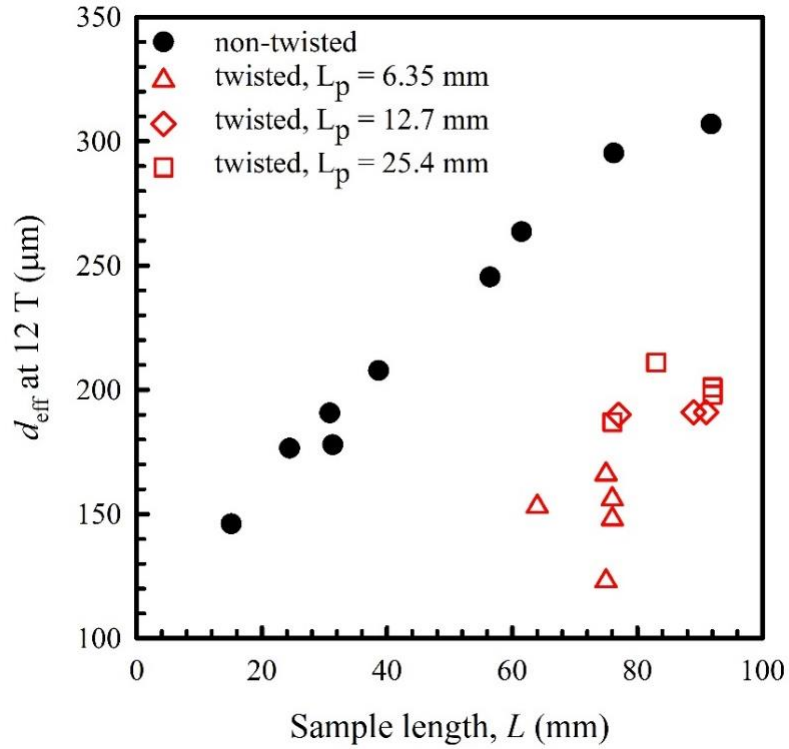


Figure 21. 12 T d_{eff} vs sample length for twisted and non-twisted samples. d_{eff} of the twisted samples is clearly smaller than that of the corresponding non-twisted sample. Published in [70].

3.5. Model for the Length Dependence of Magnetization or d_{eff}

The linear dependence of sample magnetization on length was predicted by Sumption [24]. In that work, a model was developed for Bi:2212 magnetization, which predicts an initial linear increase of magnetization (or d_{eff}) with sample length (of non-twisted samples), with a saturation at long sample lengths, where d_{eff} becomes the filamentary array diameter. A similar dependence of d_{eff} or magnetization on strand twist pitch was predicted, with, again, a saturation of d_{eff} to the filamentary array diameter. In

that work [71], the strands had relatively high levels of bridging, and saturation occurred at quite small sample lengths, making d_{eff} suppression by strand twisting impractical. Conversely, the present strands have a slower approach to saturation, implying a lower level of overall bridging, making twisting a practical approach for d_{eff} reduction.

To further illustrate the functional dependence of d_{eff} (and magnetization) on both L and L_p , the 12 T d_{eff} data for both the non-twisted and twisted coils are re-plotted versus L or L_p , in **Figure 22**. That figure showed an increase in d_{eff} with both L and L_p as expected from [24]. The level of bridging in the samples can be quantified by fitting the data of **Figure 22** to the expressions from [24]. Many non-twisted samples are available for measurement since they could be cut from a single HT sample, whereas samples of different twist pitches require separate preparation for each twist pitch value investigated. Given that fact, the non-twisted coil d_{eff} vs L data were used for the fit, as shown in **Figure 22**. The slope of this line is $2.19 \mu\text{m}/\text{mm}$ and the 12T d_{eff} -intercept is $119 \mu\text{m}$, which is close to the average bundle diameter of $130 \mu\text{m}$ determined using optical microscopy. The value of the 12 T d_{eff} -intercept indicates that the filaments within the bundles are nearly completely coupled (there is dense bridging within the bundles). In samples of finite length, the low level of bridging between the bundles allows some bundle-to-bundle coupling. Because the number of bridges per unit length is fixed, as the sample length increases, there is a linear increase in the total number of bridges which can carry supercurrent through the gap between the bundles, allowing more transverse current flow and consequently increasing the magnetization. The data in **Figure 22** imply that the bundles are not

completely coupled, even for samples up to 92 mm in length, as the d_{eff} at this length is 306 μm , which is significantly less than the diameter of the entire filamentary array.

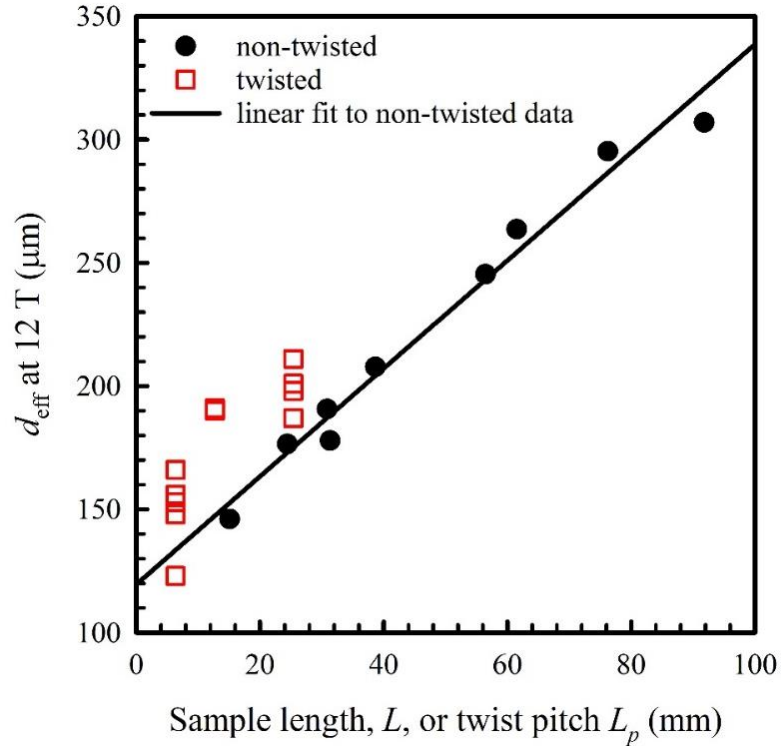


Figure 22. Dependence of 12 T d_{eff} on sample length or twist pitch. Published in [70].

The linear dependence of d_{eff} on L and L_p is shown in **Figure 22**, which is what was expected in [24]. However, the dependencies are not the same—they require different pre-factors. One reason for the difference is that the twisted sample has both filamentary J_c and

bridging J_c components, which are rotated around the strand by 90° before they are returned across the bridges.

3.5.1. Transverse Connectivity: Extraction of γ_2

The transverse electrical connectivity can be extracted from the magnetization measurements. The expressions developed in [24] include a parameter which quantifies the electrical connectivity in the transverse direction of the strands. As described in [24], the expression for the incremental magnetization, due to filament bridging, as a function of sample length (or twist pitch length) for samples which are sufficiently long that there is strong electrical coupling between the filaments is given by

$$\Delta M_s = \frac{4\gamma_1 J_{c1,1} d_{\text{eff}}}{3\pi} \left(1 - \frac{3\pi d_{\text{eff}} \beta_c}{32L} \right) \quad (3.3)$$

where γ_1 is a measure of the electrical connectivity along the length of the sample, $J_{c1,1}$ is the intrinsic critical current density along the length of the sample (normalized to filamentary area), d_{eff} is the effective filamentary diameter, L is the sample length and $\beta_c \equiv J_{c1}/J_{c2} = \gamma_1 J_{c1,1} / \gamma_2 J_{c1,2}$, (where J_{c1} is the critical current density along the length of the sample and J_{c2} is the transverse critical current density). The expression for samples which are short, such that there is a strong length dependence of the magnetization, is

$$\Delta M_s = \frac{\gamma_2 J_{c1,2} L}{2} \left(1 - \frac{4L}{3\pi \beta_c d_{\text{eff}}} \right) \quad (3.4)$$

where γ_2 is a measure of the connectivity across the sample and $J_{c1,2}$ is the intrinsic critical current density across the sample (normalized to filamentary area).

At the critical length, L_{crit} , which is the length at which the magnetization just saturates, the two expressions for the magnetization (equations 3.3 and 3.4) are equal. In fact, the initial slope of equation 3.4, can be extracted by equating the first terms of each, giving

$$\frac{\gamma_2 J_{c1,2} L_{crit}}{2} = \frac{4\gamma_1 J_{c1,1} d_{eff}}{3\pi} \quad (3.5)$$

To use this equation as is, it is necessary to assume that the current density is isotropic (i.e., $J_{c1,1} = J_{c1,2}$) and the sample has a uniform J_c along its length (i.e., it is fully connected along its length and $\gamma_1 = 1$). If we make these assumptions, the transverse electrical connectivity, γ_2 , can be extracted from the resulting expression

$$\gamma_2 = \frac{4}{\pi} \frac{2}{3} \frac{d_{eff}}{L_{crit}}. \quad (3.6)$$

In fact, if the d_{eff} vs L plot is linear until it reaches saturation, this expression is simply the slope of the linear (below saturation) region of the plot. Substituting the slope of 2.19×10^{-3} , for d_{eff}/L , gives $\gamma_2 = 1.86 \times 10^{-3}$. Thus, about 0.2% of the area between the bundles should be spanned by bridges.

However, we note that equations 3.3 and 3.4 are expressions for the incremental increase of the magnetization with increasing L and they do not express the total magnetization of the sample. That is, they do not consider the offset magnetization coming from the magnetization of the filaments themselves. In fact, an offset (12 T d_{eff} -intercept)

of 119 μm is seen in **Figure 22**. This offset value is significantly larger (~ 8 times) than the green state filamentary diameters, indicating that the filaments start out coupled to approximately this length scale (i.e., the subelements are coupled within themselves). To obtain an expression for the total magnetization, including the magnetization of the (coupled) filaments themselves, equations 3.3 and 3.4 need to be modified by adding on the offset term. If equation 3.2 is rearranged to give an expression for ΔM_s , and this result is substituted into equation 3.3, which has now been modified to include the offset term, the steps that led to equation 3.5 can be refollowed to give an expression for the transverse electrical connectivity. If the assumptions presented above are made, this expression is

$$\frac{4d_{\text{eff}}}{3\pi} = \frac{\gamma_2 J_{c1,2} L}{2} + \frac{4d_{\text{bundle}} J_c}{3\pi} \quad (3.7)$$

where d_{bundle} ($= 119 \mu\text{m}$, in this case) is the diameter of the subelement bundles (i.e., $d_{\text{subelement}}$). To extract γ_2 from this equation, the critical current density down the length of the filament must be assumed to be equal to the intrinsic transverse critical current density (i.e., $J_c = J_{c1,2}$). If this substitution is made, the second term of equation 3.7 can be rearranged to solve for γ_2 . The rearrangement gives.

$$\gamma_2 = \frac{8(d_{\text{bundle}})}{3\pi L}. \quad (3.8)$$

The results of using these expressions to calculate γ_2 for all the non-twisted sample lengths is presented in **Table 1**. If the assumptions used to extract γ_2 are correct, the γ_2 s in the table represent the fraction of the longitudinal cross-sectional area of the strand which contains

bridges. This fraction should be an intrinsic property of the strand and should not depend upon the sample length.

Table 1. γ_2 extracted using the linear part of equation 3.4. Published in [70].

Length (mm)	d_{eff} (μm)	γ_2 ($\times 10^{-3}$)
92	307	1.74
76	295	1.96
62	264	2.00
56	245	1.89
39	208	1.95
31	178	1.60
31	191	1.98
24	176	1.98
15	146	1.52

3.5.2. Correlation of Bridge Area with γ_2 via Microstructural Analysis of Bi:2212 Round Wire Cross-Sections

It should be possible to correlate the predicted transverse electrical connectivity using the equations of [24] with the number of bridges observed in the Bi:2212 round wire microstructure. SEM analysis of the microstructure of transverse cross-sections of strands extracted from the Bi:2212 coils do seem to indicate that the filament bundles are significantly bridged, as shown in **Figure 23**. Cross-sections of strands extracted from two different Bi:2212 coils are presented in the figure. However, in this figure it does not appear

that the bundles are connected to neighboring bundles. This type of bundle-to-bundle bridging is shown in **Figure 24**.

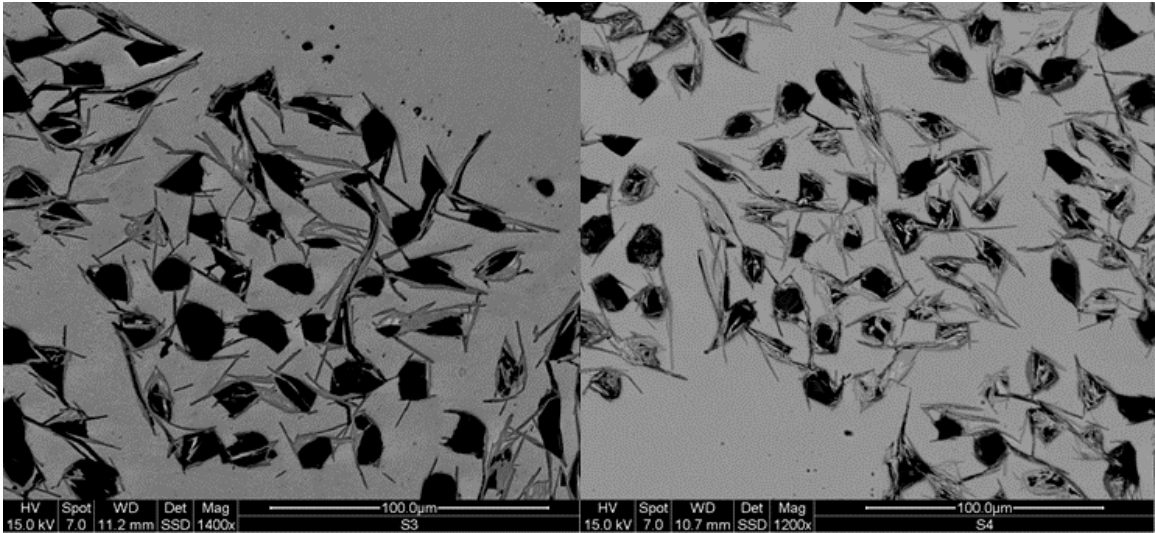


Figure 23. Transverse SEM micrographs of Bi:2212 coil strand cross-sections showing filamentary bundles being nearly fully bridged.

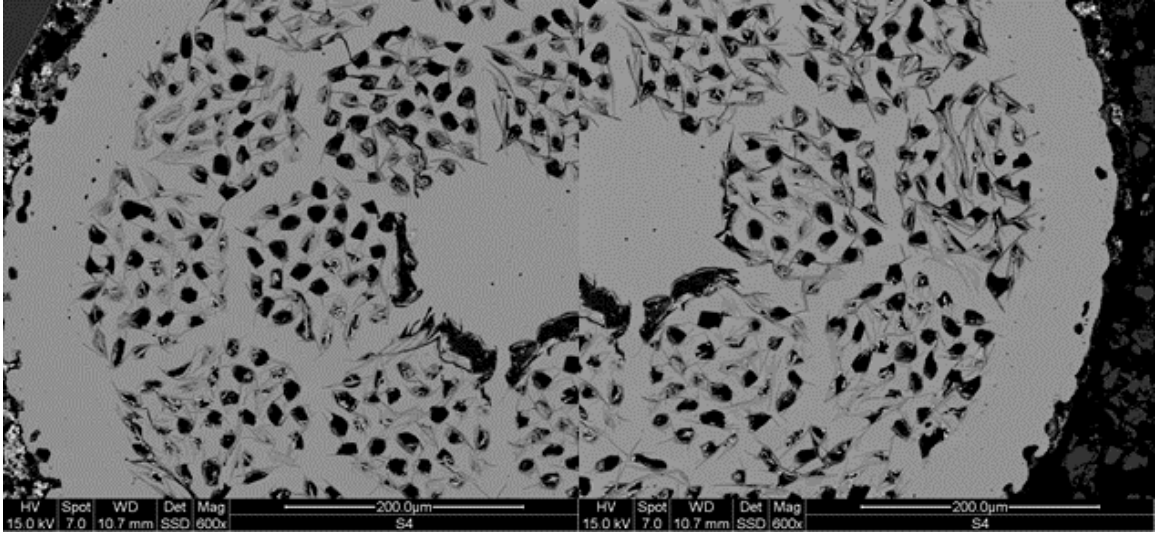


Figure 24. Transverse SEM micrographs of Bi:2212 coil strand cross-sections showing filamentary bundle bridging and inter-bundle bridging.

Qualitatively, the γ_2 calculations correlate with what is seen from the transverse micrographs. That is, there is significant bridging on the bundle size scale, but there does not appear to be significant inter-bundle bridging. However, the transverse micrographs provide a snapshot of the microstructure and do not show how the microstructure down the length of the sample evolves. Longitudinal cross-sections may provide a better idea of how the microstructure evolves with sample length. Longitudinal micrographs of strands extracted from the Bi:2212 coils are shown in **Figure 25**.

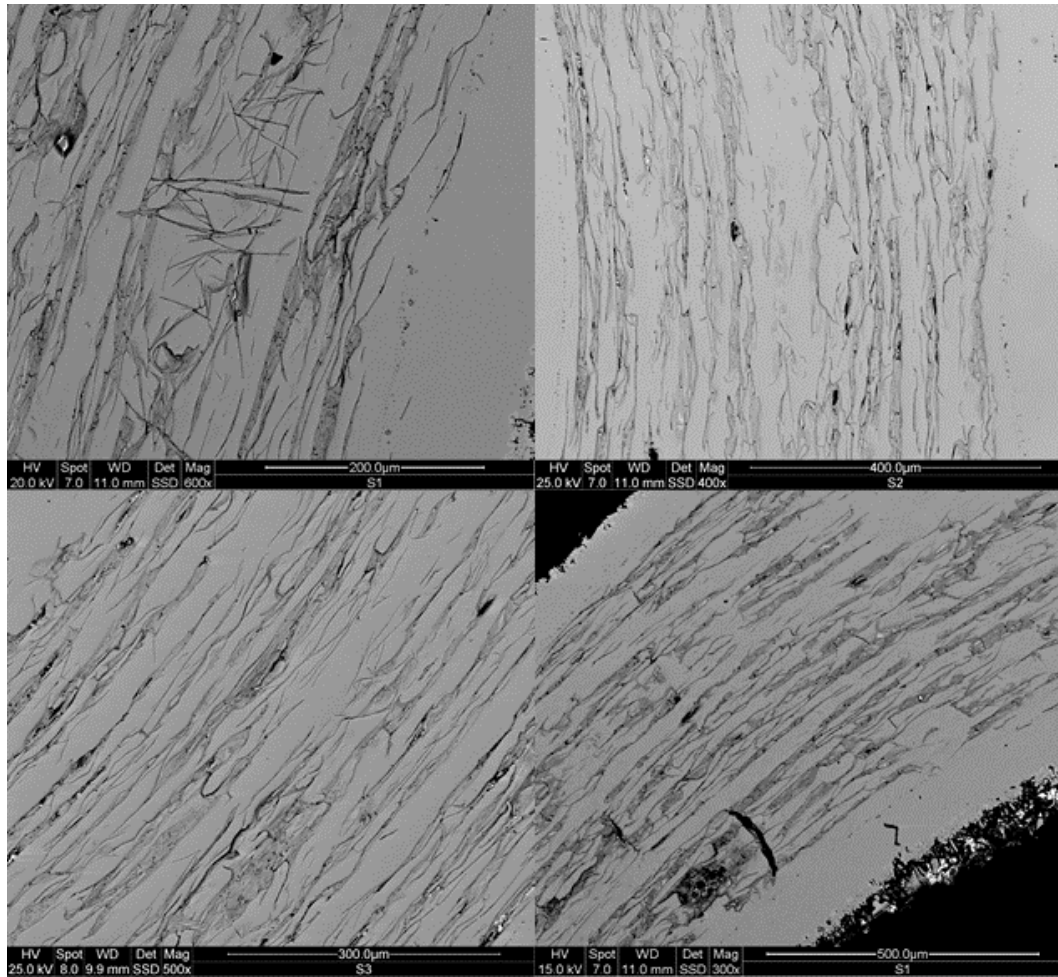


Figure 25. SEM micrographs of longitudinal cross-sections of Bi:2212 strands.

Significant bridging between filaments can be seen from the longitudinal cross-sections, but it is not quite clear if there is significant inter-bundle bridging, or how the bridging evolves with sample length. A possibility to quantitatively analyze the fraction of cross-section that is bridged could be to develop a histogram of the number of dark and light pixels along the length of the sample as a function of transverse depth. This approach

would be a sort of line-intercept method and could be accomplished in simple image analysis software. An example of this technique is shown in **Figure 26**. The red lines are drawn along the sample length and the total number of dark pixels is counted along a line. A histogram of pixels could be developed as a function of depth (the x-direction in the figure) into the sample. The ratio of the average high number of dark pixels to the average low number of dark pixels could correlate with γ_2 .

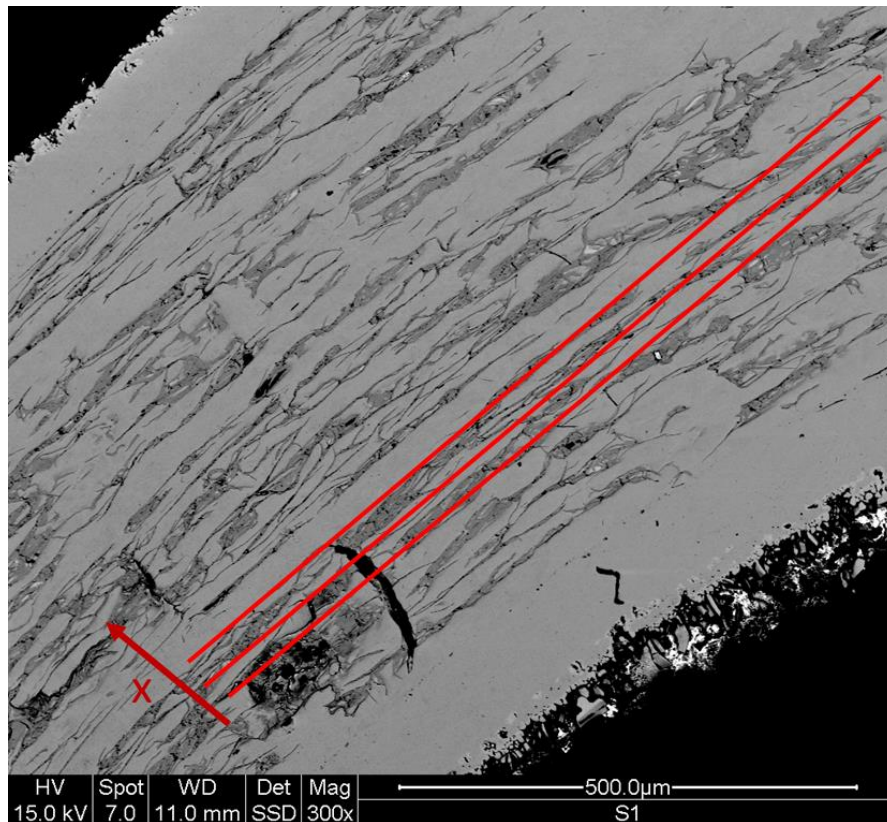


Figure 26. Longitudinal cross-section of a strand extracted from a Bi:2212 coil sample with lines drawn to count bridge intercepts.

3.6. Magnetic Relaxation

During accelerator magnet operation the current in the magnet is held constant during the particle injection phase. The constant current in the magnet should lead to a constant magnetic field generated by the magnet. However, the magnetization of high-temperature superconductors (HTS) has been shown to change with time when the superconductor is subject to a constant applied magnetic field. This phenomenon has been termed “giant flux creep” [28]. The change in magnetization with time is relatively insignificant in LTS, however, the it is expected to contribute to a noticeable temporal change in the field quality of HTS accelerator magnets during the injection plateau. Studies on the temporal change of the magnetization of Bi:2212 round wire composites are scarce. And, as of this writing, no studies, even on short samples, have been performed to determine if there is a length dependence to this change in the magnetization.

3.6.1. The Dependence of Magnetic Relaxation Rate on Sample Length

The magnetic relaxation of a straight, 5 mm long, sample and several coil samples (measured for d_{eff} in Section 3.3) of different lengths and twist pitches was measured over 2400 s, a typical injection plateau time period for an accelerator magnet (which is about 1200 s to 3600 s, at 5 K, 1 T). The results are shown in **Figure 27**. The reduction in the magnetic moment is about 7% higher for the 15 mm long sample and about 60% higher for the 92 mm long sample than that of the 5 mm long sample.

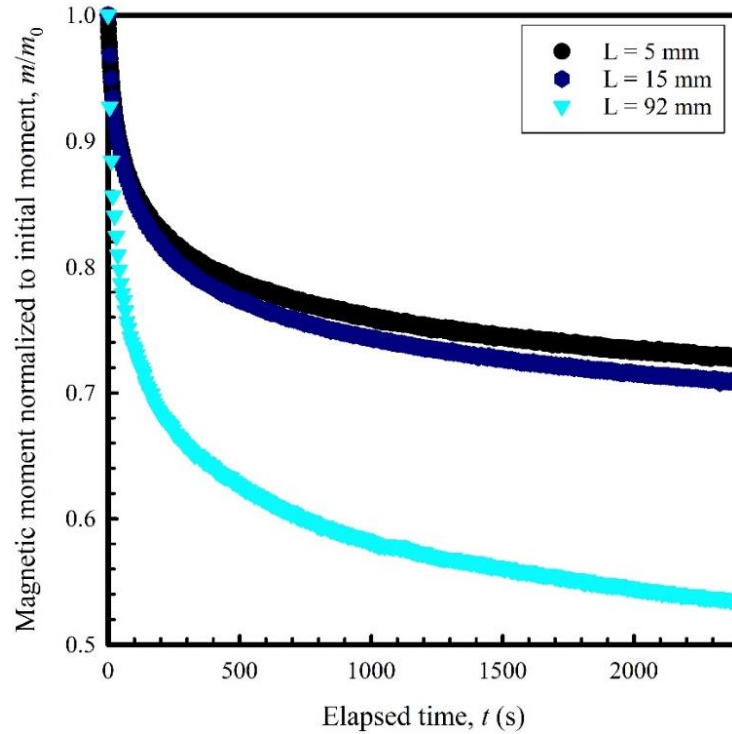


Figure 27. The magnetic relaxation of the non-twisted Bi:2212 strand samples of different lengths.

A possible explanation for the dramatic increase in magnetic relaxation rate with sample length is that the magnetic flux in the Bi:2212 material in the interfilamentary bridges creeps at a higher rate than that in the filaments. It is possible that the bridge material has a different (and lower) pinning strength compared to the filamentary material. As the sample length increases the contributions to the magnetic properties resulting from the bridges becomes a larger fraction of the overall contribution to the magnetic properties. Shorter samples would, presumably, have fewer bridges than longer samples and therefore the magnetic properties would be primarily due to that of the filamentary material. As the

sample length increases, more bridges are present in the round wire composite and the bridge material contributes more to the overall magnetic properties.

It has been seen that the magnetic creep rate is slower in samples that have lower magnetizations. It was expected that twisting the filaments would reduce the creep rate. To investigate this hypothesis the magnetic relaxations of coil samples with different twist pitches were measured over 2400 s, at 5 K, 1 T. The results are shown in **Figure 28 28**. Samples 92, 91, and 76 mm long were cut from wires with twist pitches of 25.4, 12.7, and 6.35 mm, representing L/L_p ratios of 3.6, 12, and 12, respectively. After 1200 s the reduction in moment is smallest in the sample with a L_p of 12.7 mm. It is about 5.5% smaller than the moment reduction in the sample with a L_p of 25.4 mm and about 9% smaller than the moment reduction in the sample with a L_p of 6.35 mm.

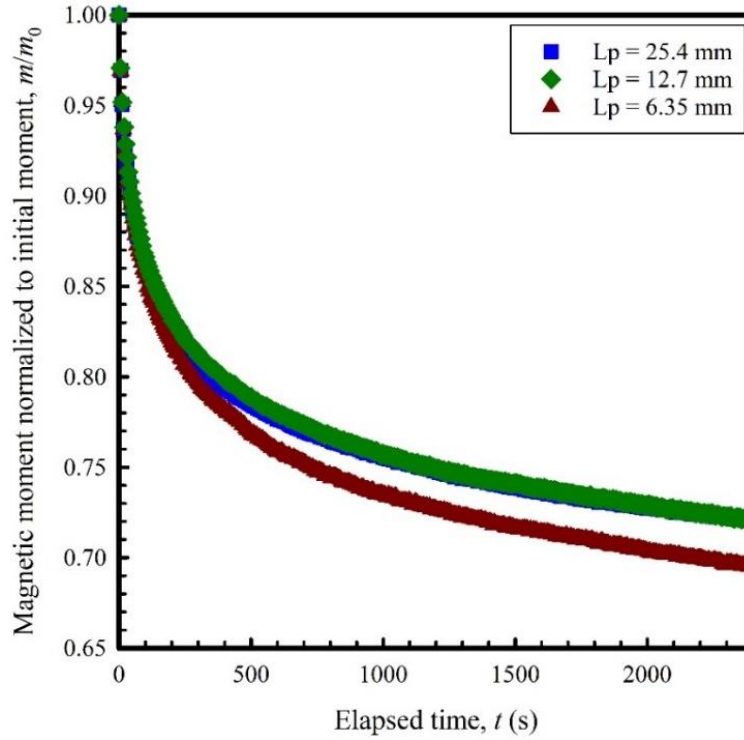


Figure 28. The magnetic relaxation of Bi:2212 strand samples with different twist pitches.

The magnetic relaxation of the non-twisted and twisted samples are plotted together, for comparison, in **Figure 29**. The reduction in moment is significantly lower in the samples which have twisted filaments when compared to the moment reduction in the longest non-twisted sample ($L = 92$ mm).

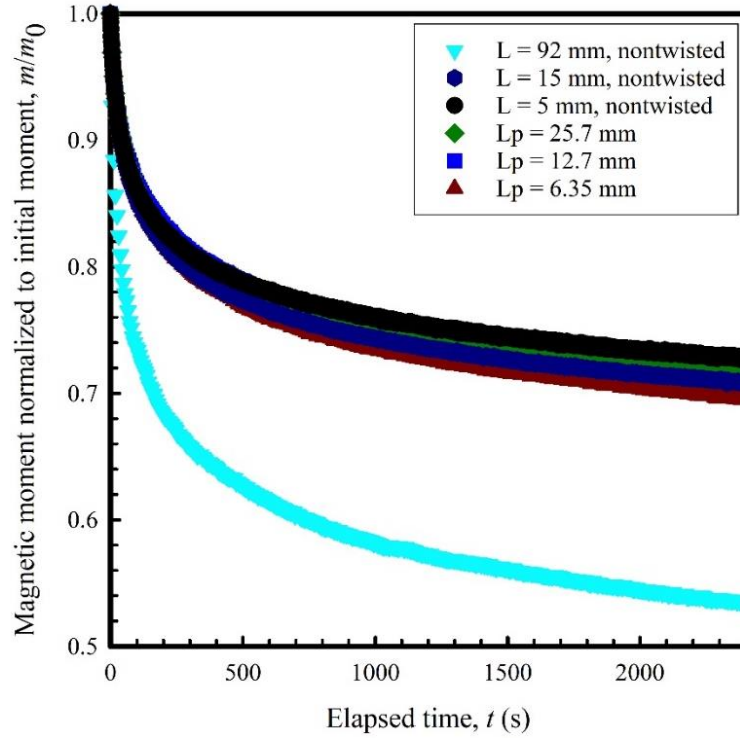


Figure 29. The magnetic relaxation of Bi:2212 strand samples with different lengths and twist pitches.

The linear approximation (equation 1.21) was used to extract an effective pinning potential, U_{eff} , for all samples at 5 K, 1 T. The results are presented in **Figure 30**. The U_{eff} decreases with L , but its dependence with L_p is less clear. The low value of U_{eff} of the sample with a L_p of 6.35 mm is possibly a result of filament damage during twisting. At the time of the sample manufacture, 6.35 mm was an aggressive twist pitch and damage had been seen in samples twisted to similar pitches.

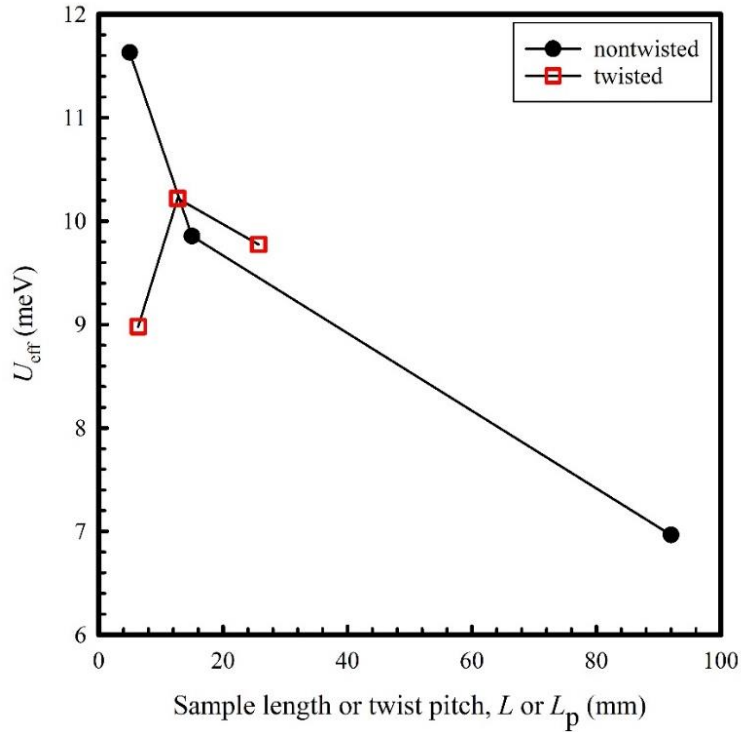


Figure 30. The effective pinning potential, U_{eff} , extracted for the non-twisted samples and twisted samples as a function of L or L_p . The lines are guides to the eye.

3.7. Two-Dimensional Random Oriented Single-Stack (2D-ROSS) Round Wire Design

Standard methods for fabricating Bi:2212 multifilament wire use the powder-in-tube double restack approach. However, these designs have suffered from a low superconducting fill factor (reducing the engineering critical current density, J_e) and significant, irregular, filament-to-filament bridging after partial melt-processing (which leads to large, unwanted parasitic magnetizations). Strands which have higher fill factors will have higher J_{eS} , and if J_c and J_e could be retained without substantial interfilament

bridging the strand would be much more useful. Several approaches to increase the fill factor have been tried. This section of chapter 3 investigates the properties of one such alternative process, denoted the 2D-ROSS approach, the origins of which are described below.

An interesting double stack approach, the ROSAT design by Okada [72], used tape-shaped multifilaments to increase the flat silver-to-ceramic interface area, thus improving the alignment of the Bi:2212 crystal structure. Transport J_c values of over 1000 A/mm² at 28 T and 4 K were obtained. However, like more conventional designs, this design is inhibited by low superconducting fraction and thus a lower J_c . It has been shown by Kumakura *et al.* [73] that grain alignment at the silver-to-ceramic interface is better than at the free surface, and that J_c increases with increasing interface area in Bi:2212/Ag tapes. References [74-77] have shown that, because of the c-axis texture, generally, J_c increases with decreasing filament diameter, up to a point, suggesting that there is an optimum filament size based on geometry. Motowidlo *et al.* [74] also suggests that the peak melt processing temperature must be adjusted for wire diameter and filament size to maximize J_c . A single stack design tends to have a higher fill factor, use less silver, and reduce processing costs, but the necessarily larger filaments lead to lower Ag-surface area contacting the filaments, leading to a lower intrinsic J_c . Even so, using a single restack design, Nachtraub *et al.* [77] achieved J_c values of 1734 A/mm² and 1570 A/mm² for filament diameters of 18 μ m and 22 μ m, respectively.

3.7.1. 2D-ROSS Samples

A novel 2D-ROSS design (ROSS standing for Randomly Oriented Single-Stack), made by SupraMagnetics, used randomly oriented Bi:2212 two-dimensional filaments to maximize surface area and fill factor while minimizing interfilament bridging. The resulting wire cross-section is shown in **Figure 31**. The filaments were rectangular in order to maximize the flat interface area between the Bi:2212 and the silver. The silver sheath improves the *c*-axis texture [78] which improves the J_c . A conventional double stack design was also fabricated for comparison. As a single-stack design, the 2D-ROSS was able to achieve a higher fill factor than the conventional double stack design. The starting silver tube for each case was 12.7 mm OD, and Nexans powder with composition $\text{Bi}_{2.17}\text{Sr}_{1.95}\text{Ca}_{0.89}\text{Cu}_{2.00}$ was used for both designs. This Sr/Ca ratio was very close to that found by Miao *et al.* [79] to give optimal J_c performance. The carbon content in the powder was approximately 1000 ppm. This concentration was high but was considered acceptable for the study of a new strand design. Both billets were reduced to a final wire diameter of 1.0 mm. Short samples were cut to 25 cm for heat treatment. The samples were sealed in small diameter quartz tubing, placed in a programmable tube oven, and heated under 100% flowing oxygen. Four sets of heat treatments, with different peak melt temperatures (T_m), were performed to determine the best melt temperature. The conductor specifications for each design are shown in **Table 2**. All strands had a 1 mm OD.

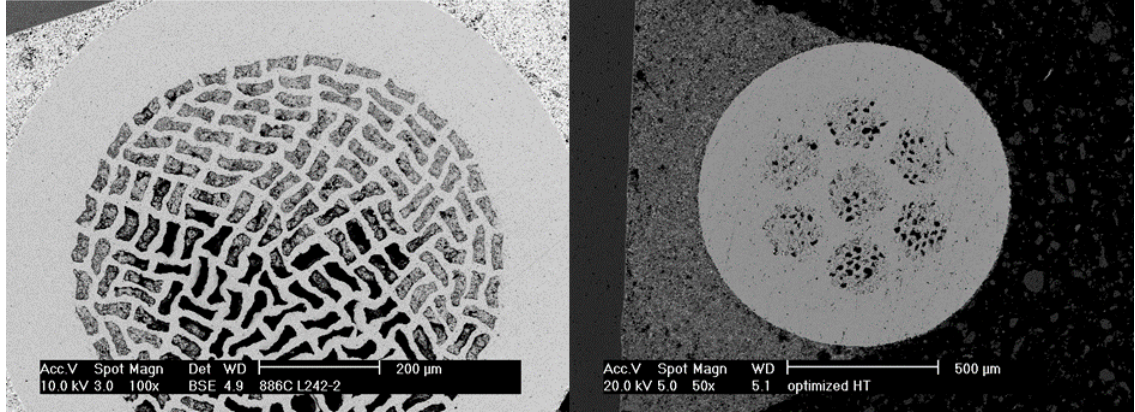


Figure 31. (Left) Cross-sections of the 2D-ROSS-186 aspected filament (filament size $\sim 20 \times 50 \mu\text{m}$) design after heat treating with a melt temp. of 886°C , and (Right) the CONV-7-37 design (fil. size $\sim 20 \mu\text{m}$) with an optimization temp. of 890°C . Published in [80].

Table 2. Bi:2212 2D-ROSS strand specifications. Published in [80].

Sample Name	Stack Type	No. of fil.	%SC*
2D-ROSS-186	Single (L242)	186	22
2D-ROSS-213	Single (L244)	213	23
CONV-7-37	Double (L240)	(7 x 37) 257	10

*The percentage of the cross-section containing superconductor (denoted %SC) was found by measuring the area of the filamentary (not subelementary) region prior to reaction.

3.7.2. Measurement

Critical current measurements were made at 4.2 K in pool boiling liquid helium using a standard four-point technique. The samples were 3 cm long, with a voltage tap spacing of 5-7 mm and an electric field criterion of $1 \mu\text{V}/\text{cm}$. One set of measurements was performed in self-field. A magnetic field was applied perpendicular to the strand for a

second set of measurements. Magnetic measurements were performed using a 14 T PPMS on samples which were approximately 3.2 and 4.4 mm long; the physical parameters of the samples are presented in **Table 3**. $M-\mu_0H$ was measured at 4.2 K with a perpendicular applied magnetic field using a ramp rate of 13 mT/s. DC susceptibility was measured with a 5 mT applied field which was also perpendicular to the strand. Scanning electron microscopy (SEM) was performed on select samples using a Philips XL-30F SEM.

Table 3. Physical parameters of the strands. Published in [80].

Sample Name	length (mm)	A_{total} (10^{-3}cm^2)	A_{sc} (10^{-3}cm^2)	V_{sc} (10^{-3}cm^3)
2D-ROSS-186	3.2	7.9	1.74	0.77
CONV-7-37	4.4	7.9	0.79	0.25

3.7.3. Magnetic Results

The zero-field critical current as a function of peak melt temperature for each design was measured and is presented in **Table 4**. J_e was calculated by dividing I_c by the total cross-sectional area of the wire. The n -values ranged from approximately 8-10.

Table 4. Critical current vs peak melt temperature of strands measured at 4.2 K and self-field. Published in [80].

Sample Name	I_c (A) (884°C)	I_c (A) (886°C)	I_c (A) (888°C)	I_c (A) (891°C)
2D-ROSS-186	0	110	120 ± 10	120 ± 10
CONV-7-37	0	45	85 ± 5	70 ± 5

The melt reaction appears to be absent at temperatures of 884°C and below (i.e., $I_c = 0$) for the 2D-ROSS-186 strand (L242). On the other hand, I_c jumps to 110 A for a melt temperature of 886°C, and it grows to 120 A at 888°C. The I_c for the conventional strand design, CONV-7-37 (L240), was lower for all T_m , and this strand also exhibited less tolerance to small changes in the peak T_m . The higher I_c s in the 2D-ROSS design can be attributed to the better final Bi:2212 alignment along the silver interface. Irregular filament-to-filament bridging is typically present after melt processing in conventional double stack designs. Because each filament in the 2D-ROSS design is highly aspected, the bridging was not as prevalent, as shown in **Figure 32**. Although the 2D-ROSS design does not show extensive bridging, secondary phases such as Bi:2201 and some 14:24 phases were observed within each filament.

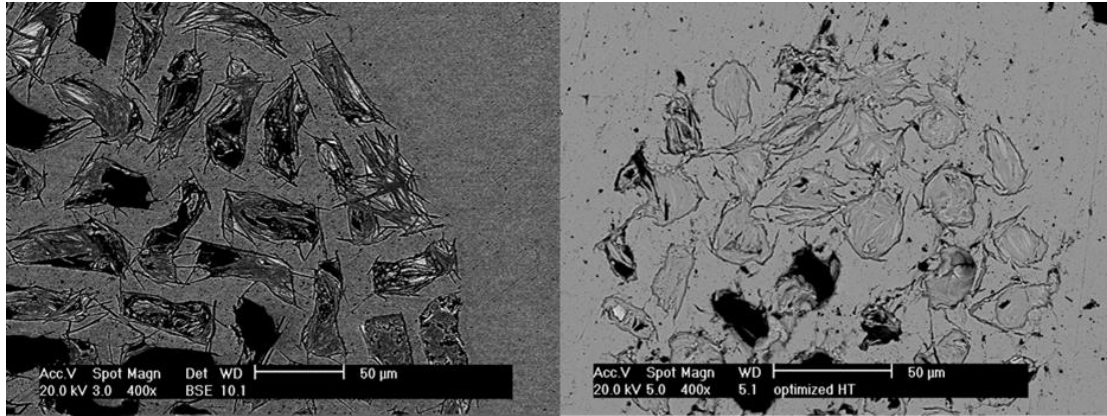


Figure 32. (Left) SEM micrograph of the transverse section of the 2D-ROSS-186 strand with HT at 886°C. (Right) The CONV-7-37 design with HT at 890°C. Fewer bridges are in the 2D-ROSS-186 strand compared to the conventional design. Published in [80].

The dependency of I_c on applied magnetic field, for both 2D-ROSS and conventional designs, was measured for samples melt processed at 888°C, and the results are shown in **Figure 33**. The 2D-ROSS design shows improvement in I_c over the conventional design. The discrepancy in I_c between **Table 4** and **Figure 33**. Is possibly due to sample-to-sample variation within the conventional double stack wire.

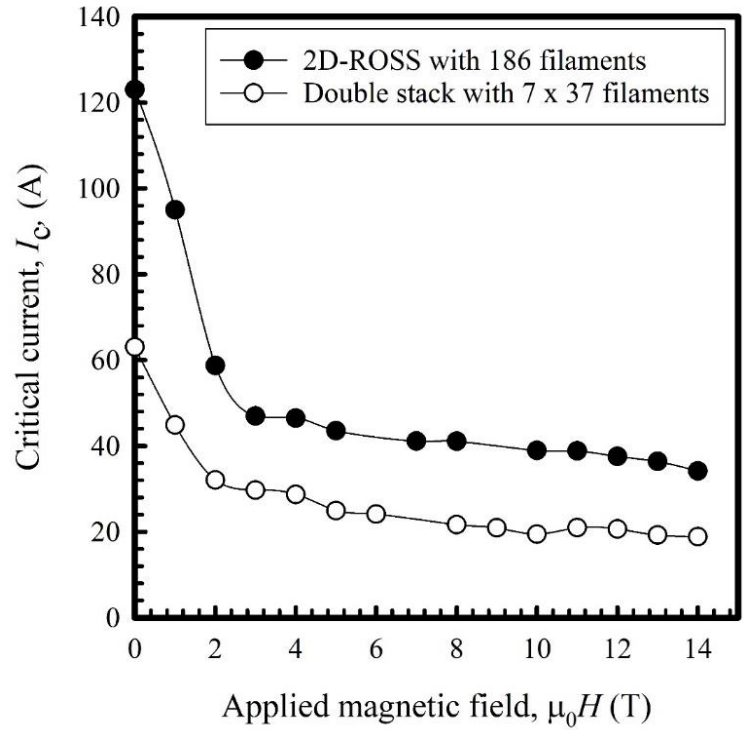


Figure 33. The critical current dependence on applied magnetic field at 4.2 K for the 2D-ROSS-186 and CONV-7-37 strands. Published in [80].

At 12 T, the J_c of 2D-ROSS-186 was approximately 48 A/mm² whereas that of CONV-7-37 was approximately 26 A/mm². At the same field, the J_c of the 2D-ROSS-186 was approximately 220 A/mm² whereas that of CONV-7-37 was approximately 260 A/mm²; these results are shown in **Table 5**.

Table 5. Critical current density, d_{eff} , filament and subelement sizes of strands measured at 12 T. Published in [80]

Sample Name	J_c (10^2 A/mm 2)	d_{eff} (μm)	fil. Size (μm)	Subelement size (μm)
2D-ROSS-186	2.2	300	~20 x 50	~741
CONV-7-37	2.6	100	~20	~183

DC susceptibility of both 2D-ROSS-186 and CONV-7-37 was measured for samples which had been given a melt temperature of 888°C. The results were normalized to the total superconducting filamentary volume (estimated prior to the reaction). This volume was defined as the sample length multiplied by a cross-sectional area which included the filaments (not the subelements) and specifically excluded both the Ag and the bridges between the filaments. This measurement and normalization allowed us to assess both the level of exclusion from the filaments as well as the level of coupling between them. The susceptibility should saturate to two when there is full flux exclusion from the filaments. When it exceeds two, then coupling between the filaments is occurring. The susceptibility results indicate that coupling between the filaments is more significant in CONV-7-37, as shown in **Figure 34**.

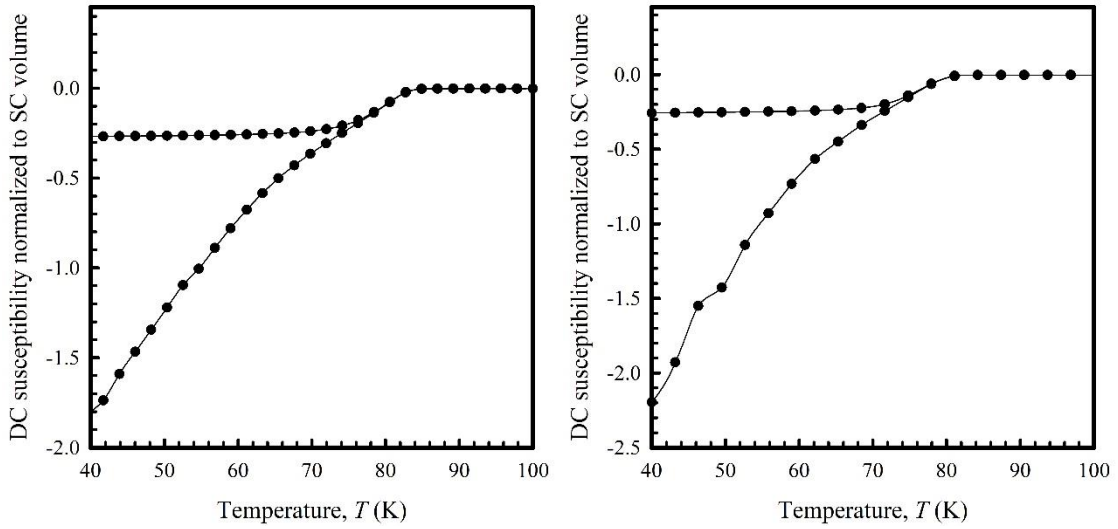


Figure 34. (Left) DC susceptibility for the 2D-ROSS-186 design and (Right) DC susceptibility for the CONV-7-37 design. Published in [80].

The 4.2 K $M-\mu_0H$ loops for 2D-ROSS-186 and CONV-7-37 are shown in **Figure 35**. The $M-\mu_0H$ has been normalized to the volume of the filamentary (not subelementary) region, excluding bridging. Using the expression for d_{eff} given in equation 3.2, a d_{eff} of 300 μm (with a strand diameter of approximately 740 μm) at 12 T was extracted for 2D-ROSS-186 and a d_{eff} of 99 μm (with a subelement size of approximately 180 μm) was found for CONV-7-37. For a fully bridged sample, the d_{eff} should be on the order of the subelement size for CONV-7-37 and on the order of the strand diameter for 2D-ROSS-186. Since the ratio of the subelement size to d_{eff} for CONV-7-37 is less than the ratio of the strand diameter to d_{eff} for the 2D-ROSS-186 design (The ratios were about 1.8 for CONV-7-37 and 2.5 for 2D-ROSS-186.), the

coupling level is lower in the 2D-ROSS design, with no penalty in terms of a decrease in transport J_c . This result is consistent with the fact that the alignment of the single stack design does not rely on the interconnect morphology present in double stack designs. This result demonstrates that there may be a potential route to gain high J_c s in Bi:2212 superconductor composites while keeping d_{eff} s lower than the presently seen values.

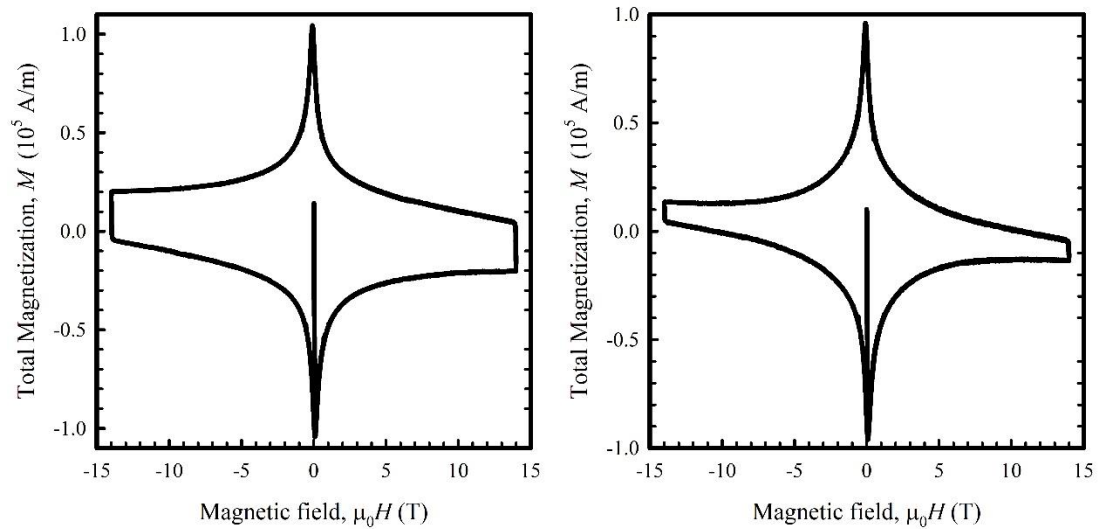


Figure 35. 4.2 K M - $\mu_0 H$ of 2D-ROSS-186 and (Right) 4.2 K M - $\mu_0 H$ of CONV-7-37. Published in [80].

3.8. Summary of the Influence of Bi:2212 Composite Sample Length and Twist Pitch on the Composite Magnetic Properties

The magnetization and its temporal change were studied for Bi:2212 round wire composites of different lengths and twist pitches. Both the magnetization and decay were found to depend upon sample length. Quantifying the magnetization in terms of an effective filament diameter, d_{eff} , will therefore not likely give an accurate measure of the magnetization of larger composites used to make the windings of accelerator magnets. The magnetization was found to depend linearly on sample length for the non-twisted samples, which allowed for the extraction of a parameter, γ_2 , which quantifies the amount of electrical connectivity across the Bi:2212 round wire composite. The results suggest that each bundle acts as a filament with the diameter of the bundle. This level of bridging is significant and undesirable, but higher levels of bridging have been observed, in which the subelements were bridged and d_{eff} was equivalent to the entire filamentary array diameter. The results of magnetic relaxation measurements also indicate that the creep rate increases with sample length for the non-twisted samples. This result may be due to the increased influence of the bridged material at longer lengths. As the sample length increases, the amount of bridging between filaments increases, and their influence on the overall magnetic properties of the strand become more pronounced. If the bridged material possesses a lower pinning strength than the filamentary material, a higher creep rate is expected.

The magnetization of the twisted samples was smaller than that of the non-twisted samples of comparable length, and the magnetization generally increased with increasing twist pitch, but the functional form of the dependence was not clear. Similar results were seen for the magnetic relaxation measurements. Again, the creep rate was slower for twisted samples when compared with non-twisted samples of comparable length, but the creep rate of the sample which had a twist pitch of 6.35 mm was slightly faster than that of the other twist pitched samples. Furthermore, the creep rate of the 15 mm long non-twisted sample was slower than this sample. It is possible that 6.35 mm was too aggressive a twist for the strands at the time of manufacture, and these samples may have been slightly damaged. In general, twisting the filaments in the Bi:2212 strands is seen as an effective method to reduce the magnetization and creep rate over non-twisted samples of similar lengths.

Chapter 4: YBCO Nanostructure, Additions, and Magnetic Property Correlation

4.1. Static Properties and their Response to Flux Pinning Additions

Secondary phases, usually in the form of precipitates such as BaZrO_3 (BZO) or Y_2BaCuO_5 (Y211), can be used to increased flux pinning in $\text{YBa}_2\text{Cu}_3\text{O}_{7-x}$ (YBCO). Increased pinning causes a larger flux density gradient in the material which subsequently increases J_c . The constituents of the secondary phases are typically introduced during thin film deposition (e.g., via PLD or MOCVD). During the subsequent heat treatment and cool down, precipitates of the secondary phase nucleate and grow. These precipitates pin flux, and act in addition to the intrinsic pinning which is already present in YBCO in the form of a high number of weak pins (due, e.g., to oxygen vacancies). Thus, by influencing the nanostructure of YBCO, we strongly affect the transport and magnetic properties of the material. In this chapter we will explore the correlation between the nanostructure of the YBCO film and its transport and magnetic properties. For the magnetic properties, both the static and time dependent properties are of interest.

As described in chapter 1, a type-II superconductor in the mixed state will contain an array of fluxons (also called vortices). If there is no pinning the fluxons will be equally spaced throughout the material, that is, no gradient in the flux density (vortex density) will be present on length scales significantly larger than the fluxon spacing, a . If a current is

applied, a Lorentz force, $F_L = J_c B$ will act on the fluxons. If there are no pins the flux lattice will flow, leading to energy dissipation and a flux flow resistivity. If a material defect is present, it can “pin” the flux. As mentioned in the introduction, such a pinning center, or pin, is a region where the condensation energy of the superconducting phase is reduced or not present, such that it is energetically favorable for the fluxons to sit inside the potential well of the pin. These pins can be, e.g., voids, or non-superconducting materials, or materials with reduced superconductivity (reduced T_c or critical field). If we assume a direct summation model is valid to describe the pinning, the total pinning force in the material can be represented as the sum of the individual pinning forces, $F_p = \sum f_p$. This total pin force matches the Lorentz force at the critical current density ($F_p = F_L$) such that at currents below some critical value, the flux remains pinned, and above that value the critical state is exceeded.

In the absence of an applied transport current, the bulk shielding currents (Bean currents) play a similar role as the transport current, generating a Lorentz force which must be matched by the force due to the pins on the fluxons. Since $dB/dx \propto J_c$, and the Bean model requires that J flow at $\pm J_c$ or 0, a superconductor in an applied field shields (or traps) magnetic flux with a macroscopic current density which causes a flux density gradient across the sample (i.e., the Bean profile shown in **Figure 9**, Chapter 1). This gradient can be visualized as a “washboard potential” where the potential energy of the fluxon can be viewed as a straight line proportional to the flux density, which is a function of position within the sample (i.e., a Bean critical state profile), with a series of potential wells where

the fluxons are trapped, see **Figure 36** below. The potential wells are associated with the local reduction of the condensation energy (pin energy) of the pin itself. The pinning of the fluxons due to the pins causes the observed transport J_c and magnetic (e.g., $M-H$) properties of superconducting samples in general and of the YBCO materials of interest in this chapter. The addition of pins has been used to increase the J_c performance of these materials, but at the same time it increases the magnetization, since $M \propto J_c d$. In the context of accelerator applications, the increase in J_c performance is desirable, but the concomitant increase in M is undesirable. In this chapter we will characterize the $M-H$ loops of some novel YBCO materials made at two different laboratories. Each laboratory used a different technique (either PLD or MOCVD) to make thin films of the materials. For each technique, a different type of secondary phase (either Y211 or BZO) was the primary addition to the nanostructure of the film to increase its J_c . We will explore the static and dynamic magnetic properties of the films in order to explore the effect different pinning additions have on these properties at low temperatures. A goal of the work is to determine if certain pins can increase J_c and reduce creep and to understand the mechanisms that allow this. This determination has both scientific and technological importance. Scientifically, it is interesting to understand how the phases alter the nanostructure of the film and interact with the fluxons to arrest their motion. Technologically, a reduced creep may lead to reduced temporal field changes in a magnet. Although these samples were fabricated by other labs, and their J_c has been previously reported [55, 81-83], here we will focus on a more detailed investigation of the static and dynamic properties of the film and their correlation with the nanostructure of the film.

4.2. Dynamic Properties and their Elucidation of the Pinning Character

As described above, Type-II superconductors have a fluxon array which can be immobilized in the presence of pins, up to a certain critical flux density gradient. However, while the fluxons are indeed restrained by the pins, they also experience thermal excitation (i.e., $k_B T$ energy). This thermal energy tends to excite them, and they have some probability of hopping out of the well, and to the next well (pin) which is lower down the flux density gradient. This excitation follows an Arrhenius type rule, as shown conceptually in **Figure 36**. Since there is a force on the fluxons due to the flux density gradient, there is a forward bias that causes them to hop down the potential energy gradient (down the flux density gradient). In the figure, P represents the probability of a fluxon to hop down the gradient and to the next well. This hopping leads to a deviation from the critical state, a phenomenon described as thermally activated flux motion. This phenomenon is present to some degree in all superconductors, but it is much stronger in HTS, leading to the famous description of giant flux creep [25, 26]. The effective activation energy, U_{eff} , for this motion is the pinning potential energy barrier U_0 (i.e., the depth of the potential wells) reduced by the flux density gradient, as shown in **Figure 36**.

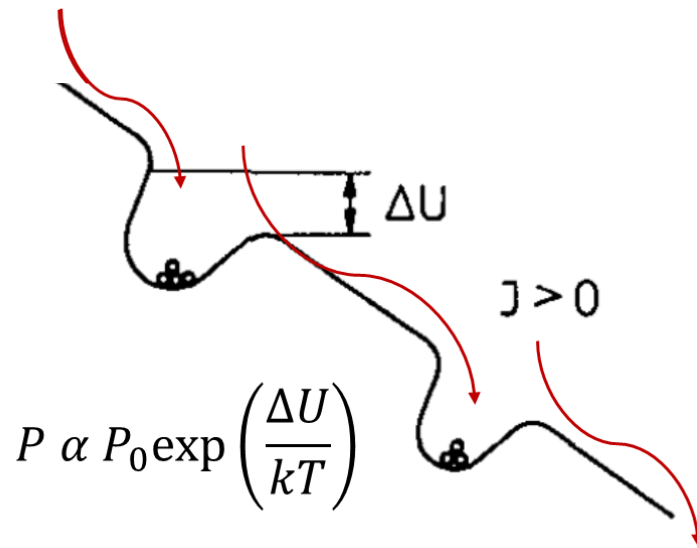


Figure 36. Conceptual “Washboard Potential” local energy for fluxon as a function of distance into the center of a superconductor in the shielding mode (outside of conductor to left, and inside to right), after [6].

In the simplest direct summation model, we can see that similar critical current density increases can be achieved using either a large density of shallow, or weak, pins, or a smaller number of deeper, or stronger, pins. This can be illustrated by considering again that the total pin force in the material can be represented as the sum of the pinning force on all the pins, $F_p = \sum f_p$. Let us first consider a given type of pin of strength f_p . If another type of pin has a different pinning strength, say 10 X stronger, an individual pin of this type has the pin force $f_p' = 10f_p$, and the total number of pins required to give F_p is fewer by a factor of 10. Thus, the same critical current density can be achieved using fewer pins which have a larger potential well depth or more pins which have a smaller potential well depth. However, the larger potential well depth of the deeper pins provides a larger activation

energy barrier to thermally activated flux motion. Thus, whereas similar increases in critical current density can be achieved in the two cases, thermally activated flux motion, or flux creep, is more rapid when there are larger numbers of pins that have a shallow pinning well depth. The more rapid motion of flux down the flux density gradient causes a more rapid decay in the magnetization of the superconductor. A rapid decay in the magnetization of the superconductor can be a problem when using the superconductor in applications that require a stable magnetic field. Precipitates which both increase critical current density and reduce the rate of thermally activated flux motion (through a larger pinning well depth) are desirable for accelerator magnet applications because these applications require a stable magnetic field. A full analysis of both flux pinning and magnetic relaxation reveal many complexities which modify the simple direct summation model picture, but measurements of the relaxation of the superconductor magnetic moment are useful tools to investigate the activation energies of flux motion. The effective activation energy can be examined over a large range of current densities by measuring the relaxation at different temperatures and applied magnetic fields. Collective flux creep [84] or vortex-glass [85] theories have been developed to explain the flux dynamics and have been used to predict U_{eff} as a function of current density. Results of magnetic measurements can be interpreted in terms of these theories in order to understand the flux dynamics.

4.3. The YBCO Samples and the Magnetic Results

In this thesis we explored the magnetization of YBCO samples made using two different thin film processing techniques (PLD and MOCVD). For each technique, there was a different main secondary phase addition (Y211 or BZO). The first set of samples were processed using pulsed laser deposition (PLD) and included a control sample (i.e., no precipitates were added), and samples with 5 vol.% Y211, 10 vol.% Y211, and 2 vol.% BZO additions. The second set of samples were processed using metal-organic chemical vapor deposition (MOCVD) and included a control sample, and samples with 7.5 mol% and 25 mol% Zr additions.

4.3.1 PLD Processed Films

The films were synthesized by the Air Force Research Lab (AFRL) [86]. Thin films were deposited by PLD from $\text{YBCO}_{1-x}\text{Y211}_x$ ($x = 0-10$ vol.%) single targets, at a temperature of 835°C . A Lamda Physik LPX 300 KrF excimer laser with 248 nm wavelength and a fluence of 3 J/cm^2 was used to deposit films on SrTiO_3 (STO) single crystal substrates in 300 mTorr oxygen. The films were annealed at 500°C for 30 minutes in an oxygen atmosphere. The deposited films were 300 nm thick and both 3.2 mm wide and 3.2 mm long. Three different concentrations of Y211 were incorporated into the films: 0, 5, and 10 vol. %. One film sample had 2 vol.% BZO incorporated into it. Sample details are given in **Table 6**.

4.3.2. MOCVD Processed Tapes

Tapes were processed at the University of Houston [82] using a reel-to-reel MOCVD system. The system was used to deposit 0, 7.5, and 25 mol.% Zr-added (Gd, Y)Ba₂Cu₃O_{7- δ} on Hastalloy C-276 substrates with a multilayer oxide buffer configuration of Al₂O₃/Y₂O₃/IBAD-MgO/MgO/LaMnO₃ as a template for REBCO growth. The films were grown at a deposition rate of 80 nm/min which resulted in film thickness of about 0.9 μ m, controlled by the tape speed. The composite width was 12 mm and the final composite thickness was about 50 μ m. Inductive coupled plasma-mass spectrometry (ICP-MS) was used to determine the final chemical composition of the films. The Zr additions resulted in the growth of BaZrO₃ (BZO) nanorods throughout the superconductor microstructure [87-89]. The sample specifications are given in **Table 6**.

Table 6. YBCO thin film specifications

Sample	Length (mm)	Width (mm)	Super-conductor thickness (μm)
PLD			
Control	3.22	3.22	0.22
5 vol.% (Y211)	3.185	3.165	0.281
10 vol.% (Y211)	3.175	3.165	0.3
2 vol.% (BZO)	3.165	3.165	0.135
MOCVD			
Control	2.3	2.1	0.9
7.5 mol.% (Zr)	4.1	2.6	0.9
25 mol.% (Zr)	2.9	1.9	0.9

4.3.3 Experimental Approach

Magnetic hysteresis and dynamic magnetic relaxation measurements were performed on both sets of samples. For the PLD processed sample, the substrates were approximately 3 mm x 3 mm. For the MOCVD processed samples, pieces approximately 2-4 mm square (see **Table 4.1**) were cut from provided lengths of tape. The magnetic measurements were performed using the Vibrating Sample Magnetometer (VSM) of a Quantum Design Physical Property Measurement System (PPMS). The system can obtain a sensitivity of $\sim 1 \times 10^{-6}$ emu. The hysteresis measurements were taken in applied magnetic

fields up to 9 T and at a variety of temperatures for the PLD processed samples. The hysteresis measurements were taken at applied magnetic fields up to 14 T at 4.2 K for the MOCVD processed samples. The magnetic field was applied parallel to the c -axis of the samples. The samples were zero-field cooled to the measurement temperature and a dwell time was incorporated to allow the samples to reach thermal equilibrium. The total magnetic moment measured by the VSM is the sum over all the microscopic circulating current paths within the superconductor, and the subsequently calculated current density is therefore a volume average. Magnetic relaxation measurements were performed in applied magnetic fields of 1-8 T, applied parallel to the c -axis of the samples, at temperatures from 4-65 K. The procedure was as follows. First, the temperature was ramped to the measurement temperature and then the magnetic field was ramped to the target field. Upon reaching the measurement field, the magnetic moment was measured continuously for 30 minutes to 3 hours. Before measurement at each field and temperature, a magnetic field ramp was applied to ensure full flux penetration in the sample at the start of the magnetic relaxation measurement.

The rate equation of flux motion is derived assuming complete flux penetration and therefore the analysis of the relaxation data is limited to fields well above the field of full penetration, H_p [46]. The field of minimum magnetization, H_m , on the virgin hysteresis curve can be used to estimate the penetration field. It is approximately given by $1.5H_m$ [10]. The minimum applied magnetic field from which magnetic relaxation measurements were

performed was 1 T, which is much larger than the penetration field of any of the samples measured here.

4.4 Results of M - μ_0H Measurements

The 5 K M - μ_0H of the PLD processed samples is presented in **Figure 37**. The magnetic moment has been normalized to the superconductor volume. From the figure we can see that the sample with a 5 vol.% Y211 addition has a reduced magnetic hysteresis loop width (ΔM) compared to that of the control sample over the entire magnetic field sweep range. On the other hand, the addition of 10 vol.% Y211 increases ΔM at low field, but at higher fields there is not a significant difference between the two. With the addition of 2 vol.% BZO, the low field width is increased significantly over that of the control sample and marginally increased over the width of the 10 vol.% Y211 addition sample. Because ΔM is proportional to J_c (and there is no significant difference in film length or width for the samples), it is evident that the additions of Zr increased the low field J_c over that of the control sample, and that the additions of Y211 marginally increased J_c for the highest concentration studied here.

The 4.2 K M - μ_0H of the MOCVD processed samples is presented in **Figure 38**. Again, the magnetic moment has been normalized to the superconductor volume. At all measured magnetic fields, the additions of Zr to the MOCVD processed samples increased ΔM (and thus J_c) over that of the control sample, with larger increases for the larger

addition amounts. We note that the overall J_c of the set was lower for the MOCVD than the PLD in this set of samples.

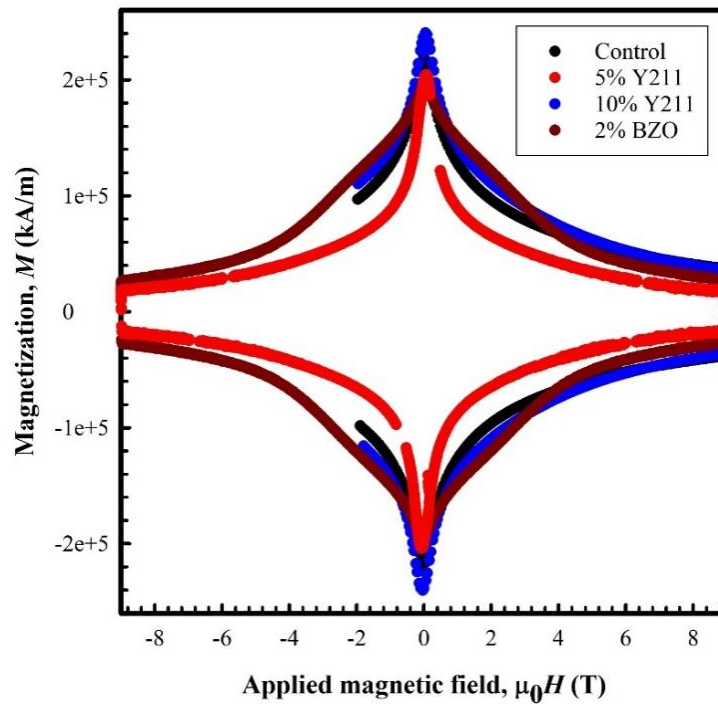


Figure 37. The 5 K M - $\mu_0 H$ of the PLD processed samples with Y211 and BZO additions. The moment is normalized to the superconductor volume.

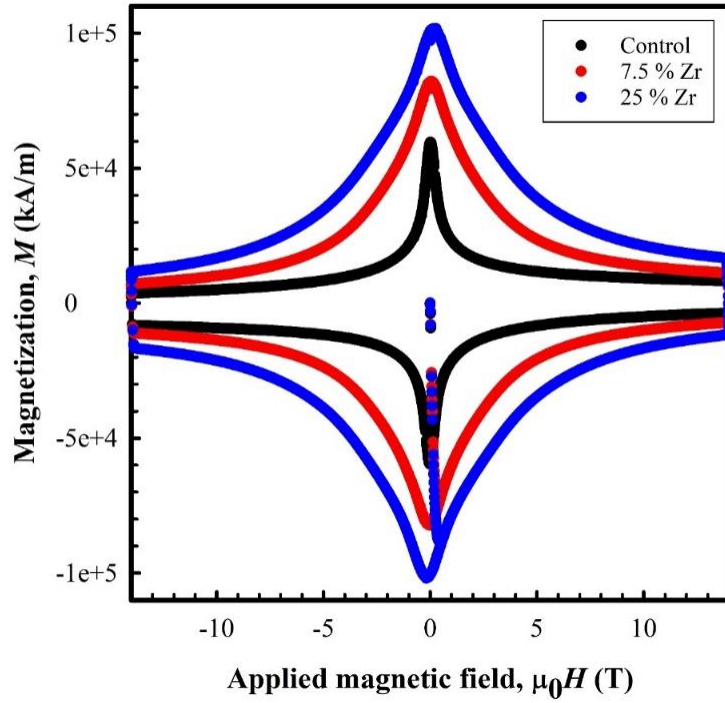


Figure 38. The 4.2 K $M-\mu_0H$ of the MOCVD processed samples with BZO additions. The moment is normalized to the superconductor volume.

4.4.1. Current Density Calculation

The current density can be derived from the measured magnetic hysteresis loops of the superconductor composites using the Bean critical state model [13, 14]. The irreversible component of the moment of the superconductor m_{irr} , is given as

$$m_{\text{irr}} = \frac{m^+ - m^-}{2}, \quad (4.1)$$

where $m^{+(-)}$ is the magnetic moment of the field increasing (decreasing) branch of the hysteresis loop. The magnetization of the superconductor is the magnetic moment normalized by its volume. The Bean critical state model can be used to directly relate the magnetization to the average circulating current density in the superconductor. The J_c s at 4-5 K and 0.1 T, calculated using the Bean critical state model, for both sets of samples is presented in **Table 7**.

Table 7. Comparison of J_c s of the PLD and MOCVD processed samples.

Addition	J_c (A/cm ²), 0.1 T
PLD processed sample	
control	3.53×10^7 (at 5 K)
5 vol.% Y211	3.48×10^7 (at 5 K)
10 vol.% Y211	3.99×10^7 (at 5 K)
2 vol.% BZO	3.67×10^7 (at 5 K)
MOCVD processed samples	
control	1.8×10^7 (at 4 K)
7.5 mol.% Zr	2.6×10^7 (at 4 K)
25 mol.% Zr	3.0×10^7 (at 4 K)

4.4.2. Connection to Nanostructure

4.4.2.1. PLD Processed YBCO Films with Y211 Additions

The Y211 precipitates in the YBCO films processed using PLD took the form of nanoparticles which were approximately 100 nm x 30 nm, with an aspect ratio of approximately 3, as shown in **Figure 39**. The typical spacing between precipitates was approximately 200 nm.

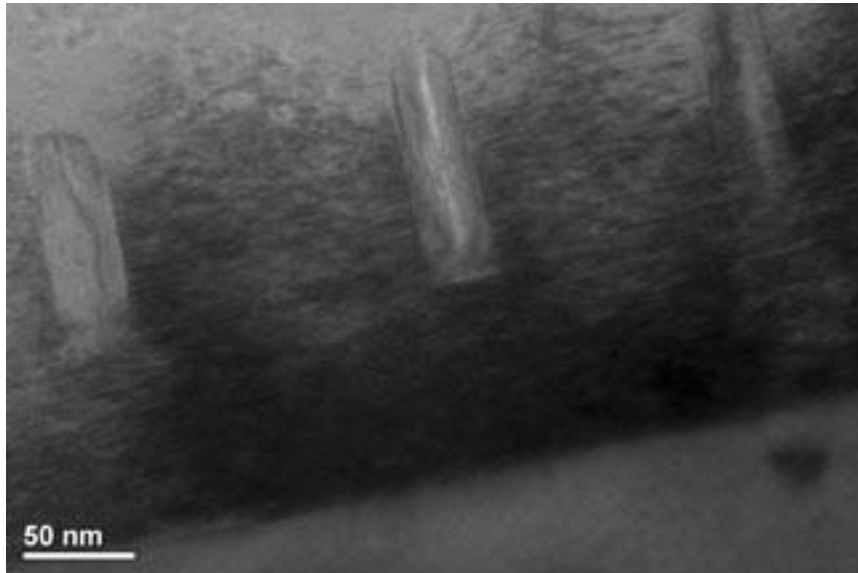


Figure 39. TEM image of Y211 precipitates in the YBCO matrix. The precipitates were approximately 100 nm by 30 nm. From [83].

The BZO in the YBCO films processed using PLD took the form of nanocolumns, that threaded the entire film thickness (about 300 nm), with an average spacing of

approximately 20-30 nm and an average width of 10 nm, as shown in **Figure 40**. The aspect ratio of the precipitates was about 30.

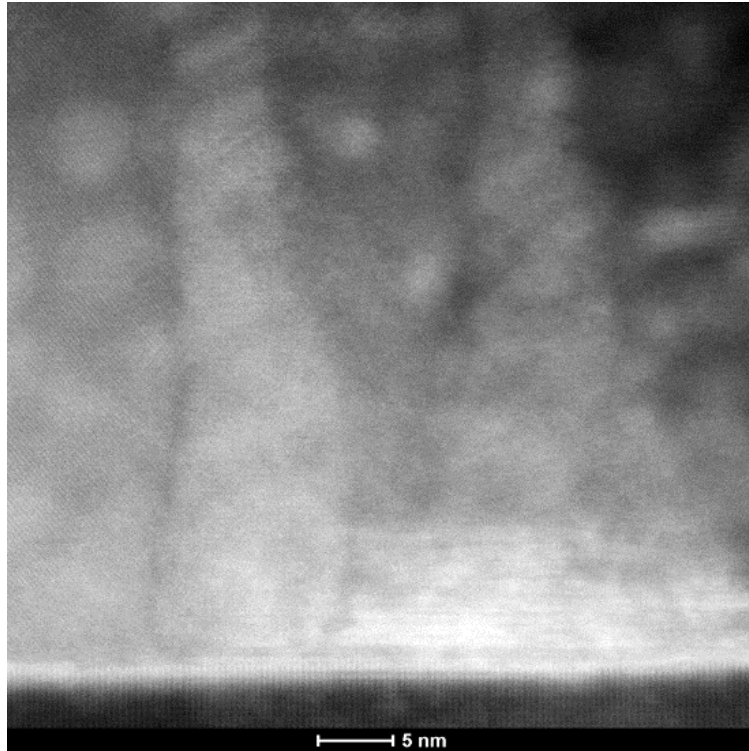


Figure 40. TEM image of BZO nanocolumns in the PLD processed YBCO thin film matrix. From [83].

4.4.2.2. MOCVD Processed Samples

The BZO precipitates in the YBCO films processed using MOCVD took the form of nanocolumns approximately 5 nm wide that threaded the entire film thickness ($\sim 0.9 \mu\text{m}$), as shown in **Figure 41** and **Figure 42**. As the mole fraction of added Zr was

increased, the spacing between the columns reduced, but their size did not change appreciably. The spacings varied from approximately 35 nm to 12 nm, depending on the amount of Zr added. In comparison to the PLD processed samples, the Y211 precipitates are generally wider and shorter than the BZO precipitates. Also, the BZO threads the entire film thickness.

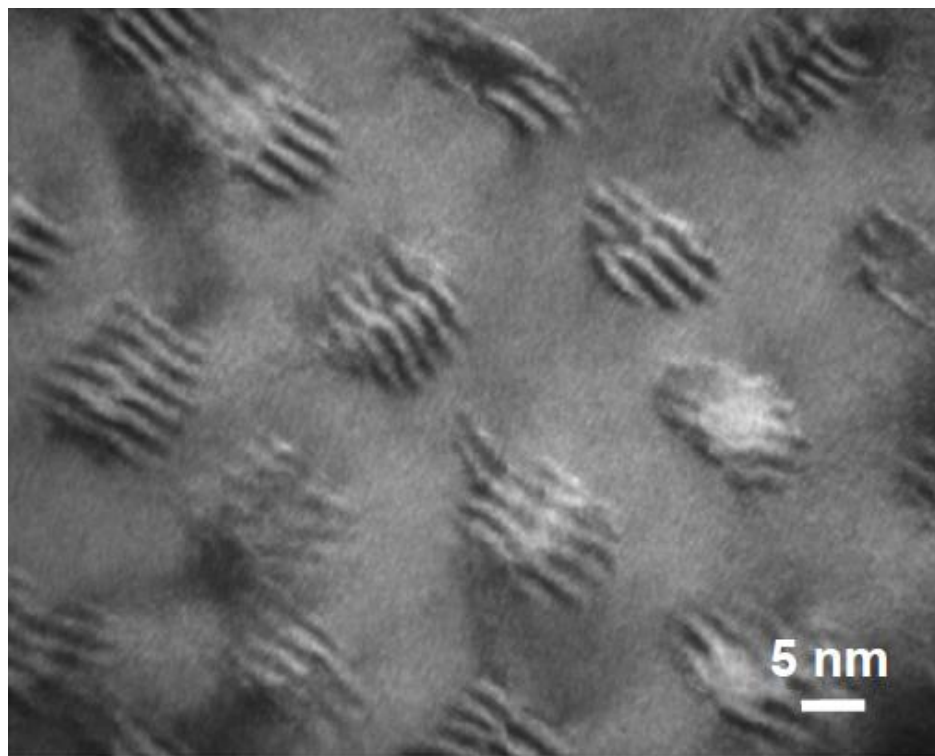


Figure 41. BZO nanocolumns in the YBCO thin film matrix. The width of the columns is 4-6 nm. From [55].

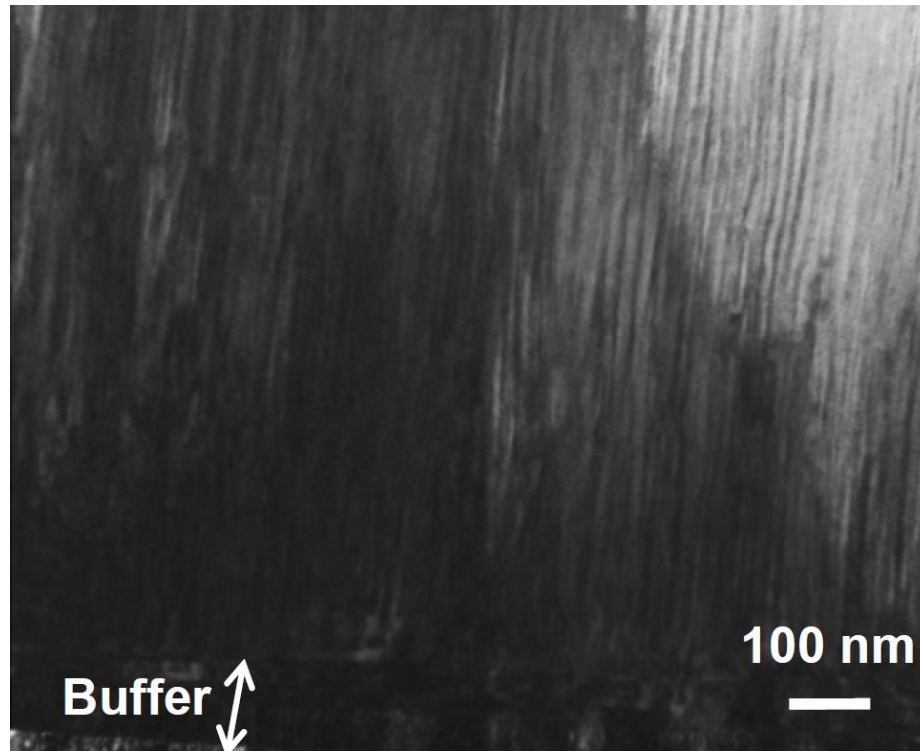


Figure 42. BZO nanocolumns shown threading the entire YBCO thin film thickness. From [55].

The difference in the precipitate morphology is schematically illustrated in **Figure 43** and **Figure 44**.

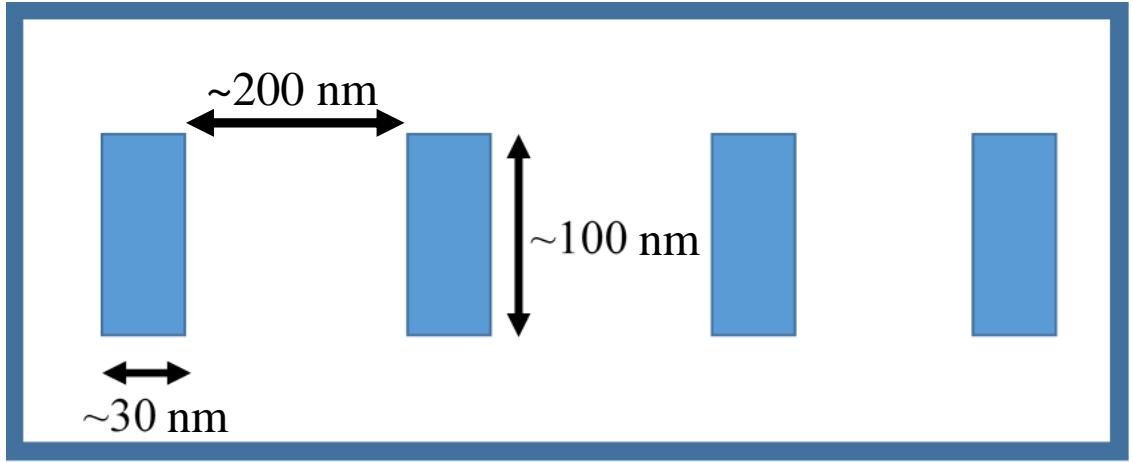


Figure 43. Schematic illustration of the Y211 precipitates in the PLD grown YBCO thin film matrix. The precipitates are sparse and short, with height = 100 nm, width = 30 nm, and spacings of approximately 200 nm.

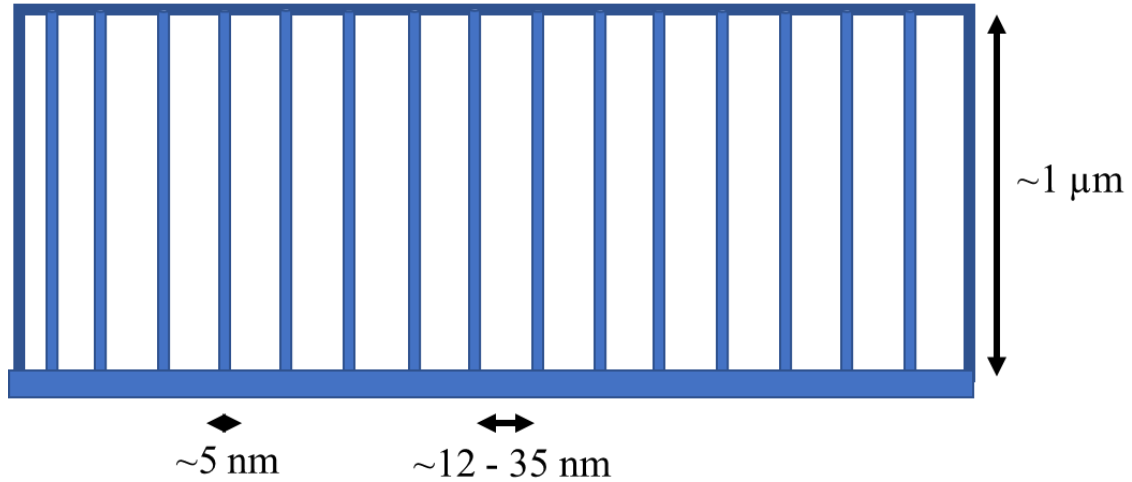


Figure 44. Schematic illustration of the BZO precipitates in the MOCVD grown YBCO thin film matrix. The precipitates are dense, long, and thinner than the Y211 precipitates.

The so-called matching field is the applied magnetic field strength that generates a fluxon density that most nearly matches that of the pin density. The expression for this is $B \propto \Phi / a^2$, where Φ is the magnetic flux quantum and a is the spacing between the pins. At this field, it is expected that the pinning force is maximized. If we substitute the respective values of a for the Y211 and BZO pin spacings (200 nm and 12 nm, respectively) into the expression, matching fields of 0.1 and 10 T are expected, respectively. Because the pinning strength, F_p , is proportional to the product of the area of the fluxon and the length of the fluxon within the pin, we might naively expect the BZO pin to be up to 10 X stronger than the Y211 pin due to its longer length.

4.5. Initial Magnetic Decay Measurements

Thermal activation causes fluxons to diffuse down the flux density gradient in a high-temperature superconductor (HTS) in a phenomenon called giant flux creep [26, 28]. Because the flux density gradient creeps towards zero due to the redistribution of the fluxons, the critical current density, and therefore the magnetization, of the superconductor creeps towards zero. The rate at which the flux redistributes should be a function of the strength, or depth, of the pins that restrict the fluxon motion. The fluxon redistribution should be slower in materials that have stronger, or deeper, pins.

Initial magnetic relaxation measurements were performed on both sets of samples (PLD and MOCVD) in fields of 1 T and 8 T. For each measurement, the applied magnetic field was cycled from 0 T to -3 T and then to the measurement field (1 or 8 T) to ensure full flux penetration of the sample. After the applied magnetic field stabilized at the measurement field, the magnetic moment from the sample was measured continuously for at least 1200 s. 1200 s was chosen because it represents a typical time period during which particles are injected into a particle accelerator. The magnetic field generated by the accelerator should be constant during this injection in order to prevent beam loss. If the moment of the superconducting composites from which the accelerator magnets are comprised changes appreciably during this phase, particle beam loss can occur [6]. Shown in **Figure 45** are the data normalized to the initial moment, measured upon reaching a stable applied magnetic field for the magnetic relaxation of the PLD processed samples at 1 T

and 5 K. Additions of 10 vol.% Y211 appear to reduce the creep rate slightly, however, additions of 2 vol.% BZO appear to reduce the creep rate significantly.

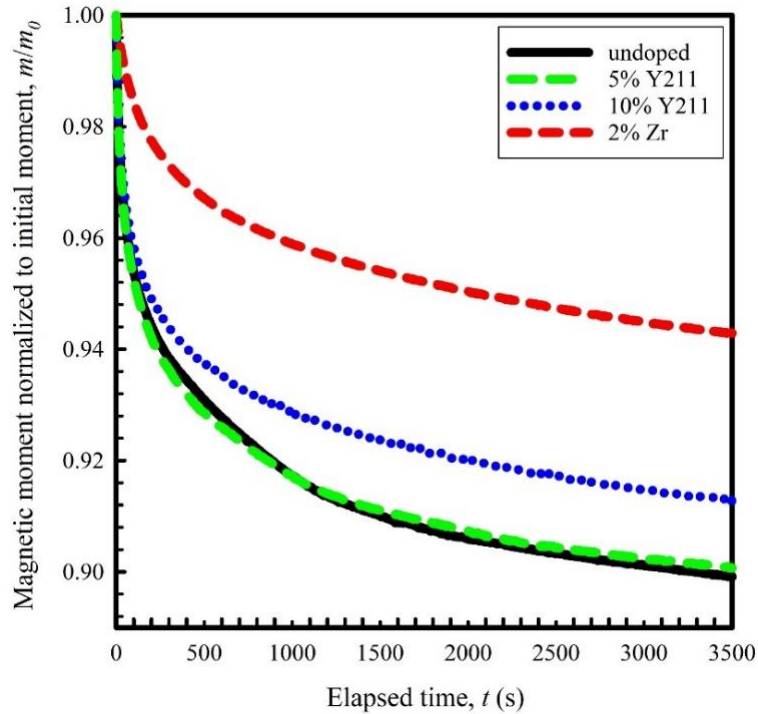


Figure 45. The magnetic relaxation of the PLD processed samples at 1 T, 5 K. Additions of 10 vol. % Y211 reduce the overall relaxation rate slightly whereas the addition of 5 vol.% Y211 increases the relaxation rate.

Shown in **Figure 46** are the data normalized to the initial moment, measured upon reaching a stable applied magnetic field for the magnetic relaxation of the PLD processed samples at 8 T and 5 K. It is apparent that they Y211 additions do not significantly affect the creep

rate at this field and temperature, but the BZO addition appears to increase the creep rate at this field and temperature.

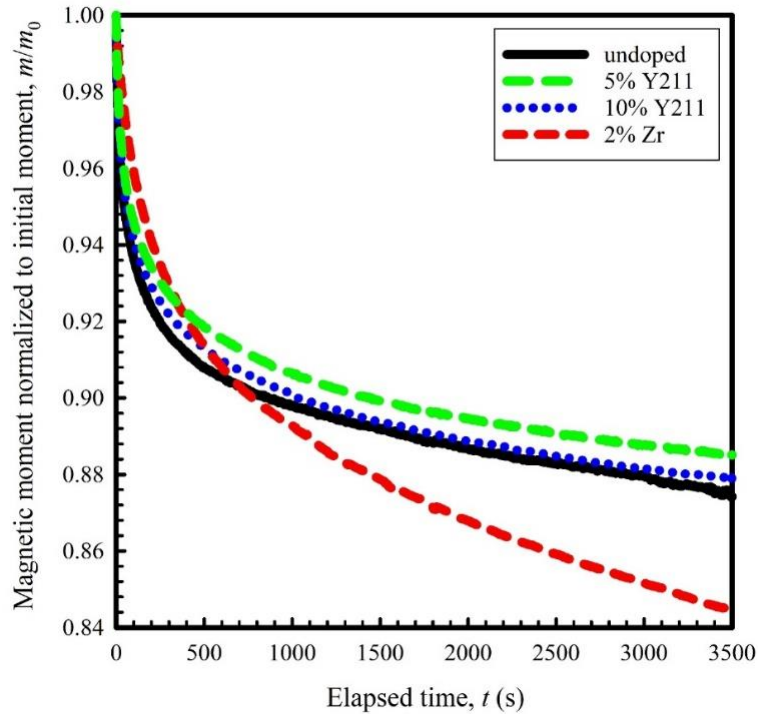


Figure 46. The magnetic relaxation of the PLD processed samples at 8 T, 5 K. Additions of 10 vol. % Y211 reduce the overall relaxation rate slightly (and less so than at 1 T) whereas the addition of 5 vol.% Y211 again increases the relaxation rate.

Shown in **Figure 47** are the data normalized to the initial moment, measured upon reaching a stable applied magnetic field for the magnetic relaxation of the MOCVD processed

samples at 1 T and 4 K. Additions of Zr significantly reduce the creep rate at this field and temperature.

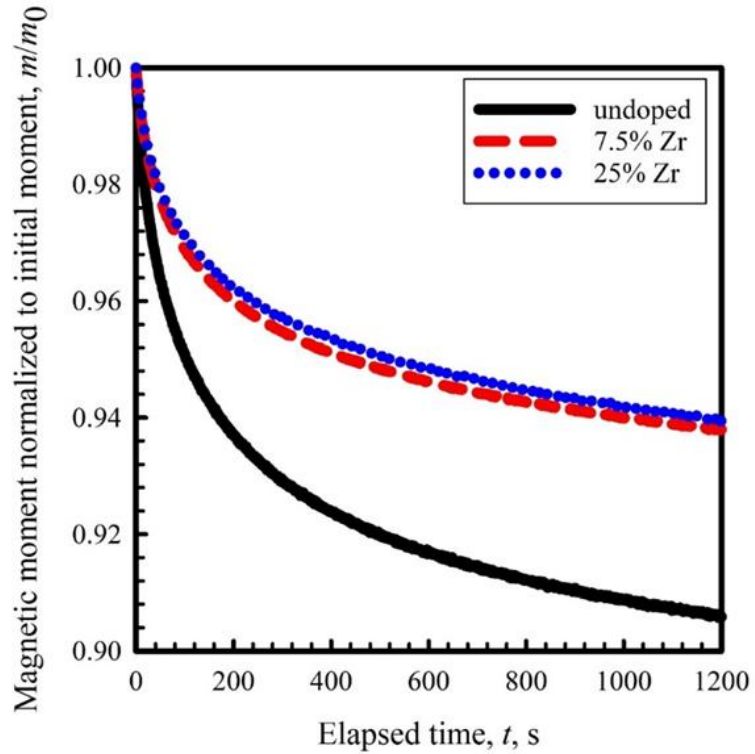


Figure 47. The magnetic relaxation of the MOCVD processed samples at 1 T, 4 K. Additions of Zr reduce the overall relaxation rate by about 1.5 X, but there is little difference in the rate for the samples with additions.

Shown in **Figure 48** are the data normalized to the initial moment, measured upon reaching a stable applied magnetic field for the magnetic relaxation of the MOCVD processed

samples at 8 T and 4 K. Additions of Zr still reduce the creep rate at this field and temperature.

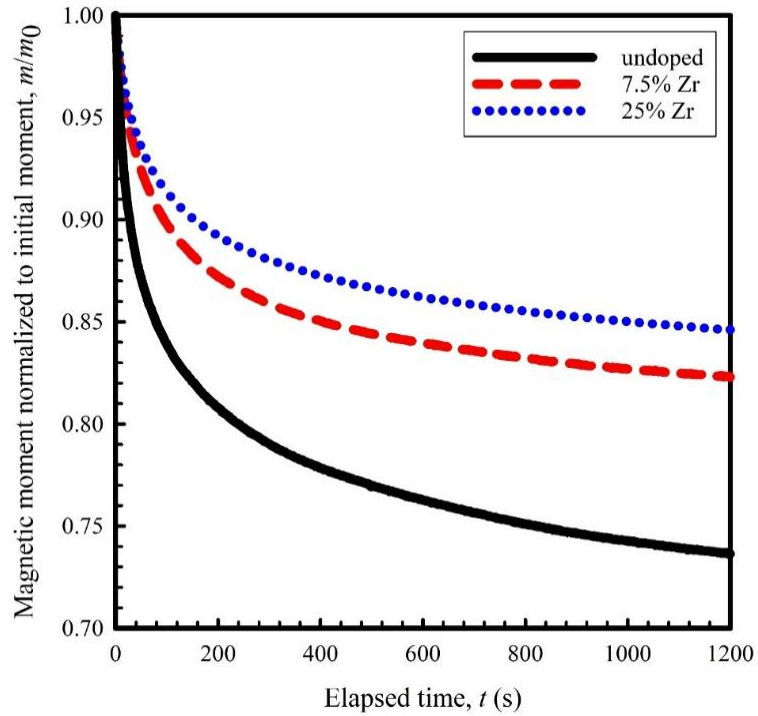


Figure 48. The magnetic relaxation of the MOCVD processed samples at 8 T, 4 K. Additions of 25 mol.% Zr reduce the overall relaxation rate by about 1.6 X over the control sample. There is some difference in the relaxation rate of the 7.5% and 25% Zr-added samples.

4.5.1 Analysis of the Initial Decay Measurement Set

The BZO precipitates appear to increase J_c (see **Table 8**) and reduce the creep rate, whereas the Y211 precipitates may increase the J_c at some applied fields and temperatures, they do not appreciably reduce the creep rate. A possible explanation of these results is that the BZO precipitate geometry and size matches the fluxon geometry and size better than those of the Y211 precipitates. The BZO precipitates as nanocolumns that thread the entire film thickness whereas the Y211 precipitates as shorter and wider nanoparticles embedded in the YBCO matrix. However, it is important to analyze these results in greater detail to see if these initial conclusions are valid. To do so, we will use a Maley approach to analyze the data.

Table 8. Comparison of J_c modification and raw decay measurements in PLD and MOCVD samples.

Precipitate	Control J_c (A/cm ²)	J_c increase at 1 T	Creep reduction ratio	J_c increase at 8 T	Creep reduction ratio
BZO	3.53×10^7	~5 X	~1.5 X	2.5 X	~1.6 X
Y211	1.83×10^7	2 X	~1 X	1.4 X	~1 X

4.5.2. Basic Flux Creep Model

Magnetic relaxation of high temperature superconductors (HTS) has been interpreted using an Arrhenius rate equation:

$$t = t_0 \exp \left[\frac{-U_{\text{eff}}}{k_B T} \right], \quad (4.2)$$

where t represents the hopping time, t_0 is the “effective” hopping attempt time, k_B is the Boltzmann constant, and U_{eff} is an effective energy barrier to flux motion [10]. This effective barrier energy approximates the true volume pinning energy of the material only when *small* currents exist in the conductor. When shielding or transport currents are present, the pinning energy is reduced by an energy which can be associated with the Lorentz force density multiplied by a suitably correlated volume and hop distance. Therefore, the potential energy landscape inside the superconductor is that of a “washboard” potential.

The effective energy barrier for thermally activated flux flow has often been assumed to depend linearly on the current density [10]

$$U_{\text{eff}} = U_0 \left[1 - \frac{J}{J_{c0}} \right] \quad (4.3)$$

near the critical surface ($J/J_{c0} \approx 1$), where U_0 is the barrier height in the absence of a driving force, and J_{c0} corresponds to the critical current density required to tilt the barrier to zero. Following [10], and combining the previous two equations and solving for J gives

$$J = J_{c0} \left[1 - \frac{k_B T}{U_0} \ln \left(\frac{t}{t_0} \right) \right], \quad (4.4)$$

which given in terms of magnetization, M , becomes

$$M = M_0 \left[1 - \frac{k_B T}{U_0} \ln \left(\frac{t}{t_0} \right) \right]. \quad (4.5)$$

Here, M_0 is the magnetization before any relaxation has taken place. This equation is commonly rewritten as:

$$M = M_0 \left[1 - r \ln \left(\frac{t}{t_0} \right) \right], \quad (4.6)$$

where $r = -k_B T / U_0$ is the so-called relaxation rate. Therefore, if one takes the slope of the magnetization vs $\ln(t)$ data, a value for r and therefore U_0 can be obtained.

However, pinning energies extracted in this way are only accurate if a linear relationship exists between the effective barrier energy and M (or J). Assuming a linear relationship leads to the inference of an apparent activation energy $U_a = k_B T M_0 / r$ which is a monotonically increasing function of temperature [40]. The magnetic relaxation data of the MOCVD processed samples can be used to show this result. The magnetic moment was recorded as a function of the logarithm of elapsed time at several applied fields, and at several different temperatures, for the control and 25 mol.% Zr added samples. A line was fitted to the data set at each temperature and field and r and U_{eff} were extracted using the slope of the line in accordance with equation 4.6. The extracted creep rate, r , at the different

temperatures and different applied fields is presented in **Figure 49**, and the effective pinning potential is presented in **Figure 50**. In general, r and U_{eff} increase with temperature for both samples. Technologically, r may be useful to estimate how quickly the magnetic field will change in an accelerator built from the measured composite. Another way of representing the creep rate is to normalize the magnetic moment by the initial moment present at the start of the measurement. The results of this calculation are presented, as a percentage, in **Figure 51** for the moment measured after 1200 s have elapsed. The U_{eff} s extracted using the linear approximation will be compared to the results from a more sophisticated analysis technique later in the chapter.

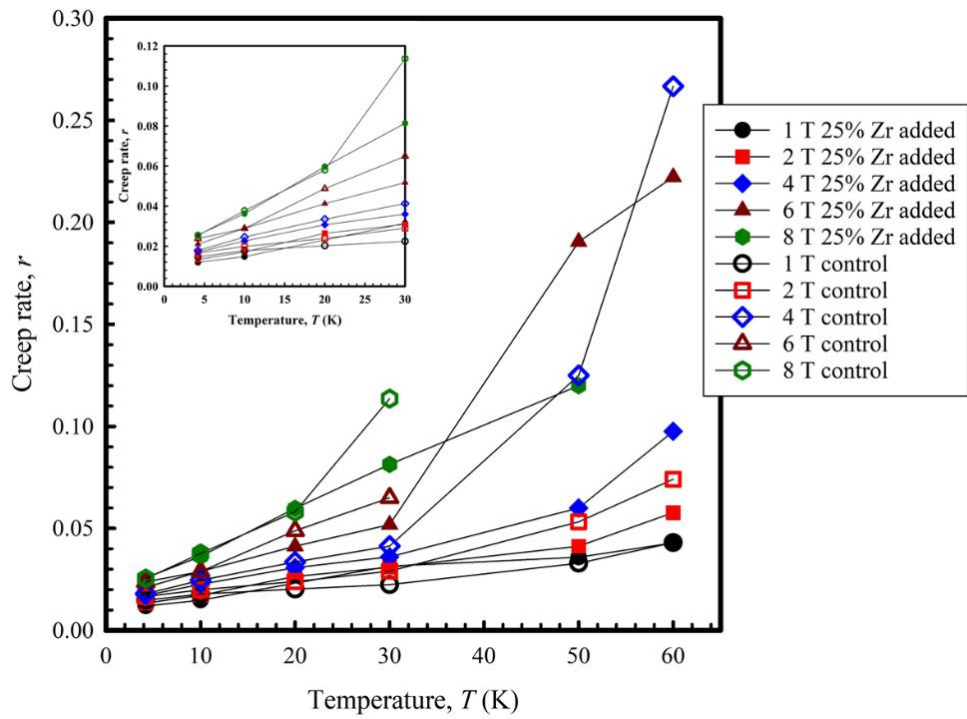


Figure 49. The creep rate, r , extracted using (4.6) for the MOCVD processed control sample (open symbols) and the 25 mol.% Zr-added MOCVD sample (closed symbols).

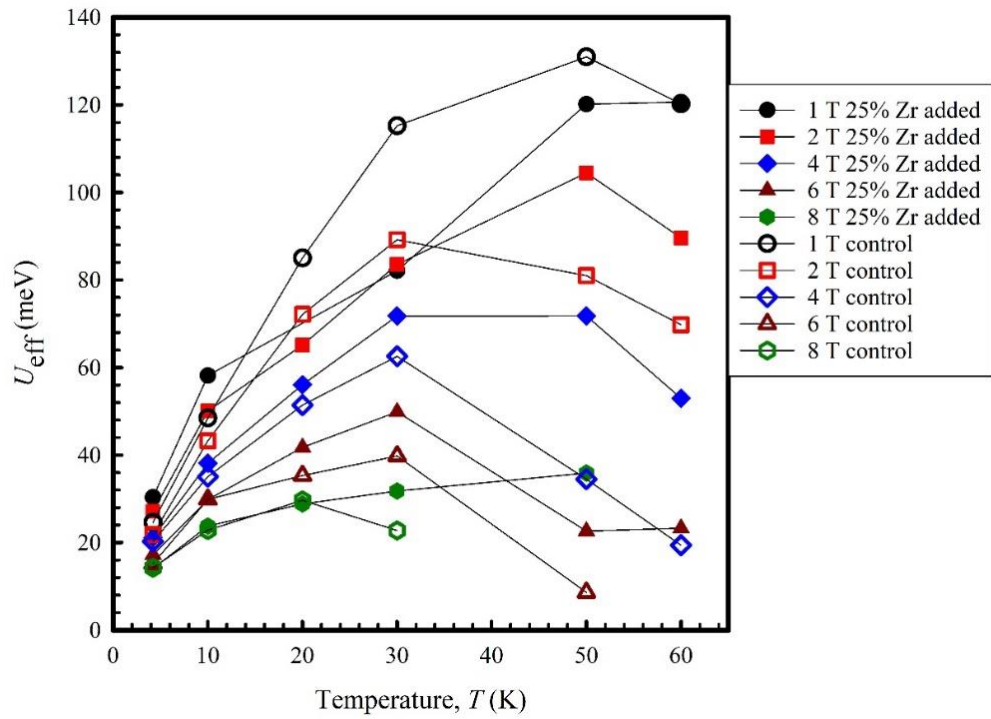


Figure 50. U_{eff} extracted by fitting the magnetic relaxation data to the creep equation, (4.6), assuming the potential has a linear dependence on J for the MOCVD control (open symbols) and the 25 mol.% Zr-added MOCVD samples (closed symbols).

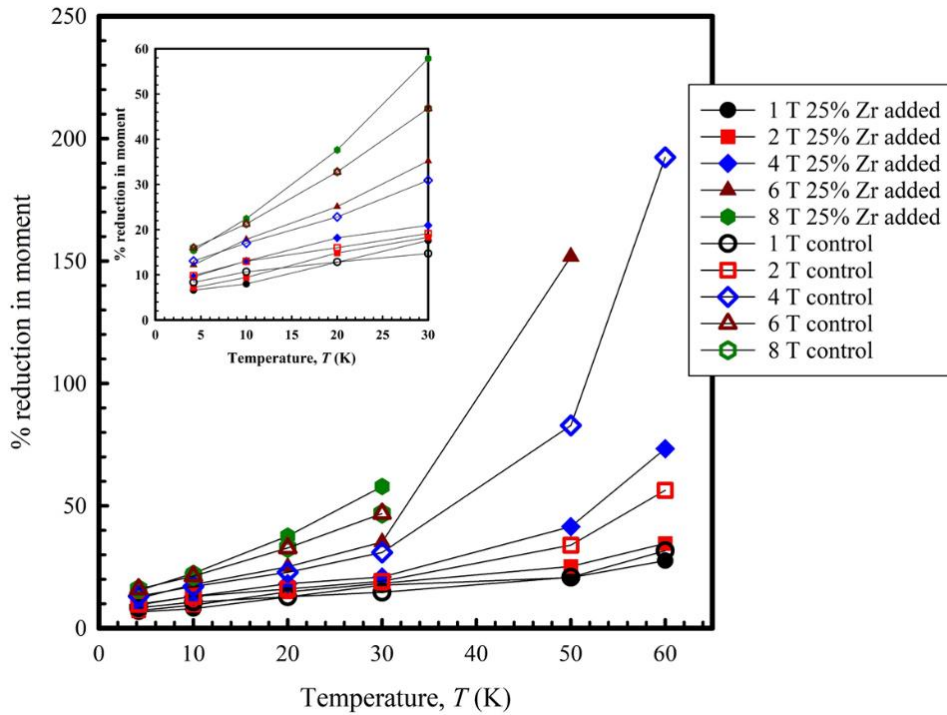


Figure 51. The percentage of the moment from the sample that exist at the beginning of the relaxation measurement, after 1200 s, for the MOCVD processed control sample (open symbols) and the 25 mol.% Zr-added MOCVD (closed symbols).

4.6. Determination of the Intrinsic Pinning Potential (U_0 or U_c)

At temperature T , the pinning potential, U , is a function of the applied field, B , and the associated persistent current density, J . At $T = B = J = 0$ the pinning potential assumes its “intrinsic” or characteristic value U_0 , a quantity that can be extracted from the results of a series of magnetization creep measurements using a procedure devised by Maley *et al.* [45]. They started from the rate equation for thermally activated motion of flux and used the form of the one dimensional flux density rate equation derived by Beasley *et al.* [38]

$$\frac{dB}{dt} = \nabla \cdot \left[Bav_0 \exp\left(\frac{-U_{\text{eff}}}{k_B T}\right) \right], \quad (4.7)$$

where a is an average hop distance of the flux bundles and v_0 is an attempt frequency. This expression was then integrated over the sample volume to obtain the rate of change of the average flux density $\langle B \rangle$. If it is assumed that the sample is an infinite slab of thickness d , the divergence theorem can be used to get the expression

$$\frac{d \langle B \rangle}{dt} = 4\pi \frac{dM}{dt} + \frac{dH}{dt} = \frac{2Hav_0}{d} \exp\left(\frac{-U_{\text{eff}}}{k_B T}\right), \quad (4.8)$$

where the flux density has been expanded in terms of the magnetization, M , and the magnetic field strength, H , and it is assumed that $B \sim H$ for fields much higher than the penetration field. If the temporal decay of the magnetization is measured under a constant applied magnetic field, the term dH/dt in the above equation is zero and the equation can be rearranged to give an expression for the effective activation energy,

$$\frac{U_{\text{eff}}}{k_B} = -T \left[\ln\left(\frac{dM}{dt}\right) - \ln\left(\frac{Hav_0}{2\pi d}\right) \right], \quad (4.9)$$

where the term $\ln(2av_0/d)$ is a constant whose values cannot be probed from the experimental relaxation measurements. The expression indicates that the current dependence of the effective activation energy can be determined experimentally, to within an additive constant. Therefore, plots of the flux creep data, in the form of M vs $-T \ln|dM/dt|$, at different temperatures give a set of curves which should be within an additive constant

of U/k_B vs M . Aligning each curve along the same smooth, continuous, $U(J)$ curve can be achieved by adding in the CT term with the correct choice of C , which is assumed to be temperature independent or nearly temperature independent. Although a and v_0 are temperature dependent, they are arguments of the logarithm of the constant and therefore the temperature dependence is neglected [46]. A set of curves aligned in this way then represents the experimental determination of $U(M)$, or alternatively $U(J)$.

At higher temperatures, C is a strong function of applied field, B [46]. McHenry *et al.* [46] suggested that this unphysical variation of C on B is an artifact which can be removed by appropriate temperature scaling of the effective energy barrier, which accounts for the change in the pinning potential barrier height at high temperatures. They argue that the data at lower fields and higher temperatures is more apt to show problems associated with the inevitable temperature dependence of the correlated volume for flux motion and the hop distance. Therefore, high temperature data can be fit only after an appropriate scaling with temperature. A series of flux creep data plotted in this way can be brought to overlap by scaling the data by a power of the applied field, B^v , thus generating the experimental $U(J, B)$ curve. In this work, we followed the approach of Maley *et al.* and McHenry *et al.* to generate $U(J, B)$ for both sets of samples. The magnetic moment was measured over a period of 1-3 h at several different temperatures and applied magnetic fields. At a fixed field, each set of points represents a magnetic relaxation measurement made at a different temperature.

The analysis of Maley *et al.* led to a plot of a modification of U/k_B vs a time-dependent J in which J was determined from the time-dependent (decaying) magnetic moment where J is given for a shorter sample by

$$J_c = \frac{2\Delta M}{w_1} \left[1 - \frac{w_1}{3w_2} \right]^{-1} \approx \frac{3\Delta M}{w} \quad (4.10)$$

in which w_1 and w_2 are the width and length of the sample. Here ΔM is the magnetic moment normalized to the superconductor volume. Modifications to U/k_B involve scaling it by a temperature-dependent scaling factor, $G(T)$

$$G(T) = \left[1 - \left(\frac{T}{T_x} \right)^n \right]^p \quad (4.11)$$

where n , p and T_x are fitting parameters. The parameters were chosen to give the most continuous U_{eff}/k_B vs J curve. Next, a value of C was chosen to enable a best fit to the curves at each applied magnetic field. Finally, the $U/k_B G(T)$ curves were scaled by the applied field raised to a power (B^v) so that the data at different fields and temperatures overlapped on one smooth, “continuous”, curve of the form

$$U(J) = \frac{U_0}{\mu} \left[\left(\frac{J_c}{J} \right)^\mu - 1 \right], \quad (4.12)$$

in which J_c is the current density at the lowest field and temperature and μ is the glassy exponent that varies with the dimensionality of the pinning. This interpolation formula was

developed to account for the majority of the current dependencies predicted by the collective creep, vortex-glass, and other theories [90]. The U of the above equation is assumed to have no intrinsic temperature and field dependence and as such is equivalent to $UB^\nu/k_B G(T)$. The results of fitting the interpolation expression to the $UB^\nu/k_B G(T)$ vs J_c data is shown in **Figure 52-Figure 55** for the PLD processed samples.

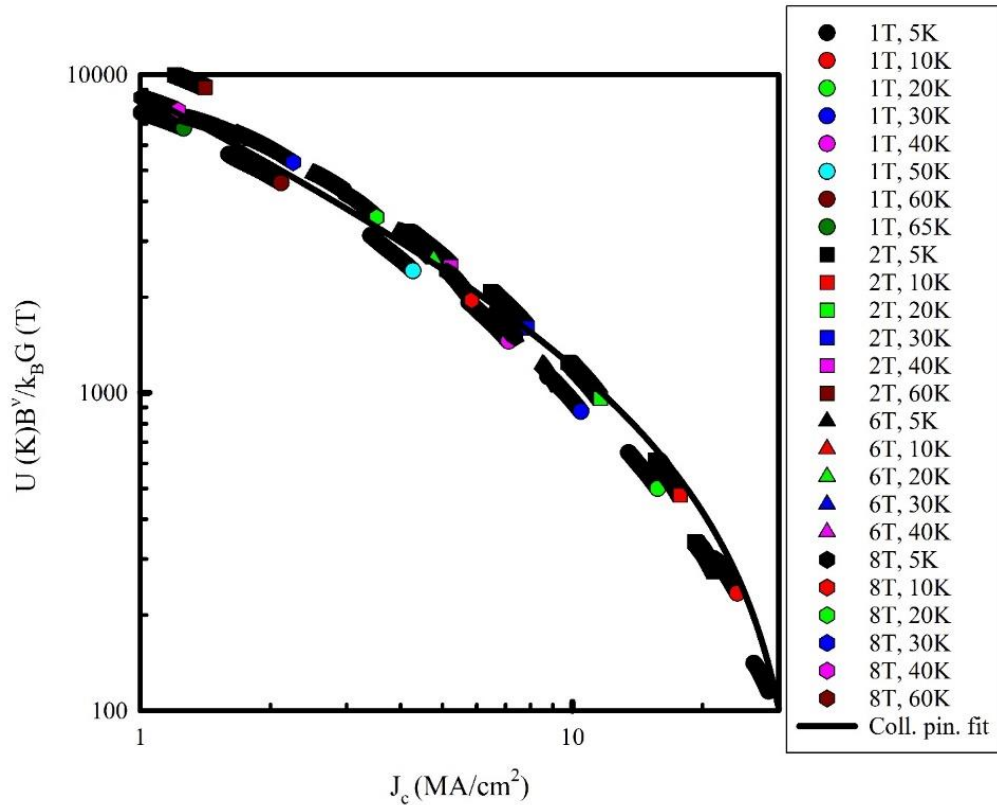


Figure 52. Magnetic relaxation-generated $U(J)$ for the PLD processed control sample. Measurements are shown for 65, 60, 50, 40, 30, 20, 10, and 5 K. At each temperature, measurements were made at 1 T, 2 T, 6 T, and 8 T.

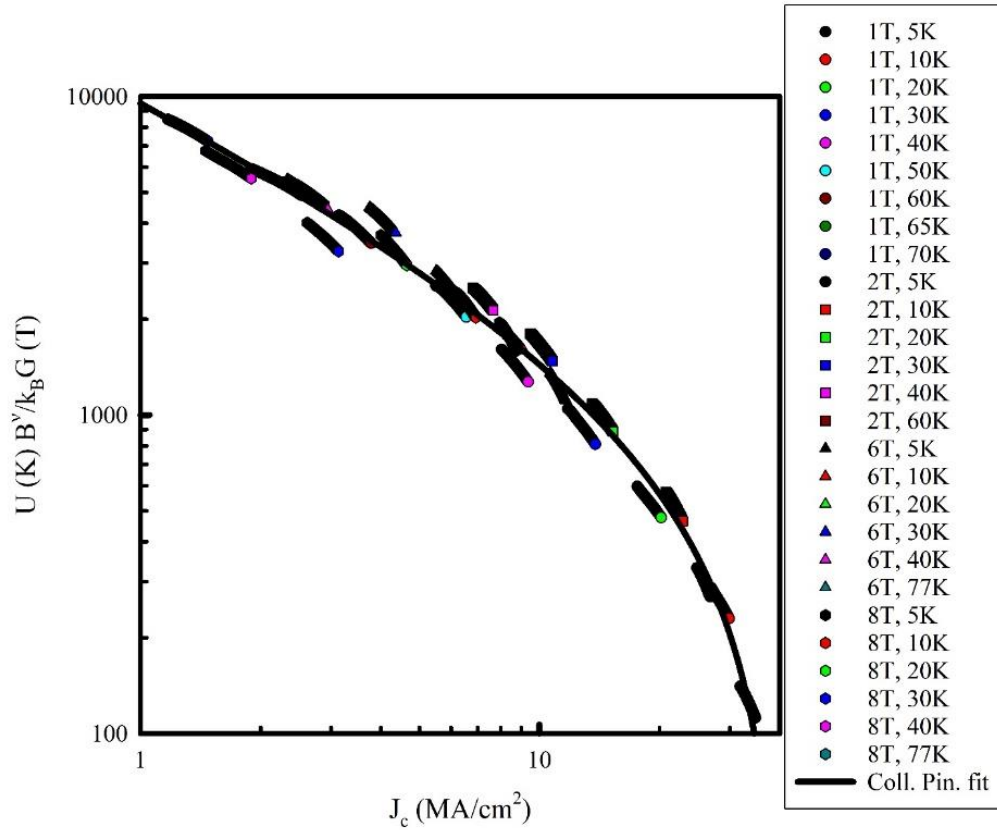


Figure 53. Magnetic relaxation-generated $U(J)$ for the 5 vol.% Y211 sample. Measurements are shown for 77, 70, 65, 60, 50, 40, 30, 20, 10, and 5 K. At each temperature, measurements were made at 1 T, 2 T, 6 T, and 8 T.

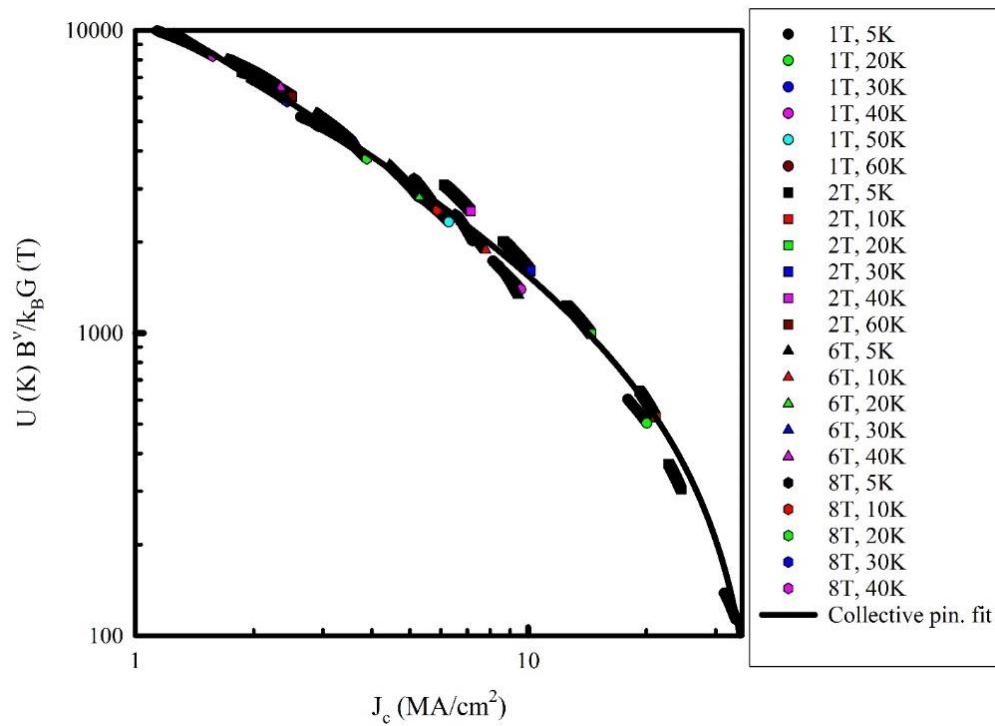


Figure 54. Magnetic relaxation-generated $U(J)$ for the 10 vol.% Y211 sample. Measurements are shown for 77, 70, 65, 60, 50, 40, 30, 20, 10, and 5 K. At each temperature, measurements were made at 1 T, 2 T, 6 T, and 8 T.

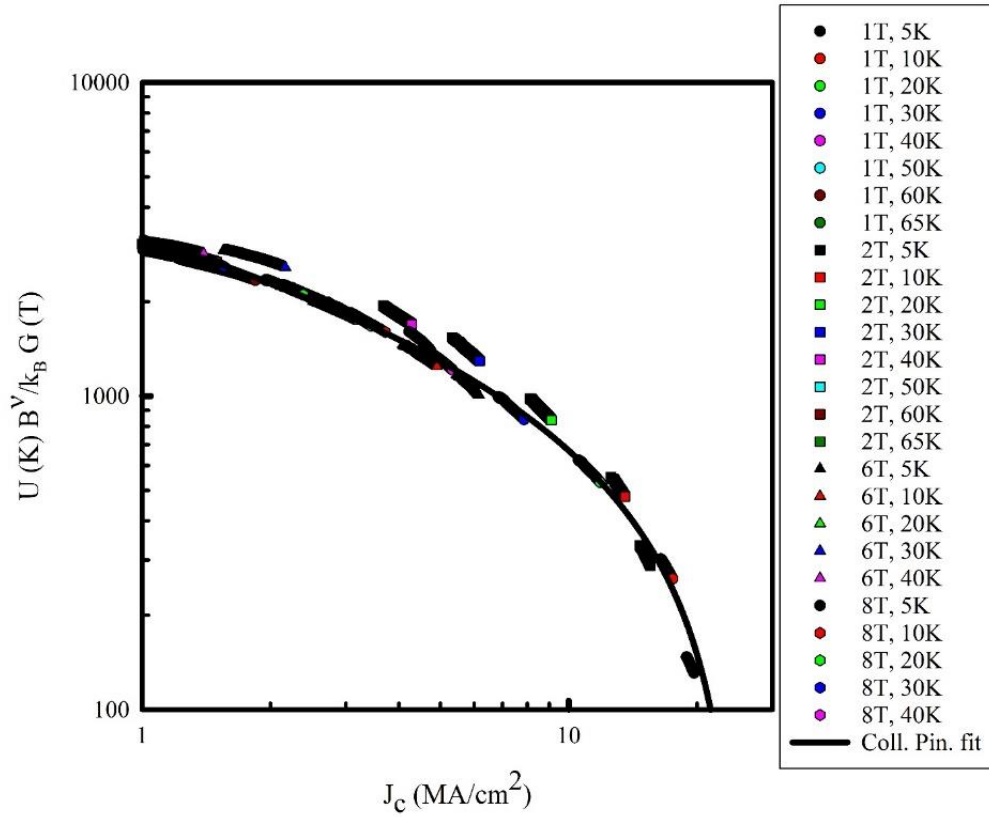


Figure 55. Magnetic relaxation-generated $U(J)$ for the 2 vol.% BZO sample. Measurements are shown for 65, 60, 50, 40, 30, 20, 10, and 5 K. At each temperature, measurements were made at 1 T, 2 T, 6 T, and 8 T.

The scaling parameters used to align the magnetic relaxation data of the PLD processed samples are presented in **Table 9**. The parameters used in the collective creep interpolation expression are presented in **Table 10**.

Table 9. Fitting parameters for the PLD processed sample magnetic relaxation measurements

Sample	p	T_c	v (5K)	v (10K)	v (20K)	v (30K)	v (40K)	v (50K)	v (60K)
Control	2	90	1	1	0.9	0.85	0.78	--	0.95
5% (211)	1.5	90	1.2	0.99	0.82	0.82	0.7	0.52	0.35
10% (211)	2	94	1.35	1.14	0.95	0.87	0.83	0.6	0.5
2% (BZO)	5/8	89	1.14	0.88	0.65	0.62	0.57	0.2	0.2

Table 10. Extracted pinning parameters from the PLD sample measurements

Sample	U_0	μ	J_c (MA/cm ²)
Control	625	0.65	35
5% (211)	650	0.7	40
10% (211)	650	0.72	40
2% (BZO)	650	0.25	25

4.6.1. Summary of PLD Processed Samples Results

It is apparent from the extracted U_0 values (presented in **Table 10**) that neither the additions of Y211 nor the addition of 2 vol.% BZO to the PLD processed samples significantly increase the pinning potential well depth over that of the PLD control sample. This finding indicates that any increase in J_c due to the introduction of the Y211 or BZO

in the concentrations presented here is not a result of deeper (or stronger) pins but could be a result of the introduction of a larger number of pins of equal or lesser strength. In the case of the BZO, the concentration is low, so this may affect our result for BZO.

4.6.2. Fitting of the MOCVD Sample Relaxation Data

The results of an identical fitting exercise to that used with the PLD sample relaxation data is shown in Figure 56-Figure 58 for the MOCVD processed samples. The exercise allowed for the extraction of μ and the intrinsic pinning potential, U_0 . The scaling parameters used to align the magnetic relaxation data of the MOCVD processed samples are presented in **Table 11**. The parameters used to fit the collective creep interpolation expression to the data are presented in **Table 12**.

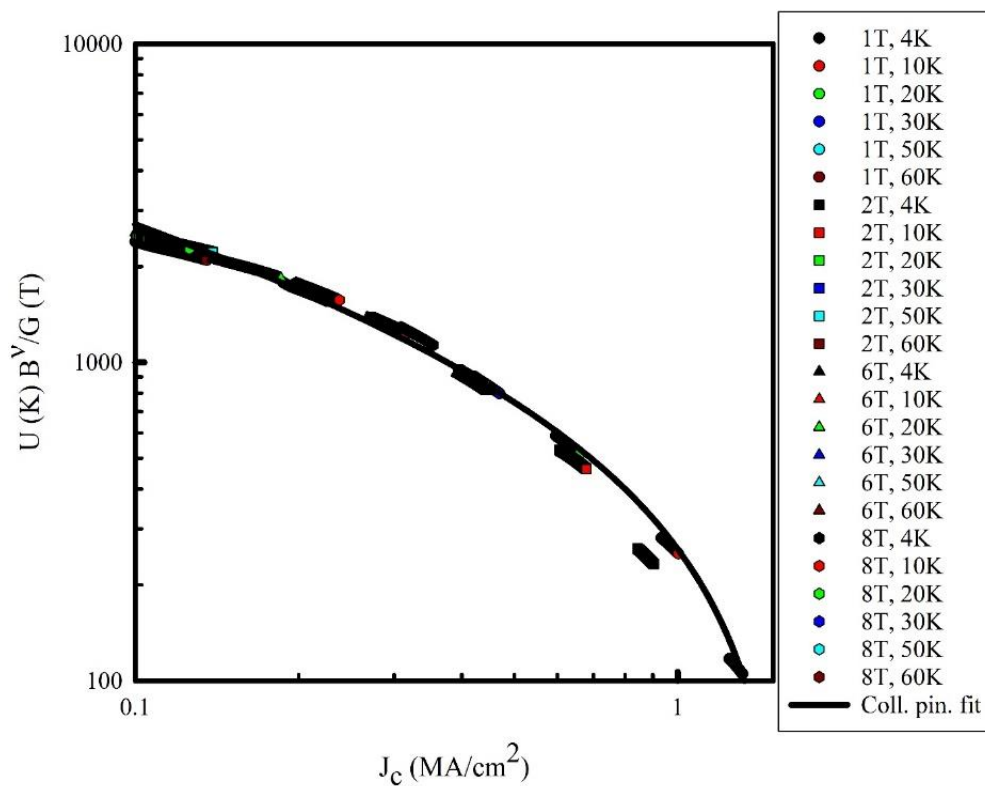


Figure 56. Magnetic relaxation-generated $U(J)$ for the MOCVD control sample. Measurements are shown for 60, 50, 30, 20, 10, and 4 K. At each temperature, measurements were made at 1 T, 2 T, 6 T, and 8 T.

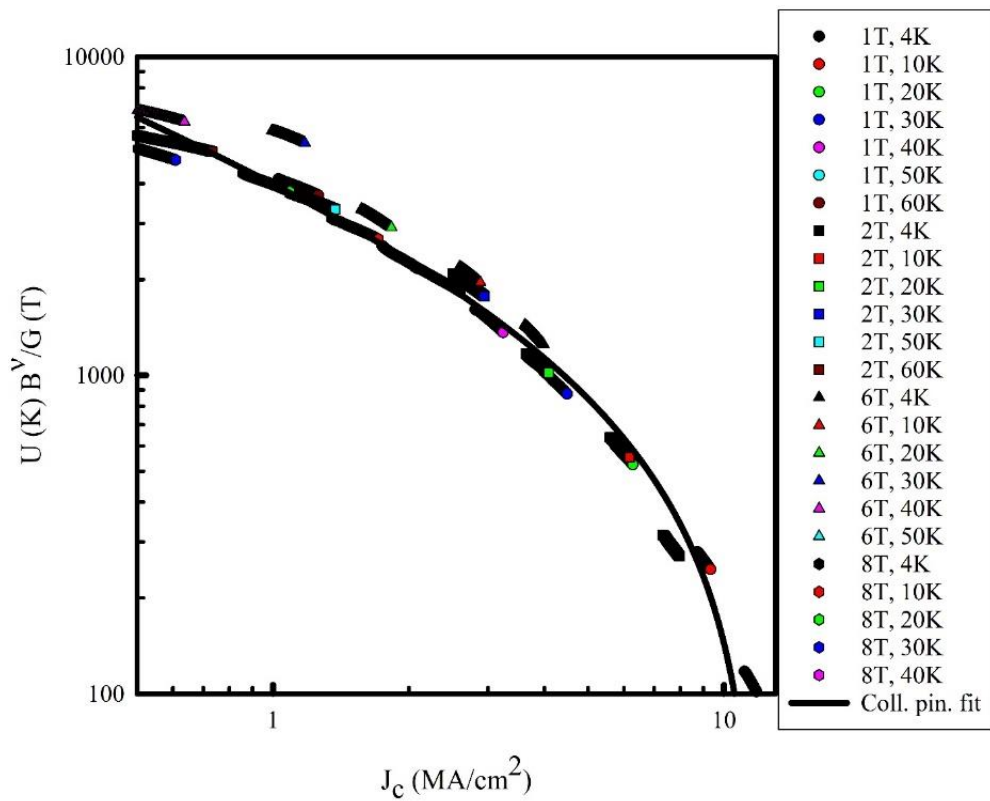


Figure 57. Magnetic relaxation-generated $U(J)$ for the MOCVD 7.5 mol.% Zr-added sample. Measurements are shown for 60, 50, 40, 30, 20, 10, and 4 K. At each temperature, measurements were made at 1 T, 2 T, 6 T, and 8 T.

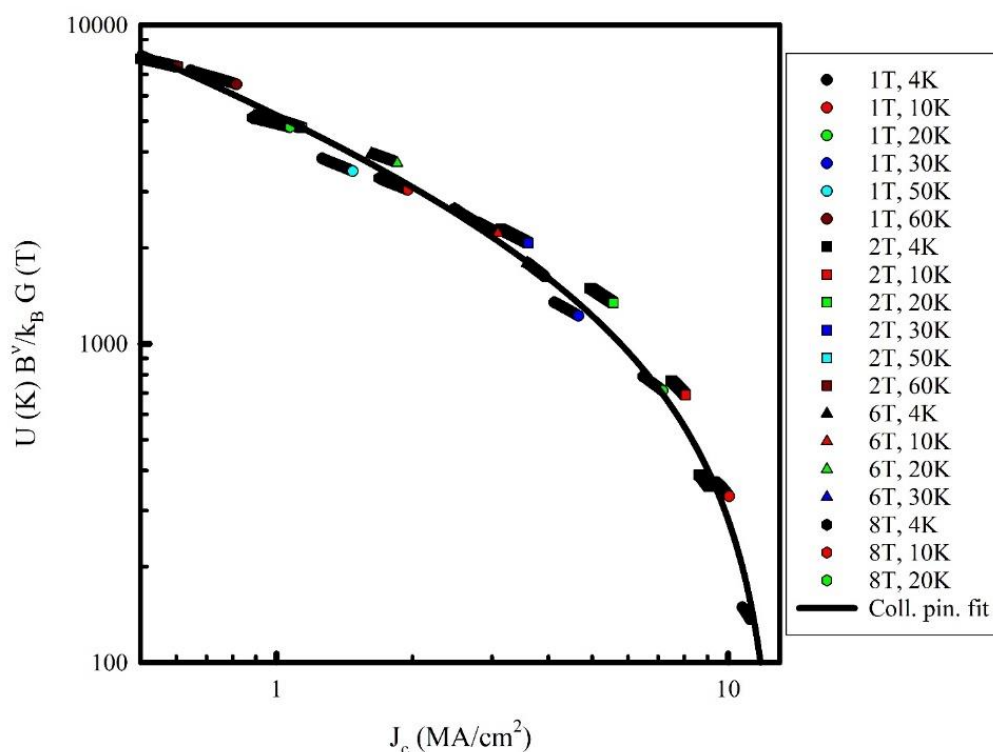


Figure 58. Magnetic relaxation-generated $U(J)$ for the MOCVD 25 mol.% Zr-added sample. Measurements are shown for 60, 50, 30, 20, 10, and 4 K. At each temperature, measurements were made at 1 T, 2 T, 6 T, and 8 T.

Table 11. Fitting parameters for the MOCVD sample magnetic relaxation measurements

Sample	p	T_c	v (4K)	v (10K)	v (20K)	v (30K)	v (40K)	v (50K)	v (60K)
0 %	0.5	90	1.14	0.88	0.71	0.65	0.5	0.51	0.51
7.5 %	1.5	90	1.4	1.15	0.95	1.1	1.1	0.58	0.5
25%	2	90	1.3	1.06	0.91	0.8	none	0.45	0.18

Table 12. Extracted pinning parameters for the MOCVD processed samples

Sample	U_0	μ	J_c (MA/cm ²)
Control	480	0.46	1.62
7.5 % (BZO)	525	0.72	14
25% (BZO)	1000	0.5	13

4.6.3. Summary of MOCVD Processed Samples Results

It is apparent from the extracted U_0 values (presented in **Table 12**) that Zr additions increase the potential well depth over that of the MOCVD control sample. This finding indicates that increases in J_c due to the introduction of the BZO in the concentrations presented here could be a result of deeper (or stronger) pins, at least as compared to the intrinsic BZO pins. $M-H$ (and J_c) measurements showed that additions of Zr (which caused BZO to precipitate in the YBCO matrix) increased J_c at low temperature and low applied magnetic field. Moment vs time measurements show that the absolute flux creep was lower with increased Zr addition. These findings are important because they indicate that different additions can give different pinning strengths. Different additions can affect the creep rate which may influence/reduce the magnetic drift in a magnet.

4.7. Summary

A simplified summary of the detailed results for each sample type given above in **Table 7-Table 12**, and **Figure 52-Figure 58**, is given below in **Figure 59-Figure 60** and **Table 13-Table 14**. It is shown in **Figure 59** that the strengths of the pins introduced when Y211 and BZO were added during PLD are not very different than the strength of the intrinsic pins created during PLD, whereas it is shown in **Figure 60** that BZO pins are significantly stronger than the intrinsic pins created during MOCVD. This fact is re-emphasized in **Table 13** and **Table 14**, where we see that the intrinsic pins of the MOCVD sample are weaker than those of the PLD, so that the BZO additions are much more effective for the MOCVD. Thus, in general, we can say that the pin strength can be ranked from weakest to strongest as: (1) intrinsic MOCVD; (2) intrinsic PLD; (3) Y211; and (4) BZO.

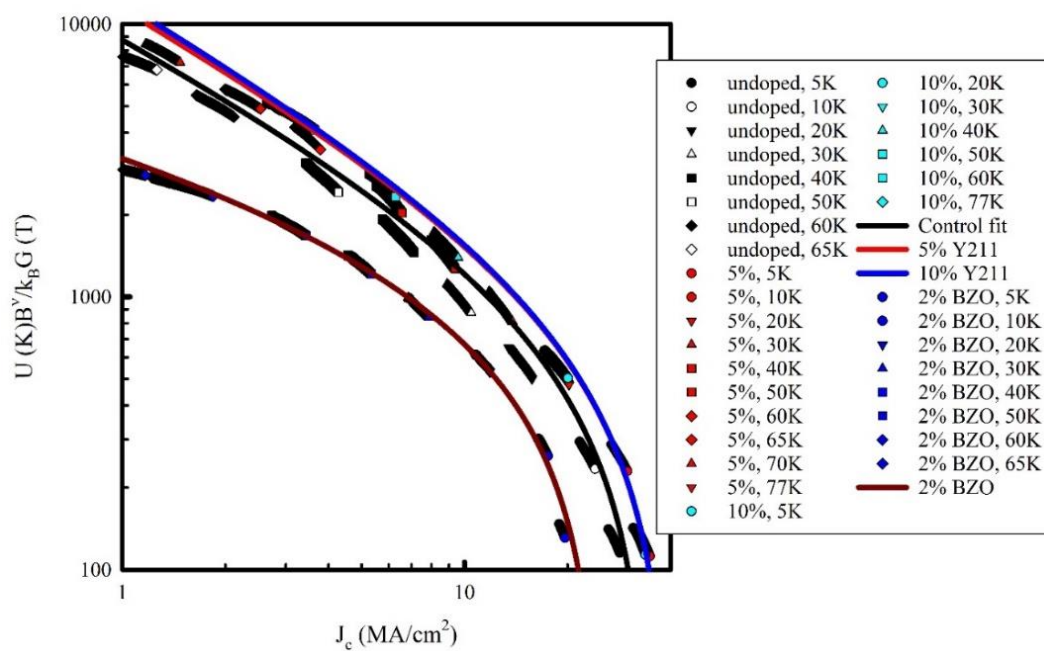


Figure 59. 1 T magnetic relaxation-generated $U(J)$ for the PLD processed samples.

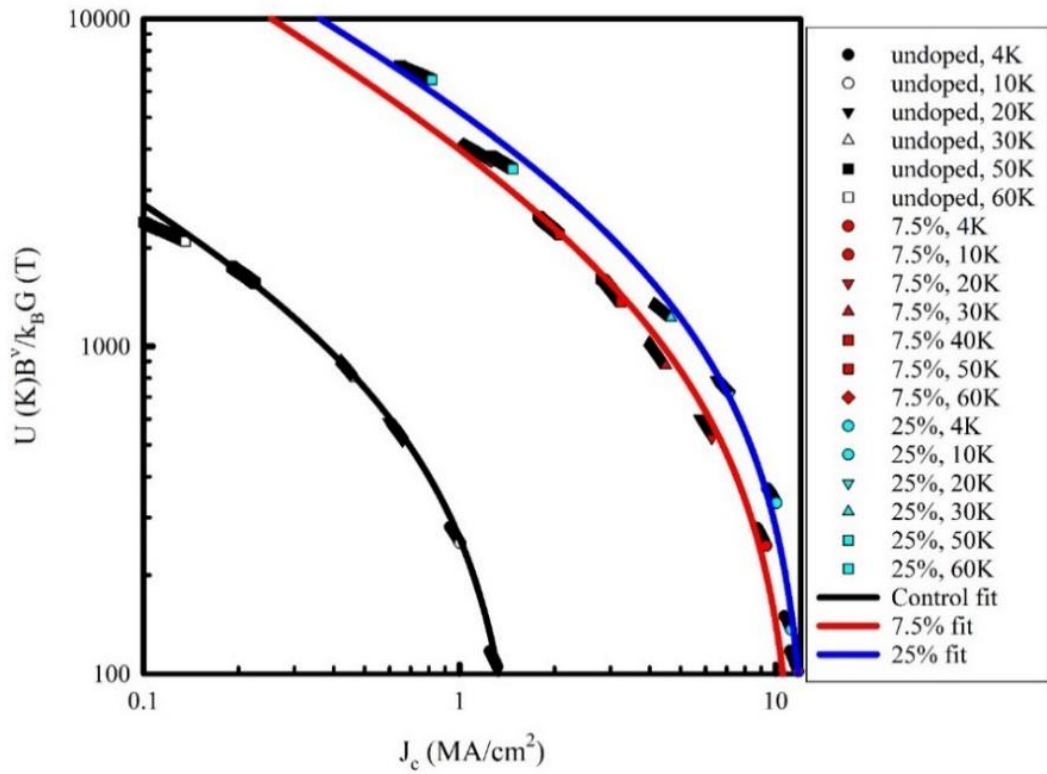


Figure 60. 1 T magnetic relaxation-generated $U(J)$ for the MOCVD processed samples.

Table 13. Extracted pinning parameters for the MOCVD processed samples

Sample	U_0	μ	$J_c (MA/cm^2)$
Control	480	0.46	1.62
7.5 % (BZO)	525	0.72	14
25% (BZO)	1000	0.5	13

Table 14. Extracted pinning parameters for the PLD processed samples.

Sample	U_0	μ	J_c (MA/cm ²)
Control	625	0.65	35
5% (211)	650	0.7	40
10% (211)	650	0.72	40
2% (BZO)	650	0.25	25

It is interesting to consider that the differences in U_0 are not as large as we might expect given the very different aspect ratios and densities of the Y211 and BZO precipitates. If the BZO precipitates were merely acting as normal state pins, we might expect the density and aspect ratio to have a much greater impact than we see. It has been noted previously that much of the pinning for Y211 additions has to do with the strain fields that these precipitates introduce. They introduce a dense network of strain fields and modest sized pins. Perhaps this is part of the answer for what is going on with the BZO pinning.

In any case, technologically, the results indicate that MOCVD processed samples need added pins to increase J_c and reduce the flux creep rate. PLD processed samples possess lower intrinsic creep, but the creep rate does not seem to reduce much with Y211 additions. The additions of Zr decreased the creep rate and increased U_0 in the MOCVD

processed samples. Conversely, although J_c was increased with Y211 additions, U_0 increases were modest with Y211 additions in the PLD processed samples.

Chapter 5: Magnetic Properties of Cables and their Influence on Accelerator Magnets

The strands of superconductor composites and conductors used to build accelerator magnets are cabled before being used as the turns in the magnet. Cables are used for accelerator magnets because they allow for high currents in the turns of the magnet and they limit inductance to generally modest values. Low inductance is desirable because it limits both the required magnet driving voltages and, more importantly, the peak voltages generated during a quench in the magnet. Cables also give redundancy and a potential for current sharing. Superconducting cables have been used from the earliest days of accelerator magnets. Even today, NbTi strands are wound into Rutherford cables for present day accelerators, and high performance Nb₃Sn-based Rutherford cables replace NbTi in some of the highest field areas of the Large Hadron Collider (LHC). As we move to the use of HTS conductors, the round strands of Bi:2212 allow us to carry over directly the Rutherford cable geometry, and prototype Bi:2212 magnets have already been made and tested at LBNL [91]. YBCO-based composites, with their flat tape geometry, are more challenging to cable, but Conductor-on-Round-Core (CORC[®]) [4] cables, Roebel cables, and tape stacks have been used to make prototype RE-Ba₂Cu₃O_{7- δ} (REBCO)-based magnets of various kinds. Some important properties of the accelerator magnet that must be considered are the magnetization at injection (M_{inj}) of the conductor used for the windings, the penetration field ($\mu_0 H_p$ or B_p) of the conductor used for the windings, and the

magnetization decay, or creep, of the conductor used for the windings. The reasons for their importance are as follows. M_{inj} influences the magnitude of the field error during particle injection. B_p determines the current range required to erase the previous magnetization in the magnet. A significant magnetization decay can lead to larger changes in accelerator field errors, as discussed in Chapter 6. However, it is important to note that the short sample properties of strands or conductors are not necessarily identical to those of magnet relevant structures built from them. The consequence of this fact is that the short sample properties may not be useful for predicting the performance (e.g., field error and field error drift performance) of magnets built from them.

In this chapter, the magnetization, and its subsequent decay, of sections of superconducting cables (CORC[®] and Bi:2212 Rutherford cable) extracted from prototype magnets were measured and compared to short sample results. It was found that the B_p of the CORC[®] cable is much higher than a short tape sample extracted from the cable. The M_{inj} is much lower than the untwisted tape when the moment of the cable is normalized by the equivalent volume of tape in the cable. The magnetization decay in the cable appears to be slower than that of the tape, and it can be reduced by cycling the magnetic field in a manner like the field cycling performed during magnet pre-injection cycles. The $M-\mu_0H$ loops presented in this chapter are used in Chapter 6 to make field error estimates for several accelerator magnet designs.

5.1 YBCO CORC[®] Cables

YBCO-based coated conductors take the form of thin tapes, often with Ni-alloy or Hastalloy substrates. They have very large current densities, with strong J_c retention in high magnetic fields, but the critical current of the YBCO conductor is anisotropic with respect to the magnetic field angle (the angle the applied magnetic field makes with the plane of the tape). The coated conductors have high tensile yield stress, a high overall axial strain range of operation [4], and they have been used in demonstrations of high-field magnets [92, 93]. As noted above, limiting magnet quench voltage and inductance requires cabling, which also gives redundancy and the potential for current sharing. Various kinds of cables have been developed with YBCO tape, including twisted stack [94], Roebel [95, 96], and CORC[®] [4] cables. CORC[®] cables are of particular interest for accelerator magnets because they have isotropic magnetic, electrical, and mechanical properties, and are easier to wind than stacked tape cables. A disadvantage of the Roebel cable is that, although it is flexible in one direction, it is relatively inflexible when bent in plane. Although this disadvantage limits the types of magnets suitable for Roebel cables, there are programs attempting to build high-field accelerator magnets using Roebel [97, 98]. We are exploring all three cable types, but a CORC[®] sample extracted from a prototype sub-scale canted cosine theta (CCT) dipole accelerator will be the focus of study in this work.

The CORC[®] cable is an isotropic high-temperature superconductor (HTS) cable that can withstand a small bending radius, which is very useful when winding the turns for a magnet. In the CORC[®] cable, individual YBCO composite tapes are helically wrapped

around a copper core, **Figure 61**. The smaller diameter cables, which are referred to by the manufacturer as “wires,” use tapes which are 2-3 mm wide to make a cable (or “wire”) that is 2.5-4.5 mm in diameter. Usually the small diameter cable is comprised of no more than 30 tapes. The cable has a bending diameter of less than 50 mm, making it useful for bending into a magnet. LBNL has made and tested prototype CCT magnets made from small diameter CORC[®] wires [3].



Figure 61. A CORC[®] wire (top of figure) and CORC[®] cable (bottom of figure), from [99].

5.2. The Development of a Hall Susceptibility System for Cable Measurements

Individual small sections of tape can be measured using conventional vibrating sample magnetometers (VSMs) or SQUIDS. Magnetization, though, is a function of conductor geometry, and sample length, twist, and cabling affect the resultant magnetization [100]. However, the sample spaces and magnet bores of VSMs and SQUIDS

are too small to measure larger samples, such as cables and twisted stacks that would be used to build accelerator magnets. Very few systems exist for the measurement of HTS cables, the required combination of larger bore and higher applied fields are unusual. Thus, it was decided to construct such a system. A Hall probe magnetometer system was designed and built at the Center for Superconducting and Magnetic Materials (CSMM) to measure the properties of larger samples. The Hall probe technique for M - $\mu_0 H$ measurements has been successfully used many times in the literature [49, 101, 102].

5.2.1 The Magnet System

The Hall probe susceptometer system that was created uses a varitemp dewar with its tail inserted into a room temperature (RT) bore of a 12 T liquid cryogen-free solenoid magnet. The system is shown in **Figure 62**. The bore of the magnet can accommodate samples 5-6 cm in length, which is an order of magnitude larger than the bore diameters of conventional magnetometers. The silver colored dewar has a tail which extends into the RT bore. The magnet system uses a minimum liquid helium skin and a cryocooler. The helium space of the varitemp is separate from the dewar.

A Hall sensor was used to measure the magnetic flux density, B , in the bore of the magnet. The applied magnetic field strength, $\mu_0 H$ was calculated programmatically using a custom-built Labview program and subtracted from the magnetic flux density in real time. The magnet constant, which gives the magnetic field strength generated by the

magnet, is 7.1536 A/T. The Labview program reads the magnet current from the magnet power supply, converts the current to an applied field strength using the magnet constant, and then subtracts this from the B read from the GM-700 Gaussmeter connected to the Hall sensor, to get a value for the magnetization of the sample. All values were read and calculated in real time and recorded in a data file.



Figure 62. The 12 T conduction-cooled superconducting magnet system used to measure the magnetic properties of the superconducting cables. The central gray cylinder is the cryogen-free magnet with a room temperature bore.

5.2.2. Probe/Sample Holder Details

The adjustable-length sample holder, see **Figure 63**, was built with electrical feedthroughs to allow for connections to instruments and sensors. It is equipped to handle transport current measurements; however, these measurements were not performed here.



Figure 63. The sample holder used to mount the cable samples.

The Hall sensor was mounted into a groove in the center of a G10 piece located in the center of the end of the holder. The Hall sensor was able to be mounted flat and lie flush with the edge of the groove. The surface of the active area of the Hall sensor was approximately 1 mm from the sample surface when a sample was mounted. The distance from sample surface to Hall sensor active surface was kept constant for all measurements presented here. A Cernox[®] sensor was mounted on the sample holder, approximately 1 cm above the sample position, to monitor the temperature during the measurements.

The samples were mounted as flush with the surface of the end of the sample holder as possible. They were adhered to the holder surface using GE varnish. A mounted CORC[®]

cable section is shown in **Figure 64**. After the varnish dried, Kapton[®] tape was used to further prevent sample motion and to prevent the sample from falling into the dewar of the magnet. The samples were removed by first removing the Kapton[®] tape and then by using Ethyl alcohol to remove the varnish.



Figure 64. A CORC[®] cable section mounted onto the end of the sample holder. GE varnish is used to adhere the ends of the sample to the holder.

5.2.3 Measurements

The magnetic measurements on the superconducting samples were performed at 4.2 K, as measured with the Cernox[®] sensor, by submerging the sample into liquid helium which had been transferred to the dewar body. A schematic of the sample setup during measurement is shown in **Figure 65**. In the figure, the Hall sensor is the blue rectangular cuboid, the sample is represented by the cylinder (light yellow), and the applied field is represented by the green arrows.

5.2.4. Background Signal Removal and Calibration

Small amounts of ferromagnetic material within the magnet structure generate a small but detectable background magnetic field in the magnet. Therefore, several $M-\mu_0H$ measurements were performed in the absence of a sample to get a quantitative measure of the background field as a function of applied field and applied field history. Such background measurements allowed for the subtraction of any background generated by the sample holder or the magnet structure from $M-\mu_0H$ measurements performed in the presence of a sample. These “no-sample” background readings were used to correct subsequent $M-\mu_0H$ and decay measurements. The background was found to be slightly hysteretic, such that the shielding branches and trapping branches had to be fit separately.

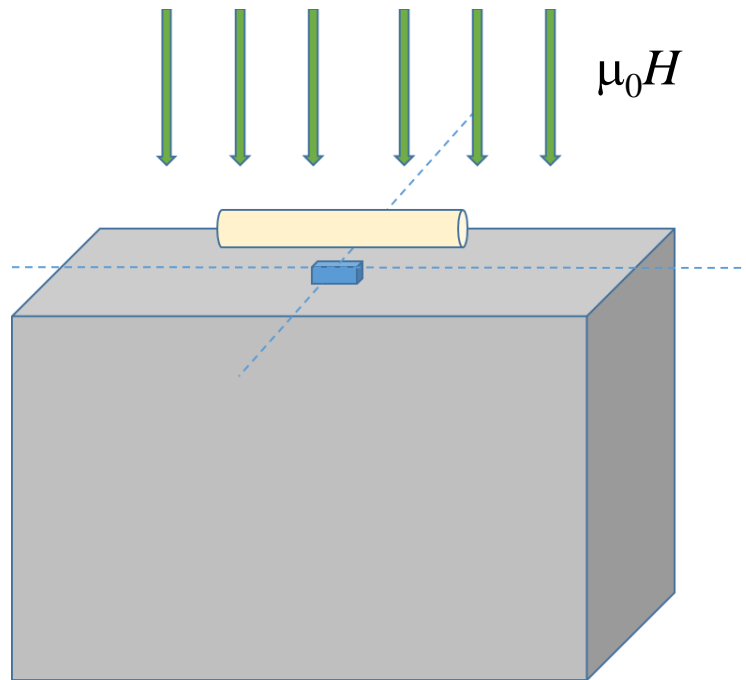


Figure 65. A schematic of the Hall probe magnetometer sample mounting setup [103].

5.2.5. Calibration by Replacement Technique

The system was calibrated in two ways; the first method used a replacement technique. The idea is that the sample acts as a moment source (e.g. a dipole) with the field generated at the sample proportional to the size of the total moment, and inversely proportional to the distance (squared) from the Hall probe to the sample [102]. In this case, because of the proximity of the sample and its relative size, it is necessary to add a sensitivity weighting function which accounts for the sensitivity (response) of the Hall probe to moment contributions as a function of x , y , and z within the sample zone.

In the first calibration sequence, 99.5% pure nickel sheets of 0.5 mm, 1.0 mm, and 2.0 mm thickness were used to calibrate the $M-\mu_0H$ data from the measurements. The sheets were 1 cm wide and 3 cm long. Stacks of nickel sheets were formed and held together using GE Varnish as the adhesive to form test samples. The samples, so formed, allowed for the measurement of $M-\mu_0H$ as a function of thickness. Nickel thicknesses of 0.5, 1.0, 1.5, 2, 2.5, 3, and 3.5 mm were used. By comparing the measured field difference between the sample and no-sample cases, B_z , to the theoretical moment of the nickel ($M_{\text{sat}} = 0.64 \text{ T} = 0.64/(4 \times 3.14 \times 10^{-7}) \text{ A/m} = 509,554 \text{ A/m} = 509.5 \text{ kA/m} = 509.5 \text{ emu/cm}^3$) we were able to determine a constant that converted the B_z to m . However, given that the active area of the sensor is much smaller than the width and length of the sample, either a sample of an identical width and length must be used, or a sensitivity factor, γ_s , must be used. We can then define

$$B_z = C' \gamma_s m \quad (5.1)$$

or

$$m = B_z C' \gamma_s \quad (5.2)$$

A linear fit to the theoretical moment, but now in emu vs B_z , as mentioned above, gives the product $1/C' \gamma_s = C/\gamma_s = 4931.6 \text{ emu/T}$ as shown in **Figure 66**.

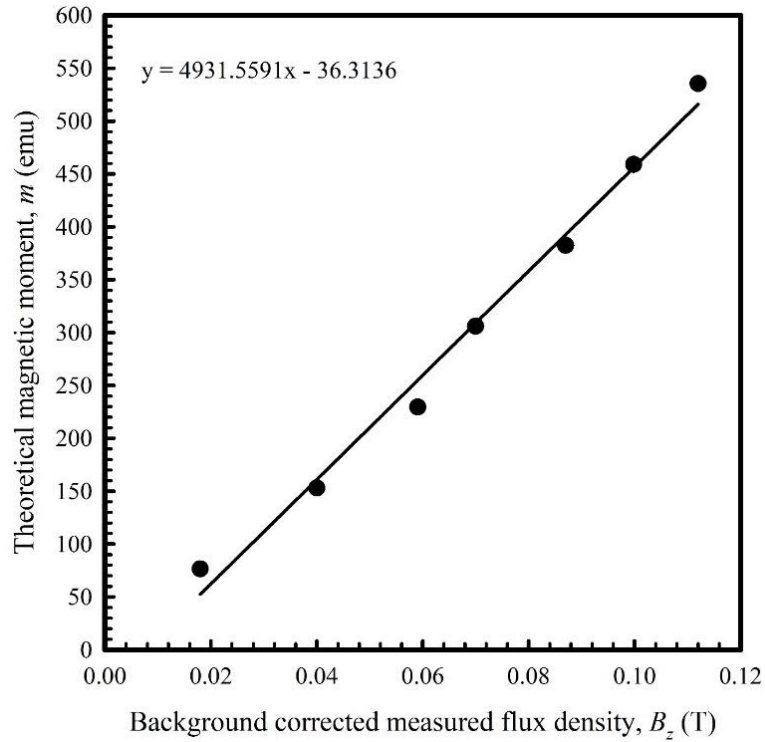


Figure 66. Plot of expected nickel magnetic moment vs measured background corrected magnetic flux density. A value of the constant which converts B_z to m is extracted by a linear fit to the data. Published in [103].

The linearity of B_z with m is shown in **Figure 66**, and since the nickel samples had the same length and width, it corresponds to samples extended further into the z -direction. The value for C' of course depends on distance from the sample to the sensor, which we chose to keep constant. Here γ_s is a dimensionless number between 0 and 1. It represents the sensitivity function, which is related to the fraction of the sample which is covered by the Hall probe active area. Because in this case our sample was not a direct shape replacement

for the nickel calibration samples, we needed to determine the shape factor. This determination was done using a flux exclusion calibration.

5.2.6. Flux Exclusion Calibration

The Meissner effect in superconductors results in full magnetic flux exclusion from the interior of a superconductor, if the applied magnetic field is lower than the lower critical field, B_{c1} . Therefore, assuming no demagnetization effects, $M = -H_a$ and the susceptibility, $\chi = -1$. Demagnetization effects can shift the local peak applied field values away from the far-field applied field values. For a round cylinder in a perpendicular applied field, such as the CORC[®] cable used here, the demagnetizing factor is 0.5, resulting in $M = -2H_a$ until the applied magnetic field reaches the B_{c1} . This fact can be used to scale the $M-\mu_0H$ results, and in conjunction with the Ni calibration, extract the value of the sensitivity function for the given sample shape. If we assume full flux exclusion from the CORC[®] cable during the initial ramp up of the applied magnetic field, the slope of the $M-\mu_0H$ curve should be -2. Making these assumptions, we find $\gamma_{\text{Ni-tape}}/\gamma_{\text{CORC}} = 0.1$, or $\gamma_{\text{CORC}} = 10\gamma_{\text{Ni-tape}}$ – that is, the sensitivity factor is 10 X greater in the region where the CORC[®] sample lies than that integrated over the region of the nickel calibration sample. This result makes sense given the active area of the Hall probe. The data below for CORC[®] magnetization and decay are plotted using this calibration.

5.3 CORC[®] Magnetization Results

CORC[®] Sample: A section was cut from a length of CORC[®] cable for magnetic measurements in OSU's Hall probe magnetometer system. The cable segment, provided by LBNL, was 2.7 cm in length and had a diameter of 3.09 mm. The Berkeley tape ID was 160823-Berkeley 250-C [3]. The average tape I_c was 69.5 A at 77 K, self-field. The cable had 16 tapes and the cable I_c was 4 kA at 4 K, self-field; the cable was used for the canted $\cos\theta$ dipole C0a. The sample specifications are given in **Table 15** [3].

Table 15. Parameters of the CORC[®] wire used for the present measurements, data from [3].

Cable Properties	
Wire OD (mm)	3.21
Cu Core OD (mm)	2.34
No. Tapes	16
Tape width (mm)	2
Cu plating thickness (μm)	5
Substrate thickness (μm)	5
Cable Pitch (mm)	6.2
Cable I_c (A)	700
Sample Properties	
Sample Length (cm)	2.7
V_{cable} (cm^3)	218
V_{strand} (cm^3)	76.1

The $M-\mu_0H$ of the CORC[®] cable sample was measured at 4.2 K with a maximum applied field sweep of ± 4.5 T. The hysteresis curve is shown in **Figure 67**. Here the magnetic moment is normalized by the total cable volume. The magnetization per unit volume of strand can be calculated by multiplying this magnetization by 2.86 (see **Table 15**, total volume of cable [V_{cable}]/total volume of tape [V_{strand}] = 2.86). The results of a second measurement are shown in **Figure 68**. In this case the $M-\mu_0H$ is asymmetric, with the measurement starting (ZFC) at $B = 0$, then going to a maximum applied field of 8 T, followed by a ramp to -2 T and finally a rise back to 8 T.

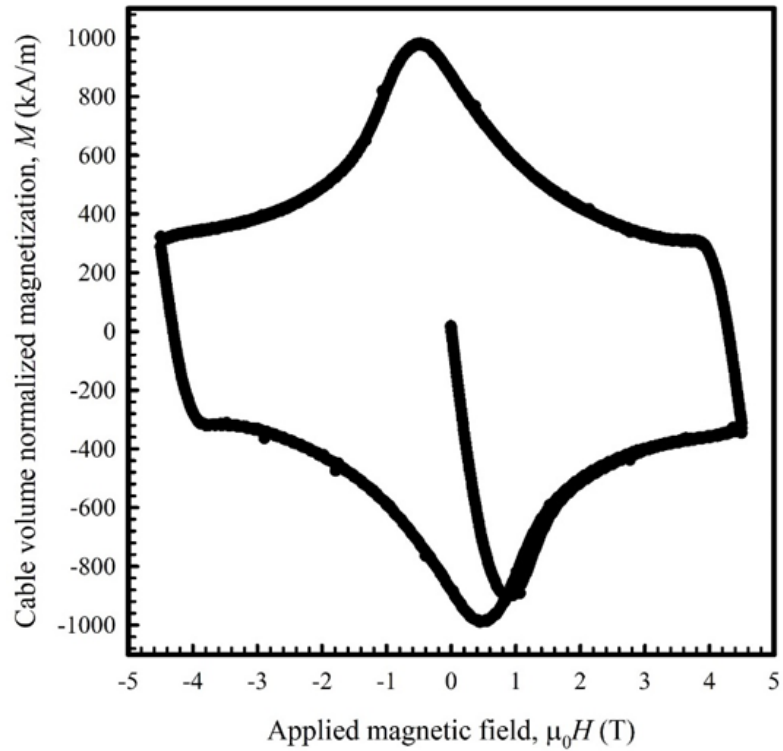


Figure 67. The 4.5 T M - $\mu_0 H$ loop of the CORC[®] cable sample. The moment has been normalized to the cable volume. Published in [103].

It is seen in **Figure 67** and **Figure 68** that $B_p = 1$ T with a corresponding magnetization at full flux penetration, M_p , of 900 kA/m. Assuming a typical accelerator magnet injection field of 1 T, M_p could be identified as M_{inj} . These results are of interest in that it seems that M_{inj} could be easily modified by suitable selection of the pre-injection cycle.

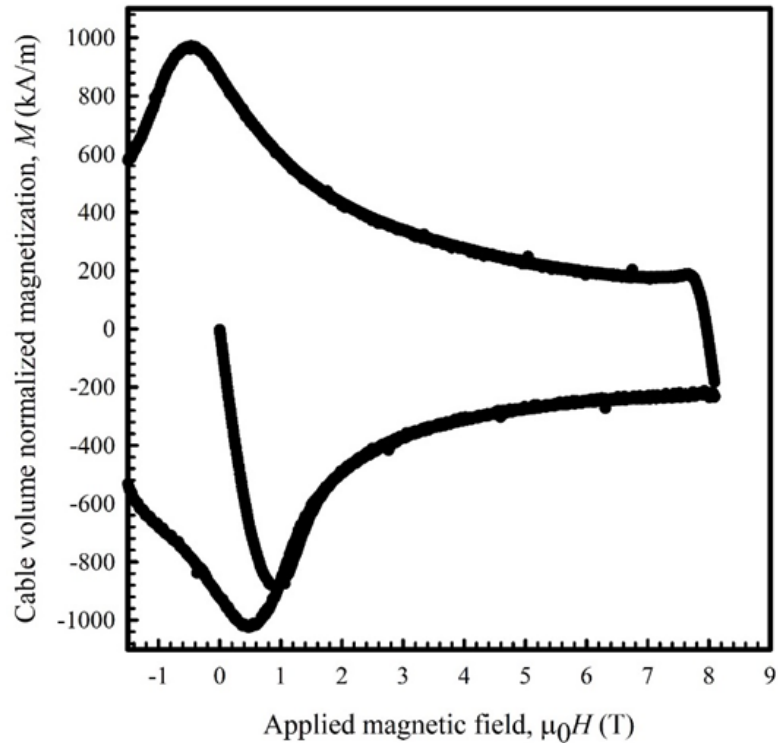


Figure 68. The 8 T M - $\mu_0 H$ loop of the CORC[®] cable sample. The moment has been normalized to the cable volume. Published in [103].

We can compare the magnetization of the cable to the magnetization expected by well-known rules for its constituent tapes. The measured I_c of the cable at 4.2 K is 4.1 kA (somewhat below short sample expectation [3]). Using Graph A1 from [3], we estimate that the tape $I_c = 690$ A per tape (0.04 mm thick, 2 mm wide, gives $J_e = 690/0.08 \text{ mm}^2 = 7666 \text{ A/mm}^2 = 7.66 \times 10^9 \text{ A/m}^2$) at 4 K in self-field. Then $M = J_c a/2 = J_c w/4 = 7.66 \times 10^9 \text{ A/m}^2 * 0.5 * 10^{-3} \text{ m} = 3833 \text{ kA/m}$. Here we should apply a factor to account for the twist of the strand in the helical shape, which is $2/\pi$ for large pitch values, leading to a twist corrected value for the CORC[®] magnetization of 2440 kA/m. This value should be

compared to the magnetization of the CORC[®] cable at zero field ($\cong 1000$ kA/m) but normalized by the strand, rather than the cable volume. We can see from **Table 15** that this increases M by a factor of 2.86 ($V_{\text{cable}}/V_{\text{strand}}$), and now $M = 2860$ kA/m. Thus, the prediction of the magnetization of a CORC[®] cable from its underlying tape is 17% in error, a value not too large given the approximations and assumptions made. Nevertheless, it is useful to have the more accurate direct measurements.

The measured M - $\mu_0 H$ of the cable and the calculations for the expected magnetization from its constituent tapes can be compared to direct measurements of M - $\mu_0 H$ performed on tape samples extracted from the CORC[®] cable. The result of this measurement, performed at 4 K, is shown in **Figure 69**. Also shown in the figure is the M - $\mu_0 H$ of the CORC[®] cable, but now the moment is normalized to the total volume of tape in the cable, rather than the cable volume. The value of the tape volume normalized magnetization, at 0 T, of the tape extracted from the CORC[®] cable is 3451 kA/m, which is about 18.5% higher than that of CORC[®] cable.

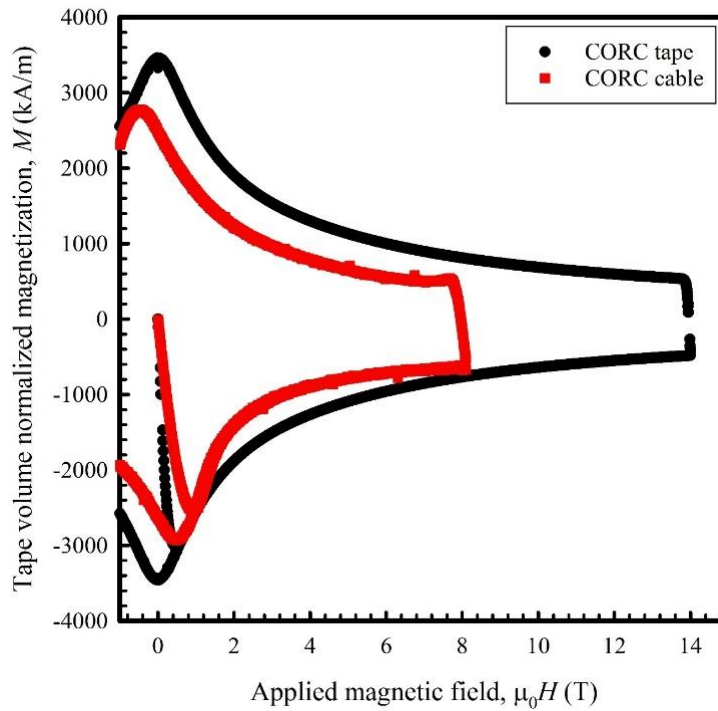


Figure 69. The 4 K M - $\mu_0 H$ loops of the CORC[®] cable sample and a tape extracted from the sample. The magnetic moment has been normalized to the total volume of tape.

The penetration field (B_p) of the CORC[®] cable is about 1 T. For the individual tapes, $B_p = 0.5$ T, a factor of 2 X smaller. This value of B_p is in fact very important, since it determines the penetration state of the cable at injection. If B_{inj} is less than B_p , modifications to the pre-injection cycle will strongly influence M_{inj} .

It is of interest to see how these results might be expected to influence the field errors of a magnet built from the cable. However, the field error will depend on the details of the magnet, including not only its basic form, for example $\cos\theta$ dipole, block dipole, or

canted $\cos\theta$ dipole, but also the details of the design and the value of field expected (assuming it is an insert). Nevertheless, it is useful to consider the result of simply “replacing” a NbTi or Nb₃Sn winding with an HTS cable. Taking the LHC as a reference, we note that the numerous measurements of b_3 which have been made on LHC “prototype” and “pre-series” dipoles [104-109] have yielded values ranging from -12 to +12, -6 to +6. If we take, for example, $b_3 = 3$, we can associate this with the shielding magnetization of an LHC-inner NbTi cable at 1.9 K, 0.54 T, viz. $M_{\text{h,cable},1.9\text{K},0.54\text{T}} = 10.3$ kA/m [110]. Nb₃Sn strands have an effective filament diameter (and thus magnetization) nearly 10 X that of NbTi, and thus a b_3 that can reach nearly 10 X higher as well (depending on magnet design) – about 30-40 units. For this HTS cable, $M_{\text{inj}} \cong 900$ kA/m, suggesting associated b_3 values of about 300 units for a direct replacement (the current density at collision is roughly similar for these cables at their point of operation, so no correction is added for that). This is a very simple and rough estimate and assumes no changes in the magnet to minimize these effects. However, it is a useful starting point when considering the application of HTS cable in dipole-insert designs.

5.4. Modifying the Field Cycle to Modify the Magnetization of CORC[®] Cable

The current in an accelerator magnet is often cycled by ramping first to a modest field at which particles can be injected, “the injection field”, B_{inj} , and then holding for a time to accumulate particles, perhaps 20 minutes or so. Once sufficient particle beam density is achieved, the field is ramped to the field at which the particles are collided (the

collision field), at which point the particles are collided and data is taken. Subsequently, the field is ramped back down to start the process over again. Typically, the field is taken down to zero or some minimum field, B_h , after which it is increased to injection again, and new particles are accumulated, and the cyclic process continues. Ramping the current in this way generates a field in the windings, and this leads to a magnetization state of the superconductor. Generally, reducing the magnetization of the windings is desirable because the spatial field errors due to the persistent current magnetization in the windings should be reduced accordingly. It is well known that cycling the magnetic field that is applied to a superconductor can reduce the magnetization of the superconductor at a given target field. This reduction is possible because, although the $M-H$ loop is hysteretic, and the magnetization reaches a saturation value with a sufficiently large field excursion (either positive or negative depending on field sweep direction), a partial field excursion can stop the magnetization mid-way between the symmetric positive and negative saturation values, i.e., zero. A systematic study of the effect of various field excursion ramps on the residual magnetization at a given target field (meant as a stand-in for B_{inj}) was undertaken and is described below.

Let us choose a nominal 1 T as our B_{inj} . The applied magnetic field was ramped in such a way so as to mimic the pre-injection cycle of a particle accelerator, but with the goal of determining if the magnetization can be reduced by using different cycles. The hypothetical pre-injection cycle of the particle accelerator is as follows: (1) ramp up from 0 T to B_{max} . In this case, $B_{max} = 4.5$ T was used; the specific field is not important if it is

more than $2B_p$ above the injection field. (2) ramp the field down to a “hold” field, B_h , which is less than B_{inj} and perhaps 0. (3) ramp from B_h to B_{inj} , which was 1 T in this case. The magnetization of the sample at B_{inj} is the hypothetical injection magnetization, M_{inj} of the sample. The chosen hold fields (B_h) were: 0, 0.2, 0.4, 0.6, and 0.8 T. The magnetization loops formed using these different B_h s are shown in **Figure 70**.

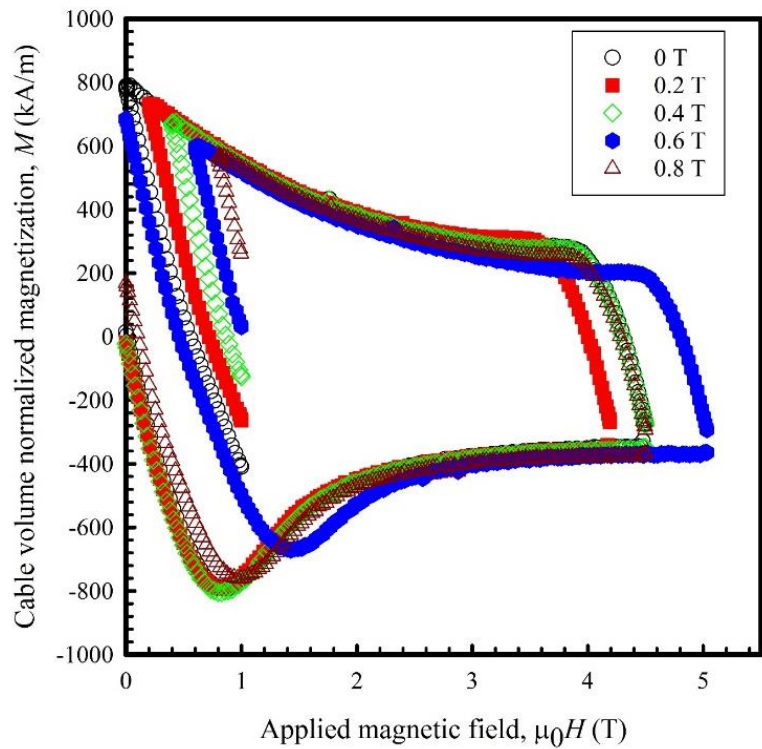


Figure 70. The M - μ_0H loops of the CORC[®] sample measured during various field cycles (“pre-injection cycles”). The moment has been normalized to the cable volume. Published in [111].

We can clearly see in **Figure 70** that M_{inj} is affected by the value chosen for B_h . Generally, as the value of B_h gets closer to B_{inj} , M_{inj} is reduced. An explanation for these

results is as follows. The flux density gradient in the superconductor is modified in the different cycles. This modification can be visualized in **Figure 71** where we show Bean critical state profiles (from [112]). Points 1 and 2 represent the flux density across the sample (modelled in this case as a semi-infinite slab of thickness $2a$) during the first field excursion from a virgin state. Point $\mu_0 H_p$ represents full penetration. Point 3 represents a field above B_p , but below collision. Point 4 represents the beginning of a down-ramp after collision, point 5 is a state somewhat further on, and point 6 is B_h (in this case $B_h = 0$). Inverting the constitutive equation for magnetic fields, $M = (B - \mu_0 H) / \mu_0$, or to put it graphically, the magnetization is proportional to the area defined by the difference between the applied field $\mu_0 H_a$ (taken as constant within the sample and equal to the applied field), and the average local B . The point of field penetration, $\mu_0 H_p$ is shown by the horizontal dotted line, the internal B by the solid line, and M is proportional to the triangular area defined by them. To fully reverse the magnetization in the superconductor, the field must be reversed by a value of at least $2B_p$. By reversing the field less than this a flux density gradient is introduced into the superconductor which leads to a reduced overall magnetization. In graphical terms, we can choose a field excursion so that equal positive and negative areas are generated, and the resultant magnetization is zero. We can achieve this if, from Point 6, we try to return to Point 3 in a second cycle.

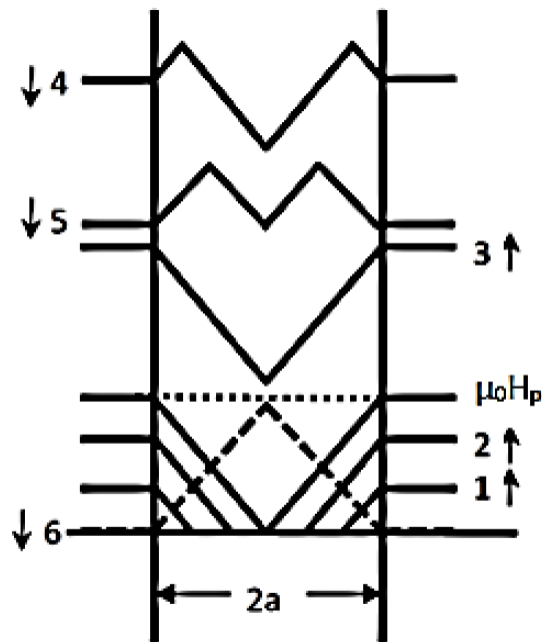


Figure 71. Bean critical state profiles, from [112].

5.5 Temporal Change of Magnetization (Magnetization Decay/Creep of CORC[®] Cable)

When taking the data for **Figure 70**, we also, as part of the experimental runs, took magnetization decay data. For each run, after reaching 1 T (the hypothetical B_{inj}), the magnetic flux density given by the Hall effect sensor was recorded every second for at least 1200 s to monitor the temporal change in the magnetization. 1200 s corresponds to the duration of a typical 20-minute injection plateau phase. The results of these measurements are shown in **Figure 72**.

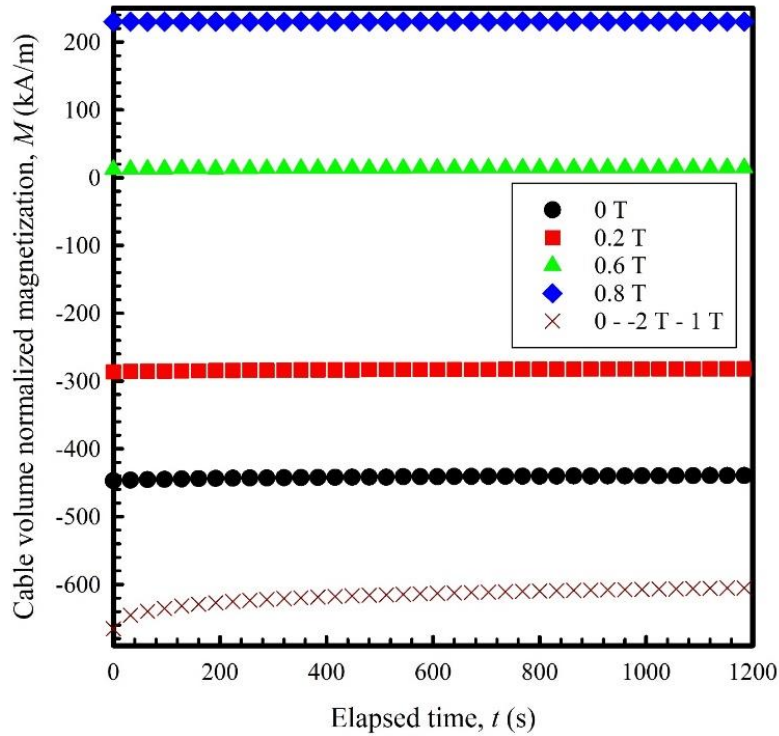


Figure 72. Magnetization decay in the CORC[®] sample at 1 T applied field after different hold fields. The moment has been normalized to the cable volume. Published in [111].

The magnetization when the applied magnetic field just reaches 1 T can be considered the initial magnetization, M_0 , for the so-called magnetization decay measurement. The change in the magnetization, ΔM_t vs M_0 over 1200 s is plotted in **Figure 73**. The values range from 0 – 690 kA/m for M_0 , and from about 0 – 54 kA/m for ΔM_t . $\Delta M_t/M_0$ varies, but it can be as high as 0.1 (10%). It is evident from the results that a lower M_0 results leads to a lower ΔM_t . Therefore, not only does adequate selection of B_h reduce M_{inj} , but it also reduces the temporal change in the magnetization. The results of the measurements on the tape sample and the CORC[®] sample are presented in **Table 16**.

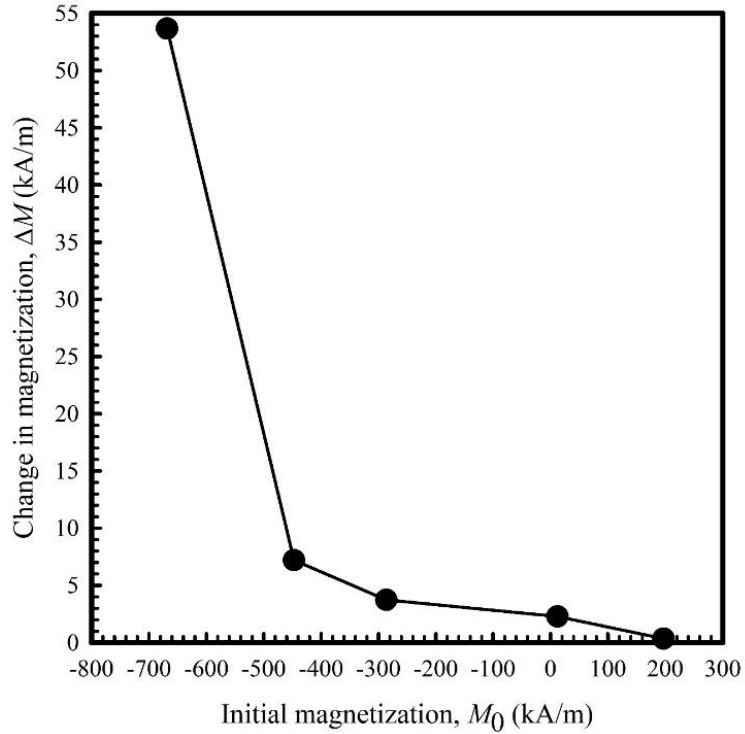


Figure 73. Absolute change in magnetization of CORC[®] cable sample, over 1200 s, at different initial magnetizations. The moment has been normalized to the cable volume. Published in [111].

The reduced absolute magnetic flux creep (reduced ΔM) at lower M_0 is expected according to the equation for the change of the magnetization due to flux creep: $M = M_0[1 - r \ln(t/\tau)]$, where r is the creep rate, τ^{-1} is a characteristic attempt frequency, and M_0 is the initial magnetization. A lower M_0 should lead to a lower M , after the same elapsed time, t . In addition to this, different regions of the sample have opposing flux gradients, from which we expect even further creep rate reduction.

Table 16. Initial magnetization and change in magnetization (ΔM) of the 2G HTS tape and the CORC[®] cable sample. Published in [111].

Sample type and hold field	$-M_0$ (kA/m)	ΔM (kA/m)
Tape 0.76 T	260	12
Tape 0.84 T	230	9.8
Tape 0.88 T	180	6.2
Tape 0.92 T	120	4.0
Tape 0.96 T	32	1.5
CORC [®] 0 T	430	7.2
CORC [®] 0.2 T	280	3.7
CORC [®] 0.6 T	19	2.3
CORC [®] 0.8 T	180	0.35

5.6. Comparison with another Tape Sample

It is of interest to know how the magnetization (and its decay) of the magnet relevant CORC[®] cable sample compares to that of a single short tape sample. A 3.1 x 2.3 mm tape sample (2G HTS tape) was cut from a spool of 4 mm wide, 0.12 mm thick REBCO-based 2G HTS tape, which has 40 μm of copper plating on the top and bottom, for magnetic hysteresis and magnetization decay measurements. The nominal critical current (I_c) of the tape is 100 A, per 4 mm width, at 77 K, self-field. The $M-\mu_0 H$ was measured in applied magnetic fields of +/- 14 T and the decay was measured at 1 T for a time interval of 1200 s. The results of the $M-\mu_0 H$ measurement are shown in **Figure 74**. The magnetic moment has been normalized to the total tape volume.

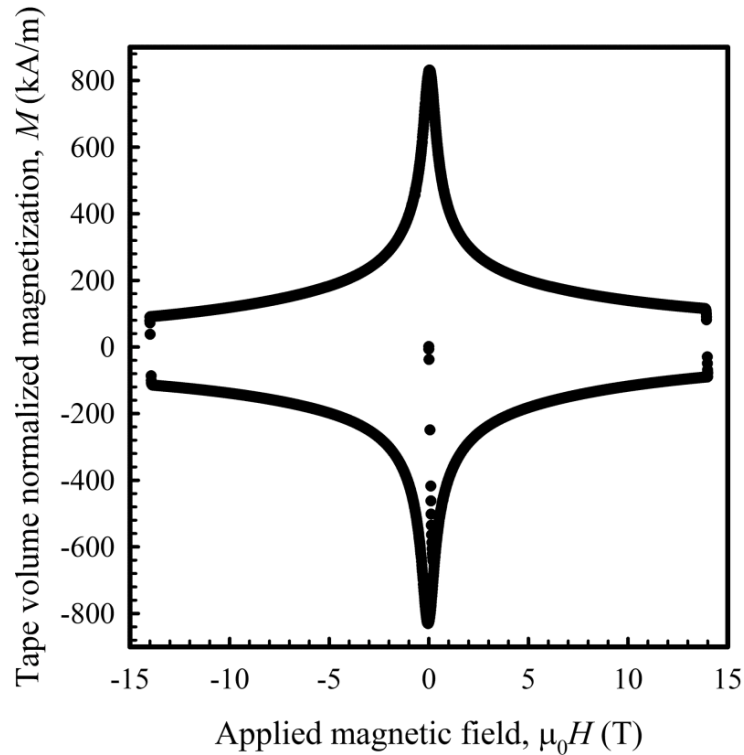


Figure 74. The 14 T M - μ_0H loop of the 2G HTS tape. The moment has been normalized to the tape volume. Published in [111].

The results of the measurement show that the magnetic penetration field, B_p , of the tape sample is approximately 0.3 T, which is about 1/3 that of the CORC[®] sample. The maximum magnetization is about 830 kA/m, which is about 19% lower than that of the maximum CORC[®] sample magnetization, but the magnetic moment of the CORC[®] sample is normalized to the cable volume rather than the tape volume.

The results of the magnetic decay measurements are shown in **Figure 75**. The change in the absolute magnetization of the tape, over 1200 s, at different initial magnetizations is shown in **Figure 76**. The data is presented in tabular form, alongside the

CORC[®] cable data, in **Table 16**. Like the CORC[®] cable magnetization decay measurement results, the magnetization change in the tape appears to be smaller as the initial magnetization is decreased. ΔM_t ranges up to 12 kA/m, and M_{inj} ranges up to 260 kA/m, for B_h values of 0.76 T (or lower), but as B_h approaches B_{inj} , both are reduced. These results are for a short, finite length, tape sample. Further analysis considering how these results may be scaled to represent those of infinitely long samples is discussed in section 5.11. In that section, a comparison of the magnetization (and its decay) of the CORC[®] cable sample and the magnetization of the tape sample to the magnetization of present day LTS composites is also made and the results are discussed.

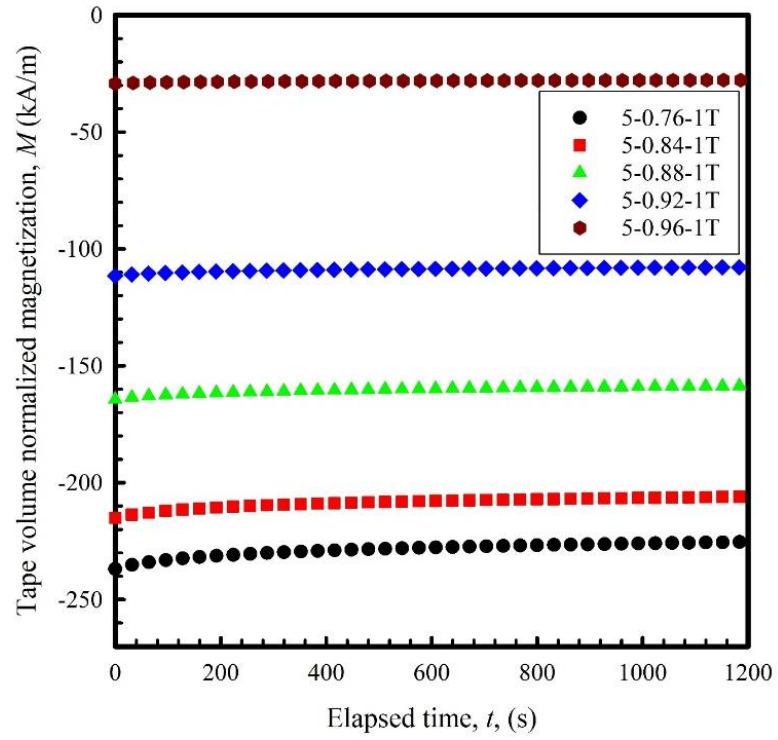


Figure 75. Magnetization decay of the 2G HTS tape at 1 T applied magnetic field after different hold fields. The moment has been normalized to the tape volume. Published in [111].

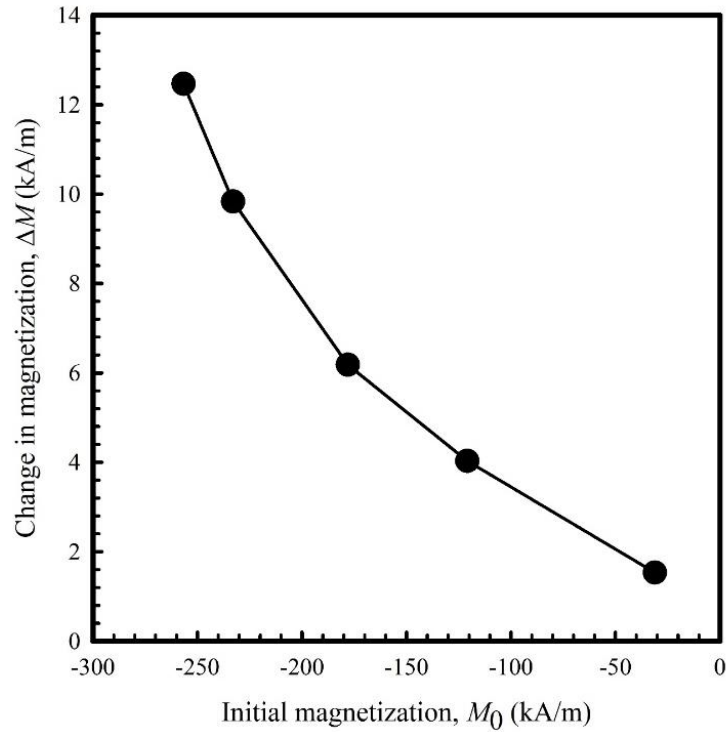


Figure 76. The absolute change in the magnetization of the 2G HTS YBCO tape, over 1200 s, at different initial magnetizations. The moment has been normalized to the tape volume. Published in [111].

5.7. Bi:2212 Rutherford cables

Rutherford cables were developed at the Rutherford Appleton Laboratory in the 1920s and have been used to build superconducting magnets since the 1970s [113]. The strands of superconductor composite are wound into a flat cable which is shaped using a powered Turks head roller. The cables provide high packing factor, good ability to be wound, good control of dimensions, and good stability. Most Rutherford cables are NbTi

or Nb₃Sn composite based, but this geometry is also the relevant one for Bi:2212 round wire composites; an image of a Bi:2212 Rutherford cable structure is shown in **Figure 77**.

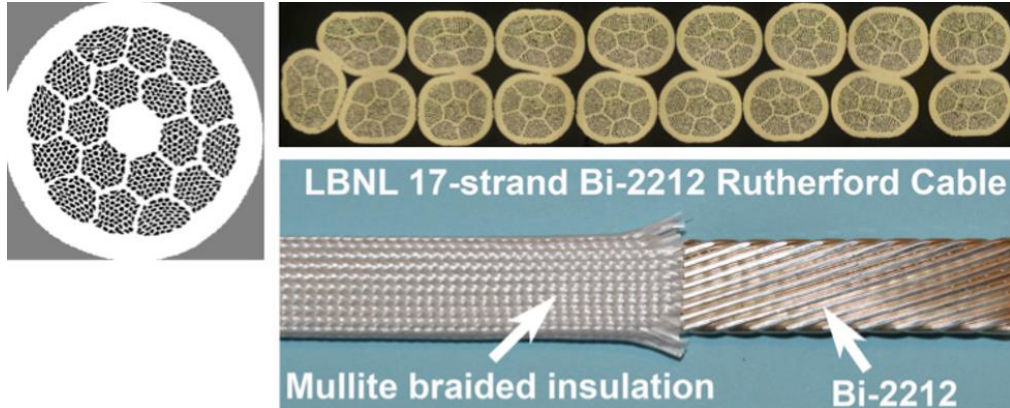


Figure 77. Rutherford cable (bottom right) with cross-sectional image of the different superconducting strands (top right) and a cross-sectional image of an individual strand (top left). See [2] for more strand details.

5.8. Bi:2212 Rutherford Cable Results

Similar magnetic measurements to those performed on the CORC[®] cable sample (presented above) were performed on a Bi:2212 Rutherford cable section extracted from a Bi:2212-based sub-size racetrack coil made by Lawrence Berkeley National Lab (LBNL). Details on the coil performance are provided in [91]. The Rutherford cables, with dimensions 1.46 mm x 7.8 mm and having a twist pitch of 50.8 mm, used to make the coil were made from Bruker OST PMM170123 non-twisted wire. Samples were cut such that two (out of the 6 which comprised the coil) cables were extracted for measurement. The

cables were embedded in epoxy. The extracted sample size is 3 mm x 10 mm x 30 mm. Like the measurements performed on the CORC[®] sample, a 12 T Hall probe system was used to perform the measurements. The sample was mounted perpendicular to the applied magnetic field direction, flat against a Hall sensor, in the manner described in [103]. The measurements were conducted at approximately 4 K with the sample submerged in liquid helium. Field sweeps of 0 → 8 → 2 → 8 T were conducted along with a series of sweeps of 0 → 2.5 → x → 1 T, where x is each of 0, 0.25, 0.75, and 0.85 T, to examine the effects of different pre-injection cycles on the magnetization at injection. As above, background measurements in the absence of a sample were also collected in order to subtract the magnetization behavior of the surroundings and the probe from the total magnetization measured by the Hall sensor.

In this case, the background $M-\mu_0H$, was fitted using the curve fitting tool in Matlab. A spline fit with a “smoothing parameter” of 0.999 was found to closely approximate the background curve without over-fitting to noise and artifacts. Some noise spikes were observed which do not pertain to the magnetization phenomenon studied here, so points which deviate by more than 3σ from the spline curve were removed. The background-subtracted data obtained in this way was calibrated using two methods: 1) Susceptibility and 2) Nickel calibration.

5.8.1 Calibrations of Bi:2212 Cable Sample Measurements using Susceptibility

The uncalibrated magnetization of the Bi:2212 Rutherford cable sample at $\mu_0 H = 0$ T is obtained by subtracting the spline fit of the background from the spline fit of the sample data. The magnetization at $\mu_0 H = 0$ T on the first down ramp of the magnetic field is 0.0202 T, and it is -0.0201 T on the second up ramp. Therefore, the width of the hysteresis loop at 0 T is $\mu_0 M = 0.0403$ T. The full flux exclusion calibration outlined in Section 5.3.7 can be used also for the Bi:2212 Rutherford cable measurements. The magnetic susceptibility, χ , of a superconducting cylinder in a magnetic field applied perpendicular to the cylinder's long axis is -2. (Note that the demagnetization factor is $\frac{1}{2}$.) This number can be used to obtain a scaling factor for the uncalibrated data using the slope of the uncalibrated M - $\mu_0 H$ curve. This slope is presented in **Figure 78**.

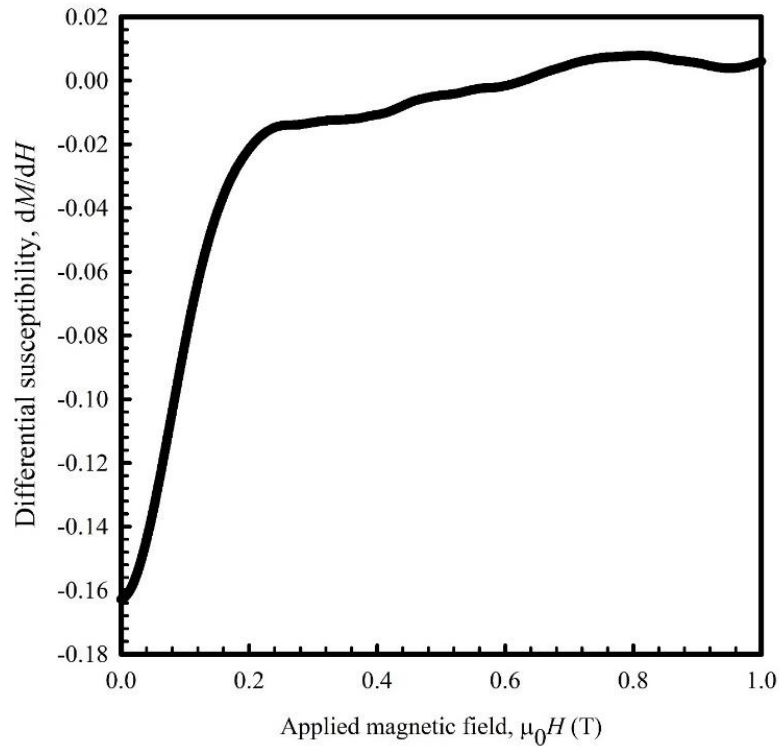


Figure 78. A plot of the derivative of the fit for the initial ramp-up of the 8 T M - μ_0H loop. The susceptibility at 0 T is -0.1628.

At 0 T, χ of the uncalibrated data is -0.1628. Therefore, the uncalibrated data should be scaled by $-2/-0.1628 = 12.285012$ to obtain the calibrated sample magnetization. Thus, the corrected width of the hysteresis loop at 0 T is $\mu_0M = 12.285012 \times 0.0403 \text{ T} = 0.495086 \text{ T}$.

The magnetization is then $\Delta M = \frac{0.495086}{4 \times 10^{-7}} = 3.94 \times 10^5 \text{ A/m} = 394 \text{ kA/m}$. The magnetic hysteresis curves generated using this method to calibrate the data are shown in **Figure 79** and **Figure 80**.

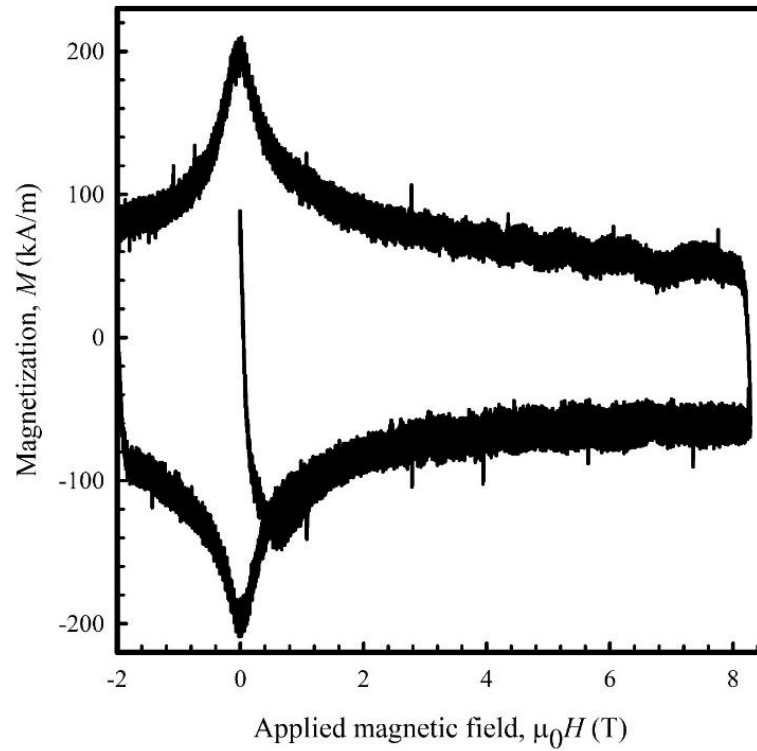


Figure 79. A plot of the 8 T M - $\mu_0 H$ loop, with no-sample background subtracted, multiplied by a susceptibility determined calibration factor to obtain the magnetization in kA/m. The moment is normalized to the sample volume.

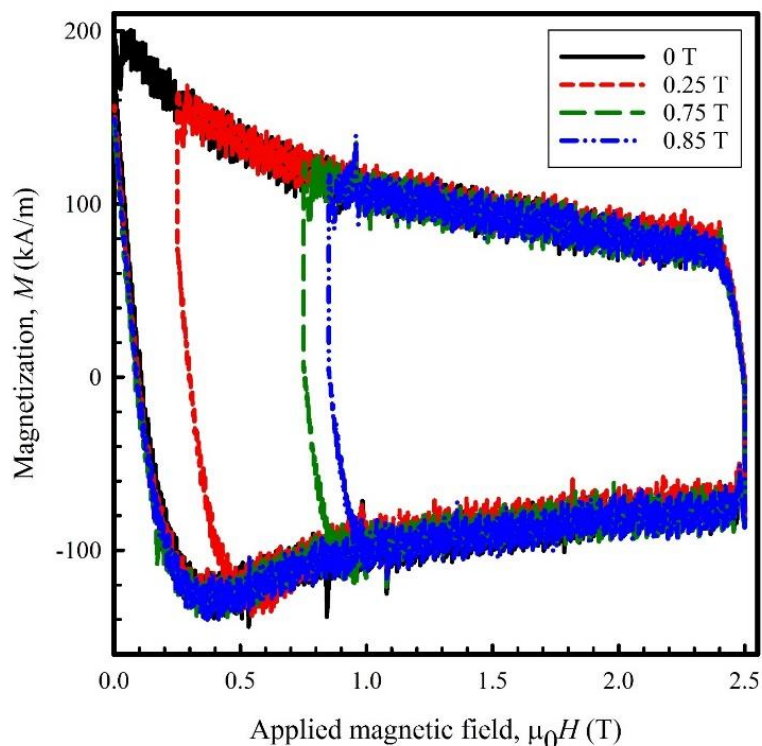


Figure 80. A plot of the $0 \rightarrow 2.5 \rightarrow x \rightarrow 1$ T M - $\mu_0 H$ loops, with no-sample background subtracted, multiplied by a susceptibility determined calibration factor to obtain the magnetization in kA/m. The moment is normalized to the sample volume.

5.8.2 Calibration of Bi:2212 Cable Sample Measurements using Nickel Standards

The second calibration technique we used is a sample replacement method. A piece of nickel (99.5% purity) 2 mm x 29 mm x 8 mm, with a volume of 464 mm³ or 0.464 cm³, was used as a standard. By comparison, the studied Bi:2212 Rutherford cable sample cut from RC5 has dimensions 3.5 mm x 30 mm x 8 mm, with a volume of 0.84 cm³. The uncalibrated, background-subtracted nickel magnetization at saturation ($\mu_0 M_{\text{sat}}$) is 0.06 T. Using the method outlined in the CORC[®] section (and in [103]), the theoretical magnetic

moment for a nickel sample of this volume can be compared to the measured magnetic flux. The theoretical nickel magnetization at saturation is $0.64 \text{ T}/\mu_0 = 509.5 \text{ emu/cm}^3$. For a 0.464 cm^3 sample, the expected magnetic moment should be 236 emu. Compared with the measured flux of 0.06 T, this yields a calibration of 3933 emu/T.

Since $\mu_0 M$, measured at $\mu_0 H = 0 \text{ T}$ on the down ramp of the hysteresis loop, is 0.0202 T, the magnetic moment of the Rutherford cable sample at this field is calculated by $m = \mu_0 M_{\text{sample}} \times C = 0.0202 \text{ T} \times 3933 \text{ emu/T} = 79.45 \text{ emu}$. The superconductor volume normalized magnetization will be calculated. The after-reaction strand diameter was 0.78 mm and the Bi:2212 occupied 20% of the strand cross-section after reaction. There are 2 cables in the sample and each cable has 17 strands. Therefore, the volume of superconductor in the sample is $= \pi(0.39^2) \cdot 0.2 \cdot 17 \cdot 2 \cdot 30 = 97.5 \text{ mm}^3 = 0.0975 \text{ cm}^3$. Then, $M = 79.45/0.0975 = 1045 \text{ kA/m}$. The magnetic hysteresis curves generated using this method to calibrate the data are shown in **Figure 81** and **Figure 82**. Note that the M - H loops of **Figure 81** and **Figure 82** are 5 X those of **Figure 79** and **Figure 80**, this is due to the fact that the moment in the former is normalized to sample volume, and the moment in the latter is normalized to superconductor volume, and the superconductor volume is 1/5 of the strand volume.

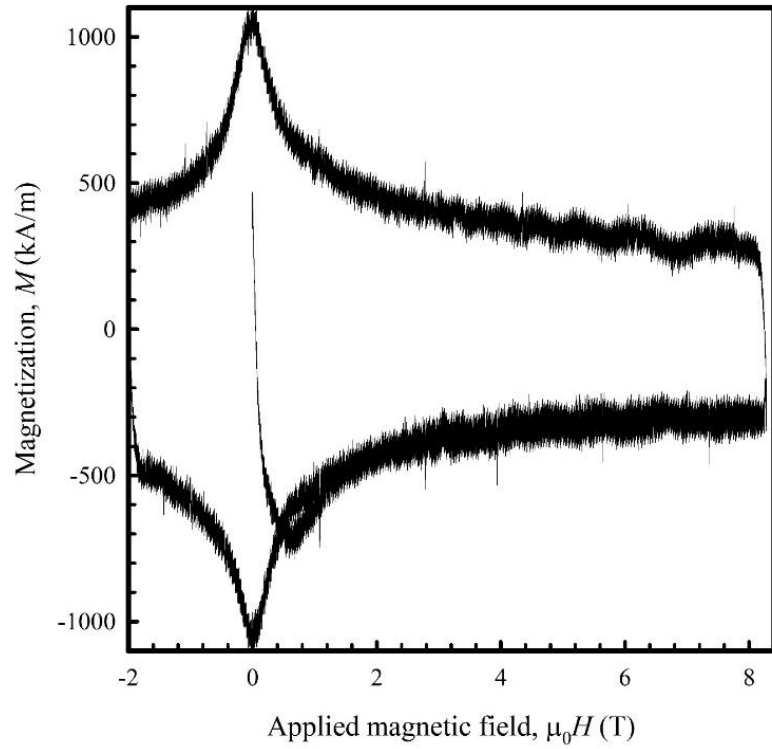


Figure 81. A plot of the 8 T M - $\mu_0 H$ loop, with no-sample background subtracted, multiplied by a nickel replacement calibration factor to obtain the magnetization in kA/m. The moment is normalized to the superconductor volume.

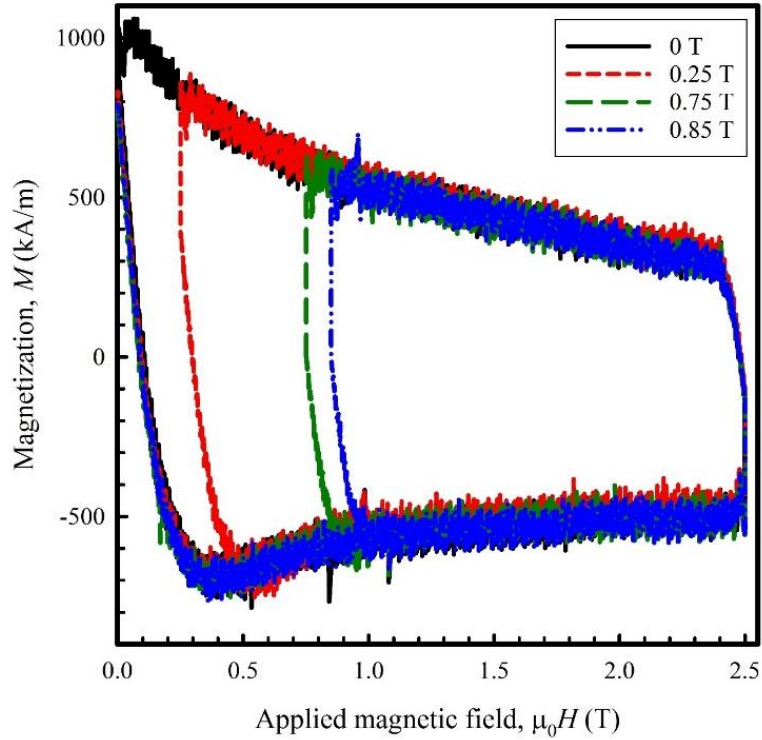


Figure 82. A plot of $0 \rightarrow 2.5 \rightarrow x \rightarrow 1$ T M - $\mu_0 H$ loops, with the no-sample background subtracted. Here x refers to a pre-injection field of 0, 0.25, 0.75, and 0.85 T. The moment is normalized to the superconductor volume.

5.9 Estimates of the Effective Filamentary Diameter (d_{eff}) of the Bi:2212 Composite

The effective filamentary diameter is an engineering parameter which estimates the diameter of the loop the supercurrents circulate to shield the composite. The expression for the magnetization of a fully filamentary composite containing cylindrical filaments, subjected to a magnetic field applied perpendicular to the cylinder's long axis is

$$\Delta M = \frac{4}{3\pi} J_c d, \quad (5.3)$$

where d is the radius of the cylindrical filament and J_c is the critical current density. In a few superconductors, the supercurrents can cross to neighboring filaments through an electrical connection, caused by, for example, interfilamentary bridging, which is seen in Bi:2212-based composites (as discussed in detail in Chapter 3). These connections allow the supercurrents to flow in loops that have radii larger than the filamentary radii and therefore shield more of the composite than simply the individual filaments. As the supercurrent loop area increases, the magnetic moment from the composite, and, therefore, the magnetization of the composite increases. Therefore, if d is evaluated using the measured J_c and ΔM of the sample, it will oftentimes be larger than the filamentary diameter. In this case the measured d is an effective filament diameter (d_{eff}), which measures the electrical connectivity of the filaments. d_{eff} is frequently used to assess the magnetization of the composite. If a large d_{eff} is measured, the magnetization of the composite is large, and any field errors from magnets built from the composite may be large.

Estimating d_{eff} of the Bi:2212 Composite Using the Susceptibility Calibration

Technique: The engineering critical current density, J_e , of the Bi:2212 Rutherford cable is 2000 A/mm² in a 4 T magnetic field applied perpendicular to the strand [91], and the after reaction Bi:2212 cross-sectional area fraction is 20%. Therefore, the J_c of the superconductor is approximately 10,000 A/mm². ΔM at 4 T is approximately 144 kA/m after the susceptibility calibration scaling factor was applied to the 8 T $M-\mu_0 H$ loop. We

must use the same area definitions to obtain d_{eff} , so here we use again the composite (or engineering J_c), obtaining $d_{\text{eff}} = \frac{3\pi}{4} \cdot \frac{1.44 \times 10^5}{2000} = 170 \text{ } \mu\text{m}$.

Estimating d_{eff} of The Bi:2212 Composite Using the Nickel Calibration Technique: ΔM

at 4 T is approximately 737 kA/m after the nickel substitution calibration scaling factor was applied to the 8 T $M-\mu_0 H$ loop. Therefore, $d_{\text{eff}} = \frac{3\pi}{4} \cdot \frac{7.37 \times 10^5}{10000} = 174 \text{ } \mu\text{m}$. Both d_{eff} values agree with one another and correspond well with the physical size of the subelement, as would be expected for untwisted strands.

5.10. Temporal Change of Magnetization (Magnetization Decay/Creep of Bi:2212 Cable)

After reaching 1 T (the hypothetical B_{inj}), the magnetic flux density given by the Hall effect sensor was recorded every second for at least 1500 s, a period of time similar to that of an injection phase in an accelerator magnet, to monitor the temporal change in the magnetization. The results of these measurements are shown in **Figure 83**. A surprisingly large change in the magnetic moment is observed. The moment decreased by about 40% when no hold field was applied. This decrease was reduced when 0.75 T and 0.85 T hold fields were applied, but it was increased with a 0.25 T hold field.

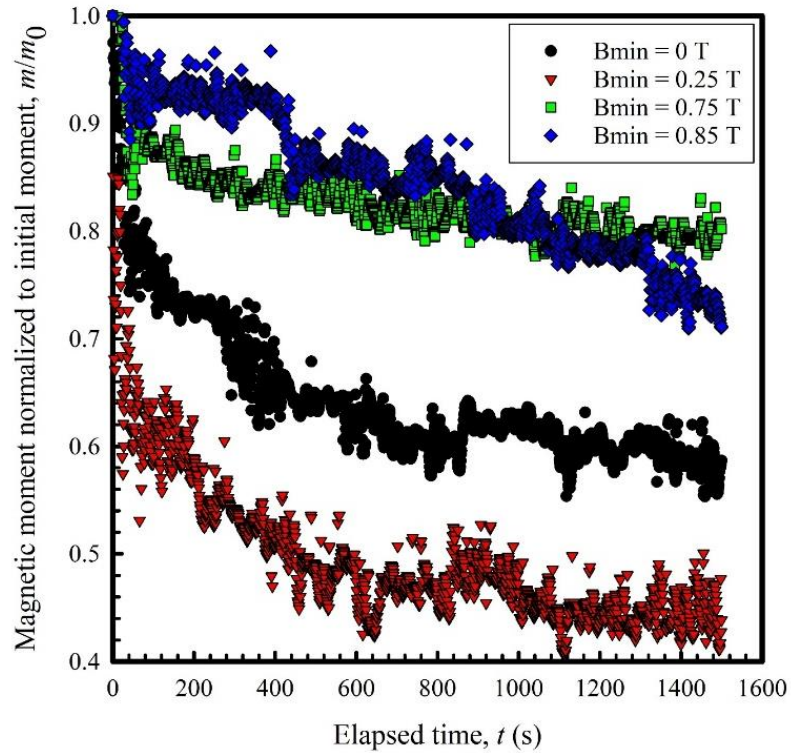


Figure 83. The temporal change in the normalized moment of the Bi:2212 Rutherford cable at 1 T, 4.2 K.

5.11. Comparison to Magnetization of Present-Day LTS Conductors

The magnetization of present-day NbTi-based round wire conductors is about 10 kA/m [110] at the injection field (B_{inj}) of 0.5 T used in the LHC. The magnetization of present-day Nb₃Sn round wire conductors is on the order of 100 kA/m [62, 63] at B_{inj} . The magnetization of the YBCO tape (2G HTS tape) sample at B_{inj} is about 400 kA/m at 1 T and about 500 kA/m at 0.5 T. Therefore, the YBCO tape M_{inj} is about 40-50 X that of the

NbTi and about 4-5 X that of the Nb₃Sn. In fact, this magnetization is that of a sample which has a finite length, which is given by [21, 22]

$$M = \left(\frac{J_c w}{8}\right) \left(1 - \frac{w}{3L}\right), \quad (5.4)$$

where w is the width of the sample and L is the length of the sample. As $L \rightarrow \infty$, the expression reduces to

$$M = \left(\frac{J_c w}{8}\right). \quad (5.5)$$

Therefore, the magnetization of a sample of finite length should be scaled by $(1-w/3L)$ to give that of an infinitely long sample. The samples used to make electromagnets will have $L \gg w$ in general. Therefore, if the sample dimensions are substituted into the expression for the short sample, an estimation can be made for the magnetization of samples which have $L \gg w$. The result of performing the substitution for the tape sample gives

$$M_{\text{short}} = M_{\text{long}} \left(1 - \frac{2}{9}\right), \quad (5.6)$$

which simplifies to

$$M_{\text{short}} = M_{\text{long}} \left(\frac{7}{18}\right). \quad (5.7)$$

Therefore, the magnetization of a long, full width sample would be $(18/7) = 2.6$ times larger than that of the measured small tape sample. Multiplying the M_{inj} values by this factor gives a new M_{inj} which is about 1300 kA/m if 0.5 T is B_{inj} and about 1000 kA/m if 1 T is B_{inj} . Multiplying the ΔM_t values by the factor gives a maximum ΔM_t of 32 kA/m.

The scaled M_{inj} is about 70 X that of the magnetization of NbTi strand used in the LHC at the injection field of 0.5 T and about 7 X that of the Nb₃Sn strand at 1 T. The scaled ΔM_t is about 3 X the magnetization of the LHC NbTi strand and about 1/3 that of the Nb₃Sn strand. In other words, the creep (or change) in the magnetization at injection for HTS might be 3 X larger than the total magnetization of the NbTi strands they would “replace”.

Beyond these two results, two important things about the magnetization emerge. First, $\Delta M_t/M_0 \sim 0.05$, or 5%. Secondly, both M_0 and ΔM_t are reduced by modifying the field (“pre-injection”) cycle. The magnetization influences the field error, and a changing magnetization may cause a change in the field error, which may require active correction techniques. Because the field cycling reduces the magnetization and its decay, it may reduce both the field error and any drift in it due to the magnetization. The magnetization of the CORC[®] cable sample is about 70 X that of the LHC NbTi and about 7 X that of Nb₃Sn strand at the expected B_{inj} . The decay of the magnetization is about 5 X the magnetization of LHC NbTi and about 1/2 X that of Nb₃Sn strand at the expected B_{inj} .

5.12 Conclusion

The $M-\mu_0 H$ of a CORC[®] cable has been measured using a Hall probe magnetometer at 4.2 K, with field sweeps of ± 4.5 T and a $0 \rightarrow 8 \rightarrow -2 \text{ T} \rightarrow 8 \text{ T}$ loop. The penetration field, B_p , of the CORC[®] cable was 1 T, corresponding to a penetration field magnetization, M_p , of 900 kA/m. This result is of interest, as this is approximately the injection field expected for future high-field accelerators. Assuming this injection field, if this cable were

to be used as a direct drop-in replacement for a NbTi LHC magnet (with $M_{inj,NbTi} = 10.3$ kA/m, $b_3 \sim 3$ units) its b_3 would be close to 300 units, which is well above the desired ~ 1 unit. Of course, used as an insert, the HTS contribution to the total magnet b_3 would be proportionately smaller. The large B_p is important to recognize when cycling the magnetic field of an accelerator magnet because a larger field sweep range will be necessary to reset the magnetization of the magnet.

Cabling of the REBCO tapes into the CORC[®] structure reduced the magnetization (normalized to total tape volume) of the composite compared to that of a short section of tape. Whereas this should reduce the field errors, the magnetization of the CORC[®] is still approximately 7 X that of Nb₃Sn composites and approximately 70 X that of NbTi composites. Both the initial magnetization and its decay was shown to be reduced significantly by appropriate cycling of the applied magnetic field. At similar initial magnetizations, the magnetization decay was faster in the tape sample, indicating that perhaps the geometry or different material in the tape influence the decay.

Measurements were also made for Bi:2212 Rutherford cables. The magnetization values here were more like those of Nb₃Sn strands and cables and corresponded more closely to measurements made on single strands, as long as, as detailed in chapter 3, those measurements were made on sufficiently long strands. Effective filamentary diameter values were extracted for the strands and corresponded to the subelement diameters, consistent with expectation.

Chapter 6: Effects of Magnetization and Creep on Magnetic Field Error in HTS Accelerator Magnets

6.1 Introduction

Future high-energy accelerators will require dipole fields greater than 16 T. Dipole magnets that generate such high fields will need high-temperature superconductors that carry high current density at 4 K and in applied magnetic fields of 16 T or greater. Both Bi:2212 and REBCO-based conductors are strong candidates for enabling future dipole fields above 16 – 20 T, and the United States Magnet Development Program (USMDP) is emphasizing the development of HTS accelerator technology.

A driving question for HTS-based accelerator magnets is, How much is the field quality of the accelerator magnets degraded by the relatively large magnetization of the HTS? There are strict requirements on the magnetic field quality of a superconducting accelerator magnet so that the particle beam stays focused and in the correct orbit. The persistent-current magnetization that occurs in the superconducting composite during the magnetic field ramp in accelerator magnets causes field errors in the aperture of the magnet [6]. Field quality is a concern especially at lower fields, such as the injection field, when the magnetization of the composite is large. Persistent-current magnetization is a big concern for HTS-based accelerator magnets because the magnetization can be at least an

order of magnitude greater than the magnetization of Nb₃Sn round wire composites. The d_{eff} of HTS-based conductors is at least an order of magnitude greater than the d_{eff} of Nb₃Sn-based round wire composites. This fact implies that the magnetization of the HTS-based composites is at least an order of magnitude larger than the LTS-based round wire composites because $d_{\text{eff}} \propto M$. It is important to know what the field quality in HTS-based accelerator magnets/hybrid magnets is, and it might be assumed that the significantly higher magnetization of the HTS-based composites, when compared to LTS-based composites, will have a significant negative influence on the field quality. However, the field quality of these types of magnets has not been studied until now.

An even greater concern for accelerator magnets could be any change in the magnetization of the composite with time. This is a concern because the field quality is influenced by the magnetization and if the magnetization changes with time, the field quality could change with time along with it. Small active compensation coils or even passive schemes could be used to reduce the field errors due to large static magnetization, but a dynamic magnetization will require more complicated active correction techniques. Contrary to the case for LTS magnetization, the magnetization of HTS decays significantly over time, even at 4 K, due to flux creep. LTS-based magnets do have some temporal field variation effects, typically referred to as “drift” [6] and some associated “snapback” [50]. These effects are associated with an interaction between long-range coupling currents and the LTS strand magnetization. However, while such effects may also be present in HTS-based magnets, the flux creep alone causes similar “drift” in the magnetization, leading to

a certain irreducible time dependence of the field error. There have been few studies on how the magnetization of HTS may cause field errors in magnets built from them. Indeed, few HTS-based prototype accelerator magnets have been built.

In this chapter, the field errors in an accelerator magnet due to persistent magnetization of HTS have been calculated using finite element software combined with experimentally measured HTS cable data (from Chapter 5). Both a CORC[®]-based block dipole design (based on HD3b [114]) and a hybrid CORC[®]-Nb₃Sn-based design were studied. In addition, analytic models were developed for the $M-\mu_0H$ of the CORC[®] cables, and these were compared to the measured magnetization ($M-\mu_0H$) and used to make field error projections. These projections were compared to the error results calculated using the experimentally measured $M-\mu_0H$ data. Finally, field quality measurements were made, at 4 K and 77 K, on a CORC[®]-based insert magnet. The insert coil had a canted $\cos\theta$ design. A rotating coil fluxmeter was used to measure the generated magnetic field harmonics and their evolution with time.

Field errors are unwanted components of the magnetic field in the magnet bore. The magnetic field in the aperture of a magnet is expressed as a multipole series expansion with normal multipole and skew multipole coefficients. The main coefficient is that of the desired polarity of the magnet, for example, dipole, quadrupole, sextupole, etc. The remaining coefficients should be as small as possible and are measured in “units,” which are parts in 1×10^{-4} of the main dipole field. Field errors can be present even when there are no magnetization effects from the coils that comprise the magnet (as would be the case

if copper coils are used). These field errors can result from minor errors in placement of the windings or other parts of the magnet structure. These geometry-dependent field errors are called geometric field errors. They occur when there is current in the windings of the magnet, but there is no magnetization from those windings. Such geometric errors can be assessed for superconducting windings when current is transported through the coils while they are in the non-superconducting state, such as is the case when the coils are at room temperature. The geometric field errors can also be modelled by setting the magnetization of the coils to zero, or by assigning them the material properties of, say, copper. (In this work, the contribution of the iron in the yokes of the magnet were included when calculating the geometric field errors.) Measuring the field errors in this way also gives an idea of how the iron in the magnet affects the field errors in addition to how any winding errors affect them.

A cross-section of a superconducting accelerator magnet design which uses Nb₃Sn-based Rutherford cables for the coils is shown in **Figure 84** (in this case, the magnet is HD3b [115]). The magnet is a block type dipole. The yoke of the magnet [shown in blue] is made of iron and contributes to the field in the bore of the magnet. The aperture of the magnet is represented by the white circle in the center of the red coils. The measured magnetic field and its harmonics (field errors) are measured at a reference radius in the aperture which generally represents the maximum deviation of the particles from the center axis of the magnet [6]. This design was previously built and tested as a full-sized accelerator magnet, and the results from those previous modelling and experimental studies

are shown below and compared with a hypothetical CORC[®] cable-based “HD3b”-type dipole modelled assuming the CORC[®] cable was a drop-in replacement for the Nb₃Sn Rutherford cables. CORC[®] replacement. The Nb₃Sn-based Rutherford cable coils are shown in red.

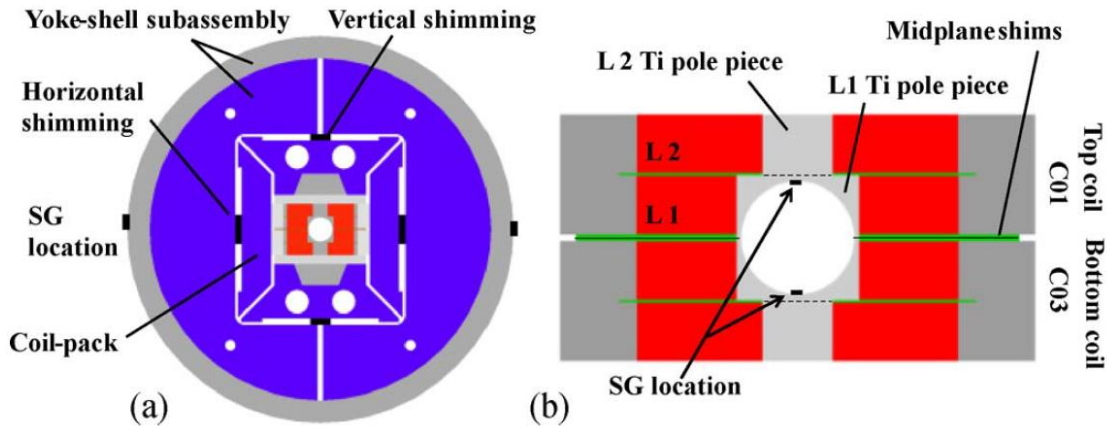


Figure 84. An illustration of the HD3b Nb₃Sn Rutherford cable-based block-type dipole accelerator magnet, from [115]. The Nb₃Sn coils are red, with the aperture centered between the coils (white). The yoke is blue and is composed of iron.

6.2 Technique for Modelling Field Error

Finite element based computational tools are frequently used to study the field errors caused by persistent current magnetization in accelerator magnets. However, they require as an input the $M-H$ or $B-H$ of the superconducting and magnetic components present in the winding. Sometimes a Bean critical-state model is used to calculate the strand magnetization, including its field-dependence, in each superconducting filament [116-

119]. Other times the measured strand magnetization is used by directly assigning it to each individual strand in the magnet [120], or by converting it to the nonlinear permeability of the coil of the magnet [121]. Good agreement between measured and calculated field values for NbTi-based accelerator magnets has been found using these methods. Tools that use the Bean critical-state model work well for LTS strands (NbTi, Nb₃Sn) and are expected to work well for Bi:2212 strands because these strands are round, making direct use of the critical state expressions straightforward. This approach is not expected to work well (if done directly) for YBCO tapes or YBCO-based cables, where the field orientation can matter (for tapes), and the $M-\mu_0H$ of CORC[®] is not well described by a critical state model (until now, see below). In the next section, we will start with the measured magnetization of CORC[®] cables and predict field errors using the measured $M-\mu_0H$ directly as an input to the FEM models. We will then follow that with a second calculation that uses a new analytic model, developed for CORC[®] conductors, to generate the $B-H$ curve to be input to the FEM model. We will show that we can obtain very similar results to those obtained using the direct experimental $M-\mu_0H$ results. This modified approach will provide great flexibility for projecting field errors in to-be-developed magnets with yet-to-be manufactured cables.

Thus, in this thesis, a finite-element method is used to model the persistent-current magnetization effects in HTS-based and HTS/LTS-based hybrid magnets. The magnetic field quality is calculated in two dimensions (2D) in the straight section of the magnet body. As mentioned above, a critical input to the model is the measured magnetic hysteresis

($M-\mu_0H$) of the strands/cables of the turns used to make the magnet [122]. The hysteresis data is converted to $B-H$ data and used as input into the finite element program, with care taken to use the internal (or intrinsic) $B-H$ curve of the material. That is, demagnetization effects have been considered, and the magnetization data have been modified accordingly. This FEM method has been validated for field error calculations with several real Nb_3Sn -based accelerator magnets [114].

Modelling of the field error was performed using Vector Fields Opera, a software package which uses the finite element method (FEM), to perform electromagnetic field analysis. The finite element method is used to solve the partial differential equations that describe the behavior of the fields. The geometry of the device is represented as a set of polygonal areas, or regions, on the 2D plane. The regions can be free space, a conductor with a prescribed or induced current density, or a permeable material with linear or non-linear material characteristics. Within each region, finite element meshes are generated automatically. The magnetic permeability is set for each region by either assigning to the region a material code and loading the $B-H$ data in tabular form, or selecting a pre-set material, such as copper or free space, and assigning its code to the region. In this work, the static analysis package, which solves for the vector or scalar potential defined by a non-linear Poisson equation, was used to obtain the magnetic vector potential and magnetic flux density in different regions of the turns of different superconducting magnet designs.

The concept of a CORC[®] cable or wire was introduced in Chapter 5. These cables and wires are being used to build prototype high-field accelerator magnets [3, 4]. A magnet

design that is being tested presently is the canted cosine theta (CCT) design, as shown in **Figure 85**. A picture of a wound layer of a 4-layer, 40 turn magnet is presented in **Figure 86**.

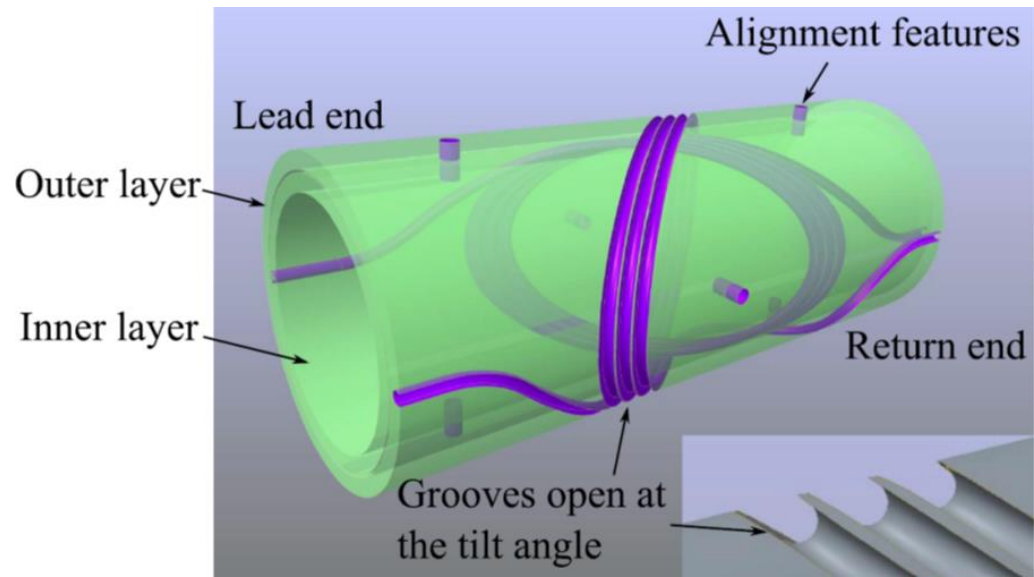


Figure 85. A schematic for a 2-layer, 3 turn canted $\cos\theta$ magnet developed at Berkeley National Lab, from [3].

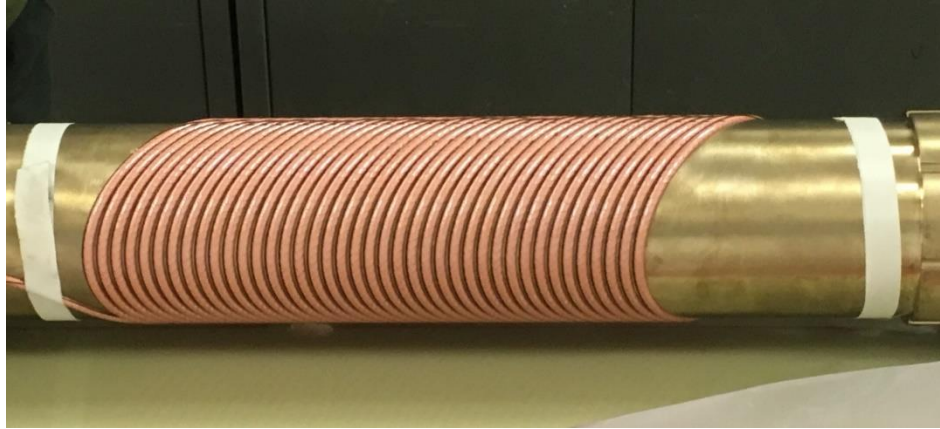


Figure 86. A layer of a 40 turn, 4-layer canted $\cos\theta$ (CCT) prototype dipole made from CORC[®] wire.

Although the canted $\cos\theta$ magnet is a strong contender for how CORC[®] cables would be used in magnets in practice, the field error calculations are somewhat more difficult with this design because the magnet windings have a 3-D geometry that is difficult to accurately treat in 2-D, as can be done for $\cos\theta$ windings or block-type dipole designs. In addition, there is some merit in a kind of head-to-head comparison with conventional designs, both cosine theta and block dipole. Thus, in this thesis, I have focused on calculating the field error of magnets which are built using CORC[®] cable as the windings and which have a block-type design. The cross-section of the magnets were drawn assuming that the CORC[®] cable would act as a drop-in replacement in the design of a pre-existing block dipole (Hd3b) magnet based on Nb₃Sn Rutherford cables. The $M-\mu_0H$ data from the CORC[®] sample presented in Chapter 5 was used to generate sets of $B-H$ data for input to the model. $B-H$ data from the virgin curve, 1st down branch, and 2nd up branch of

the $M-\mu_0H$ data was used to calculate the magnetic flux density in the bore of the magnet, the absolute field error, and the relative field error. It was very important to correct for the demagnetization effects of the measured strands before using the data as an input to Vector Fields Opera, because it assumes that the internal $B-H$ curves are used. I used

$$B = \mu_0[H_a + (1 - N)M] \quad (6.1)$$

as the total field, and

$$H_i = H_a - NM \quad (6.2)$$

as the internal field strength, where H_i is the internal field strength, H_a is the applied field, and N is the demagnetization factor, here $N = 1/2$ for cylindrical strands with fields applied perpendicular to the z -axis.

As mentioned above, Opera has been successfully used to accurately calculate field errors of Nb₃Sn-based accelerator magnets. The magnetic field quality of three different Nb₃Sn-based accelerator magnets was studied in [114]. Each magnet had a different design. A block-type dipole, cosine theta dipole, and a $\cos(2\theta)$ quadrupole were studied. The $M-\mu_0H$ data of short sections of Nb₃Sn strands were cut and measured in the VSM of a PPMS and used as inputs to the model. The cross-sections and the field lines of the magnets are shown in **Figure 87**. The calculated magnetic field quality from the Opera calculations was found to agree well with the measured magnetic field quality. The experimentally measured and calculated b_3 of the block-type dipole are shown in **Figure 88**.

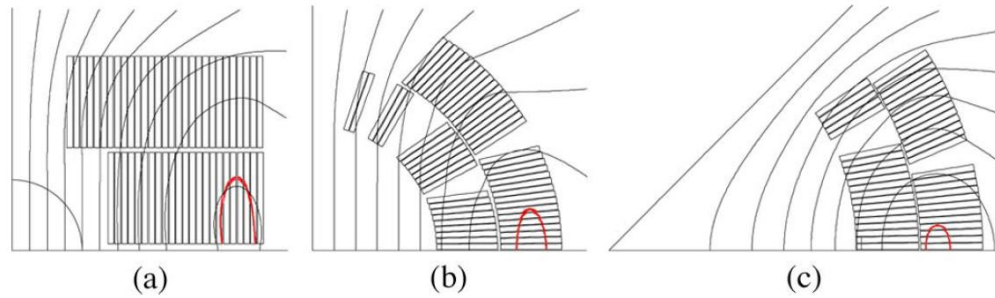


Figure 87. The cross-section and field lines of one quadrant of each of the Nb₃Sn accelerator magnets (a) HD3 block dipole. (b) MBHSP02 $\cos \theta$ dipole. (c) HQ02 $\cos(2\theta)$ quadrupole. From [114]. Individual rectangles are the Nb₃Sn cables. Each magnet has 2 layers.

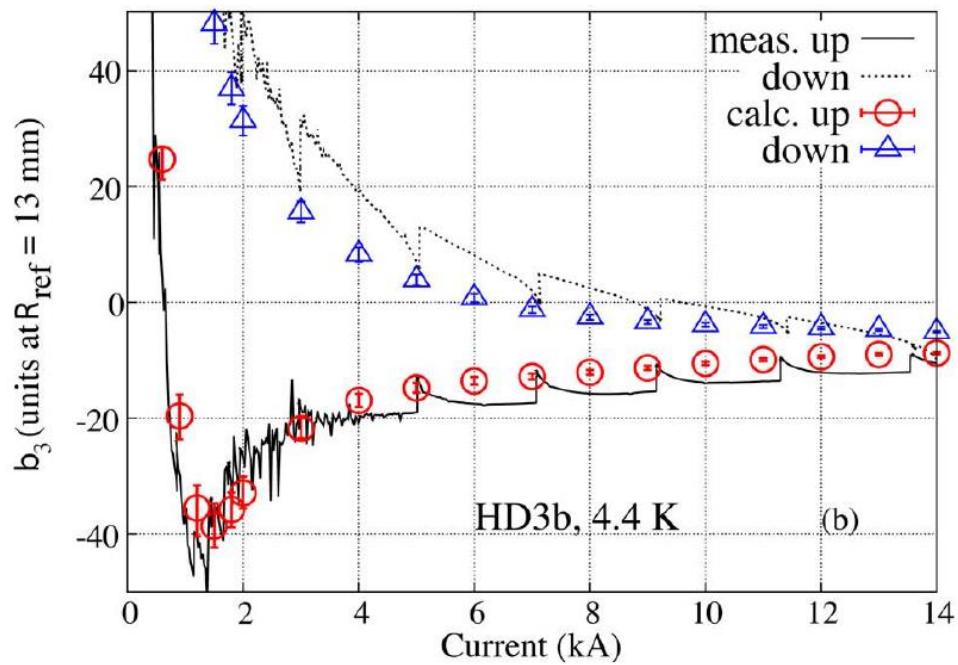


Figure 88. The results of the measurements and calculation of the sextupole component of the magnetic field of the block-type dipole magnet (HD3b) at 4.4 K. The lines are the measured values and the symbols are the calculated values. From [114].

M - $\mu_0 H$ measurements performed on CORC[®] cable were presented in Chapter 5. The 8 T M - $\mu_0 H$ of that CORC[®] cable is presented again in **Figure 89**, along with the M - $\mu_0 H$ of one of the strands of Nb₃Sn cable used to make the accelerator magnets discussed in [114].

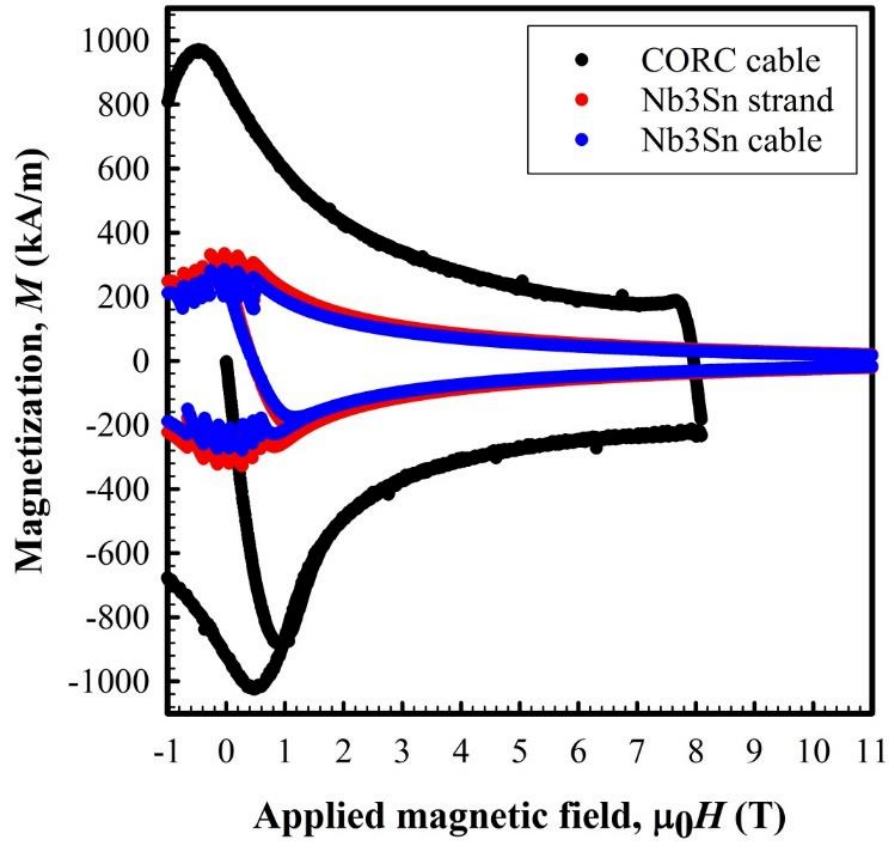


Figure 89. The M - $\mu_0 H$ loops of the CORC[®] cable presented alongside that of a Nb₃Sn strand used to build an accelerator magnet presented in [114]. The peak magnetization of the CORC[®] is greater than 2 X that of the Nb₃Sn.

The peak magnetization of the CORC[®] cable is greater than 2 X that of the Nb₃Sn composite. Furthermore, the magnetization of the Nb₃Sn composite is nearly zero at 11 T, whereas that of the CORC[®] cable will have some significant value at that field. It might be expected from the direct comparison of the magnetization results alone that a magnet built from the CORC[®] cable would have much larger field errors than that of the Nb₃Sn-based magnets. However, we will calculate the values explicitly using the $M-\mu_0H$ data of the CORC[®] cable as an input to the model.

The method to calculate field error outlined above was used to study the field quality in two different cases: (1) a standalone block dipole design (**Figure 90**) and (2) a hybrid block dipole design (**Figure 91**). The standalone (CORC[®] cable only) block dipole is of the same design as the Nb₃Sn cable-based block dipole in [114]. The Nb₃Sn Rutherford cables in that design were replaced with CORC[®] cables which had the dimensions and $M-\mu_0H$ of the cable studied in Chapter 5. The CORC[®] cable was used as a drop-in replacement, and the number of CORC[®] cables was limited by the number and dimensions of the Nb₃Sn Rutherford cables (the magnet cross-section defined by the Nb₃Sn cables was imagined to be filled with CORC[®] cables instead). As such, the first layer of the magnet could have 84 turns (or CORC[®] cables) and the second layer could have 104 turns. The inner row of the CORC[®] cables was aligned with the inner row of Nb₃Sn Rutherford cable. The insulation of the CORC[®] cables was considered by spacing the cables 2 X the width of the insulation apart. A schematic of the cross-section of the magnet created in this way is shown in **Figure 90**.

The maximum magnetic field the magnet can generate is determined by the critical current, $I_c(B)$, of the turns and the load line of the magnet. The I_c - B of the CORC[®] cable is given in [3] and used here. Here the load line is determined by the maximum magnetic field, B_{\max} , that the turns of CORC[®] are subjected to, in the magnet, as a function of magnet current. During operation, the program calculates the maximum field present in each layer as a function of the current. Because I_c of the CORC[®] cable is a function of the field experienced by the cable, it is limited by this field. The maximum field within the magnet was present in layer 2 over the entire current ramp, and therefore I - B_{\max} of layer 2 was used to define the load line. The magnet can generate magnetic fields below those at which the load line and I_c - B of the composite (which make up the turns) intersect. Above this field, the critical current of the composite would be below that of the current required to be input into the magnet to generate the field. The load line of the CORC[®] cable-based standalone block dipole design is presented in **Figure 92**. The intersection of the I_c - B curve of the CORC[®] cable and the load line is at approximately 6.7 T (with approximately 2 kA in the magnet). Theoretically then, the maximum magnetic field the magnet could generate is 6.7 T, but usually magnets are operated at some fraction of their maximum field to prevent thermal runaway. Here we assume that the magnet operates at 90% of the possible maximum field, which is about 6 T. The magnet hysteresis and field error will be examined out to 2 kA.

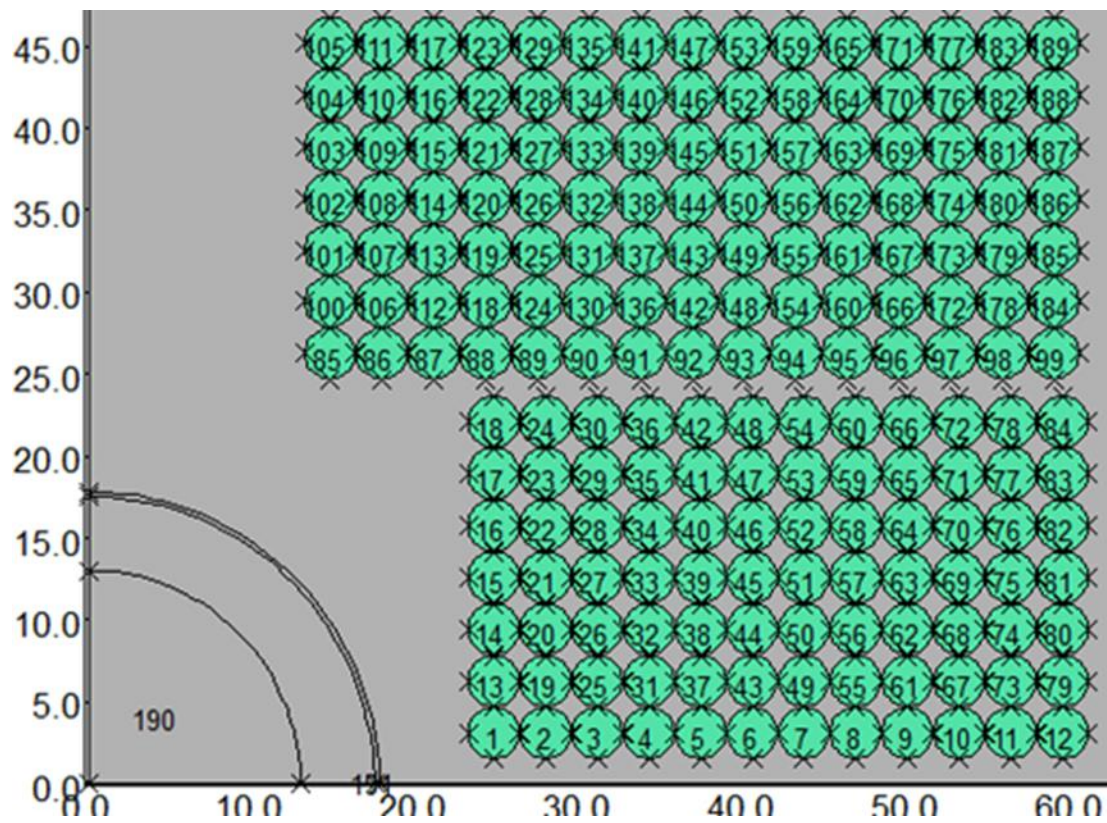


Figure 90. The block dipole layout of the Nb₃Sn magnet (HD3b), studied in [114], but with the Nb₃Sn cable substituted with the CORC[®] cable (shown in green and numbered) presented in Chapter 5.

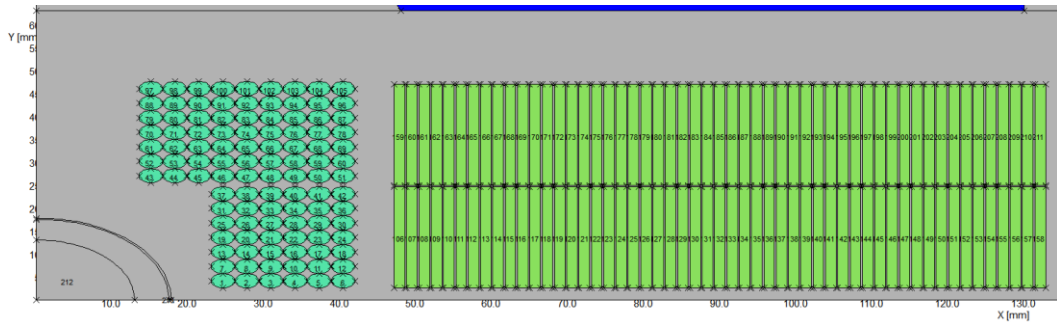


Figure 91. The hybrid CORC[®] cable and Nb₃Sn Rutherford cable magnet design. The CORC[®] cable has a round cross-section (darker green) and the Nb₃Sn cable cross-section is rectangular (lighter green).

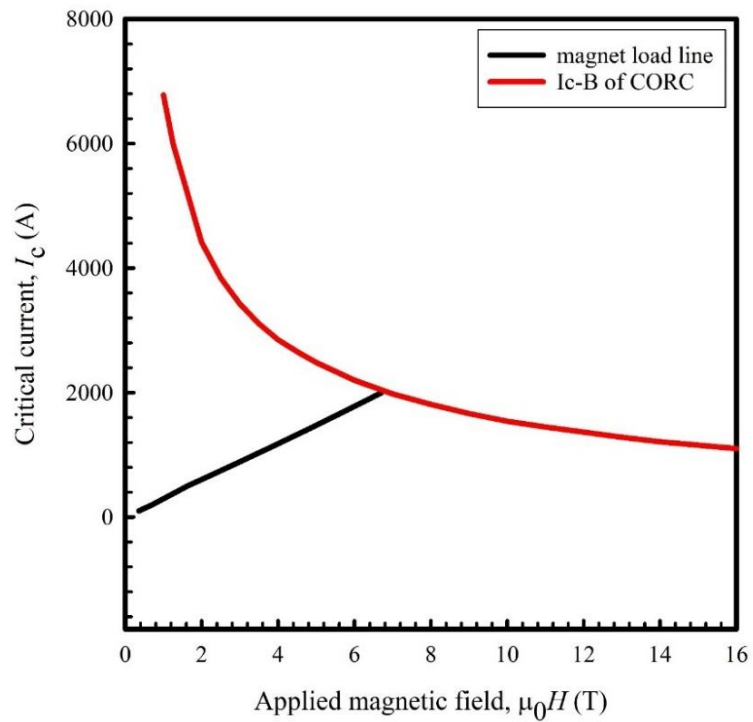


Figure 92. The magnet load line plotted with the I_c of the CORC[®] cable. The intersection of the two curves determines the maximum operating field of the magnet. In this case, it is about 6.7 T.

6.3 Transfer Function Calculation for the Standalone, CORC[®] Replacement Block Dipole

The transfer function (TF) of the magnet is the ratio of the magnetic field generated in the bore of the magnet to the total current in the windings of the magnet. The magnetic hysteresis in the magnet will be apparent when the transfer functions on different ramps of the current are plotted together. The transfer function for the standalone CORC[®] cable-based dipole magnet is presented in **Figure 93** (TF vs total magnet current) and **Figure 94** (TF vs magnet bore dipole field), for four cases: (1) the geometric ramp; (2) the virgin up ramp; (3) the 1st down ramp; and (4) the 2nd up ramp. During the geometric ramp, the CORC[®] cable turns are set to have zero magnetization, and therefore are akin to a simple non-magnetic conductor, like copper wire. Therefore, no superconducting persistent current magnetization effects are included. The iron in the magnet and the magnetic field from the current in the windings are included and affect the bore field. The next series of calculations do assume the presence of the superconducting wire (with magnetic response). The virgin up ramp is the first up ramp of current into the magnet. The conductors and iron in the magnet start out un-magnetized (at zero field) with the current in the windings starting at 0 A. Magnetization and the associated field errors develop as current is injected. The 1st down ramp is the return to 0 A from the maximum current reached on the virgin up ramp, while the second up ramp is the ramp from 0 A after the first down ramp.

At low currents, the transfer function (TF) of the virgin, 1st down, and 2nd up curves are different than the TF of the geometric curve, indicating that the magnetization of the CORC[®] cable clearly affects the magnetic field in the bore of the magnet at low currents.

The influence of the magnetization on the TF can be seen by the width between the virgin (or also the second up) up curve and the first down ramp at low current. At higher currents, the TFs of the geometric, virgin, 1st down, and 2nd up curves coincide, indicating that the magnetization has little effect on the magnetic field in the bore of the magnet at these higher currents, most likely because it is being swamped by the main field in the bore.

The TFs of the magnet designed using CORC[®] cable can be compared to those of the Nb₃Sn-based magnet, HD3b, from [114], which is shown in **Figure 95**. At 1 T, a typical injection field for accelerator magnets, the difference in the TF between the 1st down and 2nd up branches in the Nb₃Sn-based magnet is approximately 0.035 T/kA. Conversely, the difference is approximately 0.1 T/kA, a factor of about 2.8 higher, for the hypothetical CORC[®]-based dipole magnet.

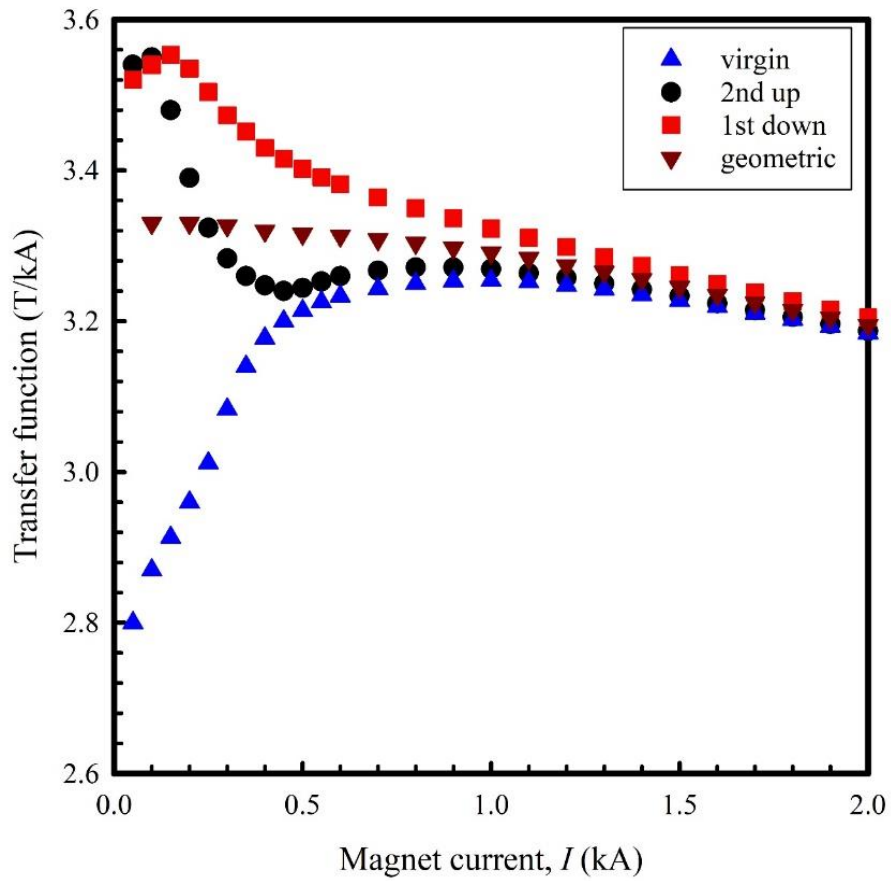


Figure 93. The calculated TF of the two-layer CORC[®]-based block dipole as a function of the current in the magnet, for 4 cases: Geometric ramp (red triangles); virgin ramp up (blue triangles); 1st down ramp (red squares); and 2nd up ramp (black circles).

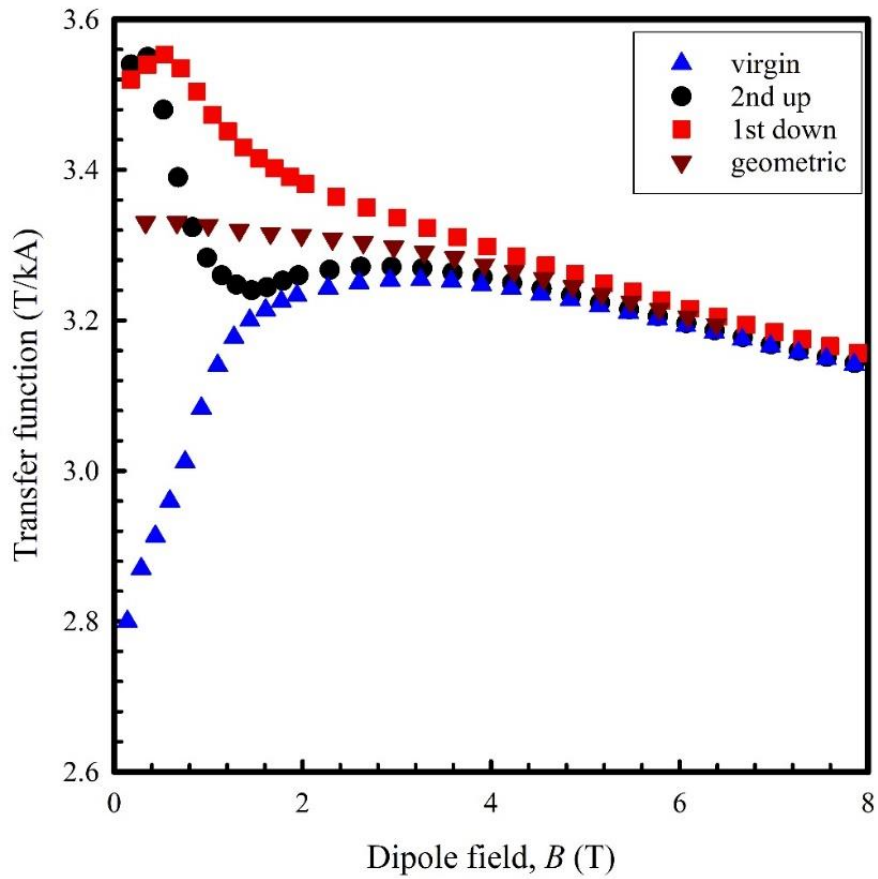


Figure 94. The calculated TF of the two-layer CORC[®]-based dipole, as a function of the field in the bore of the magnet, for 4 cases: Geometric ramp (red triangles); virgin ramp up (blue triangles); 1st down ramp (red squares); and 2nd up ramp (black circles).

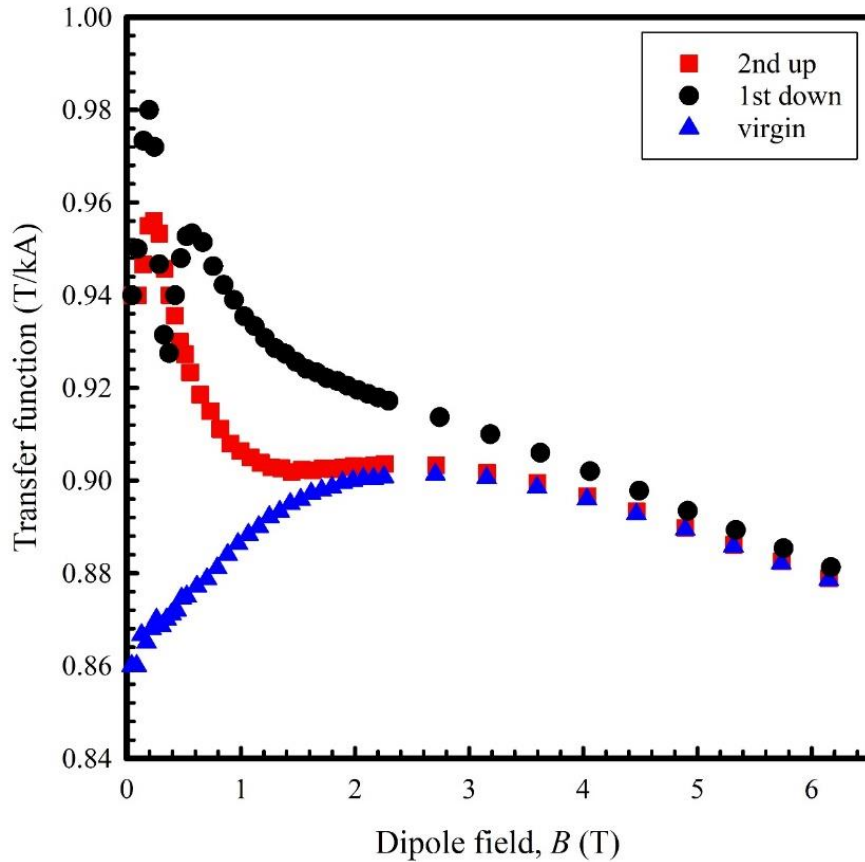


Figure 95. The calculated dipole transfer function of the two-layer Nb₃Sn-based block dipole, as a function of the dipole field in the bore of the magnet, for three different cases: virgin up ramp (blue triangles); 1st down ramp (black circles); and 2nd up ramp (red squares).

6.4. Relative Sextupole Component, b_3 , of the CORC[®] Cable Replacement Dipole

The relative sextupole component, b_3 , of the magnetic field is the most common component used to quantify the quality of the magnetic field of a dipole magnet. The b_3 , calculated using Opera, is shown as a function of bore dipole field for the hypothetical

CORC[®] cable-based magnet in **Figure 96**. Again, the results for the geometric, virgin ramp up, first down ramp, and 2nd up ramp cases are plotted. Again, a clear magnetization effect is seen at low dipole fields (low current in the magnet) and the results of the four ramps coincide at higher field (higher current in the magnet). The b_3 for the Nb₃Sn cable based Hd3b magnet is shown in **Figure 97**. The difference in b_3 between the first down and second up branches at 1 T is approximately 94.3 units for the Nb₃Sn cable-based magnet and about 71.9 units for the hypothetical CORC[®] cable-based magnet. It might be assumed that the CORC[®] cable based magnet should have higher b_3 values than that of the Nb₃Sn cable-based magnet, but it should be noted that the I_c of the CORC[®] cable is much lower than that of the Nb₃Sn cables, which consists of 51 strands of Nb₃Sn wire, and therefore, the low b_3 values are reasonable. At 15 T, the CORC[®] cable has an I_c of 1156 A, and the Nb₃Sn cable has an I_c of 25 kA. We note there are 4 times as many turns of CORC[®] cable as there are turns of Nb₃Sn cables. The total current carried in the CORC[®] cable-based magnet is then 189 (the number of CORC[®] strands) multiplied by 1156 (the I_c per turn) = 218,484 A. The total current carried in the Nb₃Sn cable-based magnet is 52 (the number of Nb₃Sn cables) multiplied by 25,000 A = 1,300,000 A. The ratio of the currents is 218,484/1,300,000 = 0.168, which is about 1/6. Therefore, if we just imagined increasing the current in the CORC[®] cable to reach the same current density as that of the Nb₃Sn cable-based magnet winding, its magnetization would increase commensurately. The b_3 of the CORC[®] cable-based magnet could be expected to also increase by a factor of 6, or $\approx 6 \times 71.9 \sim 430$ units. However, it is not quite that simple, as we will see when we develop an analytical model to make this estimation accurately.

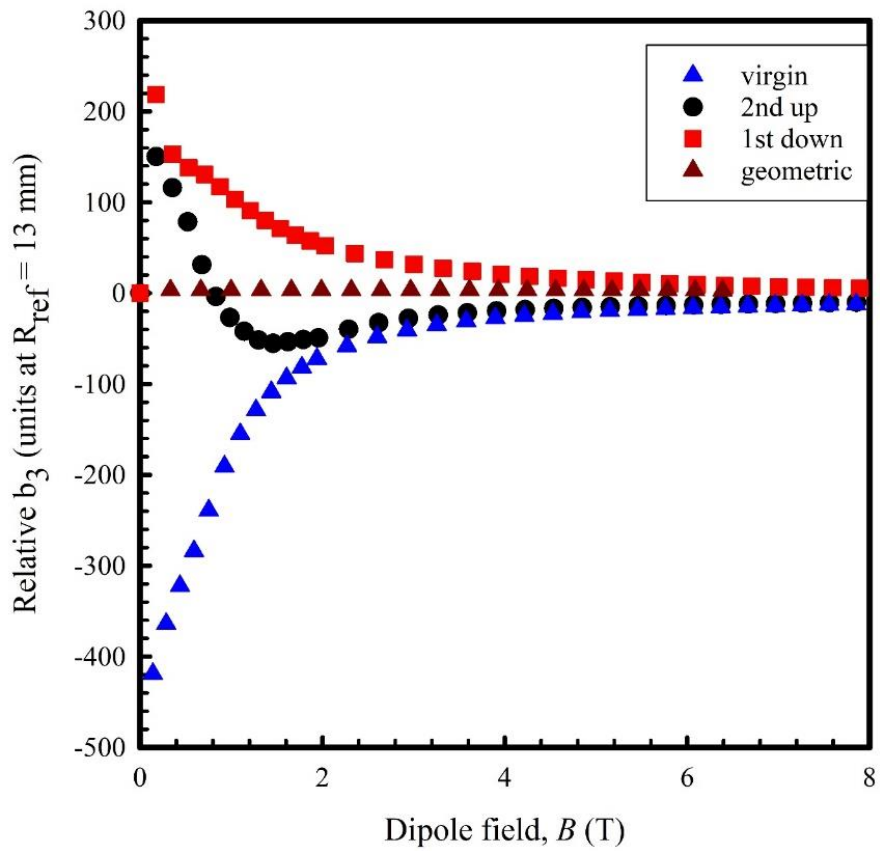


Figure 96. The calculated relative b_3 of the two-layer CORC[®]-based dipole, as a function of the bore field in the magnet, for 4 cases: Geometric ramp (red triangles); virgin ramp (blue triangles); 1st down ramp (red squares); and 2nd up ramp (black circles).

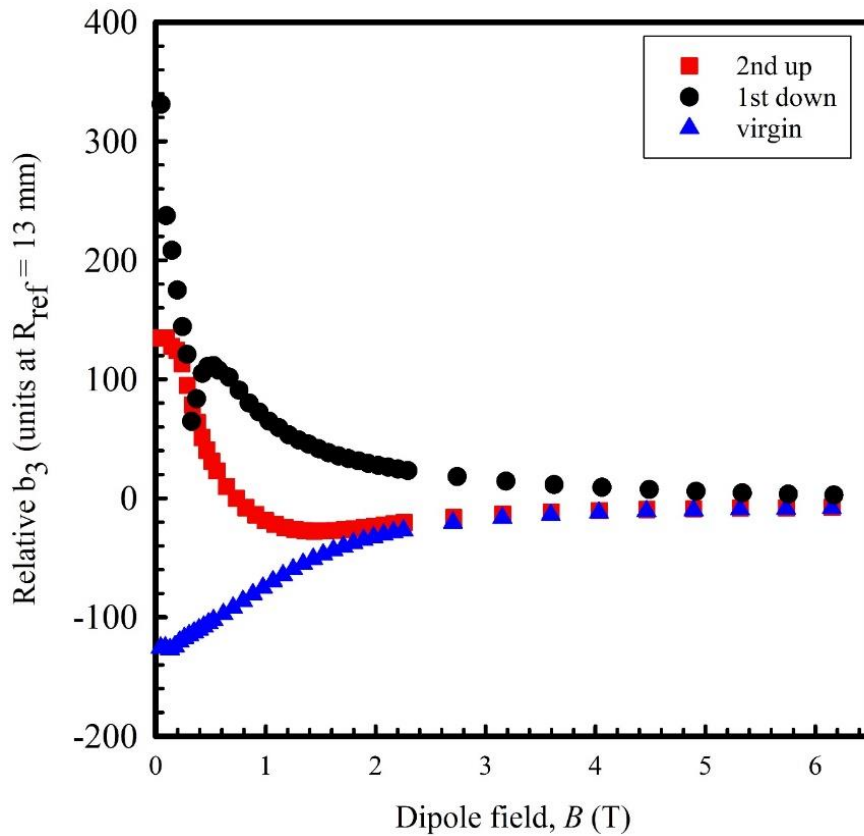


Figure 97. The calculated relative sextupole component, b_3 , of the two-layer Nb₃Sn-based block dipole for three different cases: virgin up ramp (blue triangles); 1st down ramp (black circles); and 2nd up ramp (red squares).

6.5. Hybrid CORC[®] and Nb₃Sn Cable-based Block Dipole

The standalone CORC[®]-based block dipole design could generate a maximum magnetic field of only approximately 6.7 T. This low field is because the high packing factor of the LTS windings is difficult to achieve unless the magnet is specifically designed for HTS. In any case a much more likely configuration (for cost reasons alone) is a hybrid

LTS/HTS magnet. A hypothetical design that could reach 20 T was presented in [123]. That design consisted of a hybrid magnet comprised of Bi:2212 and Nb₃Sn Rutherford cables. Again, there are two layers, but in this case, each layer has two coils. In the first layer, there are 12 Bi:2212 Rutherford cables in the first coil (closer to the bore) and 52 Nb₃Sn Rutherford cables in the second coil (further from the bore). In the second layer, there are 18 Bi:2212 Rutherford cables in the first coil and 52 Nb₃Sn Rutherford cables in the second coil. This hypothetical magnet design could reach 20 T and still maintain good field quality.

Here, we have performed field error computations for a magnet where the Bi:2212 Rutherford cable was replaced with the CORC[®] cable using the same replacement method as for the standalone CORC[®] cable-based block dipole. In this case, there was enough room for 42 turns of CORC[®] cable in the first layer and 63 turns of CORC[®] cable in the second layer. The Nb₃Sn coil was composed of 52 turns in each layer. There are, however, a few possibilities for powering the coils in a hybrid magnet design which must be considered. The magnet, if the LTS and HTS coils are powered in parallel with one another, can be excited in different orders. One coil, such as the Nb₃Sn coil, could be powered first, and then the other coil could be powered, or both regions could be powered simultaneously. The I_c - B of the CORC[®] cables and the high field experienced by the CORC[®] cables during simulated magnet operation limited the maximum current that could be carried by the CORC[®] coil to 2000 A. Therefore, the calculations of field error were confined to fields generated by applied currents of up to 2 kA (total I in both coils). In any case, the primary

interest is the magnitude of the field errors near injection, and this current range enable the study of these field errors. We studied the field error for three different powering scheme cases: (1) the CORC[®] cable-based coil powered first, (2) the Nb₃Sn cable-based coil powered first, and (3) both coils powered simultaneously. As in the previously discussed magnet design, the TFs and b_{3s} for the geometric ramp, virgin up ramp, 1st down ramp, and 2nd up ramp were calculated. The TFs for these four cases are shown in **Figure 98**. The geometric case is depicted by the red Xs; the case when the CORC[®] cable-based coil is powered first is depicted by the blue diamonds; the case when the Nb₃Sn cable-based coil is powered first is depicted by the black triangles; and the case when both coils are powered simultaneously (parallel ramp) is depicted by the gray squares. The calculated TF when ramping either the CORC[®] cable-based or Nb₃Sn cable-based coil first was similar, but not identical. However, the TFs were very different than that calculated for the geometric ramp case. This disagreement between the TFs indicates that there is a strong influence on the dipole bore field due to the magnetization of the superconductor composites, at least up to the 3.5 T, or so, ramp shown here. Conversely, when the CORC[®] cable-based and Nb₃Sn cable-based coils are powered simultaneously, the calculated TF is like the geometric TF up to about 3.5 T.

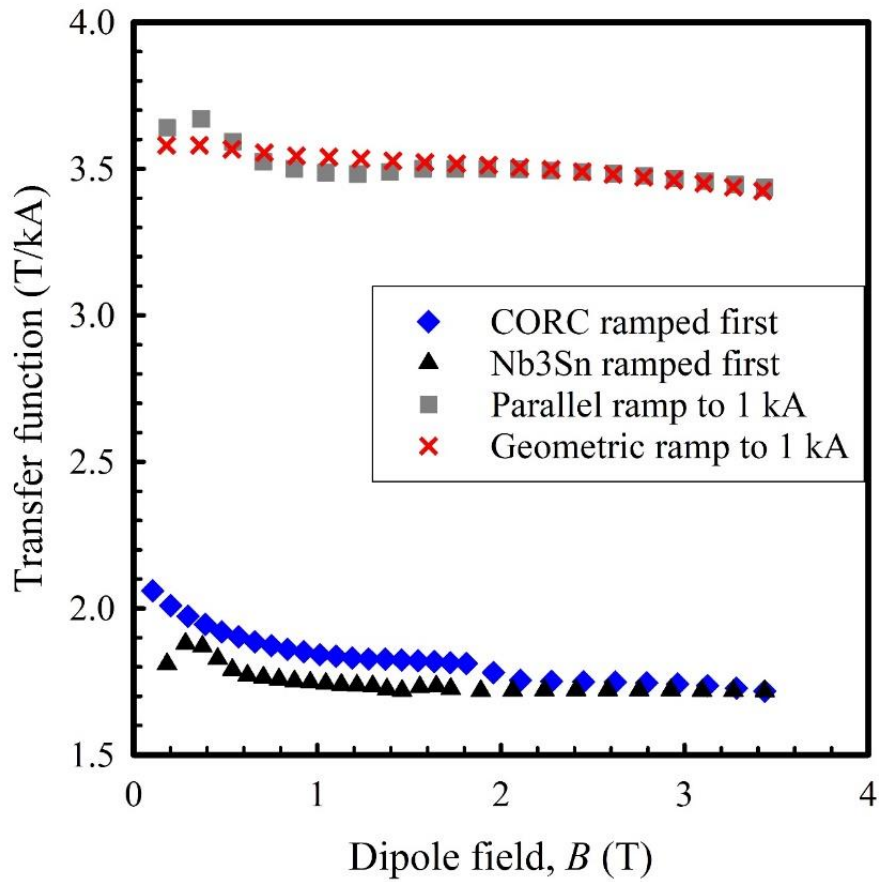


Figure 98. The calculated TF of the hybrid dipole for 4 cases: geometric ramp (red X); parallel ramp (gray squares); CORC[®] ramped and then Nb₃Sn coil ramped (blue diamonds); Nb₃Sn coil ramped and then CORC[®] coil ramped (black triangles).

The powering scheme also affects the relative harmonics of the main field. The resulting b_3 is shown for the different powering schemes in **Figure 99**. Here, b_3 is different for the cases where the regions are powered separately. For most of the ramp, the polarity of the field is different in the two cases. However, the b_3 s of all the cases converge with

the geometric b_3 at about 1 kA. When the regions are powered simultaneously, b_3 converges with the geometric b_3 at about 0.7 T. The absolute value of b_3 is lowest for this simultaneous ramp, up until the point where the values of b_3 converge for the separate powering schemes.

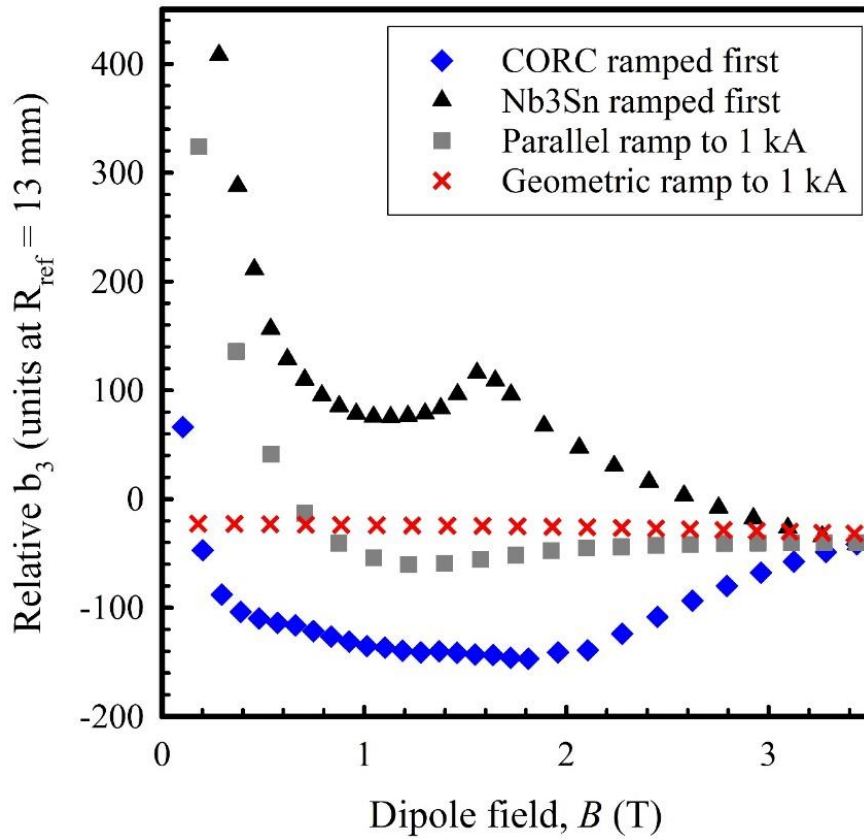


Figure 99. The calculated b_3 of the hybrid CORC[®] and Nb₃Sn-based dipole for 4 cases: geometric ramp (red X); parallel ramp (gray squares); CORC[®] ramped and then Nb₃Sn ramped (blue diamonds); Nb₃Sn ramped and then CORC[®] ramped (black triangles).

In all the cases above, the measured CORC[®] strand magnetization was used as a direct input to the FEM model (Opera). The persistent current magnetization effects are larger in an HD3b design made from CORC[®] wires (or cables) compared to the effects in the HD3b design made with Nb₃Sn-based Rutherford cables. The powering scheme affects the persistent current magnetization effects in the hybrid design. The effect seems to be reduced to near zero when the CORC[®] and Nb₃Sn coils are powered simultaneously.

6.6. Analytic Model for CORC[®] Magnetization on Various Branches of the M - H Curve and its Application to Error Field Calculations

Above, the field-dependent magnetization of a section of CORC[®] cable was measured (Chapter 5) and used as an input to an FEM model so that the field errors of two different accelerator magnet designs (stand-alone CORC[®] cable and hybrid Nb₃Sn/CORC[®] cables designs) could be calculated. Calculating the field errors of a magnet by using the measured field-dependent magnetization as an input is a straightforward approach, but it requires direct measurement of the magnetization of samples from the cable (or turns) of the magnet every time the cable properties are modified. To compare the field errors generated in a magnet when using cables with different properties (such as J_c), the magnetization of those specific cables must be measured and input into the FEM model. It would be quicker, cheaper, and easier if an analytical model could be used that would predict the field-dependent magnetization of a magnet cable (or turn) on the branches of the hysteresis loop that are relevant for accelerator magnets. The results of this model could

then be input into the FEM software to predict the field errors. Such an analytical model is developed below.

Let us start by using a Bean-type critical state model for the magnetization. That is, we are ignoring, for the moment, any field dependence of J_c . Such a model leads, once the full critical state flux profile has developed, to a magnetization which saturates to $\pm M_0$. A schematic of the hysteresis loop for this case is presented in **Figure 100-Figure 101**. The main branches for an accelerator magnet are labelled 1-5. The first branch is the virgin or initial ramp of the magnetic field from 0 current or field (with no pre-existing magnetization).

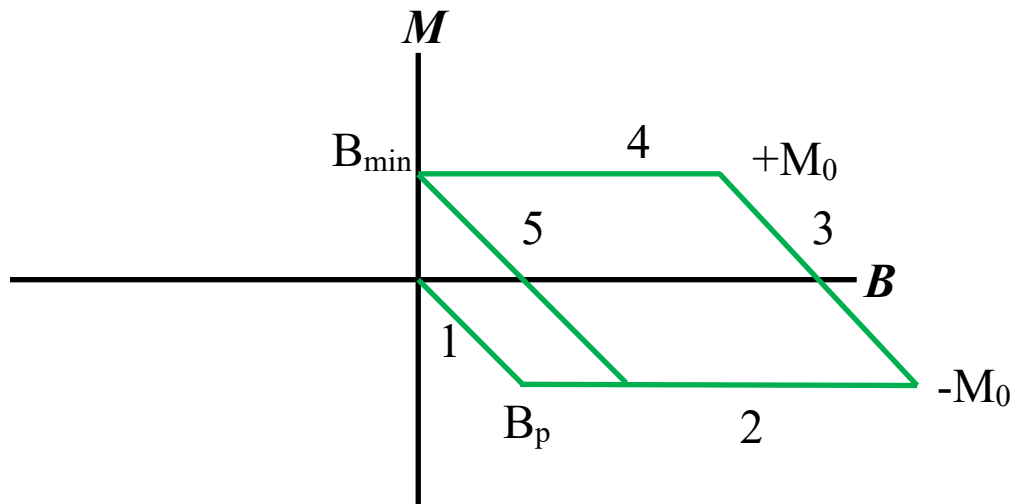


Figure 100. A schematic hysteresis loop of the Bean critical state model.

Taking for the moment the conductor to have no demagnetization (e.g., a very thin slab with field applied within the plane of the sample), the slope of the initial branch would be -1 if there is perfect diamagnetism, as is the case for the Meissner state. Here, if we ignore the Meissner contribution (i.e., the reversible magnetization), the slope starts out at -1 (for $H_a \approx 0$) but by the time the conductor has become fully penetrated with magnetic flux, the slope, $\chi = M/H$ has reached -1/2.

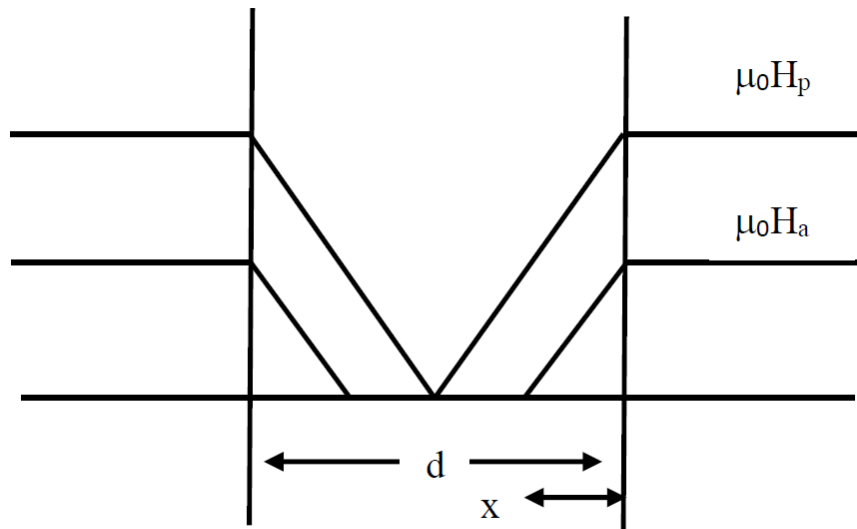


Figure 101. Bean Profile for initial virgin curve.

Then, if we use **Figure 101** to extract a magnetization curve as a 2D average, we obtain

$$M = -\frac{1}{d} \left(H_a d - \frac{x J_c x}{2} \right) = H \left(1 - \frac{H}{2H_p} \right) \quad (6.3)$$

Since $J_c x = H$, $H_p = (d/2)J_c$, and $M_0 = J_c d/4$. For the sake of simplicity, we will approximate this as linear for a first attempt, in which case if the minimum magnetization is M_0 , then the magnetization along the initial line is

$$M = -M_0 \left(\frac{H}{H_p} \right), \quad (6.4)$$

where $B_p = \mu_0 H_p$ is the penetration field. There will be some errors if this treatment is used near zero field, but the results will be accurate near the penetration field, and the treatment will also simplify the calculations for an arbitrary reversal field, as discussed below. For Branch 2, the magnetization is simply constant at the minimum value,

$$M = -M_0. \quad (6.5)$$

For Branch 3, the magnetization starts out at $-M_0$ and follows the line to the maximum magnetization, M_0 . The change in B required to go from $-M_0$ to 0 is B_p , and therefore the change in B required to go from $-M_0$ to $+M_0$ is $2B_p$. If the maximum magnetic field traversed along Branch 2 is B_{\max} , then the equation for the magnetization along Branch 3 is

$$M = -M_0 + M_0 \left(\frac{B_{\max} - B}{B_p} \right). \quad (6.6)$$

For Branch 4, the magnetization is simply constant at the maximum value

$$M = +M_0. \quad (6.7)$$

For Branch 5, the magnetization starts out as M_0 and decreases linearly depending on the value of the field when the field reversal takes place. This field may not be zero and is designated B_{\min} . The magnetization during Branch 5 is

$$M = M_0 - M_0 \left(\frac{B - B_{\min}}{B_p} \right). \quad (6.8)$$

If the reversal occurs at $B = 0$, and the field is reversed by B_p , the magnetization is expected to be 0 (there is equal shielded and trapped magnetic flux) and substituting $B = B_p$ into the above expression gives that result. For a reversal of $2B_p$, it is expected that the magnetization will have reached $-M_0$, which it does when the substitutions are made. The expressions above give the magnetization along every branch of the hysteresis loop, relevant to accelerator magnets, for a superconductor that obeys the Bean critical state model. In actuality, the critical current density of a superconductor (and thus its magnetization) depends on the magnetic field it is subjected to. This field dependence is easily incorporated into the expression for the magnetizations, in a manner like that described by Kim *et al.*, by scaling the magnetization expression above by the factor

$$\frac{1}{A + \left(\frac{B}{B^*} \right)}, \quad (6.9)$$

where A and B^* are constants. B_p is also dependent on field and should be substituted with a term, $B_p (HF)$, when a field reversal takes place at high magnetic fields. Now that the analytical model is developed, a predicted hysteresis loop can be developed. However, in the case of the CORC[®] sample presented in Chapter 5, the magnetic hysteresis loop exhibited a small, but noticeable unusual “pseudo-reversible” magnetization. Fortunately,

this magnetization can easily be modelled as an add-on term to the expressions above.

Below B_p , the add-on term is

$$M = -M_{\text{rev}} \left(\frac{1}{A_r + \left(\frac{B}{B_r^*} \right)} \right). \quad (6.10)$$

Above B_p , the add-on term is

$$M = M_{\text{rev}} \left(\frac{B}{B_p} \right). \quad (6.11)$$

Now, an attempt can be made to construct the magnetic hysteresis loop of the CORC[®] sample using the analytical model. The values of the parameters in **Table 17**, when substituted into the expressions given above, generated the hysteresis loop shown in **Figure 102**. It is labelled “calculated” and depicted by red triangles in the figure. Plotted alongside the calculated hysteresis loop is the measured hysteresis loop. Clearly, there is very good agreement between the calculated and measured values, and it appears that the model is an excellent predictor of the magnetic hysteresis loop of the CORC[®] sample.

Table 17. The parameter values used to reproduce the CORC[®] cable hysteresis loop.

B_{rev}^*	1.5
A_{rev}	0.4
M_{rev}	-140
M_0	1300
B_P	0.7
B_{min}	0
A	1.4
B^*	1.2
B_{max}	8
high B_P	0.1

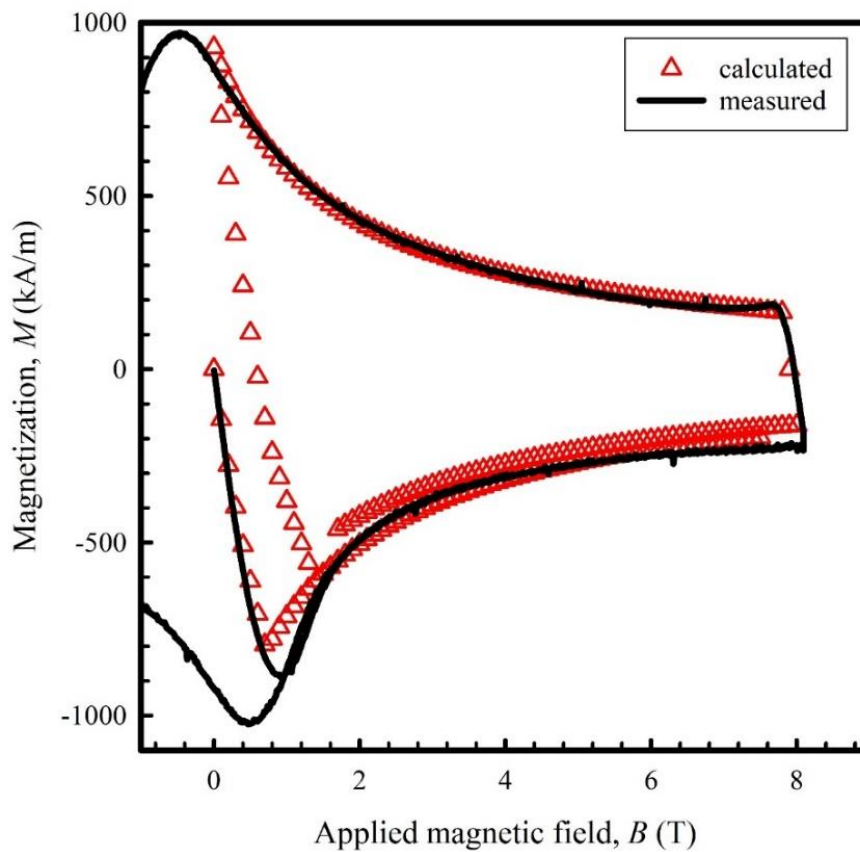


Figure 102. The magnetic hysteresis loop calculated using the analytical model (red open triangles) plotted alongside the measured hysteresis loop (black line).

We can see a small error in the fit, presumably associated with the approximation made going from equation 6.3 to equation 6.4. Because the agreement between the calculated and measured hysteresis loops is excellent, there should be good agreement between the field error calculations using the measured magnetization and the field error calculations that use the magnetizations calculated using the analytical expressions. The calculated field errors using the magnetization calculated using the analytical model are shown in **Figure 103**, alongside the field error (b_3) calculated using the measured magnetizations. As expected, there is good agreement between the b_3 values calculated using the measured magnetizations and the b_3 values calculated using the calculated magnetizations from the analytic expressions. The benefit of the model is that the magnetization of a sample does not have to be measured directly each time modifications are made, such as adding tapes or modifying J_c .

If we go back and consider the comparison between the Nb₃Sn-based Hd3b and the standalone CORC[®] cable-based block dipole design, we noted that the I_c of the Nb₃Sn Rutherford cables were much higher than that of the CORC[®] cable. This difference meant that the Amp-turns in the Nb₃Sn cable-based magnet was about 6 X higher than that of the CORC[®] cable-based magnet. It may be tempting to simply scale the magnetization of the CORC[®] cable by 6 in order to account for this current difference, and then to input this scaled $M-H$ (actually $B-H$) into Opera to make comparable field error calculations when the magnets have similar performance.

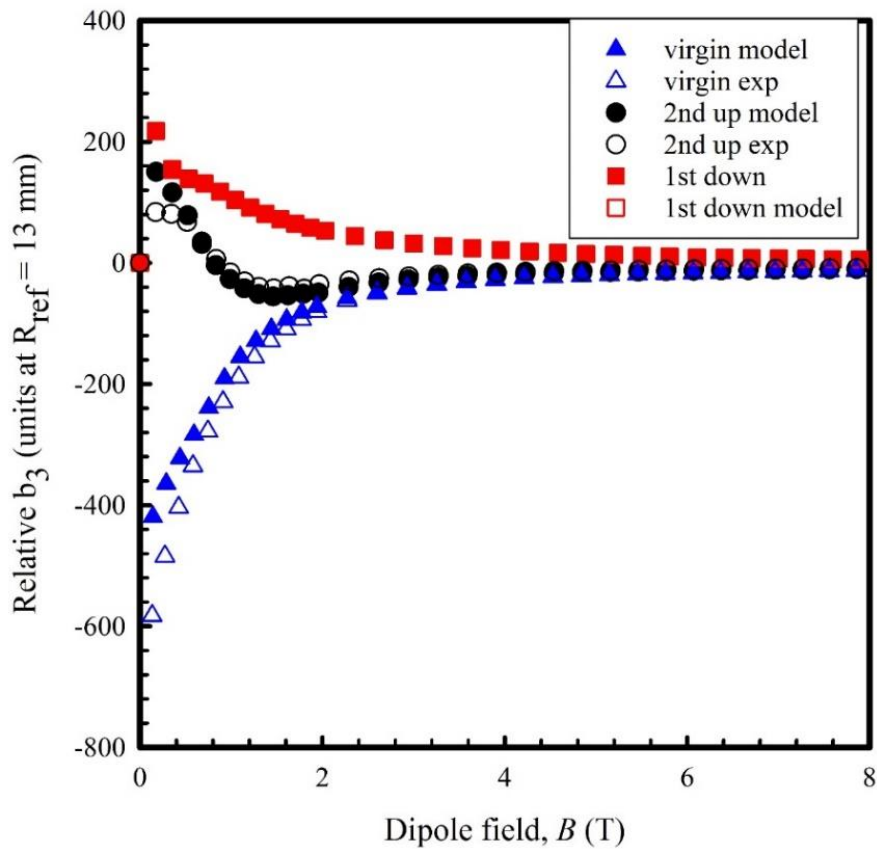


Figure 103. The b_3 calculations of the standalone CORC[®] dipole design using the calculated magnetizations (filled symbols) and the measured magnetizations (open symbols) for the virgin, 1st down, and 2nd up branches of the hysteresis loop.

However, doing this type of scaling will not account for the increased penetration field of the CORC[®] cable that would be present in a cable with this increased $M-H$. The analytic model developed above accounts for this penetration field increase, and the $M-H$ scaling can be performed accurately with the use of this model. The results of doing this $M-H$ scaling are shown in **Figure 104**. The scaled $M-H$ is clearly significantly larger than

the measured M - H , but it is also important to notice that the penetration field is pushed out to approximately 4 T. The peak in the field errors gets pushed out due to the maximum absolute value of magnetization being pushed out to 4 T. Because of the increase in the penetration field, the field errors at 1 T will not be as significant as may be expected by a simple M - H scaling.

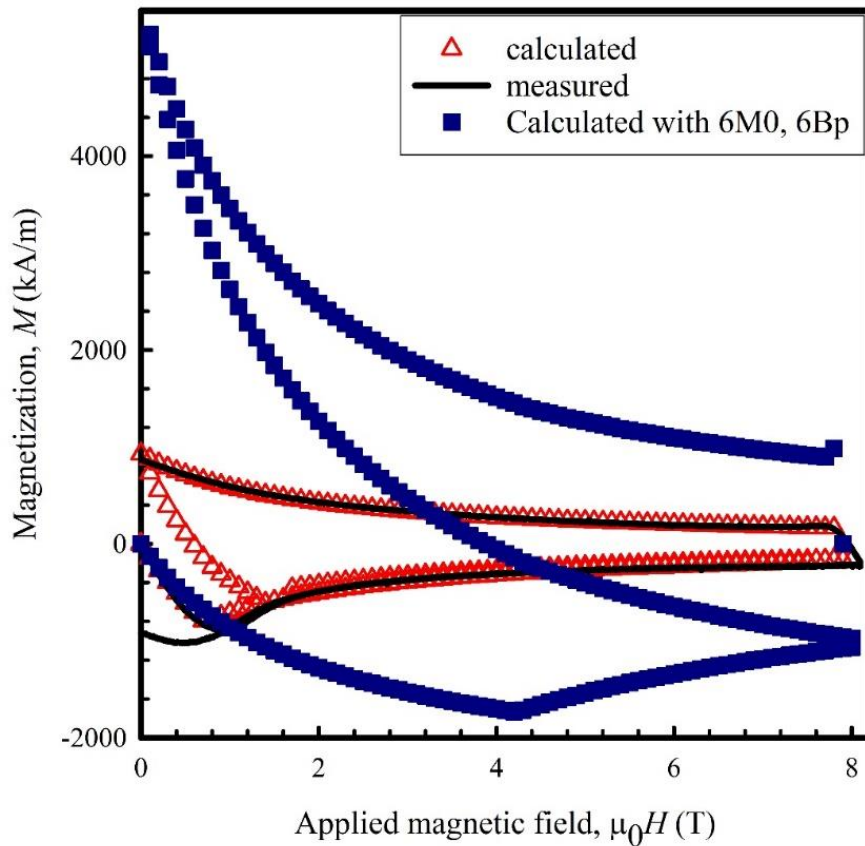


Figure 104. The scaled M - $\mu_0 H$ (blue squares) of the CORC[®] cable calculated using the analytic model. The measured values and the original model results are also plotted, using black lines and open red triangles, respectively.

The result of using the appropriately scaled CORC cable magnetization as an input to Opera to calculate b_3 is shown in **Figure 105**. At lower dipole fields, b_3 is lower in the scaled $M-H$ case than in the non-scaled $M-H$ case, contrary to what would be expected for a simply scaling of $M-H$ by 6.

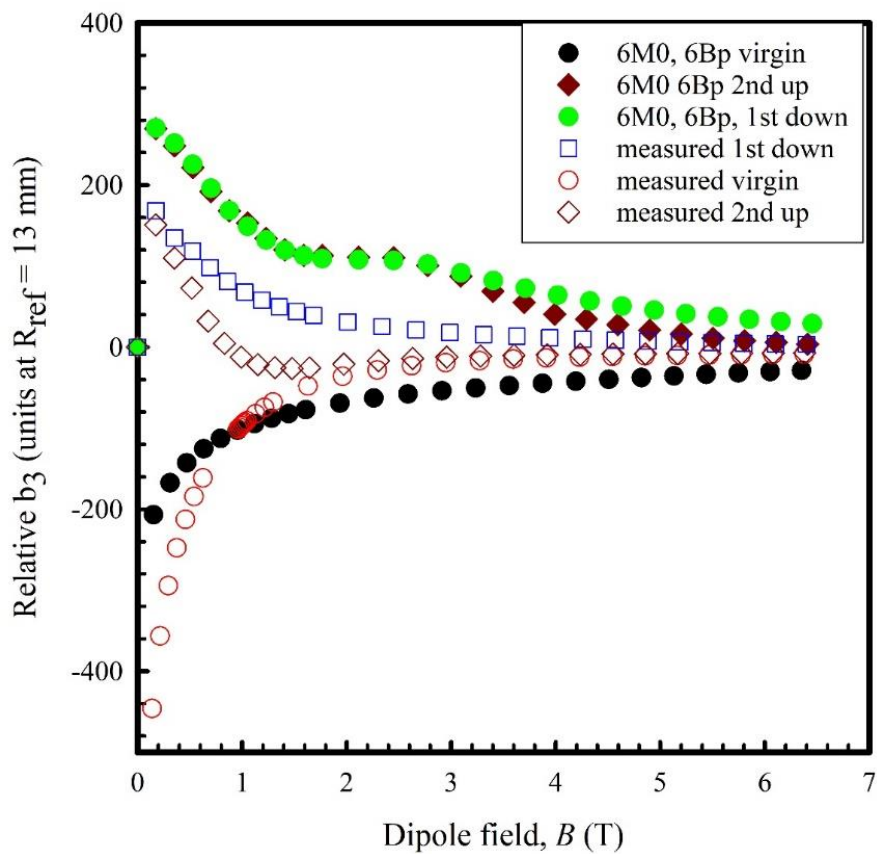


Figure 105. The calculated b_3 for different current ramps using the scaled CORC[®] cable $M-H$ (closed symbols) plotted alongside the calculated b_3 using the original measured values (open symbols).

6.7. Modelling Decay Using the Analytic Model

The software package (Opera) used to calculate the field errors of the accelerator magnet designs does not consider the possible dynamic magnetization of the superconductor. However, the evolution of the field errors can be calculated by scaling the measured magnetization, using the measured decay rates of the CORC[®] cable, and using that scaled magnetization as input to the software. The results of magnetization decay measurements performed on the CORC[®] cable, for different pre-injection cycles, were presented in Chapter 5. The decay rate was found to be higher if the field reversal was performed greater than B_p from the target (injection) field, so that the cable was fully penetrated with magnetic flux. The decay was approximately 8% after 600 s and approximately 10% after 1200 s for the CORC[®] cable in 1 T applied field in this case. Therefore, the magnetization calculated using the analytic model for the 2nd up branch of the hysteresis loop was scaled by 0.92 to represent the magnetization that would be present in the CORC[®] after the flux creeps for 10 minutes and 0.9 was used to scale the data to represent the case where the flux creeps for 20 minutes. The $M-H$ (converted to $B-H$) for the two cases were used as inputs to the Opera software to calculate the field errors for these 2 cases. The results are presented in **Figure 106**, alongside the calculated field errors, assuming no decay, of the analytic model calculated magnetization. Because the magnetization decreases by about 8% and 10% over 10 minutes and 20 minutes, respectively, one might assume that the field errors would change likewise. The results presented in **Figure 106** do appear to confirm this assumption, as the sextupole component

of the magnetic field has changed by about 3-4 units after 20 minutes at B_p . Although any change in the field error with time is not desired, this change is perhaps not so large.

However, one must also consider that the rate of decay likely depends on the tape used to make the cable. Tapes made from superconductor that have different pinning strengths will likely show different field error change rates (due to the different flux creep rates). This fact is illustrated with the decay reduction with increasing Zr addition of the MOCVD processed tapes discussed in Chapter 4. The bottom line is that the creep of the tape used to make the cable will influence the drift and that influences b_3 . It looks like for this magnet design and for this size and type of sample that the b_3 change is not particularly large, but, in general, it could potentially be large.

The results of experimental measurements of the magnetic field components and their decay of a prototype CCT dipole accelerator magnet made from CORC[®] cables are presented in the next section.

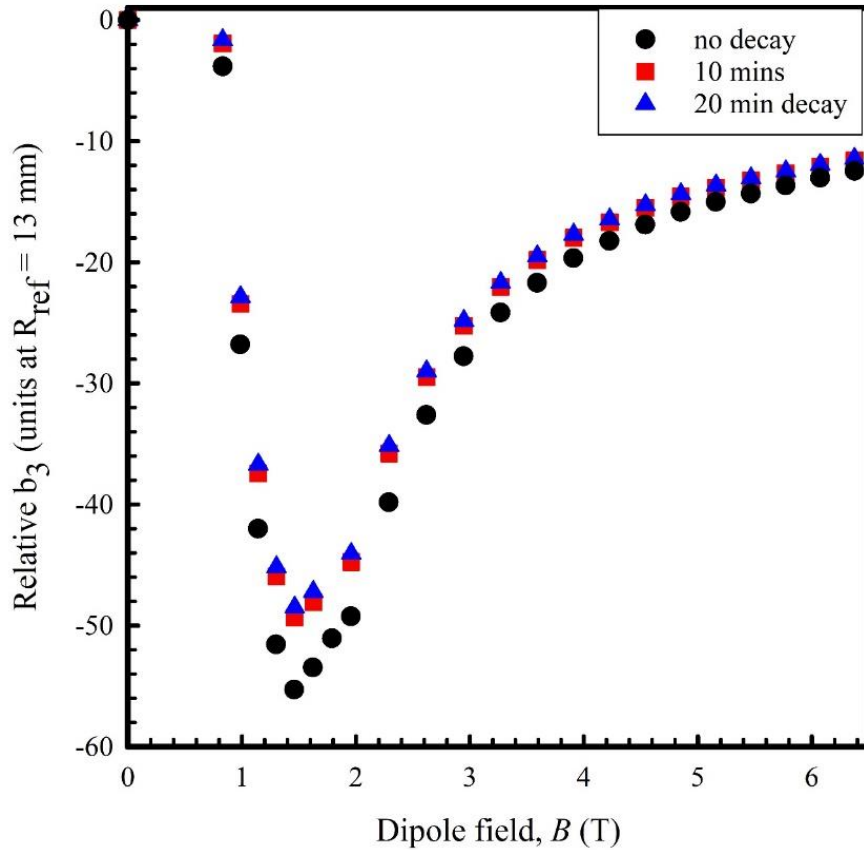


Figure 106. The calculated b_3 , of the field for the 2nd up ramp (from 0 A) of the current in the standalone block dipole magnet. The analytic model was used to calculate the $M-\mu_0H$, and it was scaled by the fraction of the original $M-\mu_0H$ seen after 10 min. and 20 min.

6.8. Field Quality Measurements of a CORC[®]-based Canted $\text{Cos}\theta$ Magnet

As part of the U.S. Magnet Development Program (USMDP), Bi:2212 and REBCO-based insert magnets are being developed for the goal of building 20 T dipole magnets. The field quality of the magnets is important to assess and limited reports on HTS

accelerator magnet field quality measurements are available. Furthermore, drift in the field quality resulting from flux creep in HTS is an important consideration.

Here the results of field quality measurements of a CORC[®]-based insert magnet measured at 77 and 4.2 K, self-field, are reported. The insert coil was based on the canted cosine theta design. The fully assembled magnet is shown in **Figure 107**. A rotating coil fluxmeter, see **Figure 108**, was used to measure the generated magnetic field harmonics and their evolution with time. This fluxmeter is described in detail in [124]. The coil is a printed circuit board (PCB) with a series of traces that form loops on the circuit board. These loops are combined with other loops to perform bucking. An example is shown in **Figure 109**. The PCB is supported inside a shaft that is rotated using a motor which resides outside the magnet. The angular position and probe signals are related to the data acquisition electronics using an internal encoder and slipring. The rotating coil shaft can be driven to different depths within the bore of a magnet using an outside motor. Using this, the magnetic field harmonics can be measured at different position along the bore of the magnet.

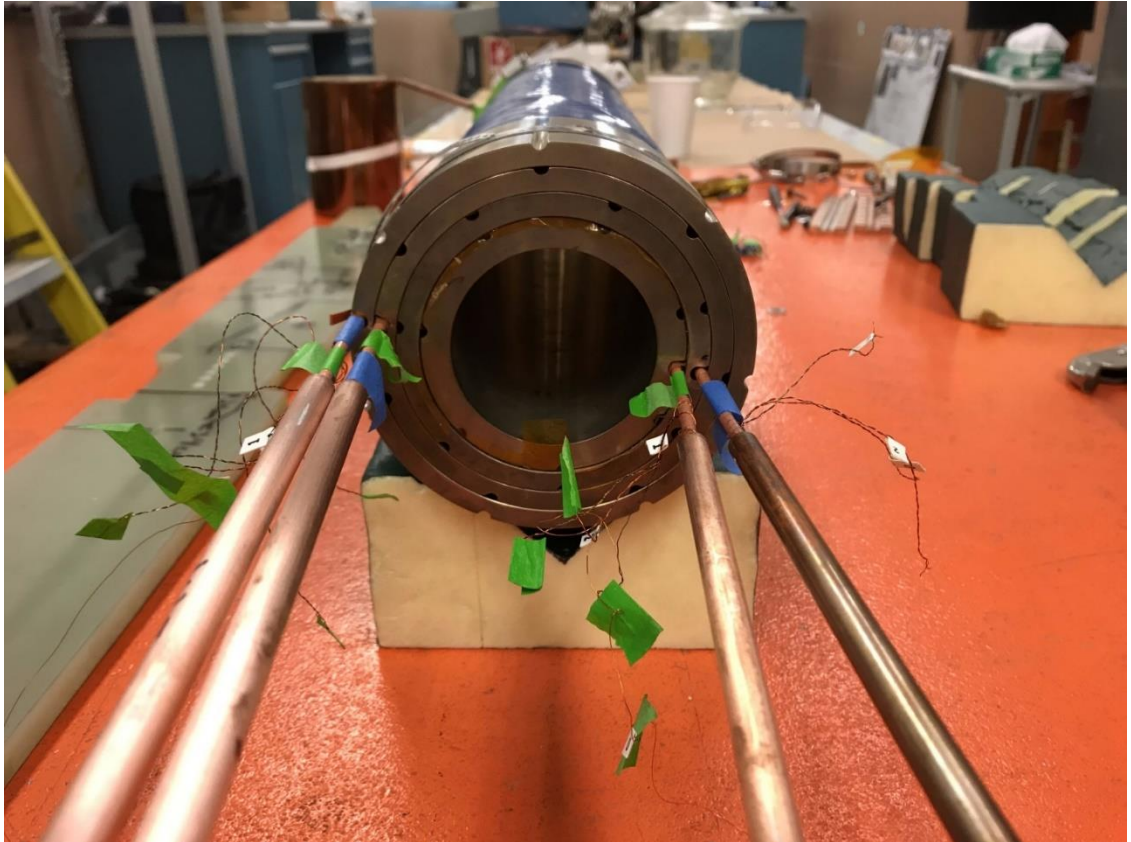


Figure 107. The fully assembled 40 turn, 4-layer canted cosine theta accelerator magnet.

6.8.1. Experimental Procedure for Direct Measurement of Dipole Field Error

The field quality of a 40 turn, 4-layer CORC[®]-based accelerator magnet was measured at 77 K and 4.2 K using a rotating coil fluxmeter, shown in **Figure 108**. The main dipole field and its harmonics were measured as a function of position to determine the magnetic center. The harmonics were also measured at the center of the magnet during current ramping, up and down. At 77 K, the field vs position scans were performed with

200 A in the magnet. The current was injected into the magnet at rates of 10, 20, 50, 100, 200, and 300 A/s, up to a maximum current of 400 A. At 4 K, the field vs position scans were performed with 4 kA in the magnet. The current was injected into the magnet at rates of 10, 20, 50, 100, 200, and 300 A/s up to 4 kA. At 4 K, the magnet current reached a maximum of 6.3 kA which generated a maximum dipole field of 2.91 T.

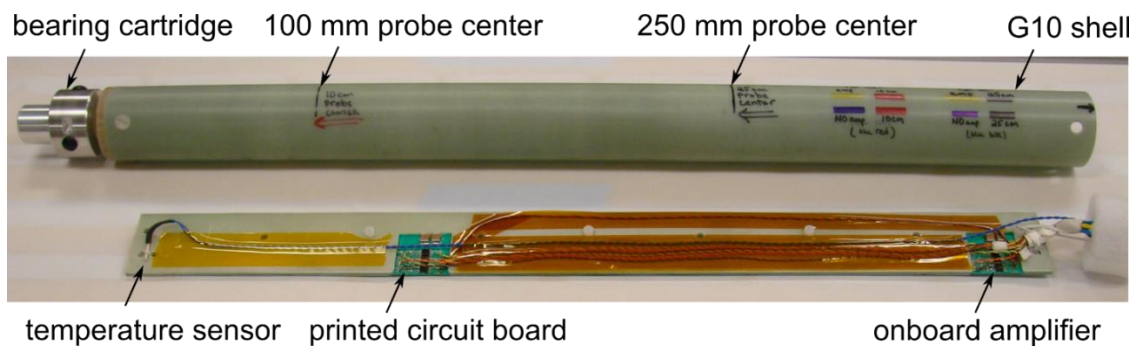


Figure 108. The rotating coil fluxmeter used to measure the magnetic fields and their decay in the 40 turn, 4-layer CORC[®]-based canted $\cos\theta$ accelerator magnet.

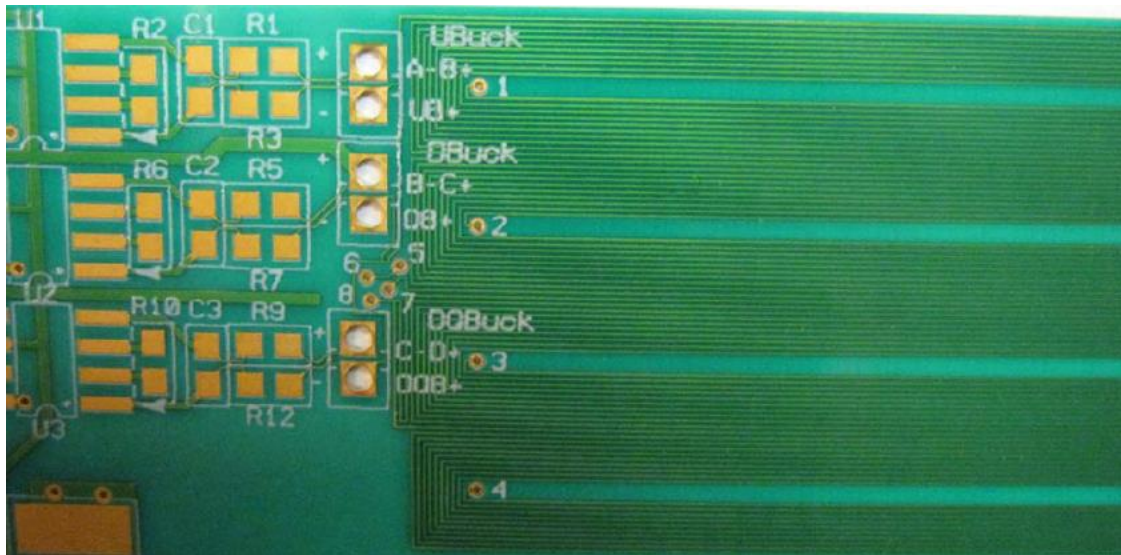


Figure 109. An example of a 20-turn (10 on front/back), 4-winding, PCB with amplifier circuit, from [124].

6.8.2. Ramp Rate Dependence of Transfer Function at 77 K

The ramp rate dependence of the dipole field (**Figure 110**) and the transfer function (**Figure 111**) was measured using ramp rates of 25, 50, 100, 150, and 200 A/s. Any contribution to the field due to Eddy currents should depend on the ramp rate of the magnet current. Because no significant dependence on ramp rate was observed, it is assumed that Eddy current contributions to the dipole field are small. The hysteresis in the magnet is evident.

6.8.3. Ramp Rate Dependence of Field Error at 77 K

The geometric field harmonics, b_3 , b_5 , and b_7 , were calculated as a function of magnet position and compared to the measured field harmonics. They are shown in **Figure 112-Figure 114**. The measured harmonics are significantly larger than expected from the geometric case wherein the wire is assumed to possess no magnetization. The calculated and measured harmonics at the magnet center are presented in **Table 18**.

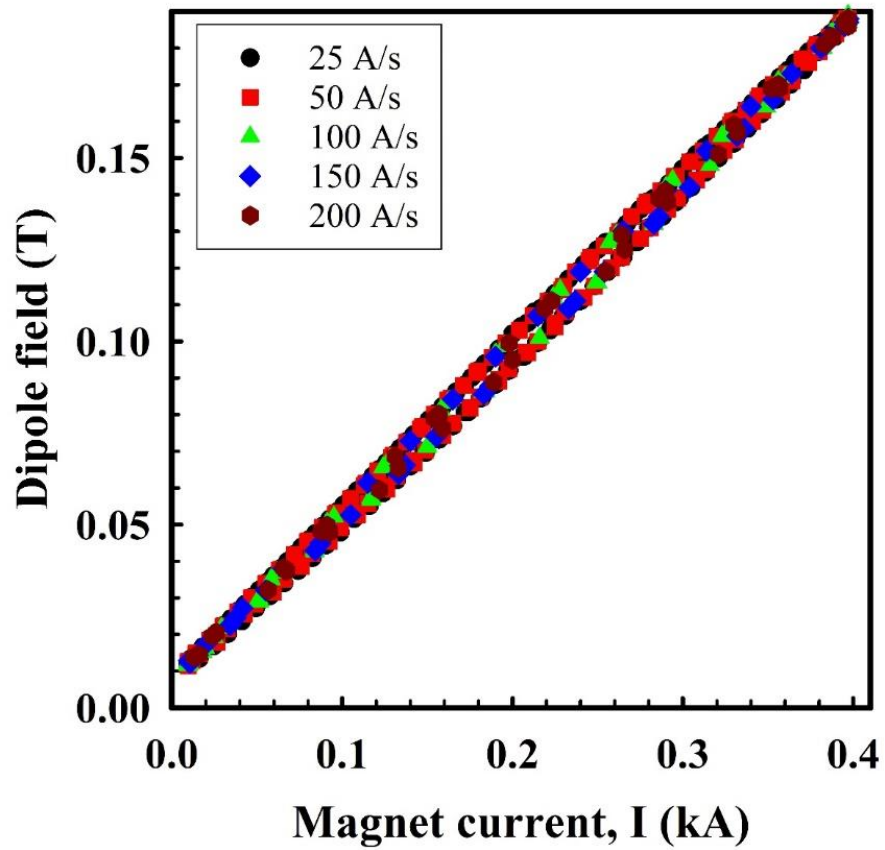


Figure 110. The dipole field generated at magnet currents up to 400 A using ramp rates of 25, 50, 100, 150, and 200 A/s. There is no significant dependence on ramp rate.

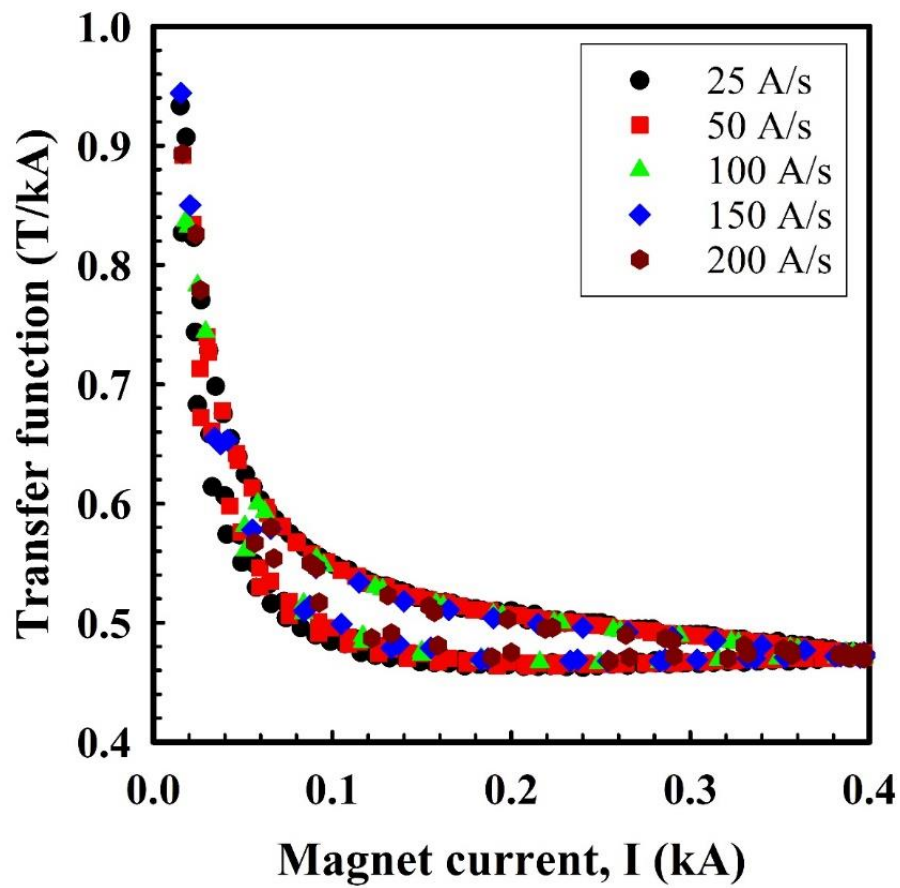


Figure 111. The transfer function generated at magnet currents up to 400 A using ramp rates of 25, 50, 100, 150, and 200 A/s. There is no significant dependence on ramp rate.

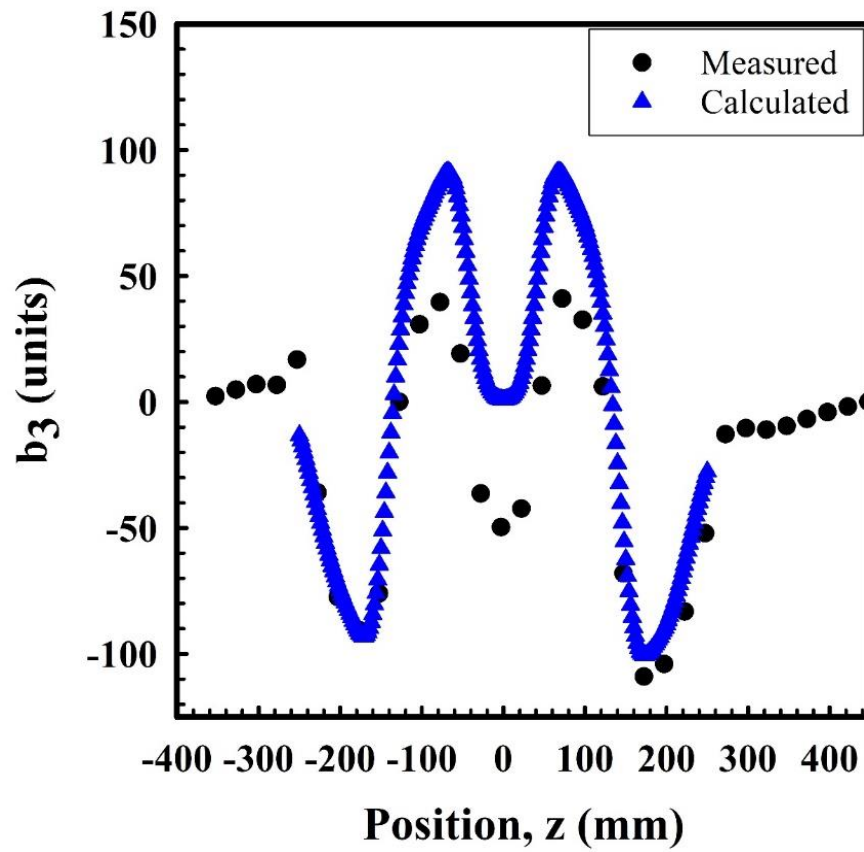


Figure 112. The calculated geometric sextupole component of the field, b_3 (blue triangles) and the measured b_3 , using the rotating coil fluxmeter, as a function of position along the bore of the magnet.

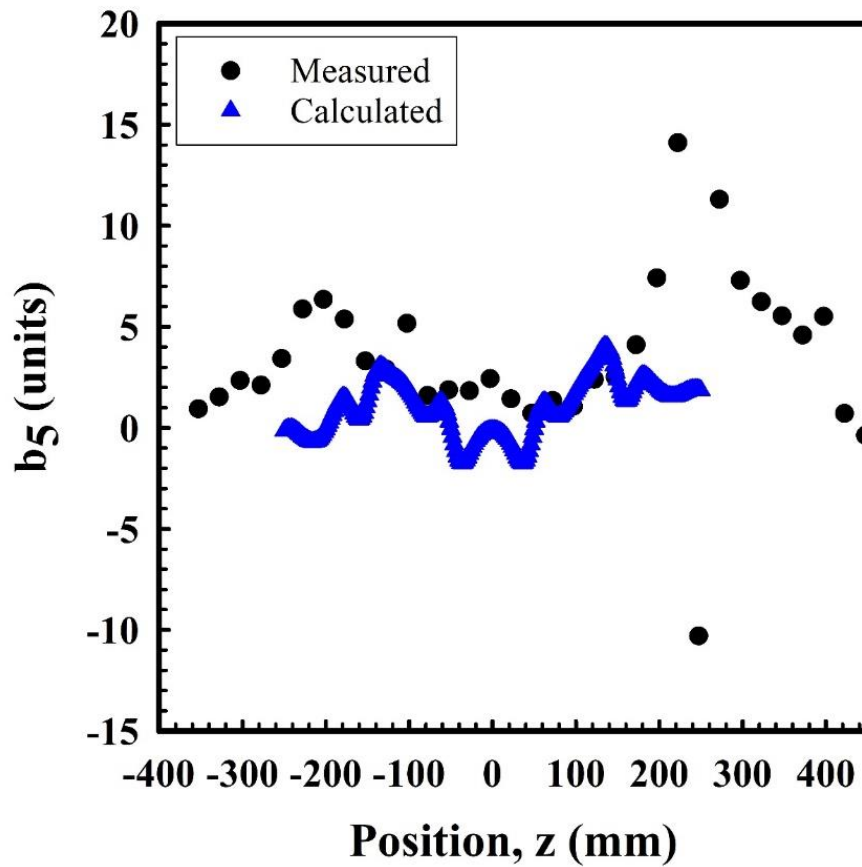


Figure 113. The calculated geometric decapole component of the field, b_5 (blue triangles) and the measured b_5 , using the rotating coil fluxmeter, as a function of position along the bore of the magnet.

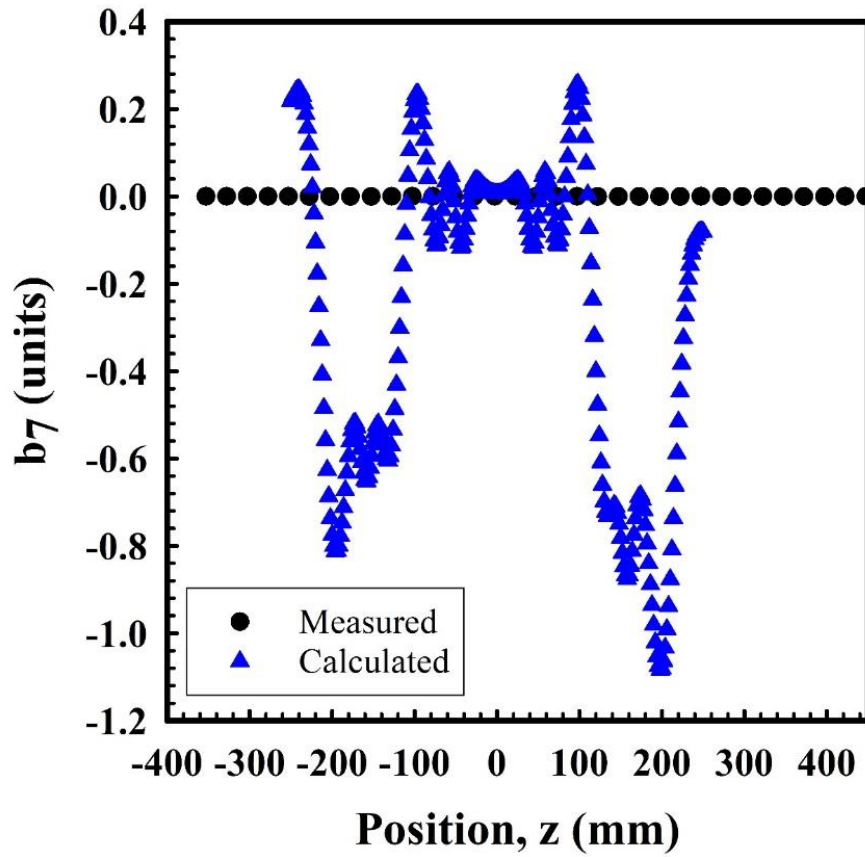


Figure 114. The calculated geometric b_7 component of the field (blue triangles) and the measured b_7 , using the rotating coil fluxmeter, as a function of position along the bore of the magnet.

Table 18. The calculated and measured harmonics at 77 K at the magnet center.

Harmonic	Calculated (units)	Measured (units)
b_3	0.8162	-49
b_5	-0.1217	2.4
b_7	0.00625	0.000143

6.8.4. Ramp Rate Dependence of Transfer Function at 4 K

The ramp rate dependence of the dipole field (**Figure 115**) and the transfer function (**Figure 116**) was measured using ramp rates of 10, 20, 50, 100, 200 A/s, and 300 A/s. Any contribution to the field due to Eddy currents should depend on the ramp rate of the magnet current. Because no significant dependence on ramp rate was observed, it is assumed that Eddy current contributions to the dipole field are small. A plot of the dipole field vs current for the slowest ramp rate (10 A/s) and the fastest ramp rate (300 A/s) is presented in **Figure 117** for a smaller range of current. The hysteresis in the magnet is evident, and there appears to be little ramp rate dependence of the generated field.

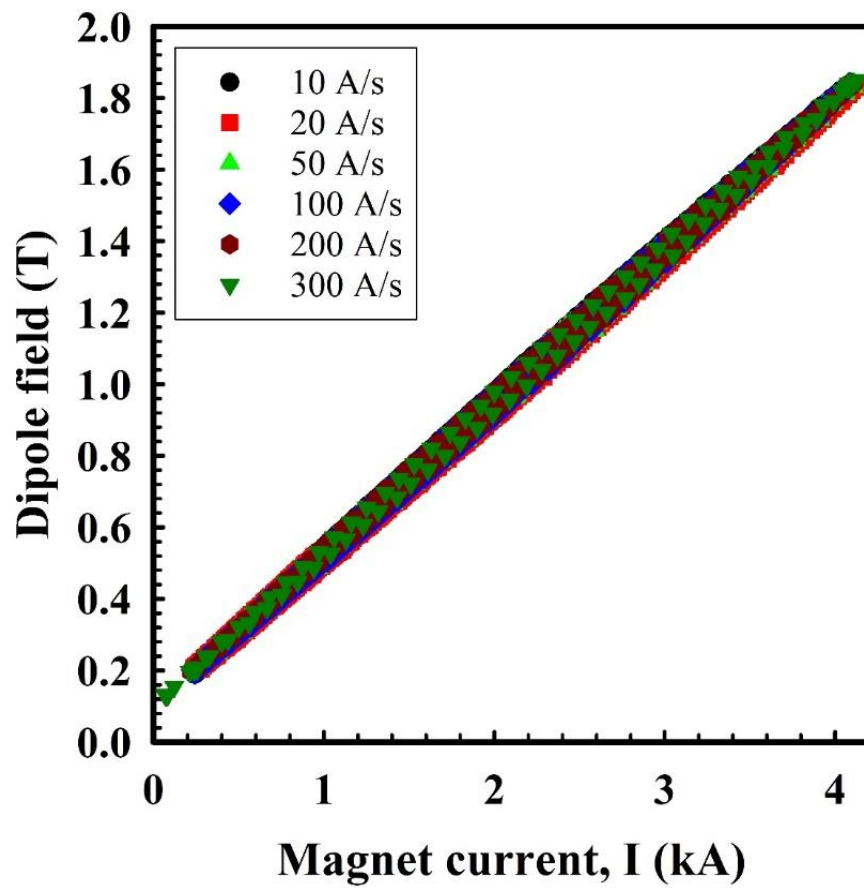


Figure 115. The dipole field as a function of magnet current (I_{mag}) at current ramp rates of 10, 20, 50, 100, 200, and 300 A/s.

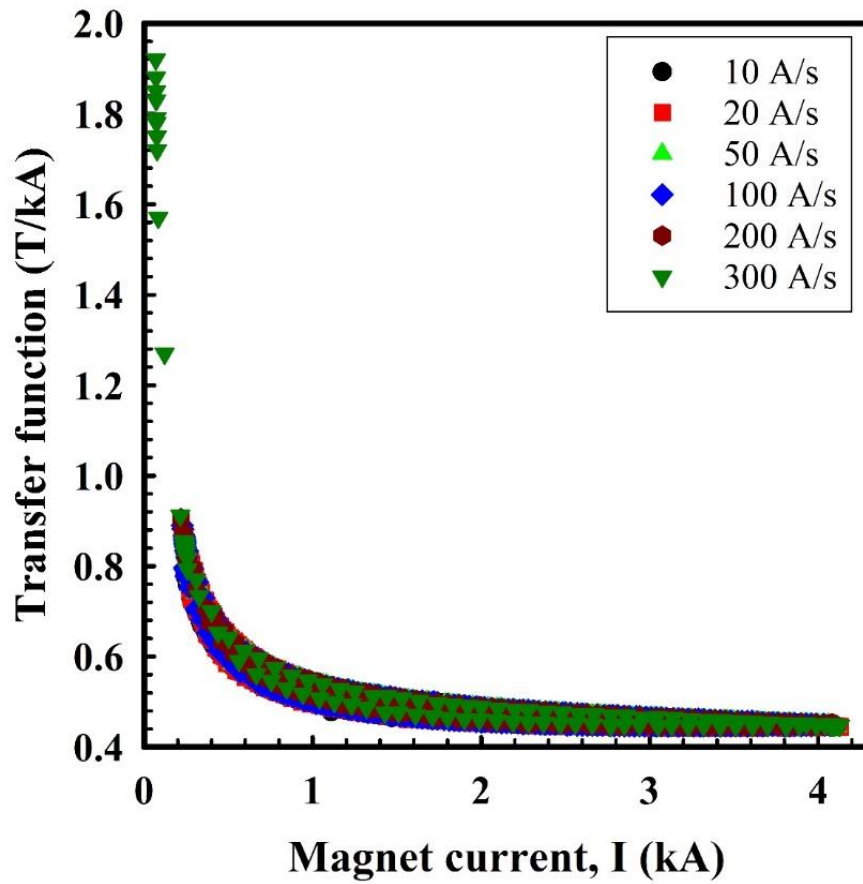


Figure 116. The transfer function (TF) as a function of magnet current (I_{mag}) using ramp rates of 10, 20, 50, 100, 200, and 300 A/s.

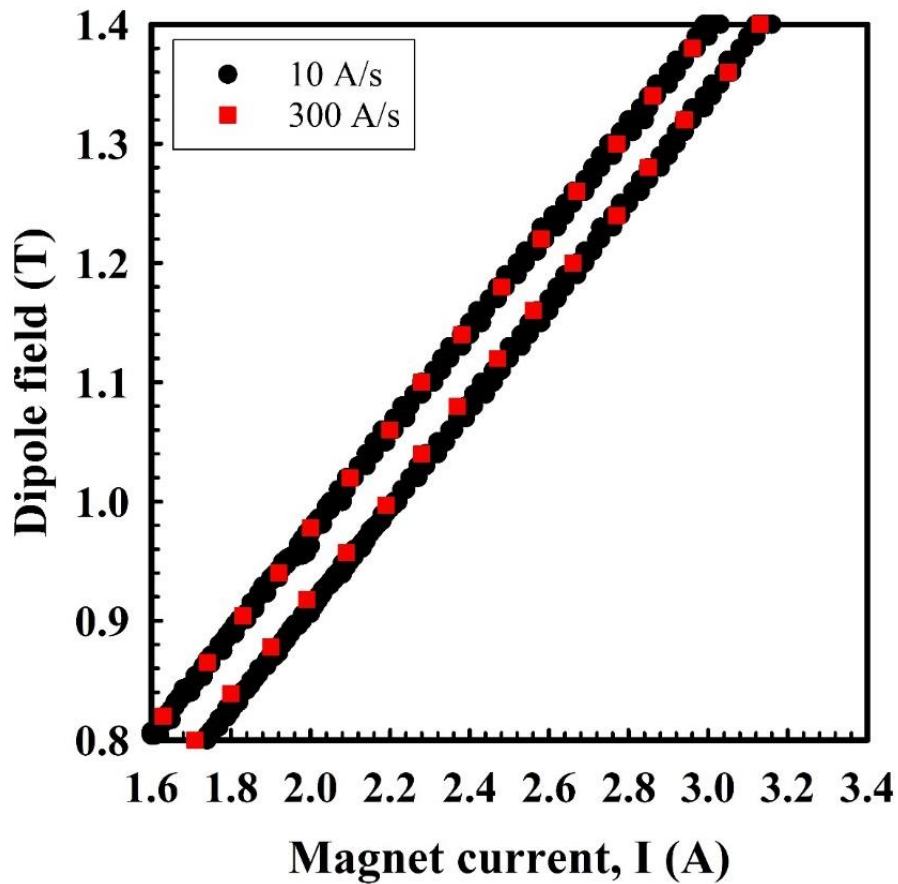


Figure 117. The dipole field as a function of magnet current (I_{mag}) using ramp rates of 10 and 300 A/s.

6.8.5. Ramp Rate Dependence of Field Error at 4 K

The geometric field harmonics, b_3 , b_5 , and b_7 , were calculated as a function of magnet position and compared to the measured field harmonics at 4 K. They are shown in **Figure 118-Figure 120**. The current in the magnet was 4 kA, which generated a dipole field in the bore at the center of the magnet of approximately 1.8 T. The measured

harmonics are significantly larger than expected from the geometric case, wherein the wire is assumed to possess no magnetization. The calculated and measured harmonics at the magnet center are presented in **Table 19**. There is a significant difference between the measured component and the component expected assuming no magnetization effects for all the cases studied here.

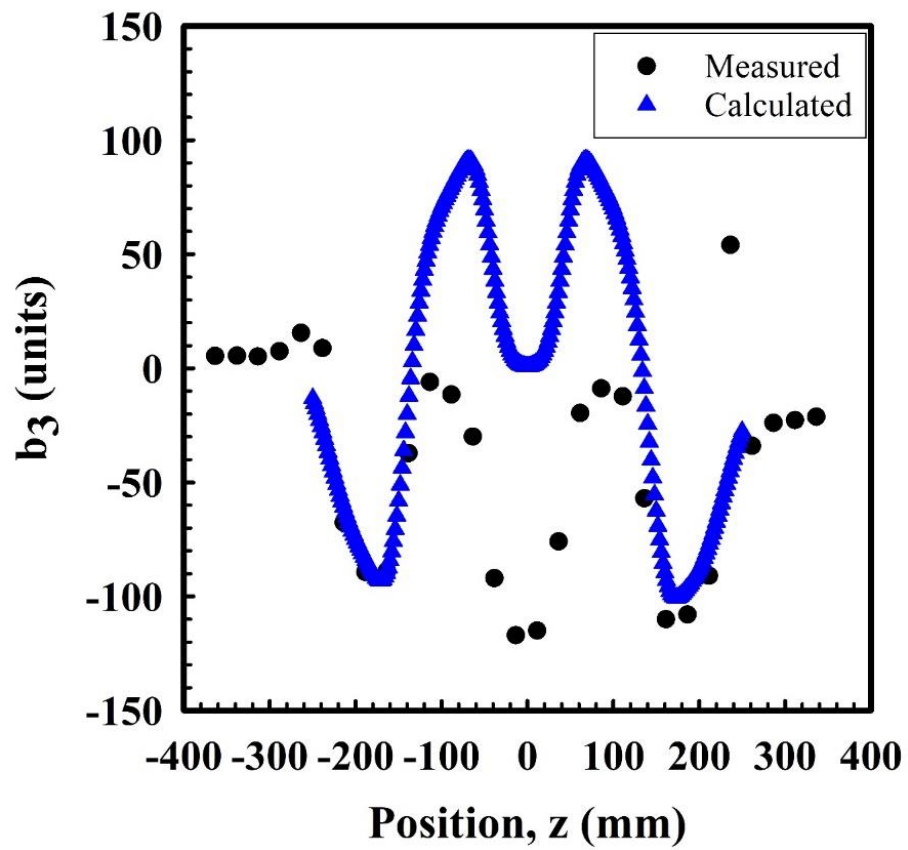


Figure 118. The calculated geometric sextupole component of the field, b_3 (blue triangles) and the measured b_3 , using the rotating coil fluxmeter, as a function of position along the bore of the magnet.

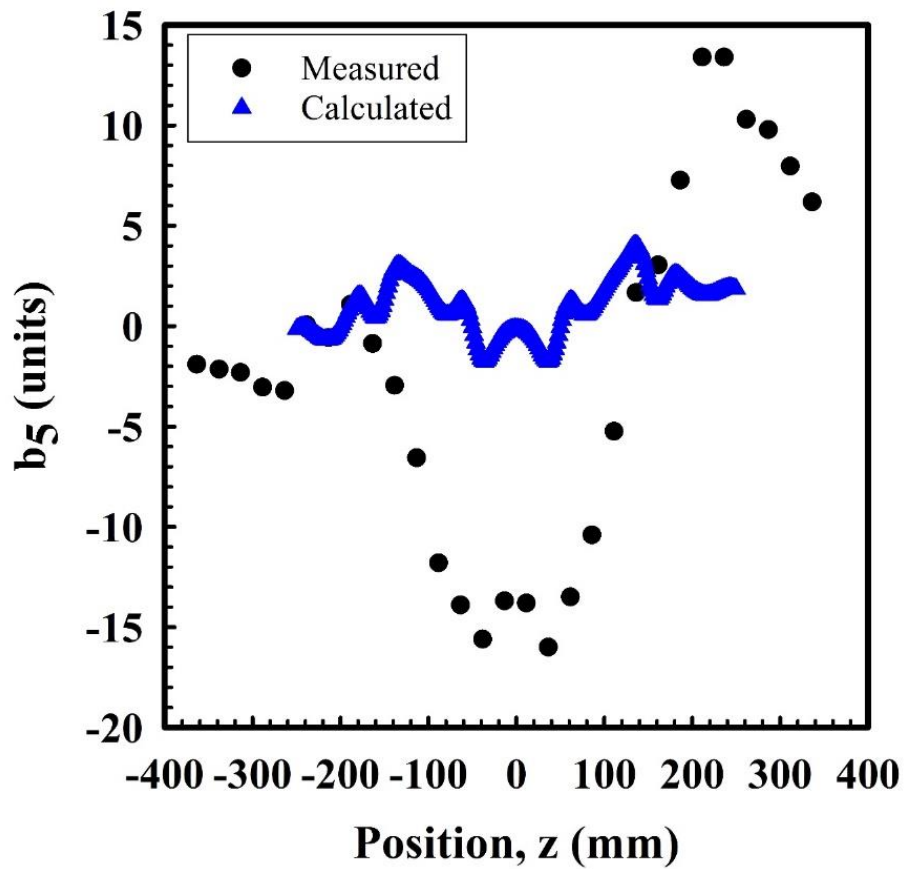


Figure 119. The calculated geometric decapole component of the field, b_5 (blue triangles) and the measured b_5 , using the rotating coil fluxmeter, as a function of position along the bore of the magnet.

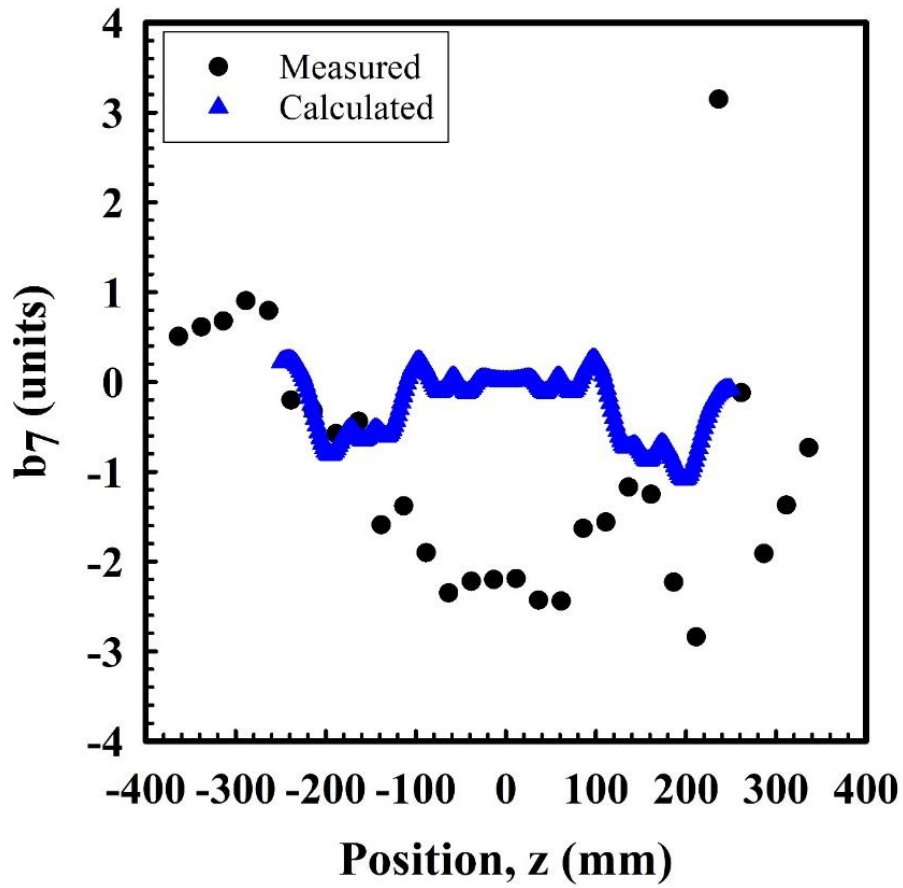


Figure 120. The calculated geometric b_7 component of the field (blue triangles) and the measured b_7 , using the rotating coil fluxmeter, as a function of position along the bore of the magnet.

Table 19. The calculated and measured field harmonics at 4 K at the magnet center.

Harmonic	Calculated (units)	Measured (units)
b_3	0.8162	-116
b_5	-0.1217	-13.8
b_7	0.00625	-2.2

6.8.6. Measured Field Harmonics as a Function of Dipole Field

The field harmonics, as a function of dipole field, were measured at the center of the magnet for the first ramp up from 0 T. The results are presented in **Figure 121** for b_3 and **Figure 122** for b_2 , b_5 , and b_7 . The sextupole component, b_3 , is the most important to consider for the dipole field, but the other components should also be as small as possible. b_3 is clearly very large at the beginning of the ramp, and it decreases as the current in the magnet is increased, which is expected as the magnetization in a superconductor decreases with applied magnetic field. At a typical injection field of 1 T, b_3 is relatively small, approximately 50 units, compared to what it is throughout the ramp. As the field is increased further, the sign of b_3 changes, and it appears to saturate around -100 units above about 2.5 T.

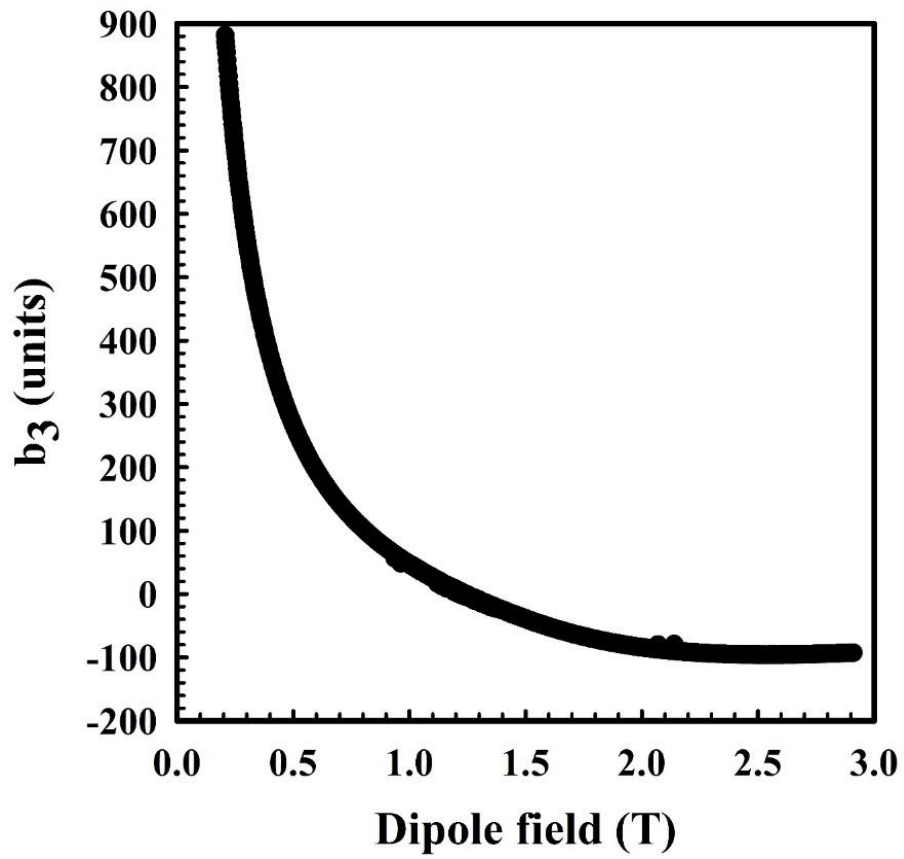


Figure 121. The sextupole component, b_3 , of the magnetic field as a function of dipole field during up ramp from 0 T.

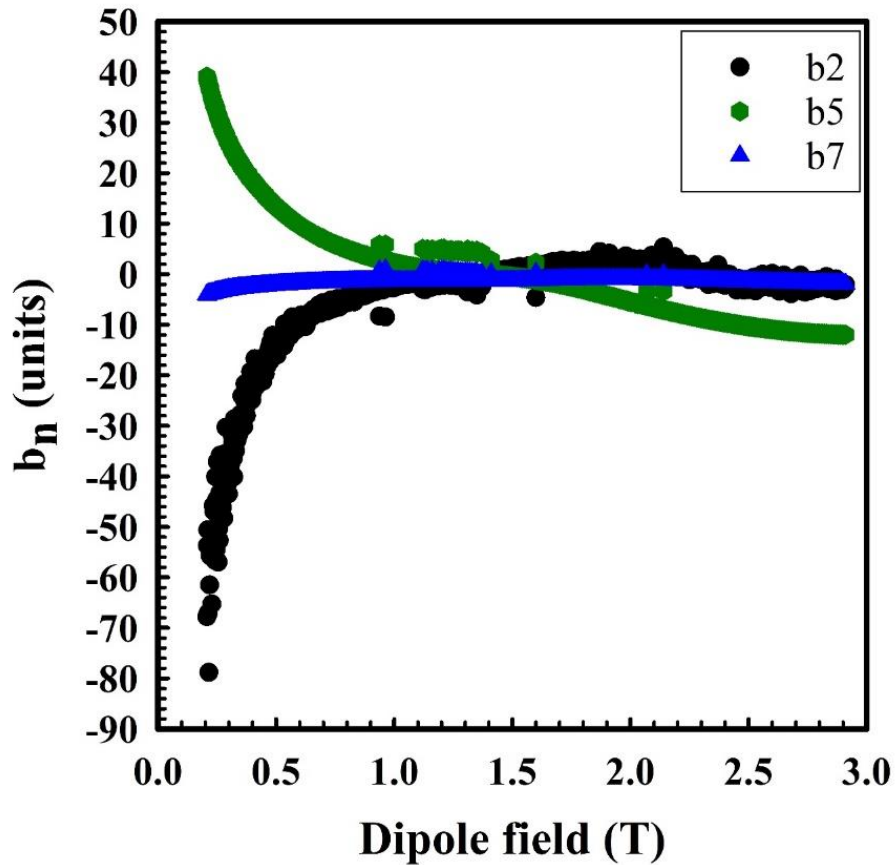


Figure 122. The relative harmonics b_2 , b_5 , and b_7 as a function of dipole field.

6.8.7. Main Field Decay over 30 Minutes after Ramping to 4 kA

The change of the main field with time was measured at 4 kA for 30 minutes. The current in the magnet was ramped continuously from 0 to 4 kA and then held constant for 30 minutes. The results are presented in **Figure 123**. The dipole field increases by approximately 7 mT over 1800 s with the magnet current (I_{mag}) held at 4 kA. The change

in the sextupole component, b_3 , over 30 minutes is shown in **Figure 124**. It is apparent that there is not much change in b_3 over 30 minutes for this magnet. This lack of change in b_3 is unexpected, but it could be due to the power supply continually seeking the set current and therefore causing oscillations in the current. These oscillations would cause the flux profile inside the superconductor of the magnet to continually change and creep would not be significant.

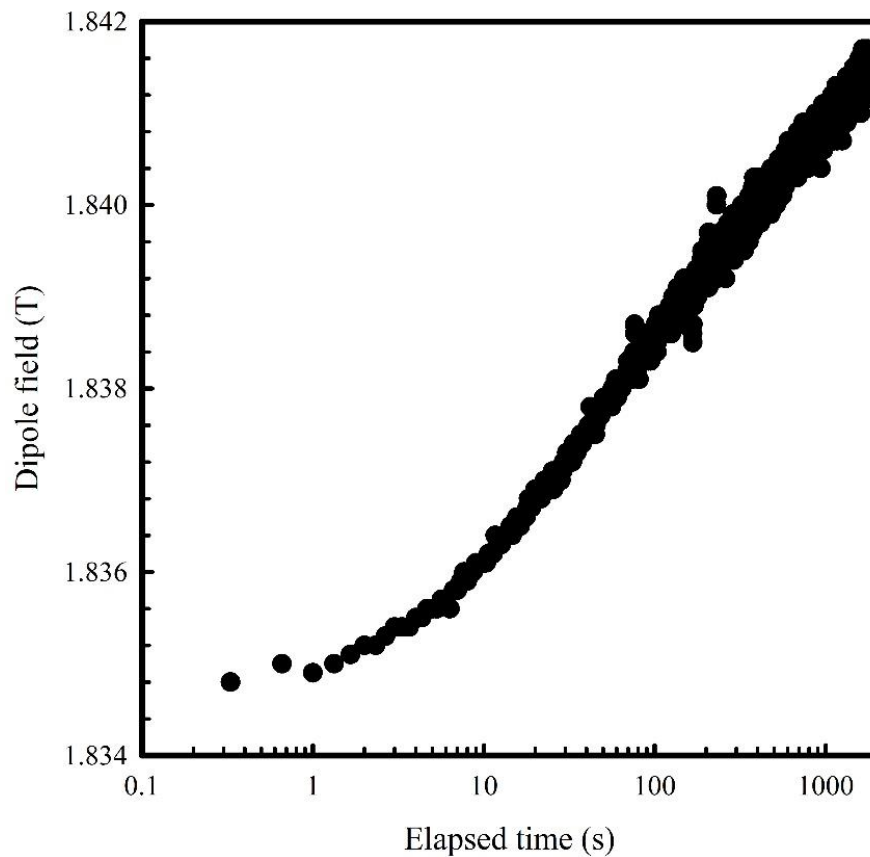


Figure 123. The main dipole change with time with the magnet current held at 4 kA.

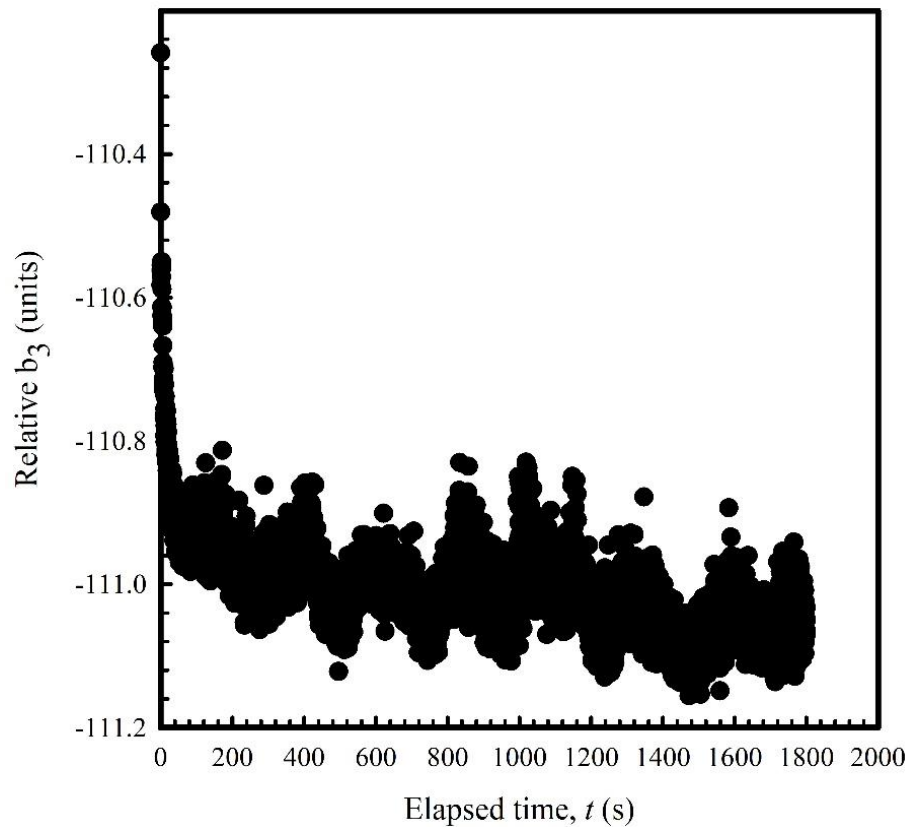


Figure 124. The change in the relative sextupole, b_3 , component of the magnetic field, in the bore of the magnet, with time.

6.9. Summary and Conclusions

The measured magnetization as a function of applied magnetic field for a CORC[®] cable was input into finite element software to calculate the generated magnetic field harmonics, during current ramps relevant to accelerator magnets, of two hypothetical accelerator magnet designs (standalone CORC[®] block dipole and hybrid CORC[®] Nb₃Sn

block dipole) made from the cable. The calculated hysteresis present in the transfer function of the standalone dipole indicated the magnetization of the CORC[®] will significantly affect the generated field of that design. The relative sextupole component, b_3 , of the magnetic field was calculated during various accelerator-relevant ramps and compared to that of the Nb₃Sn-based block dipole, HD3b. It was similar for the two designs.

The powering scheme of the hybrid block dipole design was found to influence the magnetization effects. The calculated transfer functions and b_3 s when powering the CORC[®] and Nb₃Sn coils simultaneously were like the calculated geometric transfer functions and b_3 s, indicating that powering the coils simultaneously may reduce the errors due to the superconductor magnetization. Powering the coils sequentially led to significant differences in the transfer functions and b_3 s when compared to the geometric ones.

Analytic expressions for the magnetization on different branches of the hysteresis loop were developed. These expressions include field dependence and include a term for a “pseudo-reversible” magnetization that was seen in the CORC[®] $M-\mu_0H$ data from Chapter 5. There was excellent agreement between the calculated $M-\mu_0H$ and measured $M-\mu_0H$ of the CORC[®] sample, validating the accuracy of the expressions. The calculated $M-\mu_0H$ was used as input to the finite element modelling software to generate b_3 s for the standalone CORC[®] block dipole magnet design. The calculated b_3 s using the results from the analytic expressions were found to be in excellent agreement with those calculated using the measured $M-\mu_0H$, validating the expressions. These expressions can now be used to

generate $M-\mu_0H$ curves of conductors without the need to directly measure them, saving time, money, and helium resources.

The magnetic field components and their decay of a 4-layer, 40 turn canted cosine theta magnet made from CORC[®] cable was measured at 77 K and 4 K. The maximum magnetic field generated by the magnet was 2.91 T at 4 K, with 6.3 kA in the magnet. There was no significant ramp rate dependence of generated field, indicating that there were not strong eddy currents in the magnet at these ramp rates. The measured field errors at the center of the magnet were significantly larger than the expected geometric field errors. A significant change in the dipole field over 30 minutes was observed, but b_3 did not change appreciably over this time.

Chapter 7: Summary and Conclusions

High temperature superconducting (HTS) composites are being considered for the dipole and quadrupole steering magnets of future high energy colliders (such as the future circular collider (FCC)) as they may require magnetic fields of 20 T or greater, much larger than those that low temperature superconductors (LTS) can produce. However, HTS possess persistent current magnetization values which are significantly larger than those of Nb₃Sn-based LTS composites. For Bi:2212 composites this magnetization may be more than 10 X larger than that of Nb₃Sn composites, and REBCO conductor magnetization may be up to two orders of magnitude larger than those of Nb₃Sn composites. Large magnetization (proportional to d_{eff}) is unacceptable for accelerator magnets because it distorts the field used to guide and focus the charged particle beam. These distortions can cause a loss of the beam or an increase in the spread of the beam, or both. Additionally, HTS materials exhibit a time decay (creep) of their magnetization, due to a flux creep much larger than that of LTS, even at the temperatures of operation (≈ 4 K) used for accelerator magnets. This decay can be an even greater problem than static magnetization because it may cause time-dependent field errors which might require more sophisticated error correction schemes. Therefore, it was necessary to develop accurate methods to quantify and model these magnetizations and their decay, to calculate how these magnetizations and flux creep will manifest themselves as field errors in magnets. It was also important to

examine whether there are methods to reduce the impact of both these larger magnetizations and creep rates on such field errors. This thesis describes direct measurements of the magnetization and decay of Bi:2212 strands and their connection to strand microstructure. Subsequently, the magnetization and decay of YBCO conductors and the influence of nanostructure, in terms of both YBCO-tape deposition mode and choice of dopant, is explored. The focus then moved to the magnetization of cables wound from HTS conductors, and finally the multipole field errors induced in magnets as computed via finite-element modelling.

7.1 Bi:2212 Microstructure and Magnetic Property Correlation

The magnetization of various Bi:2212 strands has been measured and correlated with microstructure in Chapter 3 of this thesis. The phenomena of filament “bridging” within subelements is well known, but what has not been fully understood has been a detailed connection to microstructure and the functional dependence of magnetization on sample parameters such as sample length (L) and sample twist pitch (L_p). This thesis has directly measured L and L_p dependencies of the magnetization of a set of Bi:2212 strands and demonstrated a strong linear increase of magnetization with increasing L and L_p . This result flows naturally from modelling the strand as an anisotropic continuum, and a relevant model is applied to explain this linear behavior. One practical result of this work is a recognition that the often-used short sample measurements of Bi:2212 samples (5 mm

length, typically) are inadequate for extracting the true magnetization or d_{eff} of the Bi:2212 strands; and a demonstration that such measurements are unreliable.

Indeed, extracted values of d_{eff} can be different if samples of different lengths are measured, especially where the lengths are sufficiently short that the magnetization has not saturated. Direct measurements on a set of Bi:2212 samples showed d_{eff} values which ranged from 150 μm to 300 μm . A set of equations has been used to describe the length dependence of the magnetization and to quantify the transverse electrical connectivity (that is independent of sample length) between Bi:2212 filaments. The resulting “connectivity factor,” γ , was found to be ≈ 0.002 , indicating an effective transverse superconducting area fraction of 0.2%. Twisting the Bi:2212 strands reduces d_{eff} , but allows the extracted γ to be constant. This fact indicates that γ is a more fundamental measure of strand bridging. Furthermore, the decay of the magnetization of longer samples (accompanied by increased interfilamentary bridging) was seen to be higher than that of shorter samples. It is postulated that the larger decay in longer samples is because the bridging material possesses a lower pinning strength than the filamentary material. This thesis work has shown that magnetization measurements, when used to estimate field errors or the field error drift of accelerator magnets built from Bi:2212 must be made on samples such that $L_p \ll L$.

7.2 YBCO Nanostructure: Additions and Magnetic Property Correlation

Chapter 4 of the thesis explores the magnetization and creep of YBCO conductors, made by two different processes: Pulsed Laser Deposition (PLD) and Metallo-Organic Chemical Vapor Deposition (MOCVD). In recent years, much effort has pursued the increase of J_c performance in these conductors with the addition of various dopants to act as or form pinning centers; here I explore two of the most successful pinning additions: 211 and BZO. The J_c increase that accompanies the inclusion of these pinners is well documented, however, the influence of the pins on flux creep is only modestly explored, especially at temperatures of interest for accelerator magnets (4 K). While the thermal activation origin of the results might at first glance suggest such creep effects are small (creep rate $\propto k_B T/U_0$), the fact that the effective pinning strength scales as $U \sim U_0(J_{c0}/J)^\mu$ shows that effective creep rate increases with the large critical currents that accompany operation at low temperatures. Magnetization creep, its parameterization at low temperatures, the extraction of intrinsic pinning well sizes, and their correlation to microstructure is the focus of Chapter 4. One of the key questions of interest was this: while we may introduce pins to increase J_c for use in accelerators operating at 4 K, do these pins increase magnetization creep, leave it the same, or reduce it? In terms of direct summation models, we might expect to increase J_c either with many small pins or a few larger ones; the former would increase creep, the latter reduce it.

Magnetization decay measurements were made on a variety of YBCO samples, and then a Maley approach was used to scale the resulting creep results to lie on a universal

(for that sample) curve of pinning vs B and T . The overall shape of the pinning force as well as its magnitude suggested that the pinning retained a collective character. It was possible to successfully fit the data using a collective creep model, and U_0 values were extracted. Initial inspection led to the observations that the 211 additions increased the J_c of PLD samples, but did not modify the creep rate significantly, suggesting that the 211 and intrinsic pins were of similar size. This is consistent with previous results which have suggested that the strain fields induced by the 211, rather than the precipitates themselves, are responsible for the enhanced J_c . The BZO pins, on the other hand, both increased the J_c of the MOCVD samples and reduced their creep rate, suggesting that the BZO pins were deeper than the intrinsic pins. Further analysis using the Maley approach and a collective pinning fit, clarified, however, that the MOCVD intrinsic pins were weaker than the intrinsic PLD pins ($U_0/k_B \approx 480$ K for MOCVD and 650 K for PLD), while the 211 pins were similar to intrinsic PLD ($U_0/k_B \approx 650$ K) and the BZO pins were stronger ($U_0/k_B \approx 1000$ K). Other, direct models for pinning were considered, but did not seem to be consistent with the measurements, both in terms of the overall shape of the U vs J curve, as well as the modest change of pin strength with a radical change in pin aspect ratio. While the many/weak vs few/strong pin picture is too simplistic a view, given the collective pinning interpretation used here, it is clear that the expectation that highly aspected and c-axis aligned pins would give very deep pinning centers is not consistent with the experimental results. Both direct decay analysis as well as more sophisticated analysis suggest that very high aspect ratio (~ 100) BZO pins are only twice as strong as low aspect

ratio (~ 5) 211 pins. For practical applications, the results indicate that different dopants can give different pinning strengths and can affect not only the J_c and magnetization but also the creep rate which in turn may influence the magnetic field drift of the generated field of a magnet. In these studies, creep rates of up to 15% of the initial magnetization value were seen at 4.2 K.

7.3 Magnetic Properties of Cables and their Influence on Accelerator Magnets

HTS conductors need to be cabled for use in the windings of accelerator magnets. These cables will not necessarily have the magnetic properties of the short tapes or strands from which they are comprised due to, for example, length dependent magnetization effects or twisting of the individual strands or tapes which make up the cables. Therefore, results of measurements on the cables, rather than the short samples, should be used to assess whether the magnetization, and its drift, are acceptable for use in an accelerator magnet. Facilities for measuring the magnetization of HTS cables are rare. Such facilities are very large and expensive, both in terms of operation cost and amount of sample required. The devices commonly used for magnetization measurements: vibrating sample magnetometers, extraction magnetometers, or squid systems, typically accommodate samples no longer than about 5 mm. Thus, it was necessary to construct a new device which could be used to measure HTS cables. Chapter 5 discusses the development of a Hall probe magnetometer to measure HTS cables. The Hall probe magnetometer, developed as part of this thesis, used a 12 T conduction cooled magnet and a variable temperature insert. The

sample was mounted on a probe fitted with a hall probe and the results were fed into a Labview system which both analyzed the results and operated the magnet system.

The Hall probe magnetometer was then used to measure the magnetization and the magnetization drift of CORC[®] and Bi:2212 Rutherford cable segments which were extracted from prototype accelerator magnets. The cable samples, at 3 cm, were too long to be measured in a typical magnetometer. The magnetization of the CORC sample was compared to that of the tape it was wound from, and the results, as expected, were quite different ($M_{\text{peak}} \approx 3500$ A/m for the tape, $M_{\text{peak}} \approx 2800$ A/m for the cable (per unit tape volume)). Just as significantly, it was found that the penetration field of the CORC[®] cable ($B_p = 1$ T) was much larger than that of the tapes ($B_p = 500$ mT) used to make the cable. This result is important because magnets built from materials which possess a large penetration field (e.g. CORC[®] cables) require a larger current sweep range to erase previous magnetizations. The CORC[®] cable was also found to have a higher magnetization at the penetration field when compared to that of the tape from which it was built. This result is important because higher magnetization could lead to larger field errors in the magnet. The magnetic decay for the CORC[®] sample was larger than that of the tape sample if no field cycling procedure is used to mitigate this decay. However, it was possible to develop a field cycle which could reduce the magnetization at the start of decay and reduce the change in magnetization over the decay time. This is important because the larger decay rate could lead to larger changes in the field errors with time, but field cycling may be able to mitigate these changes. $M-H$ was also measured for a Bi:2212 Rutherford cable, and it

was possible to extract d_{eff} values for the individual strands (170 μm). Magnetization decay was also explored for the Bi:2212 Rutherford cable.

7.4 Effects of Magnetization and Creep on Magnetic Fields Error in HTS Accelerator Magnets

Chapter 6 details the modelling of the multipole errors in a few specific accelerator magnet designs using a combination of directly measured or analytically modelled HTS cable magnetizations and FEM modelling. Finite element software, Opera 2D, was used to calculate the effects of magnetization and its decay on the field quality of two different types of accelerator magnet designs: (1) a standalone CORC[®] cable-based block dipole design; and (2) a hybrid block type dipole made from CORC[®] and Nb₃Sn Rutherford cables. The magnetization of the CORC[®] was significantly larger than that of Nb₃Sn and both the calculated transfer function and relative sextupole components of the CORC[®]-based dipole exhibited larger magnetization effects than that of the same design made using Nb₃Sn Rutherford cables. The order of the powering of the hybrid design has an influence on the magnetization effects. An analytic model was developed that can be used to predict the magnetization of a CORC[®] cable for all segments of the M - H loop cycle. This magnetization can be used as an input to FEM software to calculate field quality without the need to directly measure the M - H of each new generation of CORC[®] cable. A rotating coil fluxmeter was used to measure the field quality of a 4-layer 40 turn CORC[®] cable-based canted cosine theta (CCT) magnet at 77 K and 4 K and as a function of dipole field.

The field errors were large, and the field quality was significantly worse than that predicted assuming the windings do not become magnetized. This result indicates that the magnetization of REBCO-based cables can significantly affect the field quality of accelerator magnets. The dipole field with a constant current was measured over 30 minutes, during which a small measurable change in the dipole field was observed.

This thesis deals with the influences of nanostructure and microstructure on the magnetization and creep of Bi:2212 and YBCO coated conductors as influenced by fabrication, processing, and the introduction of dopants. Property modifications in response to cabling these conductors is then considered, particularly the magnetization and decay of Bi:2212 and YBCO-based cables is measured. Finally, the results of direct measurements of YBCO cable magnetization are used to compute field errors in a nominal drop in replacement design for a dipole magnet, and this is compared to an LTS design. An analytic model is developed for YBCO CORC[®] cable magnetization for all segments and is then used to compute the same sets of field errors, leading to results in very good agreement with the direct measurement results. Finally, we have measured and reported the results of field error measurements of a CORC[®] wound prototype HTS dipole magnet.

7.5. Possibilities for Future Work

7.5.1 Future Work Possibilities for Bi:2212 Microstructure and Magnetic Property Correlation

The correlation of the interfilamentary bridging in the Bi:2212 round wire microstructure with the transverse electrical connectivity, γ_2 , was relatively qualitative. Better methods for determining the fraction of a sample that contains bridges almost certainly exist. However, it is somewhat difficult to get an accurate account for the fraction of the sample that is bridged using two dimensional optical or SEM images. Serial sectioning is time consuming and does not necessarily preserve the morphology of the original bridge. The morphology of the bridges is not consistent and a three-dimensional image of the bridges in the sample would be better for assessing the amount of the sample that is bridged. Advances in micro-CT imaging may allow for a better determination of the fraction of the sample that is bridged. This fraction could then be compared with the γ_2 calculations.

The dependence of magnetization (or d_{eff}) on L_p could be more extensively explored, as could the dependence of creep rate on L_p . More twist pitches could be explored, and perhaps in the future the wires could be twisted with small pitch lengths without damaging the filaments. A fundamental reason for why the bridge material could have a different pinning strength than the filamentary material could be explored in greater detail.

Since the start of this work, overpressure processing is now typically applied to Bi:2212 round wires to densify the filaments. Furthermore, new Bi:2212 powder has been developed. Any effects these new developments have on the results presented here could be explored.

7.5.2 Future Work Possibilities for YBCO Nanostructure, Additions, and Magnetic Property Correlation

This work focused on the magnetization and creep rate of YBCO films processed using PLD and MOCVD. The processes typically introduced a unique secondary phase. That is, Y211 was the primary secondary phase introduced during the PLD studies and BZO was the primary secondary phase introduced during the MOCVD studies. The intrinsic pinning was seen to be different with these two processes. Further exploration could involve how extensive concentrations of other secondary phases influence the magnetic properties of the films. For example, a large range of concentrations of BZO could be added to the films during PLD. Also, a large range of concentrations of Y211 could be added to the films during MOCVD. Furthermore, there are many secondary phases that have been introduced into YBCO films to increase J_c . The pinning potentials of the films with these phases could also be studied. Perhaps there are secondary phases that introduce pins that increase J_c and decrease creep better than BZO.

The pinning potential of the pins in the films studied here were extracted using the collective pinning theory. Perhaps other theories are more relevant to pins introduced by the introduction of other secondary phases. This could be further explored.

7.5.3 Future Work Possibilities for Magnetic Properties of Cables and their Influence on Accelerator Magnets

The $M-\mu_0H$ and magnetization decay of other types of conductor, such as Roebel and YBCO twisted stack could be studied. These have been to some extent already performed using the cryogen-free magnet in CSMM at OSU. The magnet system also supports transport current measurements in applied magnetic fields. The $M-\mu_0H$ and decay measurements could be performed on a variety of conductors, including the CORC[®] and Bi:2212 Rutherford cables, in the presence of applied transport currents.

The field error of magnets built using other types of conductor, such as Roebel cable and YBCO twisted stacks could be calculated using the FEM software. More complicated magnet designs could be modelled using the CORC[®] cable as the turns.

7.5.4 Future Work Possibilities for Effects of Magnetization and Creep on Magnetic Field Error in HTS Accelerator Magnets

The field errors of one type of HTS-based magnet design were measured. Different magnet designs are also used extensively, and the field quality of HTS-based magnets built using these designs could be studied. Additionally, Bi:2212 magnets are also being considered and some smaller magnets have been built. If larger Bi:2212 magnets are built, their field quality will also need to be measured. The source of the change of the magnetic field of the CORC[®] cable based CCT magnet was not clear. The change in b_3 was not large as might be expected if the change in the field occurs due to flux creep. Further studies of the change in the magnetization of these magnets should be performed to determine the mechanism for the field change.

Appendix A: List of Acronyms

Acronym	Definition
AC	Alternating current
BSE	Backscattered electrons
BZO	BaZrO ₃
CORC	Conductor on Round Core
DC	Direct current
FIB	Focused ion beam
HTS	High temperature superconductor
ICP-MS	Inductively coupled plasma-mass spectrometry
LTS	Low temperature superconductor
MOCVD	Metalorganic vapor deposition
PLD	Pulsed laser deposition
PPMS	Physical property measurement system
REBCO	Rare earth doped YBCO
SE	Secondary electrons
SEM	Scanning electron microscopy
SQUID	Superconducting quantum interference device
TEM	Transmission electron microscopy
USMDP	United States magnet development program
VSM	Vibrating sample magnetometer
YBCO	Yttrium barium copper oxide

Y211

Y_2BaCuO_5

ZFC

Zero field cooled/cooling

2G

Second generation

2D-ROSS

Two dimensional randomly oriented single stack

Appendix B: List of Latin Symbols

Symbol	Definition
A	Area
A in Ch. 6	Parameter in loop modeling (Eq. 6.9)
a	Fluxon hop distance (Eq. 1.23)
a_0	Average distance between fluxons (Ch. 1)
$A_{\text{composite}}$	Cross-sectional area of the composite (Ch. 3)
A_{sc}	Superconductor area
A_{total}	Sample cross-sectional area
A_r	Fitting constant to model pseudo-reversible magnetization (Eq. 6.10)
B	Magnetic flux density
b_3, b_5, b_7, b_n	Various magnetic field harmonics
B	Magnetic Field
B_a	Applied magnetic field ($\mu_0 H_a$)
B_{c2}	Upper critical magnetic field ($\mu_0 H_{c2}$)
B_h	Hold magnetic field ($\mu_0 H_h$) (Ch. 5)
B_{inj}	Injection magnetic field ($\mu_0 H_{\text{inj}}$)
B_{irr}	Irreversibility field
B_{local}	Local magnetic flux density
B_{max}	Maximum magnetic field ($\mu_0 H_{\text{max}}$)

B_p	Penetration field ($\mu_0 H_p$)
B_r^*	Fitting constant to model pseudo-reversible magnetization (Eq. 6.10)
$B_{p,high}$	High-field penetration field parameter (Eq. 6.11, Table 17)
B_z	Background subtracted applied field ($\mu_0 H_a$) (Eq. 5.1)
B^*	Parameter in analytic CORC [®] cable magnetization model, for field dependence correction (Eq. 6.9)
C	Calibration constant 1, Hall probe magnetometer (Ch. 5)
C'	Calibration constant 2, Hall probe magnetometer (Eq. 5.1)
C_c	Coupling constant of VSM (Eq. 2.3)
d	Diameter of wire of composite (Ch. 3)
d'	Enhanced filamentary diameter for bridged filaments (Ch. 3)
d_g	Grain diameter (Eq. 1.23)
d_{bundle}	Filament bundle diameter (Eq. 3.7)
d_{eff}	Effective filament bundle diameter (Eq. 3.1)
$d_{subelement}$	Subelement diameter (Ch. 3)
E	Electric field (Eq. 1.1)
E_c	Free energy increase to presence of fluxon (Eq. 1.5)
f_n	Normal state Gibbs free energy (Eq. 1.2)
F_L	Lorentz force (Eq. 1.7)
F_p	Total pinning force (Ch. 4)
f_p	Individual pinning force (Ch. 4)

f_p'	Individual pinning force of pin with different strength (Ch. 4)
f_s	Superconducting state Gibbs free energy (Eq. 1.2)
G	Explicit Temperature dependence of U (Eq. 4.11)
H	Magnetic field strength
H_a	Applied magnetic field strength
H_c	Critical field of the superconductor
H_{c1}	Lower critical field
H_{c2}	Upper critical field
H_i	Internal field (Ch. 6)
H_m	Field of maximum magnetization (Ch. 4)
H_p	Penetration field strength
I	Electric current
I_c	Critical current
J	Electric current density
J_e	Engineering current density
J_c	Critical current density
$J_{c1,1}$	Intrinsic J_c along the length of composite (Eq. 3.3)
$J_{c1,2}$	Intrinsic J_c across the composite (Eq. 3.4)
J_{c0}	Critical current density (before flux creeps) (Eq. 1.18)
J_{c2}	Critical current density along x (Eq. 1.15)
J_{c3}	Critical current density along y (Eq. 1.15)
J_m	Experimentally measured current density (Ch. 1)

k_B	The Boltzmann constant
L	Length
L_{crit}	Critical length at which M saturates (Eq. 3.6)
L_p	Twist pitch length
M	Magnetization
M_0	Initial magnetization
m	Magnetic moment
m	Fitting parameter, G (Eq. 4.11)
m_0	Initial magnetic moment
M_{inj}	Magnetization at injection field
m_{irr}	Irreversible component of magnetic moment
m^+	Magnetic moment on trapping branch
m^-	Magnetic moment on shielding branch
M_{long}	Long sample magnetization (Eq. 5.6)
M_{rev}	Reversible magnetization
M_p	Magnetization at penetration field (Ch. 5)
M_{short}	Short sample magnetization (Eq. 5.6)
ΔM	Difference of magnetization between shielding and trapping branches
ΔM_t	ΔM at end of decay measurement
ΔM_0	ΔM at beginning of decay measurement
n	Number of fluxons per cm^2 (Ch. 1)
n	Fitting parameter, G (Eq. 4.11)
N	Demagnetization factor (Ch. 6)
P	Fitting parameter for the interpolation (Eq. 4.11)

R	Sample radius (Eq. 1.16)
r	Magnetic relaxation rate
t	Time
T	Temperature
T_c	Superconducting transition temperature
T_m	Fluxon Lattice Melting temperature
t_0	“Effective” hopping attempt time (Eq. 1.18)
U	Pinning potential
U_0	Fundamental pinning potential
U_c	Characteristic pinning potential
U_{eff}	Effective pinning potential
V	Electric potential
V_c	Correlated flux hop volume (Ch 1)
V_{cable}	Volume of cable
V_{strand}	Volume of strand
V_{coil}	Coil voltage (Eq. 2.1)
V_s	Sample volume
V_{sc}	Superconductor volume
w	Sample width
w_1	Sample width (Eq. 4.10)
w_2	Sample length (Eq. 4.10)
w_p	Precipitate width (Ch. 4)
x	Distance of (partial) flux penetration into sample (Eq. 6.11)
z_p	Precipitate height (Ch. 4)

Appendix C: List of Greek Symbols

Symbol	Definition
β_c	Fitting parameter (Eqs. 3.3-3.4)
γ	Connectivity parameter (Ch. 3)
γ_1	Longitudinal connectivity parameter (Ch. 3)
γ_2	Transverse connective parameter (Ch. 3)
γ_{CORC}	Sensitivity factor for the CORC® sample region (Ch. 5)
γ_{NiTape}	Sensitivity factor for the nickel sample region (Ch. 5)
γ_s	General sensitivity factor
θ	Angle
λ	Penetration depth
λ_{SC}	Fill factor (filaments in matrix) of SC composite
μ_0	Permeability of free space ($4\pi \times 10^{-7}$ H/m)
ζ	Coherence length
π	Ratio of the circumference to the diameter in a circle
τ	Time constant (Ch. 5)
ν	Fitting parameter (Ch. 4)
ν_0	Hopping frequency (Ch. 1)

ϕ	Magnetic flux (Eq. 2.1)
Φ_0	Magnetic flux quantum ($2.06783 \times 10^{-15} \text{ w}$)
χ	Magnetic susceptibility
ψ	Superconducting order parameter
ω	Attempt frequency (Eq. 1.24)

Bibliography

- [1] A. Godeke *et al.*, "Progress in wind-and-react Bi-2212 accelerator magnet technology," *IEEE Transactions on Applied Superconductivity*, vol. 19, no. 3, pp. 2228-2231, 2009.
- [2] K. Zhang *et al.*, "Tripled critical current in racetrack coils made of Bi-2212 Rutherford cables with overpressure processing and leakage control," *Superconductor Science and Technology*, vol. 31, no. 10, p. 105009, 2018.
- [3] X. Wang *et al.*, "A viable dipole magnet concept with REBCO CORC® wires and further development needs for high-field magnet applications," *Superconductor Science and Technology*, vol. 31, no. 4, p. 045007, 2018.
- [4] D. C. van der Laan, J. D WEISS, and D. McRae, "Status of CORC® cables and wires for use in high-field magnets and power systems a decade after their introduction," *Superconductor Science and Technology*, 2019.
- [5] R. Gupta *et al.*, "Hybrid high-field cosine-theta accelerator magnet R&D with second-generation HTS," *IEEE Transactions on Applied Superconductivity*, vol. 25, no. 3, pp. 1-4, 2015.
- [6] K.-H. Mess and S. Wolff, *Superconducting accelerator magnets*. World Scientific, 1996.

- [7] M. Wilson, "Pulsed Superconducting Magnets (for accelerators)," ed: CERN, 2006.
- [8] P. Lee, "Engineering Critical Current Density vs. Applied Field for Superconductors Available in Long Lengths," in *Excel*, ed. <https://nationalmaglab.org/magnet-development/applied-superconductivity-center/plots>: National High Magnetic Field Lab, 2018.
- [9] F. London and H. London, "The electromagnetic equations of the supraconductor," *Proceedings of the Royal Society of London. Series A-Mathematical and Physical Sciences*, vol. 149, no. 866, pp. 71-88, 1935.
- [10] Y. Yeshurun, A. Malozemoff, and A. Shaulov, "Magnetic relaxation in high-temperature superconductors," *Reviews of Modern Physics*, vol. 68, no. 3, p. 911, 1996.
- [11] A. A. Abrikosov, "On the magnetic properties of superconductors of the second group," *Sov. Phys. JETP*, vol. 5, pp. 1174-1182, 1957.
- [12] A. M. Campbell and J. E. Evetts, "Critical currents in superconductors," 1972.
- [13] C. P. Bean, "Magnetization of hard superconductors," *Physical review letters*, vol. 8, no. 6, p. 250, 1962.
- [14] C. P. Bean, "Magnetization of high-field superconductors," *Reviews of modern physics*, vol. 36, no. 1, p. 31, 1964.
- [15] M. A. Susner, "Influences of crystalline anisotropy, doping, porosity, and connectivity on the critical current densities of superconducting magnesium diboride bulks, wires, and thin films," The Ohio State University, 2012.

- [16] A. Campbell and J. Evetts, "Flux vortices and transport currents in type II superconductors," *Advances in Physics*, vol. 21, no. 90, pp. 199-428, 1972.
- [17] M. Waczenovsky, H. Weber, O. Hyun, D. Finnemore, and K. Mereiter, "Magnetization and susceptibility of grain-aligned $\text{HoBa}_2\text{Cu}_3\text{O}_{7-\delta}$ superconductors," *Physica C: Superconductivity*, vol. 160, no. 1, pp. 55-64, 1989.
- [18] A. Umezawa *et al.*, "Enhanced critical magnetization currents due to fast neutron irradiation in single-crystal $\text{YBa}_2\text{Cu}_3\text{O}_{7-\delta}$," *Physical Review B*, vol. 36, no. 13, p. 7151, 1987.
- [19] F. Sauerzopf, H. Wiesinger, H. Weber, G. Crabtree, and J. Liu, "Magnetization of neutron irradiated $\text{YBa}_2\text{Cu}_3\text{O}_{7-\delta}$ single crystals," *Physica C: Superconductivity and its Applications*, vol. 162, pp. 751-752, 1989.
- [20] H. W. Weber, *High-Tc Superconductors*. Springer Science & Business Media, 2013.
- [21] E. Gyorgy, R. Van Dover, K. Jackson, L. Schneemeyer, and J. Waszczak, "Anisotropic critical currents in $\text{Ba}_2\text{YCu}_3\text{O}_7$ analyzed using an extended Bean model," *Applied physics letters*, vol. 55, no. 3, pp. 283-285, 1989.
- [22] F. Sauerzopf, H. Wiesinger, and H. Weber, "Anisotropic current flow and demagnetization corrections in the Bean model," *Cryogenics*, vol. 30, no. 7, pp. 650-655, 1990.
- [23] M. Sumption, "Calculation of the magnetization of anisotropic superconductors with cylindrical geometry in transverse fields," *Applied superconductivity*, vol. 2, no. 1, pp. 41-46, 1994.

- [24] M. Sumption, "A model for bridging and coupling in superconductors," *Physica C: Superconductivity*, vol. 261, no. 3-4, pp. 245-258, 1996.
- [25] P. W. Anderson, "Theory of flux creep in hard superconductors," *Physical Review Letters*, vol. 9, no. 7, p. 309, 1962.
- [26] P. W. Anderson and Y. Kim, "Hard superconductivity: theory of the motion of Abrikosov flux lines," *Reviews of modern physics*, vol. 36, no. 1, p. 39, 1964.
- [27] Y. Kim, C. Hempstead, and A. Strnad, "Critical persistent currents in hard superconductors," *Physical Review Letters*, vol. 9, no. 7, p. 306, 1962.
- [28] Y. Yeshurun and A. Malozemoff, "Giant flux creep and irreversibility in an Y-Ba-Cu-O crystal: an alternative to the superconducting-glass model," *Physical review letters*, vol. 60, no. 21, p. 2202, 1988.
- [29] C. Gorter, "Note on the superconductivity of alloys," *Phys. Letters*, vol. 1, 1962.
- [30] J. Friedel, P. De Gennes, and J. Matricon, "Nature of the driving force in flux creep phenomena," *Applied Physics Letters*, vol. 2, no. 6, pp. 119-121, 1963.
- [31] D. Shi, M. Xu, A. Umezawa, and R. F. Fox, "Temperature and field dependence of magnetic relaxation in a Bi₂Sr₂CaCu₂O_x single crystal," *Physical Review B*, vol. 42, no. 4, p. 2062, 1990.
- [32] S. Sengupta, D. Shi, Z. Wang, M. Smith, S. Salem-Sugui Jr, and P. McGinn, "Magnetic relaxation and intrinsic pinning in a single crystal of Bi₂Sr₂CaCu₂O_x," *Physical Review B*, vol. 47, no. 9, p. 5414, 1993.

- [33] D. Shi, M. Xu, M. Fang, J. Chen, A. Cornelius, and S. Lanan, "Effect of microstructural changes on thermally activated flux-creep behavior in the Bi-Sr-Ca-Cu-O system," *Physical Review B*, vol. 41, no. 13, p. 8833, 1990.
- [34] M. Xu, D. Shi, A. Umezawa, K. Vandervoort, and G. Crabtree, "Full-penetration temperature and magnetic relaxation in a single crystal of Bi₂Sr₂CaCu₂O_x," *Physical Review B*, vol. 43, no. 16, p. 13049, 1991.
- [35] Y. Yeshurun *et al.*, "Magnetic properties of YBaCuO and BiSrCaCuO crystals: a comparative study of flux creep and irreversibility," *Cryogenics*, vol. 29, no. 3, pp. 258-262, 1989.
- [36] D. Hu, "The current dependence of the effective pinning potential in high-T_c superconductors," *Physica C: Superconductivity*, vol. 205, no. 1-2, pp. 123-128, 1993.
- [37] M. Sumption, Y. Higashida, K. Michishita, N. Koshizuka, G. Genda, and E. Collings, "Static and Dynamic Magnetizations of 3-D Textured and Monocrystalline Bi:2212," in *Advances in Superconductivity VI*: Springer, 1994, pp. 593-596.
- [38] M. Beasley, R. Labusch, and W. Webb, "Flux creep in type-II superconductors," *Physical Review*, vol. 181, no. 2, p. 682, 1969.
- [39] M. Sumption, L. Motowidlo, G. Ozeryanski, G. Galanski, and E. Collings, "Critical current, flux pinning, and hysteretic loss in round multifilamentary Bi: 2212/Ag strands," in *Advances in Cryogenic Engineering Materials*: Springer, 1996, pp. 573-580.

- [40] Y. Xu, M. Suenaga, A. Moodenbaugh, and D. Welch, "Magnetic field and temperature dependence of magnetic flux creep in c-axis-oriented YBa₂Cu₃O₇ powder," *Physical Review B*, vol. 40, no. 16, p. 10882, 1989.
- [41] R. Griessen, "Thermally activated flux motion near the absolute zero," *Physica C: Superconductivity*, vol. 172, no. 5-6, pp. 441-449, 1991.
- [42] B. Lairson, J. Sun, T. Geballe, M. Beasley, and J. Bravman, "Thermal activation of vortex motion in YBa₂Cu₃O₇- δ films at low temperatures," *Physical Review B*, vol. 43, no. 13, p. 10405, 1991.
- [43] E. Zeldov, N. Amer, G. a. Koren, A. Gupta, R. Gambino, and M. McElfresh, "Optical and electrical enhancement of flux creep in YBa₂Cu₃O₇- δ epitaxial films," *Physical review letters*, vol. 62, no. 26, p. 3093, 1989.
- [44] E. Zeldov and N. Amer, "Flux-pinning energies in high-T c superconductors," *Physical review letters*, vol. 65, no. 2, p. 278, 1990.
- [45] M. Maley, J. Willis, H. Lessure, and M. McHenry, "Dependence of flux-creep activation energy upon current density in grain-aligned YBa₂Cu₃O₇- x ," *Physical Review B*, vol. 42, no. 4, p. 2639, 1990.
- [46] M. McHenry *et al.*, "Dependence of the flux-creep activation energy on the magnetization current for a La_{1.86}Sr_{0.14}CuO₄ single crystal," *Physical Review B*, vol. 44, no. 14, p. 7614, 1991.
- [47] Y. Ren and P. A. de Groot, "Non-logarithmic relaxation in flux-grown YBa₂Cu₃O₇- δ single crystal," *Physica C: Superconductivity*, vol. 196, no. 1-2, pp. 111-116, 1992.

- [48] S. Sengupta, D. Shi, Z. Wang, M. Smith, and P. McGinn, "U-j relationship in type-II superconductors," *Physical Review B*, vol. 47, no. 9, p. 5165, 1993.
- [49] Y. Abulafia *et al.*, "Local magnetic relaxation in high-temperature superconductors," *Physical review letters*, vol. 75, no. 12, p. 2404, 1995.
- [50] T. Wijnands, L. Bottura, L. Vos, M. Lamont, and A. Burns, "Requirements for Real Time Correction of decay and snapback in the LHC superconducting magnets," CERN-LHC-Project-Note-221, 2000.
- [51] G. Blatter, M. V. Feigel'man, V. B. Geshkenbein, A. I. Larkin, and V. M. Vinokur, "Vortices in high-temperature superconductors," *Reviews of Modern Physics*, vol. 66, no. 4, p. 1125, 1994.
- [52] J. Ekin, "Experimental techniques for low-temperature measurements: cryostat design, material properties and superconductor critical-current testing." Oxford university press, 2006.
- [53] R. Eason, "Pulsed laser deposition of thin films: applications-led growth of functional materials." John Wiley & Sons, 2007.
- [54] V. Selvamanickam, Y. Xie, J. Reeves, and Y. Chen, "MOCVD-based YBCO-coated conductors," *MRS bulletin*, vol. 29, no. 8, pp. 579-582, 2004.
- [55] M. H. Gharahcheshmeh *et al.*, "Superconducting transition width (ΔT_c) characteristics of 25 mol% Zr-added (Gd, Y) $Ba_2Cu_3O_{7-\delta}$ superconductor tapes with high in-field critical current density at 30 K," *Superconductor Science and Technology*, vol. 30, no. 1, p. 015016, 2016.

- [56] H. Miao, K. R. Marken, M. Meinesz, B. Czabaj, and S. Hong, "Development of round multifilament Bi-2212/Ag wires for high field magnet applications," *IEEE Transactions on applied superconductivity*, vol. 15, no. 2, pp. 2554-2557, 2005.
- [57] H. Weijers, U. Trociewitz, K. Marken, M. Meinesz, H. Miao, and J. Schwartz, "The generation of 25.05 T using a 5.11 T Bi₂Sr₂CaCu₂O_x superconducting insert magnet," *Superconductor Science and Technology*, vol. 17, no. 4, p. 636, 2004.
- [58] T. Hasegawa *et al.*, "HTS conductors for magnets," *IEEE transactions on applied superconductivity*, vol. 12, no. 1, pp. 1136-1140, 2002.
- [59] H. Weijers *et al.*, "Development of a 5 T HTS insert magnet as part of 25 T class magnets," *IEEE transactions on applied superconductivity*, vol. 13, no. 2, pp. 1396-1399, 2003.
- [60] A. Ghosh, K. Robins, and W. Sampson, "Magnetization measurements on multifilamentary Nb₃Sn and NbTi conductors," *IEEE transactions on magnetics*, vol. 21, no. 2, pp. 328-331, 1985.
- [61] L. Bottura and A. Godeke, "Superconducting materials and conductors: Fabrication and limiting parameters," *Reviews of accelerator science and technology*, vol. 5, pp. 25-50, 2012.
- [62] E. W. Collings, M. A. Susner, M. D. Sumption, and D. R. Dietderich, "Extracted Strand Magnetizations of an HQ Type Nb₃Sn Rutherford Cable and Estimation of Transport Corrections at Operating and Injection Fields," *IEEE transactions on applied superconductivity*, vol. 24, no. 3, pp. 1-5, 2013.

- [63] B. Bordini, D. Richter, P. Alknes, A. Ballarino, L. Bottura, and L. Oberli, "Magnetization Measurements of High- J_c Nb_3Sn Strands," *IEEE transactions on applied superconductivity*, vol. 23, no. 3, pp. 7100806-7100806, 2013.
- [64] T. Shen *et al.*, "Filament to filament bridging and its influence on developing high critical current density in multifilamentary $Bi_2Sr_2CaCu_2O_x$ round wires," *Superconductor Science and Technology*, vol. 23, no. 2, p. 025009, 2009.
- [65] M. Sumption, L. Motowidlo, and E. Collings, "Determination of the true (or potential) transport- J_c of a multifilamentary Bi: HTSC/Ag strand in the presence of bridging and generalized sausaging," *Physica C: Superconductivity*, vol. 291, no. 3-4, pp. 267-273, 1997.
- [66] S. Kasai *et al.*, "Magnetization property of Bi-2212 round wires," *IEEE transactions on applied superconductivity*, vol. 14, no. 2, pp. 1098-1101, 2004.
- [67] Y. Huang, H. Miao, S. Hong, and J. A. Parrell, "Bi-2212 round wire development for high field applications," *IEEE transactions on applied superconductivity*, vol. 24, no. 3, pp. 1-5, 2013.
- [68] R. B. Goldfarb and K. Itoh, "Reduction of interfilament contact loss in Nb_3Sn superconductor wires," *Journal of applied physics*, vol. 75, no. 4, pp. 2115-2118, 1994.
- [69] D. A. Cardwell and D. S. Ginley, *Handbook of superconducting materials*. CRC Press, 2003.
- [70] C. Myers, M. Susner, H. Miao, Y. Huang, M. Sumption, and E. Collings, "Reduced Magnetization and Loss in Ag-Mg Sheathed Bi2212 Wires: Systematics With

- Sample Twist Pitch and Length," *IEEE Transactions on Applied Superconductivity*, vol. 25, no. 3, pp. 1-4, 2014.
- [71] M. Sumption, L. Motowidlo, G. Ozeryansky, G. Galinski, and E. Collings, "A comparison of ac loss, magnetization, H_r and U_0 for Bi:2212 wires, crystals and melt grown samples," *Applied superconductivity*, vol. 3, no. 7-10, pp. 521-533, 1995.
- [72] M. Okada, "Development of Bi-2212/Ag round-shaped wire and magnet application," *Superconductor Science and Technology*, vol. 13, no. 1, p. 29, 2000.
- [73] H. Kumakura, H. Kitaguchi, K. Togano, T. Muroga, J. Sato, and M. Okada, "Influence of Ag substrates on grain alignment and critical current density of Bi-2212 tape conductors," *IEEE transactions on applied superconductivity*, vol. 9, no. 2, pp. 1804-1807, 1999.
- [74] L. Motowidlo *et al.*, "The influence of filament size and atmosphere on the microstructure and J_c of round multifilament $\text{Bi}_2\text{Sr}_2\text{CaCu}_2\text{O}_x$ wires," *IEEE Transactions on Applied Superconductivity*, vol. 5, no. 2, pp. 1162-1166, 1995.
- [75] L. Motowidlo, G. Galinski, G. Ozeryansky, W. Zhang, and E. Hellstrom, "Dependence of critical current density on filament diameter in round multifilament Ag-sheathed $\text{Bi}_2\text{Sr}_2\text{CaCu}_2\text{O}_x$ wires processed in O_2 ," *Applied physics letters*, vol. 65, no. 21, pp. 2731-2733, 1994.
- [76] W. T. Nachtrab, T. Wong, X. T. Liu, and J. Schwartz, "The Effect of Filament Diameter on J_c in High Filament Count Bi2212/Ag Round Wire," *IEEE transactions on applied superconductivity*, vol. 19, no. 3, pp. 3061-3066, 2009.

- [77] W. Nachtrab *et al.*, "Development of High Superconductor Fraction Bi₂Sr₂CaCu₂O_xAg Wire for MRI," *IEEE Transactions on Applied Superconductivity*, vol. 18, no. 2, pp. 1184-1187, 2008.
- [78] S. Jin, R. Van Dover, T. Tiefel, J. Graebner, and N. Spencer, "Critical currents and magnetization in c-axis textured Bi-Pb-Sr-Ca-Cu-O superconductors," *Applied physics letters*, vol. 58, no. 8, pp. 868-870, 1991.
- [79] H. Miao *et al.*, "Studies of precursor composition effect on J_c in Bi-2212/Ag wires and tapes," in *AIP Conference Proceedings*, 2006, vol. 824, no. 1: American Institute of Physics, pp. 673-682.
- [80] C. Myers, M. Susner, L. Motowidlo, J. Distin, M. Sumption, and E. Collings, "Transport, magnetic, and SEM characterization of a novel design Bi-2212 strand," *IEEE transactions on applied superconductivity*, vol. 21, no. 3, pp. 2804-2807, 2010.
- [81] V. Selvamanickam *et al.*, "The low-temperature, high-magnetic-field critical current characteristics of Zr-added (Gd, Y) Ba₂Cu₃O_x superconducting tapes," *Superconductor Science and Technology*, vol. 25, no. 12, p. 125013, 2012.
- [82] M. H. Gharahcheshmeh *et al.*, "MOCVD of Heavily-Doped 25 mol.% Zr-Added (Gd, Y) Ba₂Cu₃O_{7-δ} Coated Conductors," *IEEE Transactions on Applied Superconductivity*, vol. 27, no. 4, pp. 1-5, 2017.
- [83] C. Myers *et al.*, "Magnetization and Creep of Y₁Ba₂Cu₃O_{7-x} Thin Films with Columnar Y₂BaCuO₅ and BaZrO₃ Pinning Center Additions," presented at the

Cryogenic Engineering Conference and International Cryogenics and Materials Conference, Hartford, Connecticut, 2019, M2Po2B-04.

- [84] M. Feigel'Man, V. Geshkenbein, A. Larkin, and V. Vinokur, "Theory of collective flux creep," *Physical review letters*, vol. 63, no. 20, p. 2303, 1989.
- [85] D. S. Fisher, M. P. Fisher, and D. A. Huse, "Thermal fluctuations, quenched disorder, phase transitions, and transport in type-II superconductors," *Physical Review B*, vol. 43, no. 1, p. 130, 1991.
- [86] M. A. P. Sebastian *et al.*, "Optimizing Flux Pinning of $\text{YBa}_2\text{Cu}_3\text{O}_{7-x-\delta}$ (YBCO) Thin Films With Unique Large Nanoparticle Size and High Concentration of Y_2BaCuO_5 (Y211) Additions," *IEEE Transactions on Applied Superconductivity*, vol. 25, no. 3, pp. 1-5, 2014.
- [87] V. Selvamanickam, M. H. Gharahcheshmeh, A. Xu, E. Galstyan, L. Delgado, and C. Cantoni, "High critical currents in heavily doped (Gd, Y) $\text{Ba}_2\text{Cu}_3\text{O}_x$ superconductor tapes," *Applied Physics Letters*, vol. 106, no. 3, p. 032601, 2015.
- [88] V. Selvamanickam, M. H. Gharahcheshmeh, A. Xu, Y. Zhang, and E. Galstyan, "Requirements to achieve high in-field critical current density at 30 K in heavily-doped (Gd, Y) $\text{Ba}_2\text{Cu}_3\text{O}_x$ superconductor tapes," *Superconductor Science and Technology*, vol. 28, no. 10, p. 104003, 2015.
- [89] V. Selvamanickam, M. H. Gharahcheshmeh, A. Xu, Y. Zhang, and E. Galstyan, "Critical current density above 15 MA cm^{-2} at 30 K, 3 T in $2.2 \mu\text{m}$ thick heavily-doped (Gd, Y) $\text{Ba}_2\text{Cu}_3\text{O}_x$ superconductor tapes," *Superconductor Science and Technology*, vol. 28, no. 7, p. 072002, 2015.

- [90] A. P. Malozemoff and M. P. Fisher, "Universality in the current decay and flux creep of Y-Ba-Cu-O high-temperature superconductors," *Physical Review B*, vol. 42, no. 10, p. 6784, 1990.
- [91] T. Shen *et al.*, "Stable, predictable and training-free operation of superconducting Bi-2212 Rutherford cable racetrack coils at the wire current density of 1000 A/mm²," *Scientific reports*, vol. 9, no. 1, pp. 1-9, 2019.
- [92] D. W. Hazelton *et al.*, "Recent developments in 2G HTS coil technology," *IEEE Transactions on Applied Superconductivity*, vol. 19, no. 3, pp. 2218-2222, 2009.
- [93] S. Yoon, J. Kim, K. Cheon, H. Lee, S. Hahn, and S.-H. Moon, "26 T 35 mm all-GdBa₂Cu₃O_{7-x} multi-width no-insulation superconducting magnet," *Superconductor Science and Technology*, vol. 29, no. 4, p. 04LT04, 2016.
- [94] M. Takayasu, L. Chiesa, L. Bromberg, and J. Minervini, "Cabling method for high current conductors made of HTS tapes," *IEEE transactions on applied superconductivity*, vol. 21, no. 3, pp. 2340-2344, 2010.
- [95] W. Goldacker *et al.*, "High current DyBCO-ROEBEL assembled coated conductor (RACC)," in *Journal of Physics: Conference Series*, 2006, vol. 43, no. 1: IOP Publishing, p. 901.
- [96] R. A. Badcock, N. J. Long, M. Mulholland, S. Hellmann, A. Wright, and K. A. Hamilton, "Progress in the manufacture of long length YBCO Roebel cables," *IEEE Transactions on Applied Superconductivity*, vol. 19, no. 3, pp. 3244-3247, 2009.
- [97] W. Goldacker, F. Grilli, E. Pardo, A. Kario, S. I. Schlachter, and M. Vojenčiak, "Roebel cables from REBCO coated conductors: a one-century-old concept for the

- superconductivity of the future," *Superconductor Science and Technology*, vol. 27, no. 9, p. 093001, 2014.
- [98] G. A. Kirby *et al.*, "First cold powering test of REBCO roebel wound coil for the EuCARD2 future magnet development project," *IEEE Transactions on Applied Superconductivity*, vol. 27, no. 4, pp. 1-7, 2017.
- [99] A. C. T. LLC. "CORC[®] ACCELERATOR MAGNET CABLES AND WIRES"
<https://www.advancedconductor.com/corccable/accelerator-cables-and-wires/>
(accessed.
- [100] K. Dong, M. Sumption, E. Collings, M. Majoros, H. Yu, and M. Hu, "Influence of field penetration ratios and filamentation on end-effect related hysteretic loss reductions for superconducting strips," in *IOP Conference Series: Materials Science and Engineering*, 2017, vol. 279, no. 1: IOP Publishing, p. 012032.
- [101] M. Konczykowski, F. Holtzberg, and P. Lejay, "Local Hall probe magnetometry: a new technique for investigation of magnetic flux penetration, exclusion and trapping in HTSC," *Superconductor Science and Technology*, vol. 4, no. 1S, p. S331, 1991.
- [102] M. Staines, S. Rupp, D. Caplin, D. Yu, and S. Fleshler, "Calibration of Hall sensor AC loss measurements," *IEEE transactions on applied superconductivity*, vol. 11, no. 1, pp. 2224-2227, 2001.
- [103] C. S. Myers, M. D. Sumption, and E. Collings, "Magnetization and flux penetration of YBCO CORC cable segments at the injection fields of accelerator magnets," *IEEE Transactions on Applied Superconductivity*, vol. 29, no. 5, pp. 1-5, 2019.

- [104] S. Amet *et al.*, "Persistent and coupling current effects in the LHC superconducting dipoles," *IEEE transactions on applied superconductivity*, vol. 13, no. 2, pp. 1239-1242, 2003.
- [105] L. Bottura, P. Pognat, A. Siemko, J. Vlogaert, and C. Wyss, "Performance of the LHC final design full scale superconducting dipole prototypes," *IEEE transactions on applied superconductivity*, vol. 11, no. 1, pp. 1554-1557, 2001.
- [106] L. Bottura *et al.*, "Performance of the LHC final prototype and first pre-series superconducting dipole magnets," *IEEE transactions on applied superconductivity*, vol. 12, no. 1, pp. 211-214, 2002.
- [107] M. Aleksa *et al.*, "Measurement and analysis of the field quality of LHC prototype and pre-series superconducting dipoles," *IEEE transactions on applied superconductivity*, vol. 12, no. 1, pp. 247-250, 2002.
- [108] L. Bottura *et al.*, "Field quality of the LHC dipole magnets in operating conditions," 2002.
- [109] L. Bottura *et al.*, "Performance of the first LHC pre-series superconducting dipoles," *IEEE transactions on applied superconductivity*, vol. 13, no. 2, pp. 1235-1238, 2003.
- [110] S. Le Naour *et al.*, "Magnetization measurements on LHC superconducting strands," *IEEE transactions on applied superconductivity*, vol. 9, no. 2, pp. 1763-1766, 1999.
- [111] C. S. Myers, M. D. Sumption, and E. W. Collings, "Magnetization and Creep in YBCO Tape and CORC Cables for Particle Accelerators: Value and Modification

- Via Preinjection Cycle," *IEEE Transactions on Applied Superconductivity*, vol. 29, no. 5, pp. 1-5, 2019.
- [112] M. D. Sumption, M. Majoros, and E. W. Collings, "AC Losses in Superconducting Materials, Wires, and Tapes," ed. Handbook of Applied Superconducting Materials: CRC Press, *manuscript in preparation*.
- [113] L. Hoddeson, A. W. Kolb, and C. Westfall, *Fermilab: Physics, the frontier, and megascience*. University of Chicago Press, 2009.
- [114] X. Wang *et al.*, "Validation of finite-element models of persistent-current effects in Nb 3 Sn accelerator magnets," *IEEE Transactions on Applied Superconductivity*, vol. 25, no. 3, pp. 1-6, 2015.
- [115] H. Felice *et al.*, "Challenges in the Support Structure Design and Assembly of HD3, a Nb₃Sn Block-Type Dipole Magnet," *IEEE transactions on applied superconductivity*, vol. 23, no. 3, pp. 4001705-4001705, 2013.
- [116] M. A. Green, "Residual fields in superconducting magnets," in *Proceedings of the MT-4 Conference at Brookhaven National Laboratory*, 1972, vol. 339.
- [117] H. Brück, R. Meinke, F. Müller, and P. Schmueser, "Field distortions from persistent currents in the superconducting HERA magnets," *Zeitschrift für Physik C Particles and Fields*, vol. 44, no. 3, pp. 385-392, 1989.
- [118] C. Völlinger, M. Aleksa, and S. Russenschuck, "Calculation of persistent currents in superconducting magnets," *Physical Review Special Topics-Accelerators and Beams*, vol. 3, no. 12, p. 122402, 2000.

- [119] S. Russenschuck, "Field computation for accelerator magnets: analytical and numerical methods for electromagnetic design and optimization." John Wiley & Sons, 2011.
- [120] R. Wolf, "Persistent currents in LHC magnets," *IEEE transactions on magnetics*, vol. 28, no. 1, pp. 374-377, 1992.
- [121] S. Caspi, W. Gilbert, M. Helm, and L. Laslett, "The effects of filament magnetization in superconducting magnets as calculated by Poisson," *IEEE transactions on magnetics*, vol. 23, no. 2, pp. 510-513, 1987.
- [122] V. Kashikhin and A. Zlobin, "Calculation of coil magnetization effect in superconducting accelerator magnets," *Fermi National Accelerator Laboratory, Tech. Rep. TD-00-010*, 2000.
- [123] G. Sabbi and X. Wang, "20 T Block Dipole: Features and Challenges," presented at the 2015 ICFA Mini Workshop on High Field Magnets for Future pp Colliders, Shanghai, China, 2015.
- [124] J. DiMarco *et al.*, "Application of PCB and FDM technologies to magnetic measurement probe system development," *IEEE transactions on applied superconductivity*, vol. 23, no. 3, pp. 9000505-9000505, 2012.